University of Cyprus

Faculty of Engineering

Department of Mechanical and Manufacturing Engineering

In silico studies for the prediction of regional aerosol deposition in the human airways

Doctor Of Philosophy Dissertation

Pantelis G. Koullapis

2018

University of Cyprus

Faculty of Engineering

Department of Mechanical and Manufacturing Engineering

In silico studies for the prediction of regional aerosol deposition in the human airways

Pantelis G. Koullapis

A Dissertation Submitted to the University of Cyprus in Partial Fulfillment of the Requirements for the Degree of Doctor of Philosophy

May 2018

VALIDATION PAGE

Doctoral Candidate: Pantelis G. Koullapis

Doctoral Thesis Title: *In silico* studies for the prediction of regional aerosol deposition in the human airways

The present Doctoral Dissertation was submitted in partial fulfillment of the requirements for the Degree of Doctor of Philosophy at the ***Department of Mechanical and Manufacturing Engineering*** *and was approved on the 28th of May of 2018 by the members of the* ***Examination Committee****.*

Examination Committee:

Research Advisor: Stavros Kassinos, Professor
University of Cyprus

Internal Committee Member: Andreas Alexandrou, Professor
University of Cyprus

Internal Committee Member: Dimokratis Grigoriadis, Assistant Professor
University of Cyprus

External Committee Member: Roberto Verzicco, Professor
University of Rome 'Tor Vergata'

External Committee Member: Michalis Lazaridis, Professor
Technical University of Crete

DECLARATION OF DOCTORAL CANDIDATE

The present doctoral dissertation was submitted in partial fulfillment of the requirements for the degree of Doctor of Philosophy of the University of Cyprus. It is a product of original work of my own, unless otherwise mentioned through references, notes, or any other statements.

Doctoral Candidate: Pantelis G. Koullapis

Περὶληψη

Η πρόβλεψη των χαρακτηριστικών της σωματιδιακής εναπόθεσης στους αεραγωγούς του ανθρώπινου πνεύμονα αποτελεί χρήσιμη πληροφορία στην ανάπτυξη εισπνεόμενων φαρμάκων αλλα και για την αξιολόγηση των επιπτώσεων στην ανθρώπινη υγεία της έκθεσης σε αιωρούμενα σωματίδια. Εκτίμηση της σωματιδιακής εναπόθεσης μπορεί να γίνει με μεθόδους ιατρικής απεικόνισης, οι οποίες όμως συνήθως επιβάλλουν έκθεση σε επιβλαβή ακτινοβολία και έτσι αποφεύγονται. Η ανάπτυξη των υπολογιστών τα τελευταία χρόνια, έχει καταστήσει τις μεθόδους υπολογιστικής ρευστομηχανικής μια προσιτή λύση που μπορεί να συμπληρώσει τις πειραματικές μεθόδους ενώ μπορεί να δώσει λεπτομερή εικόνα τόσο για τα χαρακτηριστικά της εναπόθεσης αλλά και της ροής του αέρα διαμέσου των αεραγωγών. Η παρούσα διδακτορική διατριβή έχει σαν στόχο την περαιτέρω ανάπτυξη και χρήση υπολογιστικών μεθόδων για την μελέτη της ροής του αέρα και της εναπόθεσης σωματιδίων στο ανθρώπινο αναπνευστικό σύστημα. Επιπρόσθετα, στοχεύει στην ανάπτυξη μεθόδων που θα οδηγήσουν σε μείωση του υπολογιστικού κόστους που απαιτείται για την προσομοίωση ολόκληρου του ανθρώπινου πνεύμονα.

Στο πρώτο μέρος μελετάται η μεταφορά και εναπόθεση σωματιδίων σε μια ρεαλιστική γεωμετρία του ανώτερου αναπνευστικού συστήματος που ανακατασκευάστηκε από δεδομένα ιατρικής απεικόνισης χρησιμοποιώντας την μέθοδο προσομοίωσης μεγάλων δινών για την επίλυση του πεδίου ροής. Εξετάστηκε η επίδραση ενός ρεαλιστικού προφίλ ταχύτητας εισόδου, το οποίο βρέθηκε να οδηγεί σε αυξημένη εναπόθεση κυρίως στην περιοχή της γλώσσας, συγκριτικά με την περίπτωση ομοιόμορφης κατανομής ταχύτητας στην είσοδο. Επιπλέον, εξετάστηκε η επίδραση της παροχής εισπνεόμενου αέρα και της ηλεκτροστατικής φόρτισης των σωματιδίων στα χαρακτηριστικά εναπόθεσης του ειπνεόμενου αερολύματος. Συνολικά, παρατηρήθηκε σημαντική αλληλεπίδραση μεταξύ του μεγέθους του σωματιδίου, του ηλεκτροστατικού του φορτίου και της παροχής εισπνεόμενου αέρα.

Στο δεύτερο μέρος της εργασίας μελετάται η επίδραση της γεωμετρίας των εξωθωρακικών αεραγωγών στην εναπόθεση σωματιδίων στους άνω βρογχικούς αεραγωγούς σε συνθήκες σταθερής εισπνοής που συναντώνται σε περιπτώσεις χορήγησεις εισπνεόμενων φαρμάκων. Ο στόχος είναι να διερευνηθεί κατά πόσον μπορούν να χρησιμοποιούνται τυποποιημένες γεωμετρίες εξωθωρακικών αεραγωγών για να γίνει ακριβής πρόβλεψη των

χαρακτηριστικών εναπόθεσης στους άνω βρογχικούς αεραγωγούς ενός ασθενούς. Το κέρδος από ενδεχόμενη χρήση τυποποιημένης γεωμετρίας εξωθωρακικών αεραγωγών είναι η μείωση στο χρόνο πρόβλεψης της τοπικής εναπόθεσης, που μπορεί να συνεισφέρει στην αποτελεσματικότερη χορήγηση εισπνεόμενων φαρμάκων για την θεραπεία παθήσεων των άνω βρογχικών αεραγωγών (πχ. άσθμα). Τα αποτελέσματά μας δείχνουν ότι η εναπόθεση σωματιδίων στους άνω βρογχικούς αεραγωγούς μπορεί να υπολογιστεί με αρκετή ακρίβεια εάν είναι γνωστή η κατανομή μεγέθους των σωματιδίων που εξέρχεται από τους εξωθωρακικούς αεραγωγούς. Επιπλέον, τα ευρήματά μας υποδεικνύουν ότι σε περιπτώσεις όπου μελετάται η εναπόθεση σωματιδίων στους άνω βρογχικούς αεραγωγούς για συγκεκριμένους πληθυσμούς, το υπολογιστικό κόστος μπορεί να μειωθεί χρησιμοποιώντας τυποποιημένες γεωμετρίες εξωθωρακικών αεραγωγών για τις οποίες το πεδίο ροής έχει υπολογιστεί εκ των προτέρων. Σε αυτή την περίπτωση μπορούν να αξιοποιηθούν οι διαθέσιμες βάσεις δεδομένων αξονικής τομογραφίας θώρακα για να εξαχθούν συμπεράσματα όσον αφορά τα χαρακτηριστικά εναπόθεσης στο συγκεκριμένο πληθυσμό.

Στο τρίτο μέρος της εργασίας αναπτύσσεται μέθοδος για την πρόβλεψη της σωματιδιακής εναπόθεσης σε μοντέλο που περιλαμβάνει βρογχικό δέντρο 10 γενεών ενωμένο με αναπνευστικές κυψελίδες. Για να γίνει δυνατή η προσομοίωση, το μοντέλο αποσυνδέεται λαμβάνοντας υπόψην τις συνθήκες στρωτής ροής με χαμηλούς αριθμούς Reynolds και την απλοποιημένη γεωμετρία. Συνεπακόλουθα, προσομοιώνεται μόνον μια διακλάδωση ανά γενιά στο βρογχικό δέντρο και ένα μοντέλο αναπνευστικής κυψελίδας, τόσο για την φάση του αέρα όσο και για την σωματιδιακή φάση, για την οποία λαμβάνεται υπόψην η πραγματική θέση των σωματιδίων στο μοντέλο ώστε να γίνεται ορθός υπολογισμός των δυνάμεων βαρύτητας. Αυτό έχει σαν αποτέλεσμα την σημαντική μείωση του υπολογιστικού κόστους και καθιστά εφικτή την προσομοίωση μεγάλων περιοχών του ανθρώπινου πνεύμονα. Η προτεινόμενη μέθοδολογία μπορεί να χρησιμοποιηθεί σε μελέτες εναπόθεσης σε μοντέλα ασθενούς ή παιδικού πνεύμονα. Επιπρόσθετα, μπορούν να εξαχθούν μαθηματικές σχέσεις που περιγράφουν την εναπόθεση οι οποίες στη συνέχεια να χρησιμοποιηθούν σε απλουστευμένα αναλυτικά μοντέλα για γρήγορους υπολογισμούς.

Abstract

Knowledge of aerosol deposition characteristics in the human airways is important in pulmonary drug delivery as well as in assessing health effects of inhaled pollutants. Determination of deposited aerosol dose can be accomplished *in vivo*, *in vitro* or *in silico*. *In vivo* techniques describe the real state but their usage remains limited due to insufficient spatial resolution and concerns over patient exposure to radiation. *In vitro* methods allow systematic studies on particle size and flowrate effects, but they are costly and time-consuming and cannot easily be performed on a routine basis. *In silico* methods can fill this gap by providing detailed information about regional deposition and airflow characteristics in the human airways. The objective of this thesis is to advance the use of Computational Fluid-Particle Dynamics (CFPD) tools in studies related to aerosol transport and deposition and provide new insights concerning airflow physics and deposition mechanisms in both the upper airways and the peripheral lung. In addition, towards high resolution simulations of airflow and particle deposition in the entire lung, our goal is to develop methods that lead to reductions in the associated computational costs.

In the first part, airflow and particle deposition in a realistic geometry of the human upper airways derived from computed tomography scans, is examined using Large Eddy Simulations. A realistic inlet velocity profile, measured at the breathing zone of a thermal breathing manikin was used to assess the effect of inlet conditions on deposition in the extrathoracic airways. We have found that realistic inlet conditions result in enhanced deposition, mostly on the tongue. Furthermore, the influence of inhalation flowrate and electrostatic charge carried by particles on deposition was examined. Overall, we observe a significant interplay between particle size, electrostatic charge, and flowrate.

In the second part, we have carried out a numerical investigation in order to determine the effect of the extrathoracic airways on regional deposition in the tracheobronchial airways. The goal is to examine whether standardized mouth-throat models can be utilized for accurate deposition predictions in the tracheobronchial airways resulting in significant reductions in the computational cost. Our results

suggest that accurate predictions of regional deposition in the tracheobronchial airways can be obtained if the particle size distribution that escapes filtering in the mouth-throat of a particular patient is known or can be estimated. These findings open the prospect for significant reductions in the computational expense, especially in the context of *in silico* population studies, where the aerosol size distribution and precomputed flow field from standardized mouth-throat models could be used with large numbers of tracheobronchial geometries available from chest computed tomography scans.

In the third part, we introduce an efficient CFPD-based methodology for the prediction of aerosol deposition in the deep lung under various breathing scenarios. In the proposed methodology, the computational cost is reduced by taking advantage of the flow similarity in the distal regions of the lung. Topological information is used to account for the correct gravitational force on the particles, emulating their transport characteristics in the actual tree. The developed methodology can be adopted for future studies in diseased models of the peripheral lung or models of a child's lung. Furthermore, the outcomes of the CFD methodology for a range of factors known to influence aerosol transport in the deep lung can be used to extend the predicting capabilities of simpler analytical 1-D models.

Acknowledgements

First and foremost I wish to express my deep gratitude to my academic advisor, Prof. Stavros Kassinos, for giving me the opportunity to pursue my Ph.D. at the Computational Sciences Lab. His guidance and support have been invaluable to me over the past few years, helping me to deeply understand the topics, develop my personal skills and giving me the opportunity to travel, meet and work with experts from all around the world. I appreciate his many contributions in this work including insights, advices, easy accessibility, sharing ideas on many issues and reviewing my publications and dissertation.

I am deeply grateful to Prof. Dimokratis Grigoriadis for his advises during the initial stages of my Ph.D. and also sharing his expertise on various topics with me. I would like to thank Prof. Andreas Alexandrou for his insightful comments and for participating in my dissertation committee. I wish to thank Prof. Mihalis Lazaridis for giving me the opportunity to participate in HEXACOMM, attend to very interesting training schools and meet with experts on the field of environmental aerosols. I also want to thank him for participating in my dissertation committee as an external member. I would like to thank Prof. Roberto Verzicco for finding time in his very busy schedule to serve as an external member of my dissertation committee.

I am highly indebted to my officemate Dr. Fotos Stylianou for his guidance and support in all aspects of my Ph.D., from understanding of physical mechanisms to computer related issues. I also thank him for providing a cordial and fun filled environment. I do not have enough words to express my gratitude to my fellow officemate Dr. Konstantinos Panagiotou, for his support throughout difficult times and making us laugh with his jokes and stories.

My appreciation goes to Dr. Hari Radhakrishnan for sharing his expertise as well as providing solutions to all computer related issues. I am also thankful to Dr. Nicolas Kanaris for his support as well as the memorable experiences from our journey in Australia to attend TSFP9. For their meaningful advice, the joyful lunch breaks as well as the thrilling football matches we had, I would like to thank Charalambos Frantzis, Andreas Demou and Efstratios Fonias.

I would also like to express my gratitude to the people that hosted me in their institutions and I have collaborated with: Dr. Maria Bivolarova and Prof. Arsen Melikov from Technical University of Denmark and Prof. Josue Sznitman and his group members from Technion Biofluids Lab in Haifa. My special appreciation goes to Dr. Laura Nicolaou for her contribution in my work including sharing thoughts, experise and her help in writing the manuscripts.

I would like to pay high regards to my parents who have always been proud and supportive in all my educational pursuits.

I take this opportunity to acknowledge the financial support I received from the European Union 7th framework program HEXACOMM FP7/2007-2013 under Grant agreement no. 315760. In addition, I would like to acknowledge the financial support provided by COST-European Cooperation in Science and Technology, to the COST Action MP1404: Simulation and pharmaceutical technologies for advanced patient-tailored inhaled medicines (SimInhale).

Pantelis G. Koullapis
May 2018

This thesis is dedicated to

all those who have supported me in all forms during my PhD studies

Contents

List of Figures

List of Tables

Chapter 1

Introduction

1.1 Background

Knowledge of aerosol deposition characteristics in the human airways is of major significance in two main research areas, namely, human exposure to aerosol pollutants and drug delivery via the pulmonary route. In the former case, the aim is to evaluate the health effects of inhaled pollutants on lung tissue and establish adequate environmental exposure standards (Housiadas and Lazarides, 2010). This is important if we consider that a human adult inhales over 10,000-15,000 liters of air per day which might contain potentially harmful respirable particles such as cigarette smoke, air pollutants, allergens, and microbes. A fraction of the inhaled pollutants deposits on the lung surface and if these are not properly dealt with by the lung's defense mechanisms, can lead to respiratory diseases and injury to the lungs. In pulmonary drug delivery, our goal is to achieve effective delivery of inhaled drug aerosols for both local and systemic therapies (Smyth and Hickey, 2011). Local therapies refer to the treatment of airway diseases and have been used for over 50 years. Inhaled drug aerosols can also be delivered to the bloodstream by depositing the aerosols in the alveolar region, where the drug can cross the alveolar epithelium and enter the blood (Patton et al., 2004). Recent advances in the development of particle technologies and devices now make it possible to formulate, stabilize, and accurately deliver almost any drug to the lungs. Drug administration for systemic therapies through the pulmonary route offers several advantages over conventional methods, such as through oral or by injection: it is more convenient, can have decreased adverse reactions and the lungs are far more permeable to macromolecules than any other portal of entry into the body. Moreover, no other noninvasive route of delivery provides the speed of action that an inhaled drug can provide. On the other hand, there might be limited bioavailability of certain inhaled drug formulations, resulting in poor absorption and insufficient treatment.

Determination of deposited aerosol dose can be accomplished *in vivo*, *in vitro* or

in silico. *In vivo*, deposition patterns can be determined using nuclear imaging techniques, such as 2D gamma scintigraphy, single photon emission computed tomography (SPECT), or positron emission tomography (PET), by the addition of a radiolabel to the aerosol formulation (Conway, 2012). These methods have the advantage of describing the real state, but remain limited by a number of challenges. Despite significant progress in the fidelity of pulmonary imaging (Darquenne et al., 2016), spatial resolution still remains insufficient for the visualization of localized deposition, while expense and patient exposure to radiation also remain a concern. Furthermore, the resulting data often involves a relatively large degree of uncertainty due to difficulties in controlling acquisition parameters. These include breathing and drug inhalation patterns, and a large intersubject variability associated with morphological factors.

In vitro, regional deposition in the tracheobronchial (TB) tree can be determined by using replicas of human airways derived from Computed Tomography (CT) scans, and because higher doses of radioactivity can be applied, they often provide better spatial resolution relative to *in vivo* methods. However, they are time-consuming and cannot easily be performed on a routine basis. Time and expense become prohibitive in the context of large-scale population studies, where one seeks to establish correlations between airway functional or structural parameters and regional deposition patterns. In inhaled drug delivery applications, the current industry standard is the use of pharmacopeial induction ports mounted on cascade impactors, which provides estimates of total lung deposition (Olson et al., 2013). However, when the bioavailability of the drug is less than 100%, the deposited lung dose is overpredicted due to mucociliary clearance of the dose fraction deposited in the TB region (Olsson and Backman, 2014). In this case, the efficacy of drug delivery depends, in part, on the site of deposition within the airways. Therefore, quantifying regional deposition is important in assessing and optimizing the systemic delivery of drugs with limited lung bioavailability, as well as in topical treatments requiring the targeting of specific lung sites. The above mentioned considerations elucidate the limitations of measuring deposition *in vitro*.

In silico models can complement *in vivo*/*in vitro* tests and provide detailed information on regional deposition patterns. They can be used to perform repeated numerical experiments aiming to isolate the effect of a particular variable, something that is difficult to achieve *in vitro* or *in vivo*. *In silico* methods can be divided into two broad categories: one-dimensional whole-lung models, which historically were the first to be introduced, and three-dimensional Computational Fluid Dynamics (CFD) simulations, which are now becoming increasingly prevalent (Longest and Halbrook, 2012). The first category provides deposition estimates obtained from analytical equations or empirical correlations (Hofmann, 2011). Although these models can predict deposition throughout the entire lung, they lack the ability to describe site-specific deposition within individual airways of the lung. In contrast, modern CFD tools allow for the prediction of deposition patterns within specific regions of interest in the lung

(Lambert et al., 2011; Koullapis et al., 2016). The governing equations for the airflow and particle transport are solved numerically to simulate the aerodynamics and deposition behavior of inhaled aerosols in the airways. Complex effects such as geometric variability, breathing patterns and aerosol characteristics can be taken into account in CFD models. However, their high computational cost limits these studies to a small subset of the respiratory tract. In addition, anatomically-accurate models of the upper airways are typically restricted to the first seven or eight generations due to limits imposed by medical imaging resolution. Nevertheless, CFD models can provide valuable insights into the airflow and particle dynamics in the entire human lung.

1.2 The human respiratory tract

The lungs are the primary organs of respiration in humans. The geometry of the respiratory tract is not well known, due to the much fine detail in the lung, such as the existence of millions of alveoli with diameters of the order of $300\mu m$, each of which has a different shape. Furthermore, the geometry of the respiratory tract is time-dependent since the fine structures in the lung fill and empty with breathing. The geometry also varies with gender and from individual to individual and can be modified due to disease-induced airway remodeling.

Topologically, the lungs consist of a series of bifurcating pipes that become progressively smaller and smaller. These pipes bifurcate approximately 17 times and allow for a progressive increase in surface area and a corresponding decrease in air velocity. They lead to the alveoli and the respiratory tract ends at the alveolar sacs. Fig. 1.1 displays a schematic of the airway generations in the human adult lung, along with airway dimensions (diameters, lengths and total cross sectional area) and the number of branches of a particular generation. The airway diameter decreases approximately two orders of magnitude as we move from the proximal airways of the trachea and main bronchi to the terminal bronchioles. The enormous number of branches in the respiratory zone ($\approx 2^{23}$ end branches) results in a total surface area for gas exchange of about 70-140m^2 in the adult lung. In total the respiratory zone makes up most of the lung, with its volume being about 2.5-3 litres at rest in comparison to the conducting airways that make up 150mL (anatomic dead space).

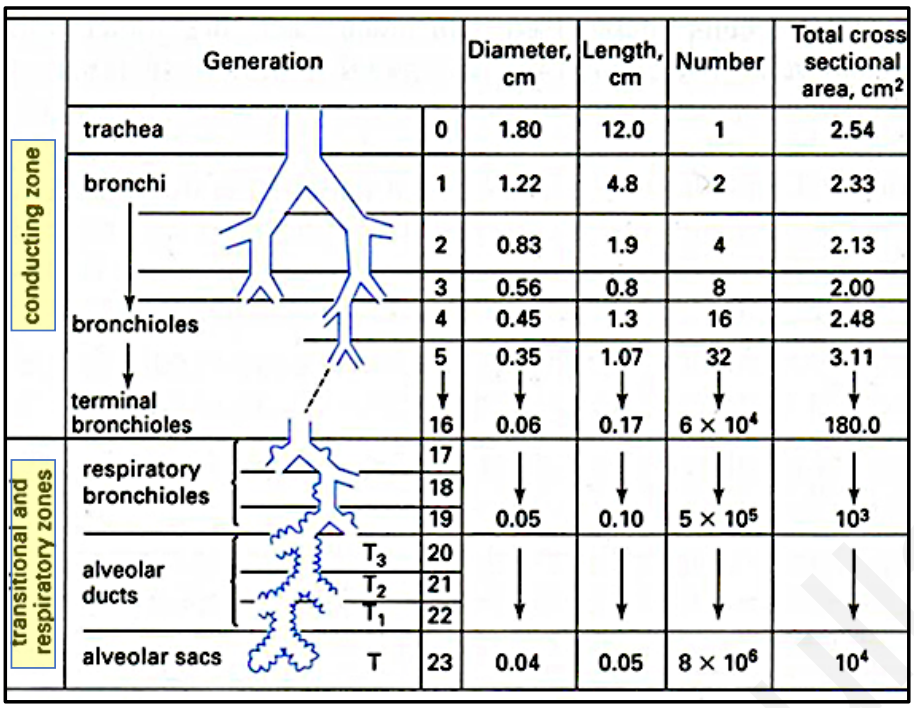

Figure 1.1: *Schematic of the airway generations in the human adult lung. Diameters, lengths, number of branches and total cross sectional area in a particular generation are reported. (redrawn from Weibel (1963)).*

The respiratory tract can be divided in three regions:

1. The extrathoracic region or the upper airways, shown in fig. 1.2(a), which consists of the respiratory tract proximal to the trachea and includes the oral cavity (or mouth), the nasal cavity (or the nose) and the throat, that contains the larynx and the pharynx.

2. The tracheobronchial region or the lower airways, which consists of the airways that conduct air from the larynx to the gas exchange regions of the lung. This region starts with the trachea, passes through the bronchi and ends at the terminal bronchioles. Taken together, the extrathoracic and the tracheobronchial airways are called the conducting airways since they conduct air to the gas-exchange regions of the lung.

3. The alveolar region (or parenchyma or pulmonary region), located distal to the tracheobronchial region and includes all parts of the lung that contain alveoli. The term acinus (meaning berry in Latin) denotes all parts distal to a single terminal bronchiole and on average is beyond the sixteenth generation (Haefeli-Bleuer and Weibel, 1988). The acinus is therefore comprised of respiratory airways and forms the functional tissue of the lung, or, the lung parenchyma. A schematic of an acinus is shown in fig. 1.2(b). The most proximal respiratory bronchioles, which originate from the terminal bronchioles, have relatively few alveoli exiting off them and as we move deeper into the lung, each generation of respiratory

bronchioles has increasingly more alveoli on them, until reaching the alveolar ducts, which are entirely covered with alveoli. The respiratory zone ends in the terminal alveolar sacs.

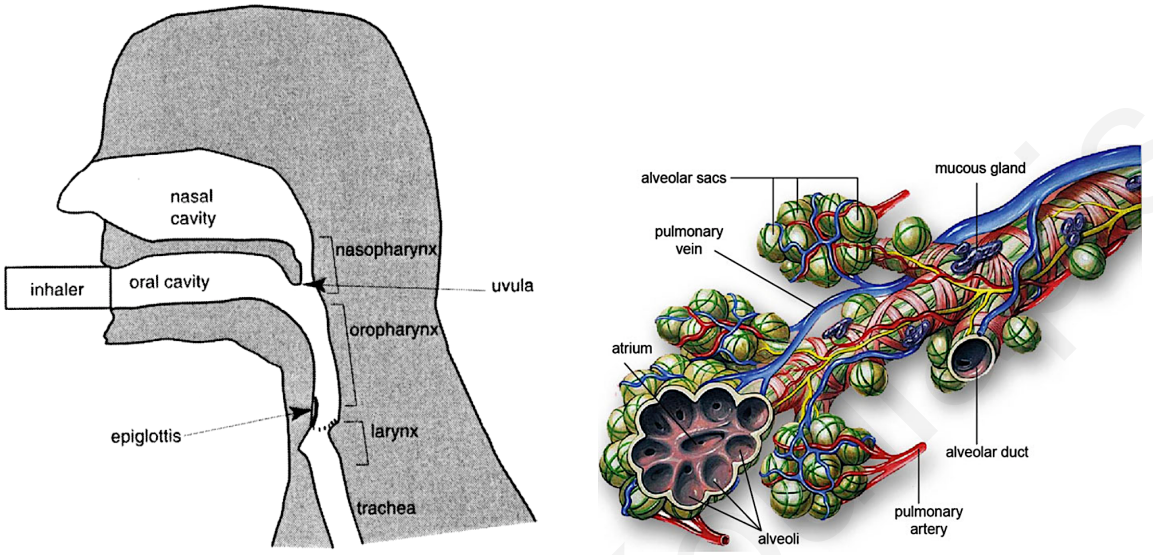

Figure 1.2: *(a) Schematic of the airways in the extrathoracic region (reproduced from Finlay (2001)). (b) Acinus region showing the alveolar ducts and sacs (original drawing courtesy of Patrick J. Lynch, medical illustrator).*

C-shaped cartilaginous rings hold and support the trachea, which cause it's inner surface to have a corrugated shape which can affect the airlow. There are 16-20 rings, which prevent the trachea from collapsing in and provide some flexibility for any neck movement. In the subsequent main bronchi, the cartilage support becomes progressively smaller and less complete. The tracheobronchial airways are composed of a gradually thinning columnar epithelium populated by many mucus and ciliated cells that collectively form the mucociliary escalator. Fig. 1.3 shows a comparison of lung epithelium at different sites within the lungs. The ciliated cells, called cilia and look like fine hairs, move back and forth in a rhythmical movement and drive the secreted mucous layer to the throat where it is swallowed into the digestive system. This mucociliary action acts as the clearing mechanism of the conducting airways from the deposited aerosols. In a healthy person, the mucus moves upward at a rate of about 1 mm/min in the small peripheral airways but can be as quick as 20 mm/min in the trachea.

There are no cilia or mucous producing cells in the alveolar epithelium; these are replaced primarily (>95% of surface) by the very broad and extremely thin type 1 cells and foreign particles are removed by alveolar macrophages instead of mucociliary action.

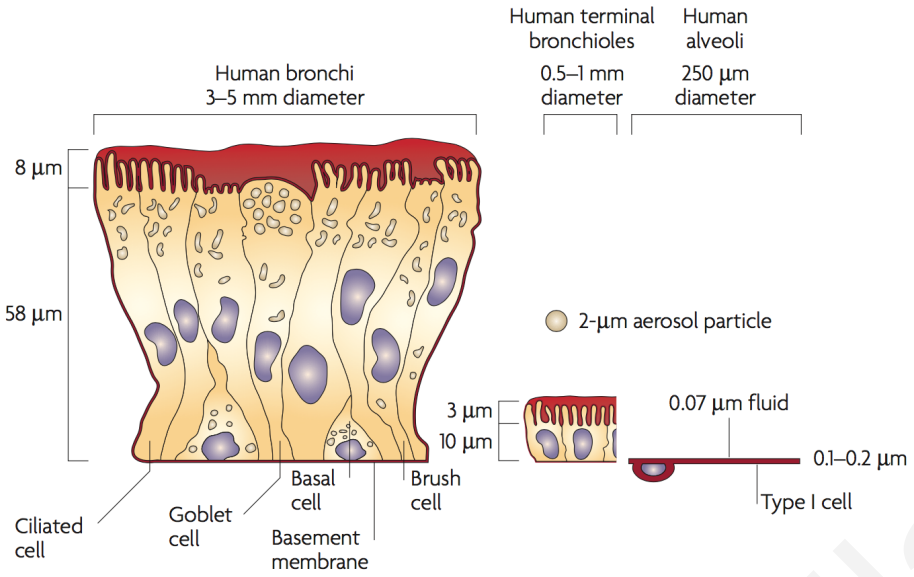

Figure 1.3: *Comparison of lung epithelium at different sites within the lungs. Reproduced from Patton and Byron (2007).*

1.3 Human exposure to aerosol contaminants

Inhalation of toxic airborne pollutants such as asbestos, acid mist, smoke, and fuel fumes is a frequent occurrence for those working in the manufacturing and processing industries. Furthermore, with more people travelling by air nowadays, pathogens can spread faster and in greater numbers in all over the planet, leading to acute epidemic outbreaks of infectious diseases (Zhang et al., 2009b; Se et al., 2010). Even indoor air in residential buildings is polluted by occupants due to the continuous body released bio-effluents, the exhaled air and by bio-aerosol shedding from the skin, clothes and hair (Bivolarova, 2017). Various routine human activities like cooking, smoking, vacuuming, cleaning and walking are also major contributors to the indoor air pollution burden (Kierat et al., 2018). Airborne particles enter the body through the nose or mouth, leading to deposition within the respiratory system, which in turn has many potential health risks. Although the human respiratory system incorporates natural defensive mechanisms, such as the mucociliary clearance, toxic respirable particles, especially in the ultrafine range, might deposit deep into the respiratory tract, penetrate the lung epithelium and cause adverse health problems.

Realistic inhalation dosimetry modeling provides valuable information on the complete exposure-dose-response relationship, as required in environmental pollutant health effects analyses. For example, local deposition sites were found to play a central role in health effect assessments (Schlesinger and Lippmann, 1978) and the prediction of lung cancer development (Balashazy et al., 2003). Therefore, evaluating the human exposure in both indoor and outdoor environments is of great significance.

1.4 Drug delivery through the pulmonary route

Drug delivery via the pulmonary route is widely used for the treatment of pulmonary infections and respiratory diseases such as asthma, Chronic Obstructive Pulmonary Disease (COPD) and cystic fibrosis. More recently, the inhaled route has also emerged as a promising method for the systemic administration of drugs (Patton and Byron, 2007). Drug delivery through the lungs can also be directed for heart and brain treatments (de Kruijf and Ehrhardt, 2017; Miragoli et al., 2018). An advantage of pulmonary drug delivery is the potential for rapid (within seconds or minutes) systemic delivery of small-molecule therapeutics. Because of the huge surface area of the lungs, the highly dispersed nature of an aerosol, (hundreds of millions of particles per dose), good epithelial permeability and small aqueous volume at the absorptive surface, small molecules deposited in the lungs are very rapidly absorbed into the systemic circulation, with the fastest uptake of any route of delivery other than intravenous. In addition, drugs with low gastrointestinal bioavailability or post-prandial effects on bioavailability could potentially be more reliably and efficiently given as aerosols.

The delivered dose is usually introduced through the mouth via an atomizing delivery device such as dry powder or metered dose inhalers and nebulisers. The drug particle is released from the device and must pass through the extrathoracic airways and reach the preferred site of action. Inefficient drug delivery can arise, owing to early deposition in the extrathoracic regions or rapid particle removal by mucociliary or phagocytic clearance mechanisms, making it difficult to prolong a residence time to allow an effective drug release. Upon deposition, the lung's defence mechanisms by either mucociliary clearance or breakdown by macrophages and enzymes need to be overcome for effective delivery. Almost all of the resistance to systemic absorption of inhaled medicines into the blood stream occurs at the plasma membrane of the lung epithelium, shown in fig. 1.3. Exactly where in the lungs it is best to deposit a drug for optimum absorption is not clear, but some general principles are emerging. In general, the premier target for drug delivery will be the alveolar region of the deep lung, which presents the largest surface area and thinnest diffusion pathway for dissolved material. Studies have shown that the trachea presents >90% resistance to transport, limiting its potential in drug delivery (Wangensteen et al., 1993). Of course, there are examples of exceptions from this general rule. High-molecular-mass andibodies, such as immunoglobulins of the IgG class (150 kDa), were found to have better absorption in the larger airways, whereas small hydrophobic molecules are thought to be rapidly absorbed (within seconds) throughout the lungs by passive diffusion through the plasma membrane (Patton, 1996). For small peptides and insulin, it seems to be important to have the drug deposit in the distal airways right before the alveoli for optimum absorption rather than in the upper airways (Codrons et al., 2004).

1.5 Airflow in the human airways

Inhalation is initiated by the contraction of the diaphragm, that results in reduced pressure inside the thorax compared to the atmospheric pressure. In exhalation, the lung and chest wall return to its equilibrium position and shape and the pressure increases to release the air from the lungs. Airflow in the respiratory tract is driven by the pressure difference between the oral opening and the alveoli, where the pressure, though time varying, is approximately spatially uniform. Under most circumstances, airflow in the lung can be reasonably approximated as incompressible (Finlay, 2001).

The Reynolds number gives the ratio of inertial to viscous effects and is defined as:

$$Re = \frac{UD}{\nu} \tag{1.1}$$

where U is the bulk velocity in an airway, D is the airway diameter and ν is the kinematic viscosity of air. The Reynolds number is used to classify the flow as laminar or turbulent. In a circular pipe, for Reynolds number below 2300 the flow is laminar and transitions to turbulence for $Re > 4000$. In the intermediate regime ($2300 < Re < 4000$), the flow will begin to transition from laminar to turbulent and then back to laminar at irregular intervals. Fig. 1.4 plots the variation of Reynolds number throughout the airway generations for two flowrates typically found during quiet breathing (18 L/min) and heavy exercise or inhalation through an inhaler (60 L/min). At these flowrates, Reynolds number in the larynx ranges between 2000 to 10000. Even at the lower flowrates, and due to the complex geometry of the extrathoracic airways, that include bends, constrictions and expansions, airflow usually transitions to turbulence in the upper airways. The laryngeal jet formed at the glottis constriction produces much of this turbulence (Lin et al., 2007). It's characteristics bear a resemblance to the flow through a constricted pipe, which can be classified as a free shear flow where the wall serves to confine the spreading of the jet rather than producing turbulence (Tawhai and Lin, 2011). As we move deeper in the airways, Reynolds number decreases due to the overall increase of cross sectional area that the air passes through (see fig. 1.1). However, turbulent eddies generated in the upper airways may propagate into distal airways that would normally carry laminar flow based on their local Reynolds number. Zhang and Kleinstreuer (2004) predicted numerically that turbulent fluctuations from the trachea can persist downstream to third generation at inspiratory flowrates higher than 30 L/min. Similar observations were made by Lin et al. (2007) using a patient-specific airway model and a more advanced flow solver.

Turbulent effects eventually dissipate in the central airways (approximately in generations 4-6, depending on the inhalation flowrate) and the flow relaminarizes. Reynolds number further reduce as we move deeper in the conducting airways and

drop at about 1-10 as the air enters the alveolar region, depending on the breathing effort. In the acinus, Reynolds numbers span more than two orders of magnitude with Poiseuille-like velocity profiles characterizing the flow patterns inside the acinar ducts. Hence, fluid inertia is anticipated to remain negligible in the alveolar region.

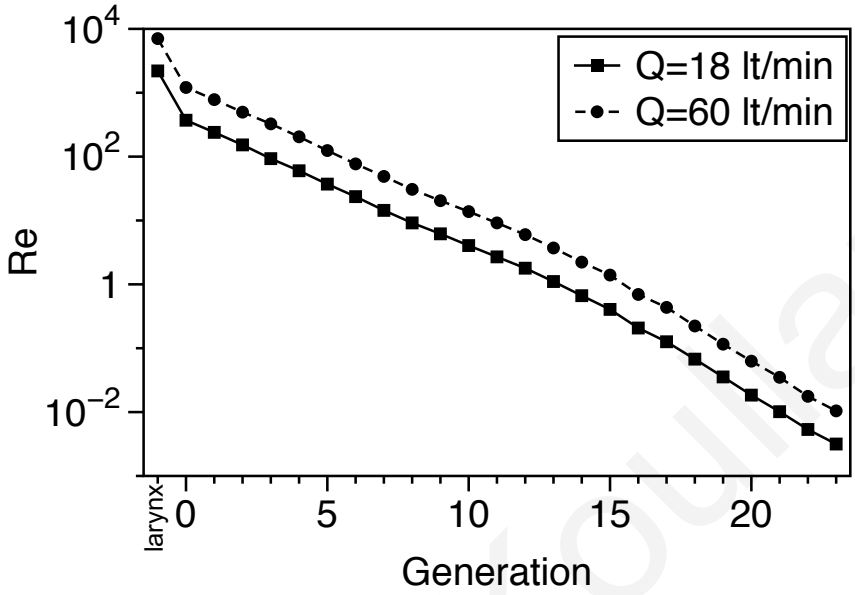

Figure 1.4: *Reynolds number versus airway generation number for two inhalation flowrates, 18 and 60 L/min (redrawn from Finlay (2001)).*

Besides classification of airflow as laminar or turbulent, the time-varying nature of breathing can also have an effect on airflow features. Two non-dimensional numbers are used to determine the importance of unsteadiness on the airflow. The Strouhal number (St) tells us how important the unsteady term is relative to the convective term and is defined as:

$$St = \frac{\tau U}{D} \tag{1.2}$$

where τ is a characteristic time, e.g. the inhalation period T. For very high St, we might be able to neglect the unsteady term relative to the convective term. The Strouhal number is used in the upper airways, where convective terms are larger than diffusive terms. The Womersley number (Wo) is more suitable to assess the importance of unsteadiness in the distal airways, since it is a measure of the importance of the unsteady to the viscous forces, given as:

$$Wo = \sqrt{\frac{Re}{St}} = D\sqrt{\frac{\omega}{\nu}} \tag{1.3}$$

where $\omega = 2\pi/T$ is the (angular) breathing frequency. At large Womersley numbers, unsteadiness is important compared to viscous forces. Fig. 1.5 plots the variation of Strouhal and Womersley number throughout the airway generations for tidal breathing (12 breaths/minute at a flowrate of 18 L/min). In the upper airways, Strouhal number

is quite high and unsteadiness in inhalation profile is not expected to play a large role in the fluid dynamics. Furthermore, from fig. 1.5 we can observe that Womersley number is lower than unity in much of the distal portions of the tracheobronchial region as well as in the respiratory zone. Therefore unsteady effects are less significant in comparison to the viscous forces in the peripheral lung. In reality, unsteady effects are important when the air velocity is low and it's rate of change is large. This usually occurs at the beginning of deep inhalation and at times between inhalation and exhalation during tidal breathing. In addition, airflow is inherently unsteady in regions where turbulence occurs.

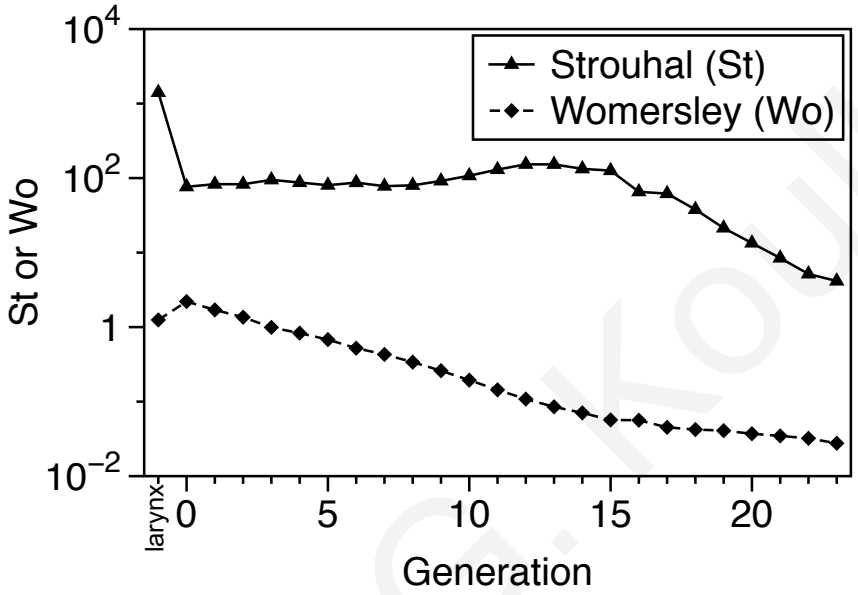

Figure 1.5: *Strouhal and Womersley number versus airway generation number for tidal breathing (12 breaths/minute at a flowrate of 18 L/min). Redrawn from Finlay (2001).*

There are three techniques for solving the Navier-Stokes equations for turbulent flow using a computer: direct numerical simulations (DNS), Reynolds averaged Navier-Stokes (RANS) and large eddy simulations (LES). DNS tracks the details of the instantaneous turbulent fluctuations at all scales, however, it is exceedingly costly to implement and beyond routine use on current computers. Presently, most CFD simulations solve only for the mean flow using the RANS equations, resulting in a tremendous reduction in computational cost. However, the laminar-turbulent-laminar flow transition in the conducting airways is challenging for RANS and care must be exercised to choose validated RANS models (Xi and Longest, 2007). In addition, dispersion of particles due to the turbulent velocity fluctuations is not well-captured with the widely used Eddy Interaction Models (Agnihotri et al., 2012) that are combined with RANS models. A more robust choice is the method of Large Eddy Simulations (LES), where only the smallest scales of motion (containing a small fraction of the kinetic energy) are discarded. The computational expense of LES is considerably higher than that of RANS, but it retains significantly more elements of the underlying turbulence physics

than RANS (Choi et al., 2009; Radhakrishnan and Kassinos, 2009). With constant gains in computing power, LES has become affordable for routine use and recent LES-based deposition studies have established the trustworthiness of the method (Jayaraju et al., 2008).

An issue that arises in CFD simulations of upper airway models derived from CT scans is the imposition of physiologically realistic boundary conditions at their multiple outlets. This is important since the ventilation distribution in the conducting airways is controlled by the boundary conditions imposed at the outlets of the model. Inappropriate specification of boundary conditions results in unrealistic ventilation and thus inaccurate particle deposition predictions. Non-uniform ventilation and pressure distribution are the hallmark chronic lung disease, such as emphysema and Chronic Obstructive Pulmonary Disease (COPD). Therefore, imposition of correct mass fractions, or pressure levels, at the outlets of a 3D CFD model must be propagated from the alveolar region back up to the distal ends of the 3D model. Several methods have been proposed in the literature to tackle this issue using reduced dimensional models (typically based on impedance or resistive models) (Comerford et al., 2010) or imaging methods (De Backer et al., 2008; Yin et al., 2013).

1.6 Aerosol transport and deposition in the human airways

The deposition of an inhaled particle is governed by its size. Inhaled aerosols, either pollutants or therapeutics, typically have diameters in the range of 0.01-100μm and they can be solid particles or droplets. Droplets have spherical shape whereas solid particles can be non spherical. When travelling along an airway, particles will be exposed to different physical mechanisms forcing them to leave the air streamlines and eventually deposit on the airway surfaces. The principal mechanisms acting upon inhaled aerosols are impaction due to inertial forces, sedimentation due to gravity and Brownian diffusion. Impaction is most effective in the upper airways, where air and particle velocities are higher than in the peripheral lung. On the other hand, particles in the alveolated region of the lung are preferentially deposited by diffusion and sedimentation due to smaller velocities and hence longer residence times. Small particles, say below 0.5μm, are deposited primarily by Brownian diffusion, while deposition by inertial impaction and sedimentation prevails for larger particles, producing the typical U-shape of the total deposition curve. Slow breathing is most effective for diffusion and sedimentation since it results in longer residence times, whereas impaction is higher for fast breathing due to higher velocities.

In addition to the above mentioned mechanisms, electrostatic charge carried by inhaled particles can also be an important determinant of deposition. Medical devices,

especially DPIs, often generate electrostatically charged aerosols (Byron et al., 1997; Kwok et al., 2005) whereas environmental aerosols may also carry significant charge and thus electrostatic charge must be taken into account in human health risk assessments (Forsyth and Liu, 1998).

In most of the current CFD studies for particle transport and deposition in the human lung, the underlying assumptions are that aerosol particles are spherical, don't interact between them and deposit upon contact with the mucus-covered airway surface. In reality, particles might be non-spherical, inter-particle collisions might occur and other complex phenomena can take place, such as hygroscopic growth or evaporation of droplets, aggregation and de-aggregation and rise of forces due to electrostatic charges carried by the particles. Only a few studies have considered such effects, namely, the motion of non-spherical particles (Feng and Kleinstreuer, 2013) and hygroscopicity effects in aerosol particles transport (Longest et al., 2010). Regarding the modelling method for the particle phase, a Lagrangian approach is usually employed for particles in the sub-micron range (Lambert et al., 2011; Koullapis et al., 2016), although its validity has also been verified for ultrafine particles ($d_p < 100nm$)(Longest and Xi, 2007). For particles below $150nm$ the Euler approach has been used in several studies Zhang and Kleinstreuer (2004). The advantage of using the Lagrangian approach combined with LES for the simulation of fluid flow and particle transport in the upper airways is that, due to the low to moderate Reynolds number of the flow and the simulation of particles with inertia, a stochastic diffusion model that accounts for the sub-grid scale contribution is usually not required since the turbulent velocity fluctuations are contained in the filtered velocity field Armenio et al. (1999).

1.7 Computational models of the human airways

Particle deposition studies in the human lung, both experimental and computational, require the existence of accurate airway models. The size ($\approx 2^{23}$ airway branches) and complexity (millions of different alveoli with effective diameters in the order of $300\mu m$) of the human lung don't allow the development or reconstruction (from medical imaging) of an entire human lung model.

Early *in silico* models relied on simplified representations of the human airways that, although being geometrically similar to the airway region of interest, left out key details that affect important output variables. Idealized models allowed us to elucidate the flow and particle dynamics in the airways without the added complexity of the realistic geometry, and can provide representative estimations of global deposition. For the extrathoracic airways, a number of idealized geometries have been developed, such as the University of Alberta replica, which is representative of a physiologically-averaged adult airway (Stapleton et al., 2000). Built from simple geometric shapes, it nonetheless

captures all the basic anatomical features of the real extrathoracic airways and has widely been used in the literature, both in numerical (Matida et al., 2004; Ball et al., 2008; Nicolaou and Zaki, 2016) and *in vitro* studies (DeHaan and Finlay, 2001; Grgic et al., 2004a; Johnstone et al., 2004). Others have adopted idealized geometries with variable circular cross-sections based on the hydraulic diameters of a human cast replica (Zhang et al., 2002; Kleinstreuer and Zhang, 2003; Radhakrishnan and Kassinos, 2009). For the tracheobronchial tree, several simplified models have been employed. One of the most commonly used is Weibel's model A, which consists of a fully symmetric tree structure (Weibel, 1963). In reality however, significant variation exists in the geometric parameters for any given generation. More realistic models consist of asymmetric branches with varying lengths, diameters and branching angles (Horsfield et al., 1971; Yeh and Schum, 1980). A number of studies have also been conducted in single and multi-level bifurcations of the tracheobronchial airways (Zhang et al., 2002; Stylianou et al., 2016).

Recent advancements in medical imaging have afforded us detailed views of the complex structures of the lung. Nowadays, patient-specific models are obtained from medical images of the airways, typically via computed tomography (CT) scans or magnetic resonance imaging (MRI), which are then digitally reconstructed via an image registration method (Choi et al., 2009; Lambert et al., 2011). Anatomically-accurate models are generally limited to the first 6 or 7 generations due to imaging resolution.

The focus of existing *in silico* studies are either the upper airways or the deep alveolar regions. In the former case, intrinsic flow phenomena and high depositional losses occur that result in high variability of the aerosol dose delivered to the lungs, whereas in the latter case the fraction of aerosol depositing in acinar region -and will most likely enter the blood circulation- can be estimated. For the upper airways, both patient-specific (Choi et al., 2009; Lambert et al., 2011; Nicolaou and Zaki, 2013) as well as characteristic models are used (Tian et al., 2011, 2015); the latter are models based on simple geometries that also retain basic anatomical features from medical scans as well as direct observations of living subjects. Regarding the alveolar region, simplified models that are based on morphometry studies are used, since image reconstruction at this scale is not feasible with current techniques (Sznitman, 2013; Hofemeier and Sznitman, 2015). Only a few studies have considered airflow and particle deposition in models of the airway tree representing the central and deep conducting airways, namely generations 4 to terminal bronchioles (Walters and Luke, 2010; Soni and Aliabadi, 2013), although idealised geometries were used in these cases. The estimated size of the computational mesh required for the simulation of the entire conducting zone of the human lung is approximately 720 billion cells, which is currently not affordable in routine computations (Walters and Luke, 2010).

1.8 Motivation, Objectives and Contributions

Regional deposition effects are important in pulmonary drug delivery as well as in assessing health effects of inhaled pollutants. Radiological imaging methods can be applied *in vivo* or *in vitro*, in order to quantify regional deposition. Although *in vivo* measurements play an irreplaceable role as they describe the real state, studies remain limited by the spatial and temporal resolutions of current imaging techniques, and by patient exposure to radiation. *In vitro* methods have the advantage of known geometric characteristics, allowing systematic studies on particle size and flow rate effects. However, they are costly and time-consuming and cannot easily be performed on a routine basis. *In silico* methods can fill this gap by providing detailed information about regional deposition in the human airways. It is therefore not surprising that the last 15 years have seen an exponential growth in the application of Computational Fluid-Particle Dynamics (CFPD) methods in this area. CFPD offer a powerful tool to predict localized deposition in the airways, in order to further our understanding of the aerosol dynamics and optimize inhaled drug delivery.

The objective of this thesis is to advance the use of CFPD tools in studies related to aerosol transport and deposition in the human airways. Specifically, we aim to provide new insights concerning airflow physics and deposition mechanisms in both the upper airways and the peripheral lung. Towards high resolution simulations of airflow and particle deposition in the entire lung, our goal is to develop methods that lead to reductions in the associated computational costs.

Below we list the contributions of this work:

- We assess the effect of a realistic inlet velocity profile on airflow and particle deposition in a patient specific geometry of the human upper airways. The realistic inlet velocity profile was measured at the breathing zone of a thermal breathing manikin using Laser Doppler Anemometry. We have found that realistic inlet conditions result in enhanced deposition, mostly on the tongue.

- The impact of electrostatic charge carried by aerosol particles on their deposition in the human upper airways is examined. Electrostatic charge is found to increase the overall deposition fraction of smaller particles by as much as sevenfold, with most of the increase located in the mouth-throat. Moreover, significant enhancement in deposition was found in the tracheobronchial airways in both left and right lung sub-regions. Overall, we observe a significant interplay between particle size, electrostatic charge, and flowrate.

- We carried out a numerical investigation in order to determine the effect of the extrathoracic airways on regional deposition in the tracheobronchial airways. The goal is to examine whether standardized mouth-throat models can be utilized for

accurate deposition predictions in the tracheobronchial airways resulting in significant reductions in the computational cost. Our results suggest that accurate predictions of regional deposition in the tracheobronchial airways can be obtained if the particle size distribution that escapes filtering in the mouth-throat of a particular patient is known or can be estimated. These findings open the prospect for significant reductions in the computational expense, especially in the context of *in silico* population studies, where the aerosol size distribution and precomputed flow field from standardized mouth-throat models could be used with large numbers of tracheobronchial trees available in chest-CT databases.

- We introduce an efficient CFD-based methodology for the prediction of aerosol deposition in the deep lung under various breathing scenarios. In the proposed methodology, the computational cost is reduced by taking advantage of the flow similarity in the distal regions of the lung. Eventually, airflow and particle transport at a certain generation level of the bronchial tree are simulated in single bifurcations, whereas a single acinar model is used for the alveolar region. The ability of the developed model to predict aerosol deposition is demonstrated for two case studies in chapter 5. The developed methodology can be adopted for future studies in diseased models of the peripheral lung or models of a child's lung. Furthermore, the outcomes of the CFD methodology for a range of factors known to influence aerosol transport in the deep lung can be used to extend the predicting capabilities of simpler analytical 1-D models.

1.9 Thesis Overview

This thesis is structured as follows. Chapter 2 introduces the mathematical equations that describe the airflow and the motion of the aerosol particles. Details on the modelling of the sub-grid scales in LES simulations and the relevance of the forces acting on the particles are discussed. The numerical methods used to solve the equations for the continuous and disperse phases are also presented.

In chapter 3, airflow patterns and deposition of inhaled aerosols in a patient-specific geometry of the human upper airways is investigated using LES. In particular, we assess the effects of inlet flow conditions, inhalation flowrate, particle size and electrostatic charge on the deposition characteristics.

In Chapter 4, we quantify the effect of geometric variation in the mouth and throat on regional deposition in the first generations of a realistic TB tree. The objective of this part is to examine whether standardized mouth-throat models can be utilized for accurate deposition predictions in the tracheobronchial airways resulting in significant reductions in the computational cost.

In Chapter 5, an efficient CFD methodology to predict aerosol deposition in the deep lung under various conditions is presented. The overall deposition predictions of the newly developed method agree rather well with the known deposition trends reported in the literature and the output of a 1D deposition model. The developed methodology can be adopted in future studies that deal with deposition in the diseased peripheral lung or the developing lung of children.

Chapter 6 completes this thesis by summarizing the main findings, as well as the concluding remarks related to this work.

Finally, the Appendices contain supplementary material linked to particular Chapters of this thesis.

Chapter 2

Computational Methodology

2.1 Outline

In this chapter, the mathematical equations that describe the airflow and the motion of the aerosol particles are presented. Details on the modelling of the sub-grid scales in LES simulations as well as their importance on the motion of the particles are discussed. The relevance of the forces acting on the particles is also analysed. The numerical methods used to solve the equations for the continuous and disperse phases, are presented in Sections 2.2.3 and 2.3.5, respectively.

2.2 Continuous Phase

2.2.1 Governing equations

As discussed in the previous chapter, airflow in the lungs can be laminar or turbulent, depending on the airway generation. In the current study, applications in the upper airways, where the flow transitions to turbulence, as well as in the more distal regions, where the flow is laminar, are examined. Thus the governing equations can differentiate depending on the case. In general, the airflow is described by the incompressible, isothermal Navier-Stokes equations:

$$\frac{\partial u_j}{\partial x_j} = 0 \tag{2.1}$$

$$\frac{\partial u_i}{\partial t} + \frac{\partial}{\partial x_j}(u_i u_j) = -\frac{1}{\rho}\frac{\partial p}{\partial x_i} + \frac{\partial}{\partial x_j}\left[\nu \frac{\partial u_i}{\partial x_j}\right]. \tag{2.2}$$

where $\mathbf{u}$ is the fluid velocity, p is the pressure and ρ and ν the density and the kinematic viscosity of air, respectively. These equations apply directly in DNS of turbulent flow or when the flow is laminar. In other words, these equations describe the airflow when

not any turbulence modelling is needed.

For applications where the flow transitions to turbulence, LES are performed. In this case, the airflow is described by the filtered set of incompressible Navier-Stokes equations, which are derived when a filtering process is applied to the Navier-Stokes equations,

$$\frac{\partial \bar{u}_j}{\partial x_j} = 0 \tag{2.3}$$

$$\frac{\partial \bar{u}_i}{\partial t} + \frac{\partial}{\partial x_j}(\overline{u_i u_j}) = -\frac{1}{\rho}\frac{\partial \bar{p}}{\partial x_i} + \frac{\partial}{\partial x_j}\Big[\nu \frac{\partial \bar{u}_i}{\partial x_j}\Big]. \tag{2.4}$$

Here, $\bar{u}_i$ and $\bar{p}$ are the resolved velocity component in the i-direction and the resolved pressure, respectively (the overbar denotes resolved quantities). In the above equations, the term $\overline{u_i u_j}$ requires knowledge of the unfiltered velocity field, which is unknown, so it must be modeled. The sub-grid scale (SGS) stress tensor τ_{ij} is defined as:

$$\tau_{ij} = \overline{u_i u_j} - \bar{u}_i \bar{u}_j \tag{2.5}$$

The functionally of sub-grid scale stress tensor is similar to the Reynolds stress in RANS modelling. The difference lies in the fact that the SGS stresses represent a much smaller part of the turbulent energy spectrum than the RANS turbulent energy. Therefore, the accuracy of the stress model in LES is less crucial than in RANS. It must be noted however, that if the turbulent dissipation in the small scales is not accurately represented by the SGS model it can lead to a buildup of energy in the resolved scales and computational instability. Substituting eqn. 2.5 in eqn. 2.4 yields:

$$\frac{\partial \bar{u}_i}{\partial t} + \frac{\partial}{\partial x_j}(\bar{u}_i \bar{u}_j) = -\frac{1}{\rho}\frac{\partial \bar{p}}{\partial x_i} + \frac{\partial}{\partial x_j}\Big[\nu \frac{\partial \bar{u}_i}{\partial x_j}\Big] - \frac{\partial \tau_{ij}}{\partial x_j} \tag{2.6}$$

2.2.2 Sub-grid Scale Modelling in LES

The sub-grid scale stress tensor in eqn. 2.6 must be modelled. The majority of existing sub-grid scale models are eddy-viscosity models of the form:

$$\tau_{ij} - \frac{\delta_{ij}}{3}\tau_{kk} = -2\nu_T \bar{S}_{ij}, \tag{2.7}$$

that relate the sub-grid scale stress tensor to the large-scale strain-rate tensor $\bar{S}_{ij} = \frac{1}{2}\big(\frac{\partial \bar{u}_i}{\partial x_j} + \frac{\partial \bar{u}_j}{\partial x_i}\big)$. In most cases, algebraic equations are used to obtain the eddy viscosity. This can be explained by the fact that small scales tend to be more homogeneous and isotropic than the larger ones and it is expected that even simple algebraic models can capture their influence on the flowfield. In addition, since the sub-grid scale stress only account for a fraction of the total stresses, modeling errors should not affect the overall accuracy of the results. Finally, algebraic models are preferred than solving additional

partial differential equations that will increase the computational cost of the simulation. The first algebraic model, introduced back in 1963, was the Smagorinsky model,

$$\nu_T = (C_s\bar{\Delta})^2|\bar{S}| \tag{2.8}$$

where C_s is the Smagorinsky constant and $\bar{\Delta}$ is the filter size, usually taken as the cubic root of the cell's volume in arbitrary unstructured meshes. This model was derived from the simplifying assumption that the small scales are in equilibrium and dissipate entirely and instantaneously all the energy received from the resolved scales. The major drawback of Smagorinsky model relies on its excessive dissipation in laminar or high shear regions (caused by high $\bar{S}_{ij}$). A solution would be to decrease the value of C_S constant in these situations. This has been accomplished with some success for near-wall flows by using the van Driest damping function, which reduces the sub-grid eddy-viscosity as a function of wall-normal distance. This is however somewhat undesirable, as the SGS model should preferably depend exclusively on the local flow properties.

Another possibility is to use dynamic models. Germano et al. (1991) first proposed dynamic procedures in an attempt to formulate a more universal approach to SGS models. In dynamic models, the coefficients of the SGS model are computed dynamically as the calculation progresses, based on the energy content of the smallest resolved scales, rather than *a priori* input as in the Smagorinsky model. This is accomplished by assuming that the behaviour of the smallest resolved scales scales is very similar to the sub-grid scales. A second or "test" filter is defined, whose width $\widehat{\Delta}$ is larger than the original filter width, $\bar{\Delta}$ (typically $\widehat{\Delta} = 2\bar{\Delta}$). If this test filter is applied to the once-filtered Navier-Stokes equations eqn. 2.6 , the sub-grid stress that must be modeled in the test-filter level LES is given by,

$$T_{ij} = \widehat{\overline{u_i u_j}} - \widehat{\bar{u}}_i\widehat{\bar{u}}_j \tag{2.9}$$

At the test filter level, the large scale or resolved part of the SGS stress L_{ij} can be explicitly computed from the LES field as follows:

$$L_{ij} = \widehat{\bar{u}_i\bar{u}_j} - \widehat{\bar{u}}_i\widehat{\bar{u}}_j \tag{2.10}$$

Combining eqn. 2.5, 2.9 and 2.10 results in the Germano identity, that forms the basis of the dynamic model:

$$L_{ij} = T_{ij} - \widehat{\tau}_{ij} \tag{2.11}$$

Based on the above, Piomelli (1999) derived the following procedure for the calculation of SGS model coefficients. Firstly, a generalised eddy-viscosity model is defined to relate both sub-grid and sub-test grid stresses to their respective resolved fields, α_{ij}

and β_{ij}:

$$\tau_{ij} = -2C\alpha_{ij}, \qquad T_{ij} = -2C\beta_{ij} \tag{2.12}$$

Since the SGS stresses are modeled as above, substituting eqn. 2.12 into 2.11, the Germano identity can be satisfied only approximately. Moreover, the system is over-determined, with five independent equations available to determine a single coefficient. In order to overcome this problem, Lilly (1992) proposed that the error produced by the approximation be minimized in a least-squares sense. The error is:

$$e_{ij} = L_{ij} - T_{ij} + \widehat{\tau}_{ij} = L_{ij} + 2CM_{ij} \tag{2.13}$$

where $M_{ij} = \beta_{ij} - \widehat{\alpha}_{ij}$. The least-squares minimization preocedure requires that

$$\frac{\partial \langle e_{ij} e_{ij} \rangle}{\partial C} = 2 \Big\langle e_{ij} \frac{\partial e_{ij}}{\partial C} \Big\rangle = 0 \tag{2.14}$$

where the brackets denote an appropriate ensemble average. Substituting eq. 2.13 and its derivative in 2.14 implies:

$$\big\langle (L_{ij} + 2CM_{ij}) M_{ij} \big\rangle = 0 \tag{2.15}$$

which simplifies to give the required coefficient:

$$C = -\frac{1}{2} \frac{\langle L_{ij} M_{ij} \rangle}{\langle M_{ij} M_{ij} \rangle} \tag{2.16}$$

When the model coefficient is known, the sub-grid stresses can be evaluated using eqn. 2.12,

$$\tau_{ij} = -2C\bar{\Delta}^2 |\bar{S}| \bar{S}_{ij} \tag{2.17}$$

In eqn. 2.16, the ensemble average has the purpose of removing very sharp fluctuations of the coefficients, which tend to destabilize numerical calculations and make the model inconsistent. Germano et al. (1991) averaged the model coefficient over all homogeneous directions, thereby removing completely the mathematical inconsistency. However, this is possible only for flows with some degree of homogeneity. Another possibility is to perform localized filtering, for example over the scale of the test filter $\widehat{\Delta}$. Zang et al. (1993) performed this type of averaging and observed that the inclusion of the scale-similar part into their model decreased the magnitude of the dynamically computed model coefficient and prevent any excessive fluctuations. Besides the local averaging, they also applied a cut-off such that the total viscosity $(\nu + \nu_T)$ is greater than zero. This was required since the value of the model coefficient can be negative with magnitude greater than the molecular viscosity, resulting in negative total viscosity that can lead to unstable solutions.

2.2.3 Numerical solution

The three more common methods used for solving the Navier-Stokes equations are Finite Element (FE), Finite Differences (FD) and Finite Volume (FV). Other non-conventional approaches include spectral and the Lattice-Boltzmann methods. FD are simple to implement but their use is limited in rather simple canonical cases where cartesian grids can be generated. Due to their simple formulation, they allow the use of higher order schemes. For these reasons, FD are nowadays mainly used in research-orientated investigations.

FE methods do not require these considerations while retaining the potential for higher order accuracy. In FE, the solution is approximated by a linear shape function within each element such that continuity of the solution is guaranteed across element boundaries. Such a function can be constructed from its values at the corners of the elements. This approximation is then substituted into the weighted integral of the conservation law and the equations to be solved are derived by requiring the derivative of the integral with respect to each nodal value to be zero. This condition corresponds to selecting the best solution within the set of allowed functions. An important advantage of finite element methods is the ability to deal with arbitrary geometries. However, FE must be carefully formulated to be conservative in fluid dynamics problems, require more memory and has slower solution times than the FV.

FV methods are the most widely used nowadays, since it provides the best compromise of flexibility and accuracy for the problem at hand. The FV method uses the integral form of the conservation equations as its starting point. The solution domain is subdivided into a finite number of contiguous control volumes (cells) and the conservation equations are applied to each cell. Interpolation is used to express variable values at the cell surfaces using nodal or cell-center values. Algebraic equations for each CV are then derived, in which a number of neighbor nodal (or cell-center) values appear. An important advantage of the FV methods is the ability to deal with arbitrary geometries since any type of grid can be accommodated.

The flow equations that have to be solved are equation 2.2, in the case of laminar flows, and equation 2.6 when LES are performed. In the current study, the aforementioned equations are discretized and solved using the finite volume method in OpenFOAM, an open-source CFD code (OpenFOAM Foundation, 2013a,b). In this framework, unstructured boundary fitted meshes are used with a collocated cell-centred variable arrangement. The finite volume method in OpenFOAM is in general 2nd order accurate in space, depending on the convection differencing scheme (CDS) used. Whenever possible (usually in laminar flow cases), the 2nd order linear CDS is used. The order of accuracy had to be decreased in some cases in order to stabilize the simulation. In these cases, the clippedLinear scheme was used which provides a good compromise between the accuracy of the (2nd order) linear scheme and the stability of

the (1st order) mid-point scheme. The temporal derivative is discretized using backward differencing, which is is also second order accurate in time and implicit. Details on the finite volume discretization procedure and schemes in OpenFOAM are given in appendix A.

The non-linearity in the momentum equation is lagged in OpenFOAM (linearization of equation before discretisation, see appendix A.4). The system of partial differential equations is treated in a segregated way, with each equation being solved separately with explicit coupling between the results. Two algorithms are used in OpenFOAM for the pressure-velocity coupling. In turbulent flow applications, where the time step is kept small enough to capture the smaller turbulent time scales, the pressure-implicit split-operator algorithm, or PISO-algorithm, is used. The steps performed in this algorithm are:

- Predictor step: the momentum equation are solved resulting in an intermediate velocity field, which doesn't satisfy the continuity equation.
- First corrector step: a pressure equation is solved to obtain an intermediate pressure field. The solution of the pressure is followed by the projection of the velocities and fluxes into a divergence free form.
- Additional corrector step: the corrector step can be repeated until the dependent variables stop changing. Since the time steps in LES are generally small, this rarely requires more than 2-3 corrector steps.

In the case of unsteady laminar flows in the distal airways, larger time steps can be used to accelerate the simulation due to the quasi-steady character of the flow. The merged PISO-SIMPLE algorithm is used for the pressure velocity coupling in these situations. In PISO-SIMPLE algorithm, the momentum and pressure equations are solved multiple times in a time step until a predefined convergence criterion is reached. Usually one pressure corrector step and under-relaxation is used to achieve convergence. The derivation of the discretised form of the momentum equations and the pressure equation are explained in appendix A.

2.3 Dispersed phase

2.3.1 Particle equation of motion

Particle transport and deposition in the human airways can be analysed by the Eulerian and Lagrangian point-particle approaches. In the Lagrangian point-particle approach the motion of an individual particle is tracked as it moves through the fluid. In contrast,

particles are treated as a second continuous phase in Eulerian methods and partial differential equations for particle concentration and velocity have to be solved. As the number or the volume fraction of particles in the simulation increases, the computational cost in Lagrangian tracking can become prohibitively high and thus the Eulerian approach is used. On the other hand, Eulerian methods require constitutive modelling of the interaction forces and may have to be adjusted for different flow regimes whereas Lagrangian methods include microscopic transport processes and can also provide detailed information such as individual particle location, residence times and deposition sites. In the current work, a Lagrangian point-particle approach is adopted for the simulation of transport and deposition of particles in the human airways. The equation of motion for a spherical particle in a viscous fluid was derived by Maxey and Riley (1983):

$$m_p \frac{d\vec{u}_p}{dt} = \sum \vec{F} \tag{2.18}$$

where m_p and $\vec{u}_p$ is the mass and the instantaneous particle velocity, respectively, and $\sum \vec{F}$ is the sum of all forces acting on the particle. The position of the particle can be obtained from the kinematic equation:

$$\frac{d\vec{x}_p}{dt} = \vec{u}_p \tag{2.19}$$

The forces acting on the particles can be distinguished in body, surface and interaction forces.

$$\vec{F}_{body} = \vec{F}_{Buoyancy} \tag{2.20a}$$

$$\sum \vec{F}_{surface} = \vec{F}_D + \vec{F}_{PG} + \vec{F}_{Basset} + \vec{F}_{AM} + \vec{F}_{L,S} + \vec{F}_{L,R} \tag{2.20b}$$

$$\sum \vec{F}_{interaction} = \vec{F}_B + \vec{F}_{pp} + \vec{F}_{pw} \tag{2.20c}$$

Body forces include buoyancy or gravity forces:

$$\vec{F}_{Buoyancy} = m_p \vec{g}(1 - \frac{\rho_f}{\rho_p}) \tag{2.21}$$

where $\vec{g}$ is the gravitational vector and ρ_f, ρ_p are the densities of the fluid and particle, respectively.

Surface forces include forces due to the fluid flow surrounding the particle. The drag force acting on the spherical particles is given by,

$$\vec{F}_D = \frac{m_p}{\tau_p/\alpha}(\vec{u} - \vec{u}_p)\,, \tag{2.22}$$

where $\vec{u}$ is the fluid velocity interpolated at the position of the particle, $\alpha = C_D \frac{Re_p}{24}$

and τ_p is the particle response time, defined as:

$$\tau_p = \frac{\rho_p d_p^2 C_c}{18\mu_f}\,, \tag{2.23}$$

with d_p being the particle diameter, μ_f the dynamic fluid viscosity and $Re_p = d_p|\vec{\vec{u}} - \vec{u}_p|/\nu_f$ the particle Reynolds number. C_c is the Cunningham correction factor, defined as:

$$C_c = 1 + \frac{2\lambda}{d_p}\big[1.257 + 0.4\exp(-0.55 d_p/\lambda)\big] \tag{2.24}$$

where λ=0.070μm is the mean free path of air. This factor accounts for slip at the particle surface due to non-continuum effects, which appear when the size of the particle becomes comparable to the mean free path of the molecules of the surrounding gas. In our applications this is practically important when $d_p < 1\mu$m. The drag coefficient, C_D, is based on the correlation proposed by Schiller and Naumann (1935):

$$C_D = \begin{cases} \frac{24}{Re_p}(1 + 0.15 Re_p^{0.687}) & \text{if } Re_p \leq 1000 \\ 0.44 & \text{if } Re_p > 1000\,. \end{cases} \tag{2.25}$$

The second term in the right-hand side of eqn. 2.20b is the force due to the undisturbed velocity field,

$$\vec{F}_{PG} = m_f \frac{D\vec{u}}{Dt} \tag{2.26}$$

where m_f is the mass of fluid occupying the particle volume and $\frac{D}{Dt}$ is the material derivative, evaluated at the particle position. This force is often called pressure gradient force, since in an earlier derivation of the particle equation of motion, the viscous contribution to this term was neglected. However, Maxey and Riley (1983) showed that both the pressure gradient and the viscous force should be included.

The third term in the right-hand side of eqn. 2.20b is the Basset or history force that describes the unsteady drag force that acts on an accelerating particle and is given as,

$$\vec{F}_{Basset} = \frac{3}{2} d_p^2 \sqrt{\pi \rho_f \mu)} \int_0^t \frac{\frac{d}{d\tau}[\vec{u}(\tau) - \vec{u}_p(\tau)]}{\sqrt{(t-\tau)}} d\tau \tag{2.27}$$

The Basset force is due to the lagging boundary layer development with changing relative velocity when particles move through a fluid. It accounts for viscous effects and addresses the temporal delay in boundary layer development as the relative velocity changes with time.

The fourth term in the right-hand side of eqn. 2.20b is the added (or virtual) mass force and can be written as

$$\vec{F}_{AM} = \frac{1}{2}\rho_f V_p \left(\frac{D\vec{u}}{Dt} - \frac{D\vec{u}_p}{Dt} \right) \tag{2.28}$$

The added mass force is a result of the accelerating fluid surrounding the accelerating particle and tends to keep the particle from being accelerated in any direction. The origin of the force is that the fluid will gain kinetic energy at the expense of the work done by the accelerating particle.

The last two terms in the right-hand side of eqn. 2.20b are the lift forces due to shear ($\vec{F}_{L,S}$) and rotation ($\vec{F}_{L,R}$). The shear-induced or Saffman lift force acts perpendicular to the relative velocity between the fluid and particle. The expression for the shear lift first obtained by Saffman (1965, 1968) is given as,

$$\vec{F}_{L,S} = 1.615 d_p^2 (\rho_f \mu_f)^{1/2} \left(\frac{1}{|\vec{\omega}|} \right)^{1/2} [(\vec{u} - \vec{u}_p) \times \vec{\omega}] f(Re_p, Re_G) \tag{2.29}$$

where $\vec{\omega}$ is the local vorticity of the fluid and $Re_G = \rho d_p^2 |\omega| / \mu_f$ the shear Reynolds number of the particle. Mei (1992) proposed the following expression for $f(Re_p, Re_G)$

$$f(Re_p, Re_G) = \begin{cases} (1 - 0.3314\alpha^{1/2}) exp(-0.1 Re_p) + 0.3314\alpha^{1/2} & \text{for } Re_p \leq 40 \\ 0.0524(\alpha Re_p)^{1/2} & \text{for } Re_p > 40\,. \end{cases} \tag{2.30}$$

where $\alpha = 0.5 Re_G / Re_p$.

The rotation-induced or Magnus lift force is similar to the aerodynamic lift, i.e. velocity differences between the upper and lower side of the particle result in pressure differences that create the lift force. The velocity differences in the upper and lower boundary layers are caused by particle rotation. The expression for this force is:

$$\vec{F}_{L,R} = \frac{1}{8} \pi d_p^2 \rho_f [\vec{\omega}_p \times (\vec{u} - \vec{u}_p)] \tag{2.31}$$

where $\vec{\omega}_p$ is the angular velocity vector of the particle.

Interaction forces (eqn. 2.20c) include Brownian diffusion force ($\vec{F}_B$) and forces due to particle-particle ($\vec{F}_{pp}$) or wall ($\vec{F}_{pw}$) collisions. The Brownian force is important for submicron particles and causes diffusion due to collisions with the air molecules (Finlay, 2001). The expression for the amplitude of its ith component is based on the correlation proposed by Li and Ahmadi (1992),

$$F_{Brownian,i} = \zeta_i \sqrt{\frac{1}{\tilde{D}} \frac{2 k_B^2 T^2}{\Delta t_p}}\,, \tag{2.32}$$

where ζ_i is a zero mean variant from a Gaussian probability density function, T=310K is the absolute temperature in the lungs, $\tilde{D} = (k_B T C_c)/(3\pi\mu_f d_p)$ is the Brownian diffusion coefficient, $k_B = 1.3806488 \times 10^{-23}$ m^2 kg /s$^2 K$ is the Boltzmann constant and Δt is the time step used for integration of the particle equations.

Forces due to collision between particles become important in the case of dense

aerosol suspensions. In other words, as the volume fraction of the particle phase increases, collisions between particles influence the simulation results. In addition, the flow is affected by the presence of the particles and thus particle force source terms must be included in the momentum equations of the fluid phase. This case is known as four-way coupling. The Lagrangian method may not be suitable for very high volume fractions since there are too many particles to track and the model must also analyse too many collisions. In these cases, the Eulerian approach is preferred. On the other hand, if the particle volume fraction is sufficiently low, the particles do not collide to each other and also the flow remains unaffected by their presence. This is known as one-way coupling. In an intermediate state, named two-way coupling, the flow is affected by the particles but particle collisions do not have significant impact and therefore collision effects can be discarded in the simulation. The limits of validity of the coupling regimes are reported by Elghobashi (1994).

Forces on particles can also arise due to interaction with the walls. For example, DPIs are designed such that a sufficient number of wall collisions occur on the device walls in order to achieve the desired aerosol size distribution. Regarding the human airways, since the airway walls are covered with the mucus gel, it is assumed that the particles are retained upon contact with the wall. Therefore, wall forces on the particles are disregarded in the current work.

2.3.2 Relevance of various forces in lung deposition studies

Not all the forces described above are important in applications related to aerosol deposition in the human airways. In these applications, two major assumptions hold true that simplify the problem under consideration:

1. the particles are assumed to be spherical and
2. the particle density is much greater than the density of the surrounding fluid.

The first assumption is usually reasonable for inhaled aerosols, either environmental or pharmaceuticals. For example, it is certainly reasonable for liquid inhaled pharmaceutical aerosol droplets, since such small liquid droplets are spherical. However, for dry powder aerosols and evaporated metered dose inhaler aerosols, an assumption of sphericity is not exact. Nevertheless most such aerosols consist of reasonably compact particles, so that they can be considered spherical and eqn. 2.18 can be used.

The second assumption is quite reasonable since the air density is much smaller than the the densities of pharmaceutical compounds that are usually about 1000 times larger. This assumption results in the drag force being much larger than all other fluid forces acting on the particle. Specifically, when $\rho_p >> \rho_f$ and submicron particles are considered, pressure gradient, added mass and Basset history forces are small compared

to the drag force (Kleinstreuer and Feng, 2013). Shear lift force is more relevant in cases where the particle density is comparable to the fluid density and can thus be neglected in our application. Magnus lift force can also be neglected for submicron particles.

Regarding interaction forces, in the current work we have assumed dilute particle suspensions and thus particle-particle interactions are not taken into account. This assumption is valid in the distal regions of the lung, where the airspace volume increases and thus the particle volume fraction decreases. However, in drug delivery via an inhaler device, the aerosol bolus enters the patient's mouth at high volume fractions and flow-particle and particle-particle interactions can become important in the extrathoracic airways Wong et al. (2012). In the current study, since we mainly focus on regional deposition patterns in the airway walls, and in order to keep the computational cost affordable in the cases where LES are performed, one-way coupling is considered assuming dilute particle suspensions.

Therefore, the important forces that need to be taken into account in lung deposition studies are drag, gravity and Brownian motion force.

2.3.3 Electrostatic image charge force

When particles carry charge on their surface, electrostatic forces can arise and affect their motion and deposition behaviour (Finlay, 2001). There are two type of electrostatic forces on particles: image (or induced) charge and space charge forces. Image charge force is the attractive force experienced by a particle with a charge q (in Coulombs) near a conducting wall. This force arises because a charged particle sets up an electric field around it, which causes the molecules in the tissues in the lung to orient themselves (called the dielectric effect), which in turn alters the electric field around the particle such that there is in fact a net force on the particle. The expression image charge force is given by:

$$\overrightarrow{F}_{image} = \frac{q^2}{16\pi\epsilon_0|\overrightarrow{r}_{p,w}|^2}\frac{\overrightarrow{r}_{p,w}}{|\overrightarrow{r}_{p,w}|} \tag{2.33}$$

where $\overrightarrow{r}_{p,w}$ is the minimum distance vector between the particle and the conducting wall and $\epsilon_0 = 8.854{\cdot}10^{-12}\frac{C^2}{N{\cdot}m^2}$ is the permittivity of free space. The unit vector $\frac{\overrightarrow{r}_{p,w}}{|\overrightarrow{r}_{p,w}|}$ is normal to the wall surface and points away from the space occupied by the air passage, such that the image force always acts in the direction of the wall.

Space charge force arises due to the Coulombic repulsion of particles all having the same sign of charge. For two interacting particles, it is given by:

$$|\overrightarrow{F}_{space}| = \frac{q_1 q_2}{4\pi\epsilon_0|\overrightarrow{x}_1 - \overrightarrow{x}_2|^2} \tag{2.34}$$

where $\overrightarrow{x}_1$ and $\overrightarrow{x}_2$ are the positions of the interacting particles. When a large number of particles is present, the actual force on a particle will be the sum of all the Coulombic forces of its neighboring particles. Thus, space charge force is more relevant at high concentrations of particles and depends on their charge levels. In practice, space charge effects can become significant in inhalation devices, where the aerosol concentrations are high and charge levels can reach higher levels than in the humid environment of the lung (Karner and Urbanetz, 2011).

In the current study, the effect of image charge force on deposition in the upper airways is examined in chapter 3. A validation test case for the implementation of the electrostatic image charge force is included in appendix B.

2.3.4 Effect of the sub-grid scales on particle motion in LES

In LES, the effect of the unresolved scales of the continuous phase over the dispersed phase is lost due to the filtering procedure. In particular, the resolved velocities are used in the calculation of forces acting on the particles. Thus, the effect of the small-scale (unresolved) motion on particle dispersion and deposition must be either modeled separately, or neglected. Armenio et al. (1999) examined the effects of small-scale velocity fluctuations on the motion of tracer and inertial particles in a turbulent channel flow at $Re_\tau = 175$. In their first test, DNS calculations were performed to obtain the velocity field and several filters were applied to remove the small-scale fluctuations. Then, tracer particles were tracked in time using the resolved DNS field and the filtered velocity fields. Differences in particle statistics were observed only when a significant percentage of the energy was removed from the velocity field (about 20% error compared to the unfiltered data). In their second test, inertial particles were tracked in independent DNS and LES fields, thus including the effect of interpolation and sub-grid modeling errors on the dispersion statistics. Three LES computations were performed, on a fine and two coarser meshes, using the dynamic and Smagorinsky eddy-viscosity models. Good agreement in dispersion statistics was found between DNS and well-resolved LES with the dynamic model (differences less than 8%) whereas rather higher errors were recorded for the coarser meshes. Variations in this case can be attributed to the LES filtering operation than to sub-grid modelling errors. On the other hand, the Smagorinsky model resulted in very inaccurate estimations of the statistics. They concluded that well-resolved LES with an adequate model can provide fairly accurate particle statistics for moderate Reynolds number flows. Since tracer particles were used, which are the most sensitive to the small-scale fluctuations, the study of Armenio et al. (1999) provides conservative estimates of the accuracy of LES in the prediction of particle-laden flow. In the case of particles with inertia, the errors are expected to be smaller. Based on these findings, in the current study we are not employing a model to account for particle sub-grid dispersion. This can be further sup-

ported by the low to moderate Reynolds number of the flow in the human extrathoracic airways and the simulation of particles with inertia. This approach is also adopted in the vast majority of related studies.

2.3.5 Particle tracking algorithm

Particle tracking is performed using the computationally efficient and robust tracking algorithm proposed and implemented in OpenFOAM by Macpherson et al. (2009), with some additional improvements that were introduced in the latest versions of OpenFOAM (e.g. tracking of the particles using implicit decomposition of each cell into tetrahedra). A brief description of the numerical procedure follows.

Once the flow field has been advanced for a discrete time step Δt_f, the advancement of all particles follows for the same time window. Firstly, the particle's new position ($\vec{x}_p^{n+1}$) is computed explicitly using the particle velocity calculated at the end of the previous time step ($\vec{u}_p^n$):

$$\vec{x}_p^{n+1} = \vec{x}_p^n + \vec{u}_p^n \Delta t_p \tag{2.35}$$

The time step Δt_p used in the above equation can differ from the flow time step since the particles are tracked from cell to cell by calculating and identifying face crossings. The advantage of the face crossing approach is the much more efficient tracking of the particles in complex geometries that comprises of unstructured, arbitrary polyhedral cells, compared to methods which redetermine the hosting grid cell in every iteration. In this manner, for a flow time step Δt_f, the motion of a particle can be performed as a series of individual tracking events, each ending when the particle either crosses a face of a cell or arrives at the final destination. Thus, the maximum time step used to track a particle is the one defined for the continuous phase simulation (Δt_f). At the particle new position, which is either on a face that has been crossed or the final destination of the particle, eq. 2.18 is integrated using the implicit Euler scheme to compute the new particle velocity:

$$\vec{u_p}^{n+1} = \frac{\frac{\Delta t_p}{\tau_p/\alpha}\vec{u} + \vec{u}_p^n + \frac{\Delta t_p}{m_p}(\vec{F}_{Buoyancy} + \vec{F}_{Brownian} + \vec{F}_{image})}{1 + \frac{\Delta t_p}{\tau_p/\alpha}} \tag{2.36}$$

The non-linear terms in the above equation (such as $\alpha(Re_p(\vec{u}_p))$) are linearised using the particle's known properties from the previous time step. Spatial interpolation is used to approximate the fluid velocity $\vec{u}$ and the minimum distance vector $\vec{r}_{p,w}$ at the position of a particle, which are needed in the calculation of drag and electrostatic image charge forces, respectively. Both these vectors are mesh variables, i.e. their values are stored at the cell centres: $\vec{u}$ is obtained at each time step from the solution of flow equations while $\vec{r}_{p,w}$ is computed once in the beginning of the simulation for each cell and fitted to the mesh in order to reduce the computational cost. The spatial interpolation

method used decomposes the grid cell that hosts the particle to tetrahedra, using the cell centre-point, face centre-point and two vertices. In this manner, a tetrahedral cell is decomposed into 12 tetrahedra and a prismatic cell into 18 tetrahedra. Then, it searches for the tetrahedron enclosing the position of the particle and when it finds it, linear interpolation is performed based on the 4 vertices of the tetrahedron (Baker, 2003). This strategy leads to an interpolated fluid velocity that is continuous inside each grid cell as well as across the grid cells.

The above procedure, i.e. determination of new position and velocity of the particle is repeated until the particle reaches it's final destination at the end of the flow time step.

The accuracy and validity of the tracking algorithm and the selected integration and interpolation schemes was tested by the authors for a 90^o bent pipe configuration under laminar flow conditions. Details of these tests and comparisons with data in the literature (Breuer et al., 2006) are given in appendix B. Furthermore, the implementation of electrostatic image charge and Brownian forces in OpenFOAM were validated against analytical solutions and the results are also shown in appendix B.

2.3.6 Particle dimensionless numbers

Particle dimensionless numbers for the main deposition mechanisms are introduced in order to indicate the relative importance between forces acting on a particle.

The Stokes number (Stk) is used to measure the relative importance of inertial effects in determining particle trajectories (Finlay, 2001). In particular, the Stokes number is used to describe the response of a particle suspended in a fluid flow to the changes in this flow field. It is defined as ratio of the relaxation time of the particle τ_p to the characteristic time scale of the continuous phase τ_f , such that:

$$Stk = \frac{\tau_p}{\tau_f} = \frac{\rho_p d_p^2 U_0 C_c}{18 \mu_f D} \tag{2.37}$$

where τ_p is given in eq. 2.23 and the characteristic time scale of the continuous phase is taken as $\tau_f = D/U_0$, with U_0 and D being the mean fluid velocity and the local hydraulic diameter of the airway at the current particle location, respectively.

When examining the effect of electrostatic attraction on deposition in the airways (section 3.4.3), a dimensionless parameter to account for the importance of the image charge force $\vec{F}_{image}$ is introduced (Finlay, 2001):

$$Inc = \frac{C_c}{3\pi U_0 d_p} \frac{q^2}{16\pi\epsilon_0 D^2} \frac{1}{x'^2} \tag{2.38}$$

where $x' = \frac{x}{d}$ is the non-dimensional distance of the particle from the airway wall. The

ratio of the above defined dimensionless numbers can be used to determine the relative importance of electrostatic charge effects:

$$\frac{Inc}{Stk} = \frac{3q^2}{8\pi^2 U_0^2 d_p^3 \rho_p \epsilon_0 D} \frac{1}{x'^2} \tag{2.39}$$

Chapter 3

Particle deposition in a realistic geometry of the human conducting airways: effects of inlet velocity profile, inhalation flowrate and electrostatic charge

Journal Publication: *P. G. Koullapis, S.C. Kassinos, M. P. Bivolarova, A. K. Melikov. Particle deposition in a realistic geometry of the human conducting airways: effects of inlet velocity profile, inhalation flowrate and electrostatic charge. Journal of Biomechanics, 49:2201-2212, 2016.*

Conference Presentation: *P. G. Koullapis, S.C. Kassinos, C.-L. Lin. Computational Fluid Dynamics (CFD) simulations of aerosol deposition in the lungs. TSFP 9, Melbourne, Australia (2015).*

Conference Presentation: *P. G. Koullapis, S.C. Kassinos. The effect of flow rate and electrostatic charge on aerosol deposition in a realistic lung geometry DLES 10, Limassol, Cyprus (2015).*

3.1 Outline

In this work, we use Large Eddy Simulations (LES) to investigate the deposition of inhaled aerosol particles with diameters of d_p = 0.1, 0.5, 1, 2.5, 5 and 10μm (particle density of 1200 kg/m^3). We use a reconstructed geometry of the human airways obtained via computed tomography and assess the effects of inlet flow conditions, particle size, electrostatic charge, and flowrate. While most computer simulations assume a uniform velocity at the mouth inlet, we found that using a more realistic inlet profile based on Laser Doppler Anemometry measurements resulted in enhanced deposition, mostly on the tongue. Nevertheless, flow field differences due to the inlet conditions are

largely smoothed out just a short distance downstream of the mouth inlet as a result of the complex geometry. Increasing the inhalation flowrate from sedentary to activity conditions left the mean flowfield structures largely unaffected. Nevertheless, at the higher flowrates turbulent intensities persisted further downstream in the main bronchi. For $d_p > 2.5\mu$m, the overall Deposition Fractions (DF) increased with flowrate due to greater inertial impaction in the oropharynx. Below $d_p = 1.0\mu$m, the DF was largely independent of particle size; it also increased with flowrate, but remained significantly lower. Electrostatic charge increased the overall DF of smaller particles by as much as sevenfold, with most of the increase located in the mouth-throat. Moreover, significant enhancement in deposition was found in the left and right lung sub-regions of our reconstructed geometry. Although there was a relatively small impact of inhalation flow rate on the deposition of charged particles for sizes $d_p < 2.5\mu$m, impaction prevailed over electrostatic deposition for larger particles as the flow rate was increased. Overall, we report a significant interplay between particle size, electrostatic charge, and flowrate. Our results suggest that in silico models should be customized for specific applications, ensuring all relevant physical effects are accounted for in a self-consistent fashion.

3.2 Introduction

Aerosol particle deposition in the airways depends on several parameters, such as the physical and hydrodynamic characteristics of the particles themselves, the inhalation flowrate, the health state of the individual and the geometrical and morphological details of the airways. To complicate matters further, anatomical variations between individuals, which can be either hereditary or due to disease-induced airway remodeling, alter deposition to a degree that is modulated by particle size and charge, flowrate, and other factors.

Recent studies revealed the unsteady and turbulent nature of the flow in regions downstream of the glottis, with turbulent effects dissipating only in the deeper conducting airways where the local Reynolds number decreases gradually(Kleinstreuer and Zhang, 2010; Tawhai and Lin, 2011). An important determinant of the level of the generated turbulence in the human airways is the respiratory flowrate. Flowrates of 15, 30 and 60 lt/min are considered to correspond to sedentary, light and heavy activity conditions (Xi and Longest, 2007), while in the cases of rapid inhalation, typically encountered during the use of pharmaceutical aerosol inhalation devices, inhalation flowrate can reach values up to 120 lt/min (Johnstone et al., 2004). A higher flowrate causes earlier transition to turbulence in the upper airways and the ensuing fluctuations make aerosol particles move erratically, thus altering deposition patterns in a size-dependent fashion. Also, turbulence produced in the oropharynx can be advected

to several generations of the tracheobronchial tree, as estimated in Finlay (2001), for a simplified cylinder-based airway model and for airflow Reynolds numbers above 2000 in the larynx.

In the case of inhaled pollutants, ambient conditions such as the air and aerosol characteristics in the breathing zone of an occupant can be expected to play a role in determining deposition in the airways. Longest et al. (2008) investigated the deposition characteristics of ambient and capillary-generated spray aerosols in a realistic mouth-throat geometry. They found that spray momentum effects induce significantly more deposition than ambient aerosols, especially in the first section of the mouth-throat geometry as a result of spray inertia interacting with the tongue. In the absence of a free stream airflow (e.g. as caused by a ventilation system), the air flowfield in the breathing zone results from the interaction between the occupant's breath with a free convection flow around the body. Temperature differences between the body surface and the surrounding air drive the free convective flow, which starts slow and laminar with a thin boundary layer at the lower parts of the body, but becomes faster and turbulent with a thick boundary layer at the height of the head (Lewis et al., 1969; Licina et al., 2014). Airborne particles close to the ground can be transported by the convective flow into the breathing zone, a process that has a potentially negative impact on the quality of the inhaled air. (Licina et al., 2015a,b). Aerosols and air parcels are transported by the free convective flow with sufficient momentum and turbulence intensities to alter the characteristics of the flowfield in the pharyngeal cavities during inhalation, but these effects remain largely unexplored.

Electrostatic charge carried by inhaled particles is also an important determinant of deposition, especially in the case of drug delivery. Medical devices such as nebulisers, Metered Dose Inhalers (MDI) and Dry Powder Inhalers (DPI) often generate electrostatically charged aerosols (Byron et al., 1997; Kwok et al., 2005). But even environmental aerosols may have charges well above the Boltzmann equilibrium and thus electrostatic charge must be taken into account in human health risk assessments (Forsyth and Liu, 1998). Several theoretical studies in lung models (Yu (1985) and Hashish (1988)), experiments in man (Melandri et al. (1983); Prodi and Mularoni (1985)) as well as clinical measurements confirmed that charge carried by particles enhances the deposition of the particles in the lung considerably. This is not desirable for drugs intended for systemic uptake, which must pass into circulation through the alveolar epithelium, but might be desirable for drug delivery in certain upper regions of the airway tree or even leveraged for the removal of pollutant particles using electrostatic charge effects (Ali et al., 2008).

In this work, we use LES to study the effects of the mouth inlet velocity profile and of electrostatic charge at various inhalation flowrates on particle deposition patterns inside a realistic model of the human upper airways. Specifically, two different inlet conditions are examined under steady inhalation at a flowrate of 4.5 lt/min. The

first is a uniform velocity profile, as used in most current computational studies. The second is a velocity profile measured by us in the breathing zone of a breathing thermal manikin using Laser Dopler Anemometry (LDA), which is closer to the real case. The experiments to generate the measured profile are beyond the scope of the present paper and will be described in a separate publication. The effect of inhalation flowrate is examined by considering flowrates of 15, 30 and 60 lt/min, while assuming uniform inlet velocity. Finally, deposition enhancement in the lungs due to electrostatic effects is also assessed as a function of inhalation flowrate.

3.3 Computational details

3.3.1 Airway geometry

Early in silico models relied on simplified representations of the human airways, with many of them employing the symmetric model of Weibel (Weibel, 1963). It is now possible to reconstruct the human respiratory tract from Multi-Detector Computed Tomography (MDCT) scans and compute airflow in domains that are patient specific and anatomically accurate. The geometry considered in this study, (see fig. 3.1(a) and (b) - coordinate system is also shown) is reconstructed from Multi-Detector Computed Tomography (MDCT) scans and it represents a non-smoking 20 year old female. This geometry was provided to us by the Department of Mechanical and Industrial Engineering of the University of Iowa (USA) and was also used in the study of Choi et al. (2009), where more details regarding the MDCT reconstruction method and the airway dimensions can be found. The respiratory tract includes the extrathoracic airways of the mouth, the oropharynx, the laryngopharynx, the larynx and the trachea as well as the intrathoracic airways up to generation 7. Table 3.1 summarizes the geometrical features of the reconstructed airways (average cross sectional area A and corresponding hydraulic diameter D_h) along with the key flow parameters (bulk velocity U and Reynolds number Re) for the three higher flowrates considered in this study.

When studying the effect of different velocity profiles imposed at the mouth inlet, the airway geometry is truncated at the end of the trachea in order to reduce the mesh size and computational cost. This simplification is based on preliminary numerical experiments that had shown that all differences in the flowfield due to inlet conditions dissipate in the upper airways and well before the flow reaches the tracheal bifurcation. Also, in order to match the velocity profile measured at the breathing zone of the breathing thermal manikin with the mouth inlet of the airway model, the initial geometry (fig. 3.1(a) was extruded slightly in the mouth inlet section as shown in fig. 3.1(c).

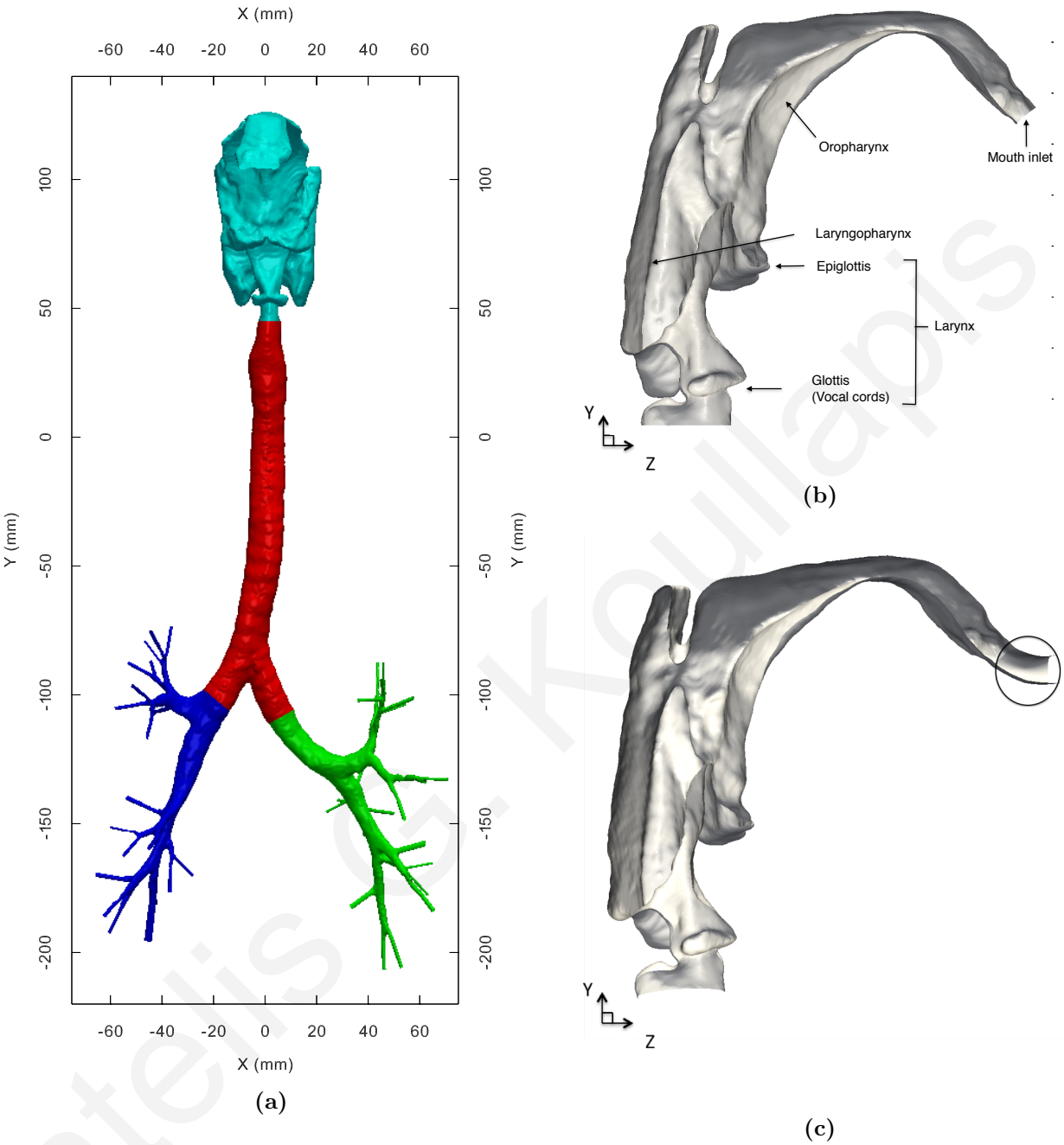

Figure 3.1: *Realistic human upper airways geometry (Choi et al., 2009)). (a) Full geometry and sub-regions, i.e. mouth-throat (cyan), tracheal (red), left (green) and right lung (blue). (b) Inside side view of the upper airways. (c) Modified airway geometry used in the case of different inlet velocity profiles (extruded part in the mouth inlet section in circle). Coordinate system is also shown.*

Table 3.1: *Geometrical and flow properties on the cross-sections of interest.*

Cross section	**A**(mm^2)/ **D$_h$**(mm)	**U** $= \frac{Q}{A}$(m/s)	**Re** $= \frac{UD}{\nu} = \frac{2Q}{\nu\sqrt{\pi A}}$
		$\dot{Q} = 15.2\,/\,30\,/\,60 \frac{lt}{min}$	$\dot{Q} = 15.2\,/\,30\,/\,60 \frac{lt}{min}$
Midpharynx	401 / 22.6	0.630 / 1.247 / 2.494	838 / 1654 / 3308
Glottis	39.3 / 7.074	6.43 / 12.725 / 25.45	2676 / 5084 / 10168
Trachea	157.8 / 14.2	1.6 / 3.17 / 6.34	1337 / 2639 / 5278

3.3.2 Continuous phase

We are employing Large Eddy Simulations (LES) using the dynamic version of the Smagorinsky-Lilly subgrid scale model (Lilly, 1992) in order to study the unsteady flow in the realistic human airway geometry. The airflow is described by the filtered set of incompressible Navier-Stokes equations 2.4. To ensure numerical stability the time steps used were 10, 5, 2.5 and 1 10 6 s for the cases of 4.5,15.2, 30 and 60 L/min, respectively. Concerning the outlet boundary conditions, that determine the ventilation distribution in the CT-resolved 3D airway model, there are sophisticated methods for their derivation. These methods are based on in-vivo medical imaging (Choi et al., 2009; De Backer et al., 2008) and can also employ multiscale 3D-1D strategies (Yin et al., 2010). Another alternative approach was utilized in the work of Choi et al. (2009), where the flow partition to the left and right lungs was set equal to the ratio of air volumes, as determined from MDCT images, resulting in a subject-specific flow partition. A similar flow partition to the left and right lungs was achieved in our simulations by specifying zero pressure at the outlets of the model (4% difference compared to the flow division reported in Choi et al. (2009)). A no-slip velocity condition is imposed on the airway walls and atmospheric pressure is set at the inlet boundary. The velocity inlet conditions are discussed in section 3.4.1.

3.3.3 Particle phase

Spherical, rigid and non rotating particles are introduced at the mouth inlet. The motion of each particle is individually computed (Lagrangian approach) by solving equations 2.18 and 2.19 to determine the particle velocity, $\vec{u}_p$, and position, $\vec{x}_p$. The forces acting on each particle include gravity, Drag, Brownian and electrostatic image charge forces. At each time step, 10 particles are released from random positions at the mouth inlet boundary and the injection stops after 120,000 particles of each size have been introduced. The total number and release time of particles was chosen in order to have a sufficient sample and also take into account the time scales of the flow. The initial velocity of the particles is set to match the air velocity at the inlet and hence, differences in the initial momentum of the particles are taken into account when the inlet velocity profile is modified.

3.3.4 Mesh sensitivity study and validations

Two unstructured hybrid meshes with 23 (Mesh 1) and 34 (Mesh 2) million control volumes were generated using ANSYS ICEM software. Cross-sectional views of the two meshes are shown in fig. 3.2 at the middle of the trachea. The bulk region was discretised using tetrahedral elements, while four layers of prismatic elements were used in the near wall region. The inclusion of near-wall prisms is supported by the recent

findings of Frank-Ito et al. (2015), who studied airflow and particle deposition in a sinonasal airway model and found that tetrahedral-only meshes over-predict particle deposition and are less accurate than hybrid tetrahedral-prism meshes.

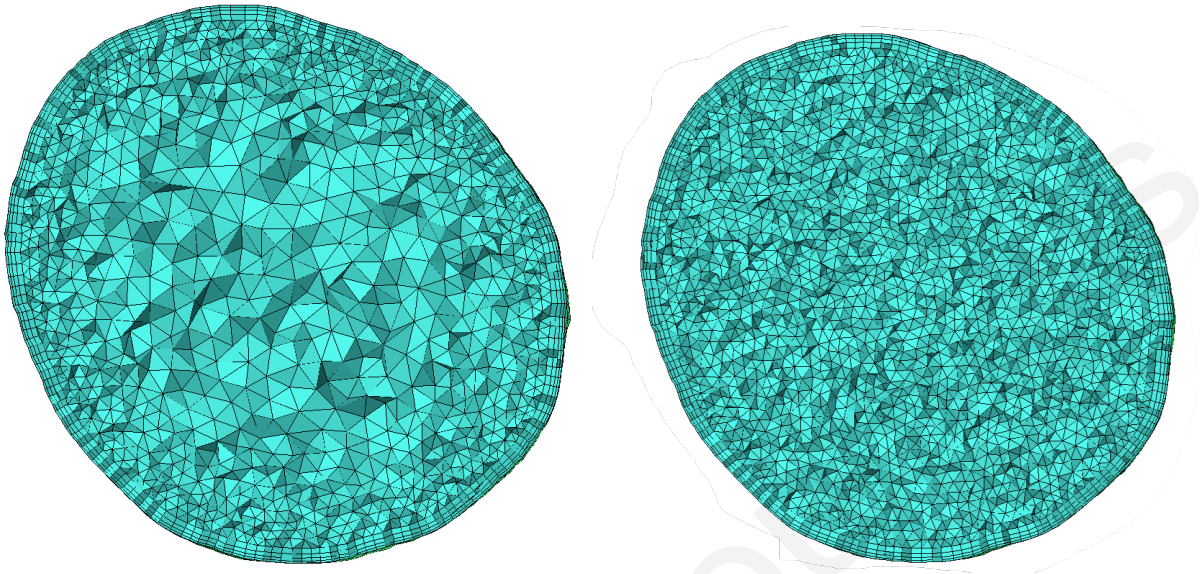

(a) **(b)**

Figure 3.2: *Cross-sectional views of the two generated meshes at the middle of the trachea. (a) Mesh 1 - 23M cells, (b) Mesh 2 - 34M cells.*

In order to examine the sensitivity of our results on mesh size, two tests were carried out at Q=30 L/min. The first test is about the distribution of the normalised mean and root-mean-squared (rms) velocity fluctuations along the jet centerline, which is defined as the loci where the maximum mean velocity at each axial station is located, and is shown in fig. 3.3(a). The plots show good agreement between the two meshes.

The second test is carried out in order to assess the effect of grid size on overall and regional Deposition Fractions (DF, number of deposited particles over the total number of injected particles) of uncharged particles (q=0). For the regional deposition study, the geometry was divided in four sub-regions as shown in fig. 3.1, i.e. mouth-throat (cyan), tracheal (red), left (green) and right lung (blue). Fig. 3.3(b) shows that negligible variations for the particle DF are observed between the two meshes considered.

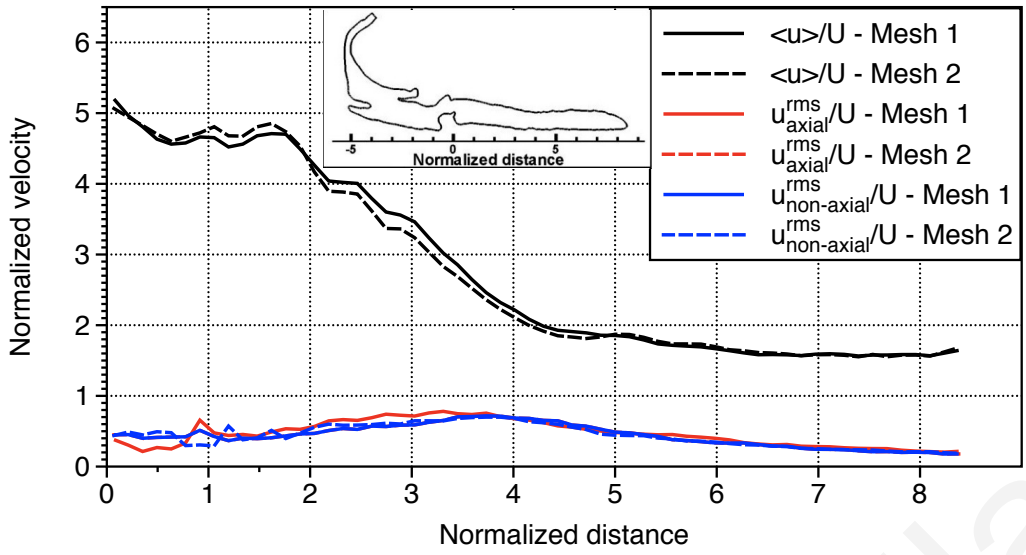

(a)

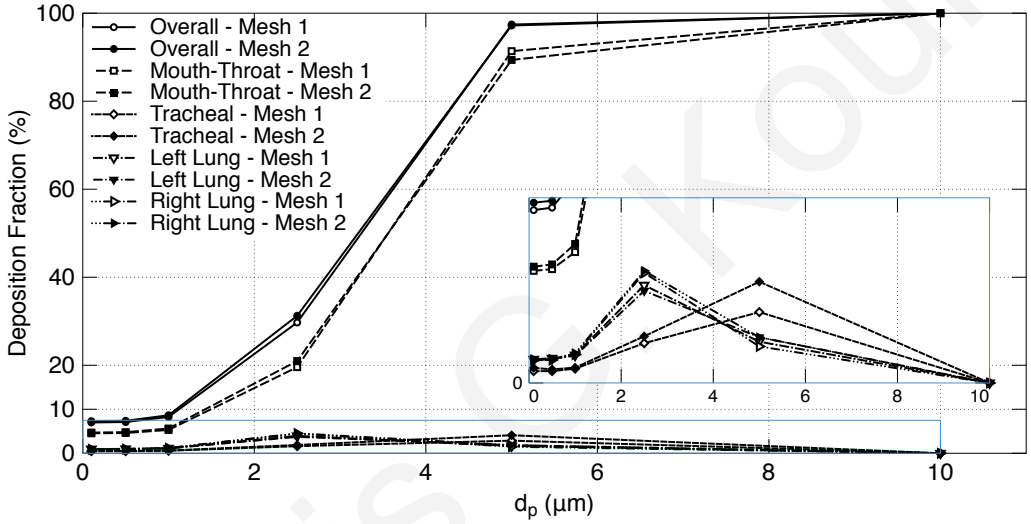

(b)

Figure 3.3: *Sensitivity of results on mesh size. (a) Distribution of the normalised mean and rms velocity fluctuations along the jet centerline at Q=30L/min for Meshes 1 and 2 (U=3.17 m/s is the tracheal average velocity), (b) Overall and regional DF as a function of particle size for Meshes 1 and 2 (Q=30 L/min, q=0).*

Based on the results of grid sensitivity study, Mesh 1 is used for the case of Q=4.5 L/min, while Mesh 2 is used for the higher flow rate cases of 30 and 60 Lt/min. In the case of the truncated geometry, used to study the effect of different velocity profiles imposed at the mouth inlet at Q=4.5 L/min, the mesh density is very similar to that of Mesh 1. The average y^+ values in the regions with high Turbulent Kinetic Energy (TKE), i.e. oropharynx, glottis and upper trachea, resulting from these meshes are approximately 0.2, 0.5, 0.8 and 1.3 for the cases of 4.5, 15.2, 30 and 60 lt/min.

In addition, to test the mesh resolution, the LES solutions were compared with DNS solutions, both computed on Mesh 2 at Q=30 L/min. The relative L1 norm of the turbulent kinetic energy estimates from these solutions was 10.8%, which is within

the typical range of a LES model and indicates that the mesh was fine enough for well-resolved LES.

For validation purposes, our predicted flowfield characteristics were compared with the results from the extensive work of Choi et al. (2009), who used LES to study the airflow in the considered geometry (fig. 3.1(a)) at a flow rate of 15.2 lt/min. Fig. 3.4 shows the distribution of the normalized mean velocity and rms velocity fluctuations along the jet centerline. In general, there is good agreement between the results of the two studies. The small differences with published results most probably resulted from the different turbulence models, discretisation methods and sampling times of turbulent statistics.

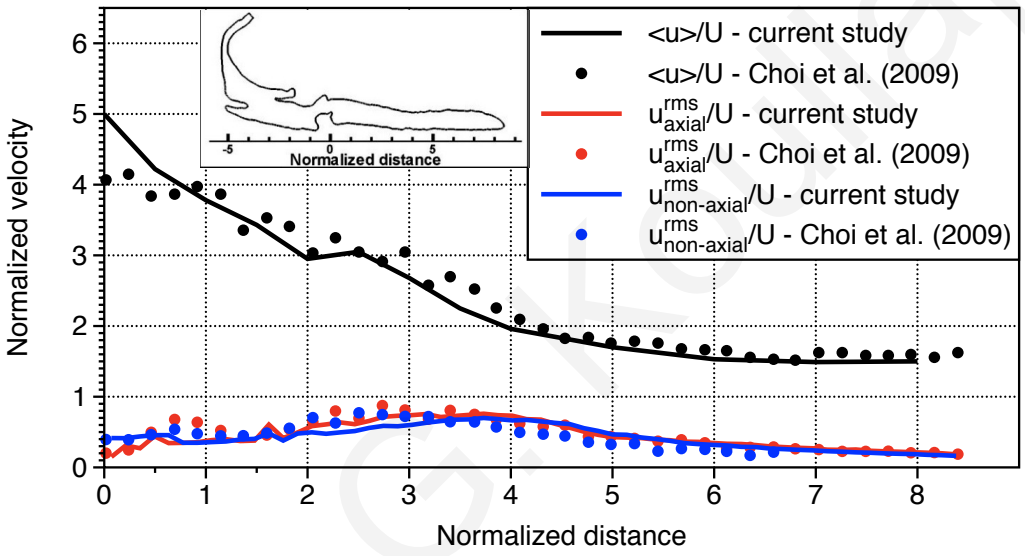

Figure 3.4: *Comparison of our results with the results of Choi et al. (2009). Distribution of the normalized mean and rms velocity fluctuations along the jet centerline at Q=15.2 L/min.*

3.4 Results

In this section, simulation results for the effects of the inlet velocity profile, inhalation flowrate and electrostatic charge on particle deposition are presented and discussed. The particle sizes considered in all cases are 0.1, 0.5, 1, 2.5, 5 and 10μm and the particle density is equal to 1200 kg/m^3.

3.4.1 Effect of inlet velocity profile

As mentioned previously, two different inlet velocity profiles were considered at a steady inspiratory flowrate of 4.5 Lt/min. In the first simulation, a uniform velocity profile was set at the extruded mouth inlet of the airway geometry, while in the second simulation, the time averaged values of the measured velocities were applied. The two inlet profiles

are shown in fig. 3.5.

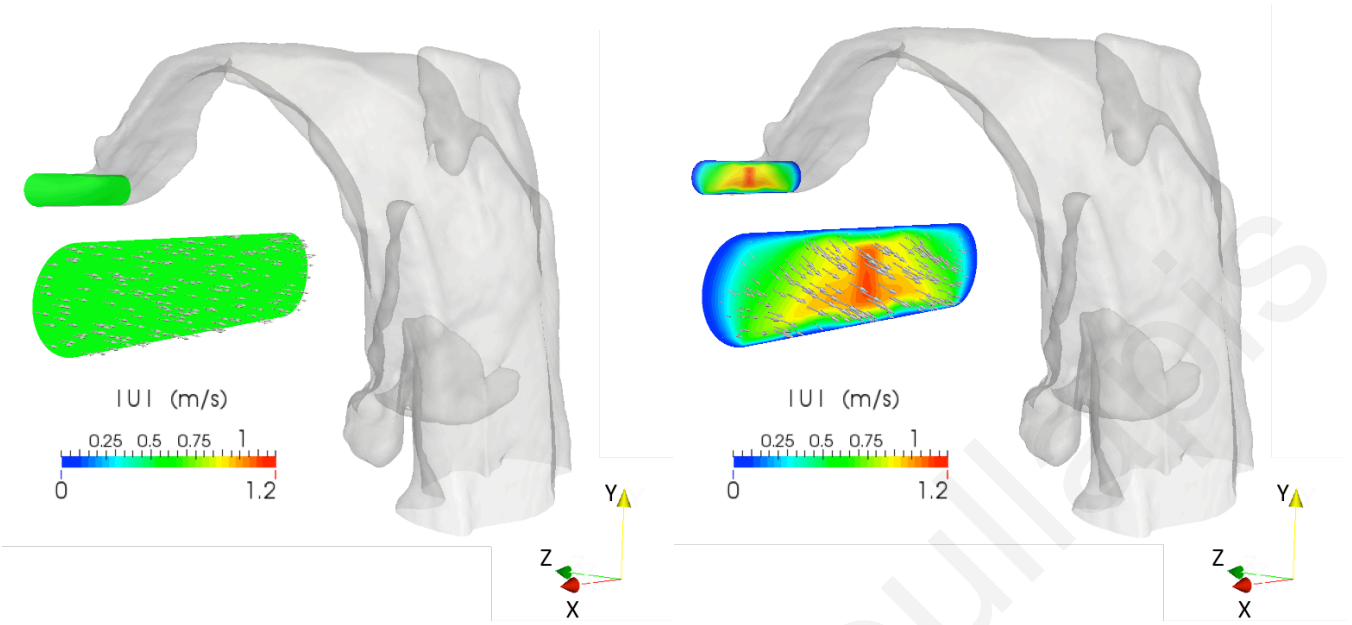

(a) **(b)**

Figure 3.5: *Different inlet velocity profiles: (a) uniform, (b) LDA-measured.*

Fig. 3.6 displays the contours of the mean velocities in several vertical and horizontal cut-planes, for the two inlet velocity conditions. Even in the first cut-plane (slice 1), just a short distance downstream of the mouth inlet, the differences in the initial velocity profiles have been largely smoothed out as a result of geometrical effects. Specifically, the cross sectional area is reduced as we move from the mouth inlet to the oral cavity and therefore the mean velocity accelerates in the region above the tongue and transitions to a more uniform profile. As a result, any upstream flowfield differences dissipate. Surprisingly, some minor differences can be seen in the two cut-planes in the wide passages of oropharynx and laryngopharynx (slices 3 and 4), but most probably these are resulting from having averaged over a relatively small sample for turbulent statistics. Downstream of the glottis constriction the mean velocity fields are identical.

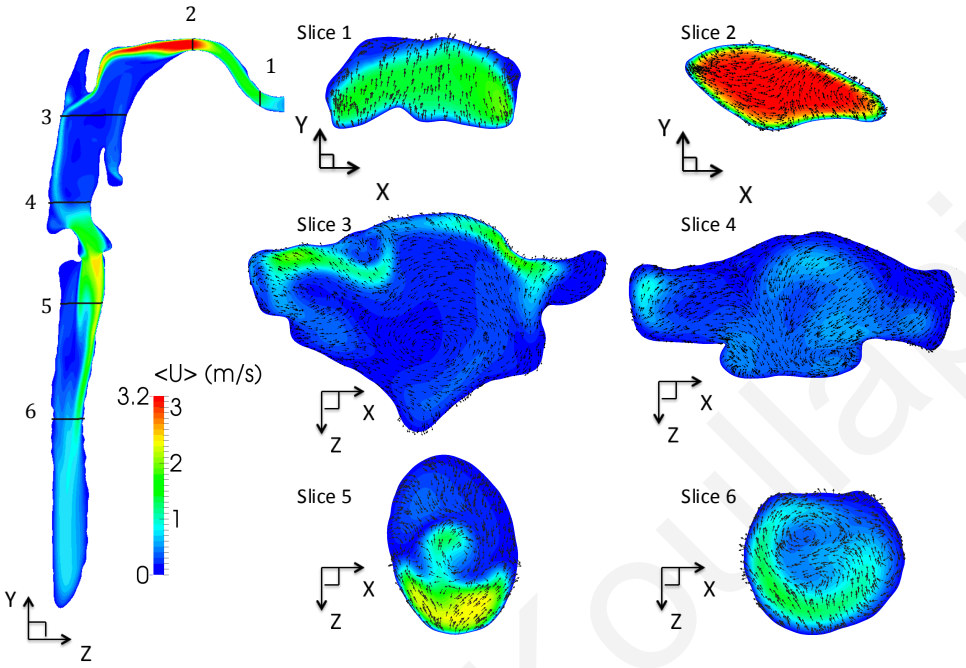

(a)

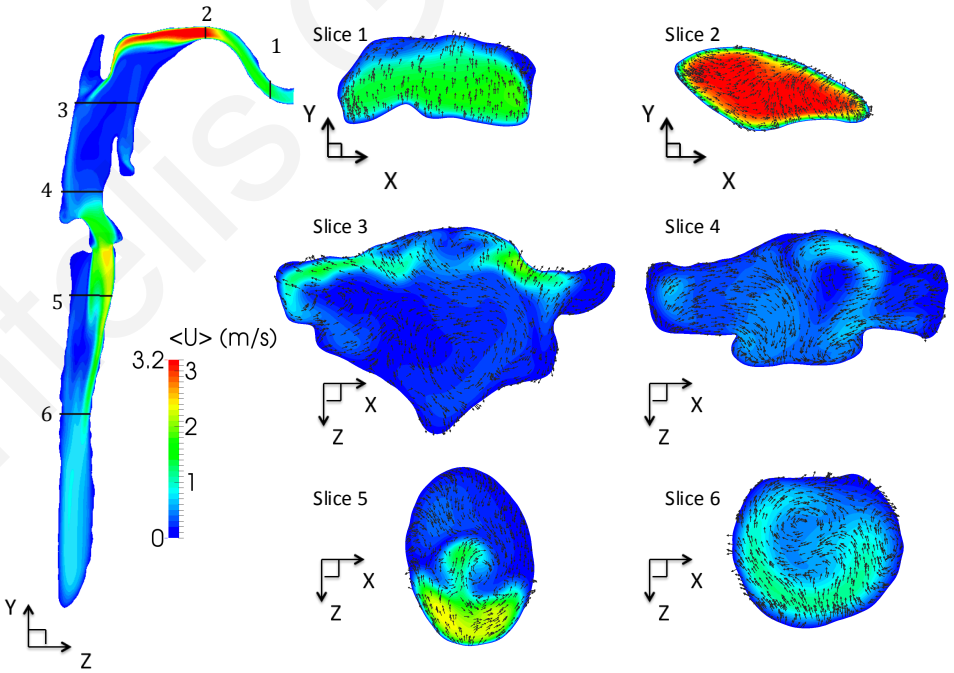

(b)

Figure 3.6: *Contours and vectors of mean velocity for the cases of different inlet velocity profiles (a) uniform, (b) LDA-measured.*

Fig. 3.7(a) shows the overall DF as a function of particle size, for the two cases considered. As shown, the measured inlet velocity profile corresponds to a higher deposition fractions for all particle sizes. The rise in DF is ranging between 3 and 5%.

In order to investigate the regions with enhanced particle deposition, the upper airway geometry was subdivided in five sub-regions, as shown in fig. 3.7(f). The first sub-region consists of the region from the mouth inlet to the end of the first curvature, above the tongue and below the hard and soft palate (referred as tongue). The second sub-region includes the area of high velocity jet in the oral cavity and extends to the entrance of oropharynx (referred as oral cavity). The third sub-region includes the nasopharynx, oropharynx and extends to the tip of epiglottis (referred as oropharynx) while the fourth sub-region consists of the larynx from the tip of the epiglottis to just below the vocal cords (referred as larynx). The fifth sub-region includes the trachea.

The Deposition Efficiencies (DE, number of deposited particles over the total number of particles that entered the sub-region) were then evaluated for each sub-region (fig. 3.7(b)-(f)). Most of the deposition enhancement in the case of the measured inlet velocity occurs in the tongue sub-region, for all particle sizes.

For larger particles, the greater deposition is resulting from greater inertial impaction due to higher horizontal velocities and a downward vertical velocity component at the mouth inlet. The downward velocity in conjunction with the upward inclination of the geometry in the tongue region causes larger particles to impinge on the lower walls (tongue), as shown in fig. 3.8. In the case of sub-micron particles, Brownian diffusion seems to play a significant role as evidenced by the uniform distribution of the deposition sites in the region close to the mouth. In the case of LDA-measured inlet conditions, velocities are diminished near the mouth walls (no-slip condition) and this affords particles a longer residence time in the wall proximity. The result is a higher probability of them being deposited due to random motion, at least under these particular flow conditions, i.e. non-uniform inlet velocities and quite low flowrate (4.5 lt/min). The region of enhanced deposition has a rather clearly marked downstream border, especially for the sub-micron particles. This corresponds to the location where the geometry transitions from a converging to a diverging shape while undergoing a simultaneous change in curvature.

For particle sizes below $5\mu m$, the DEs in the subsequent (downstream) sub-regions remain unaffected by the details of the inlet profile. In the case of the largest particles, however, some differences in DE can be observed in the oral cavity and the larynx sub-regions. In the oral cavity, the uniform inlet velocity profile seems to contribute to a higher DE than the measured profile. Apparently, the more efficient filtering of these large particles near the mouth inlet in the case of the measured profile removes some of the particles that, in the case of the uniform inlet profile, manage to escape early deposition and eventually deposit in the oral cavity. In other words, $10\mu m$ particles that

as a result of their initial conditions are prone to early deposition are more efficiently filtered out in the tongue sub-region when the measured profile is used; the particles left to enter the oral sub-region are those that are less likely to deposit early.

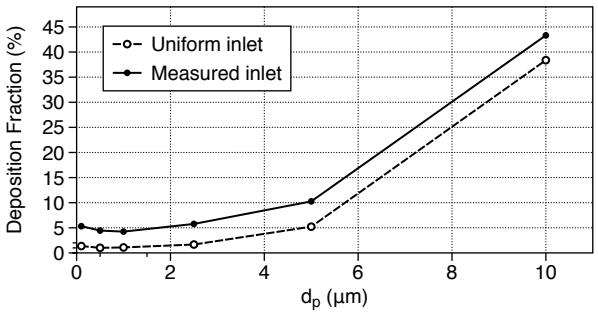

(a) DF - Overall

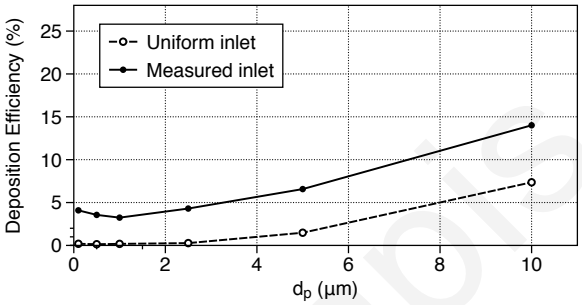

(b) DE - Tongue sub-region

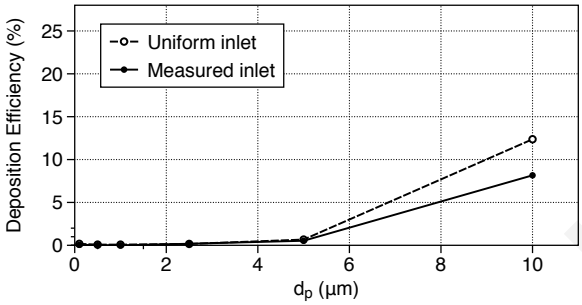

(c) DE - Oral cavity sub-region

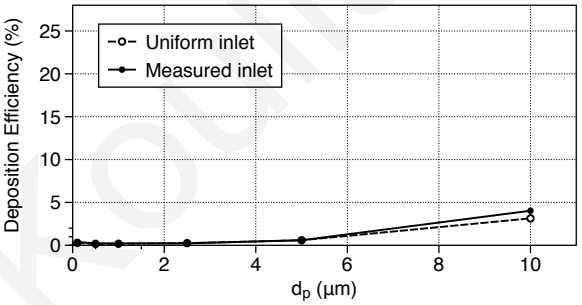

(d) Oropharynx sub-region

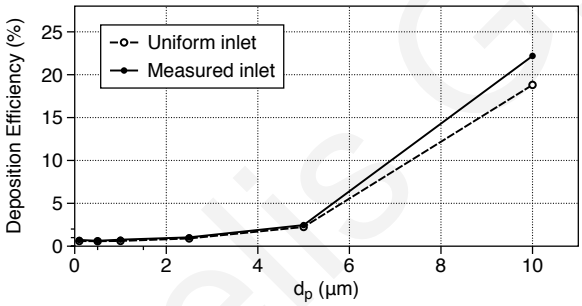

(e) DE - Larynx sub-region

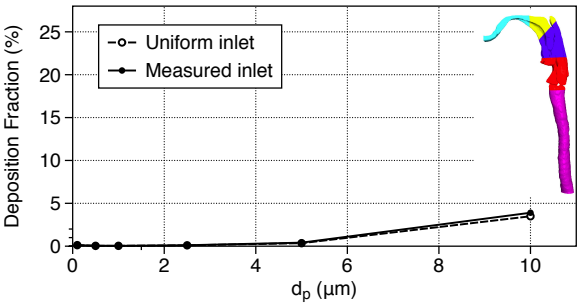

(f) DE - Trachea sub-region

Figure 3.7: *Modification of deposition as a result of inlet velocity profile. (a) Overall Deposition Fraction, (b)-(f) Deposition Efficiencies in the sub-regions. Sub-regions are shown in (f). Cyan: Tongue. Yellow: Oral cavity. Blue: Oropharynx. Red: Larynx. Purple: Trachea.*

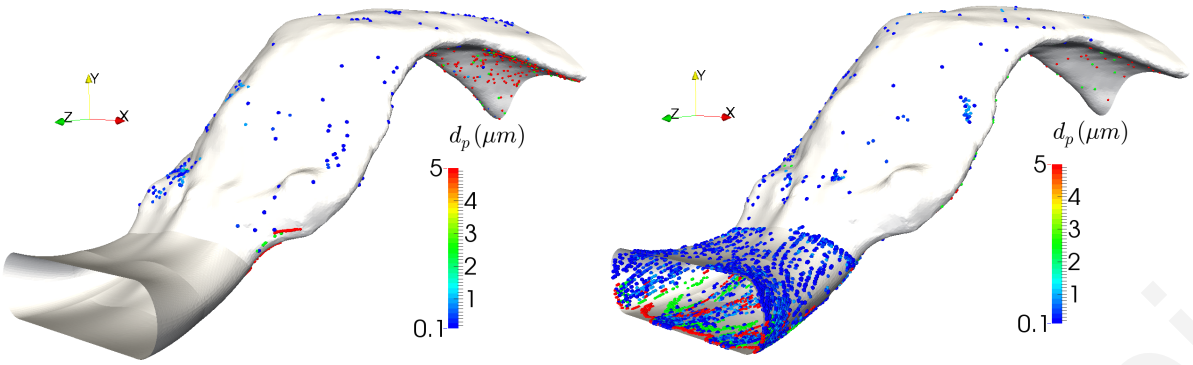

(a) **(b)**

Figure 3.8: *Deposition locations in the tongue sub-region: (a) Uniform velocity profile. (b) Measured velocity profile.*

3.4.2 Effect of inhalation flowrate

In this section, we show the effects of inhalation flowrate (15.2, 30, 60 Lt/min) on the characteristics of the flowfield and particle deposition in the upper airway geometry (fig. 3.1(a)).

Flowfield

The inclusion of the lowest inhalation rate (15.2 Lt/min) allows us to compare and validate our results with those of Choi et al. (2009), who carried a very detailed analysis of the flowfield in the same geometry at this flowrate. The inclusion of the higher flowrates allows us to assess how the flow structure is modified at inhalation rates that can be more relavant to drug delivery.

Fig. 3.9 shows a side view of the velocity magnitude contours of the normalized mean velocity in a vertical mid-plane of the upper airways. Contours and secondary component vectors are also shown at selected horizontal cut planes (A, B and C). At the lines of intersection of the two planes (vertical and horizontal), the corresponding mean velocity profiles are shown in black color. These results are in good agreement and confirm the observations made by Choi et al. (2009).

Mean flow structures are qualitatively similar for the three flowrates regardless of Reynolds number. The normalized mean velocity initially exhibits a high speed jet in the oral region and then decelerates when passing through the wide and curved passage of the oropharynx and the laryngopharynx. This oral jet develops in a shorter axial distance at higher Reynolds number (jet core velocity decays more rapidly), which agrees qualitatively with the experimental findings for circular jets of Kwon and Seo (2005). The different oral jet characteristics are most probably the reason behind the differences in the secondary motions in the oropharynx (slice A), observed under the

various flowrates. The jet entering the oral cavity causes a recirculation zone close to the anterior wall. The laryngeal jet is formed starting slightly upstream of the glottis due to the constricted cross-sectional area and it impinges on the tracheal front wall. This jetting effect creates a large recirculation zone near the dorsal wall of the upper trachea. Asymmetric counter-rotating secondary motions are generated as we move downstream in the trachea (slices B and C), which well agrees with experimental observations (Johnstone et al., 2004). Further downstream, the jet is dispersed and the secondary motions are weakened.

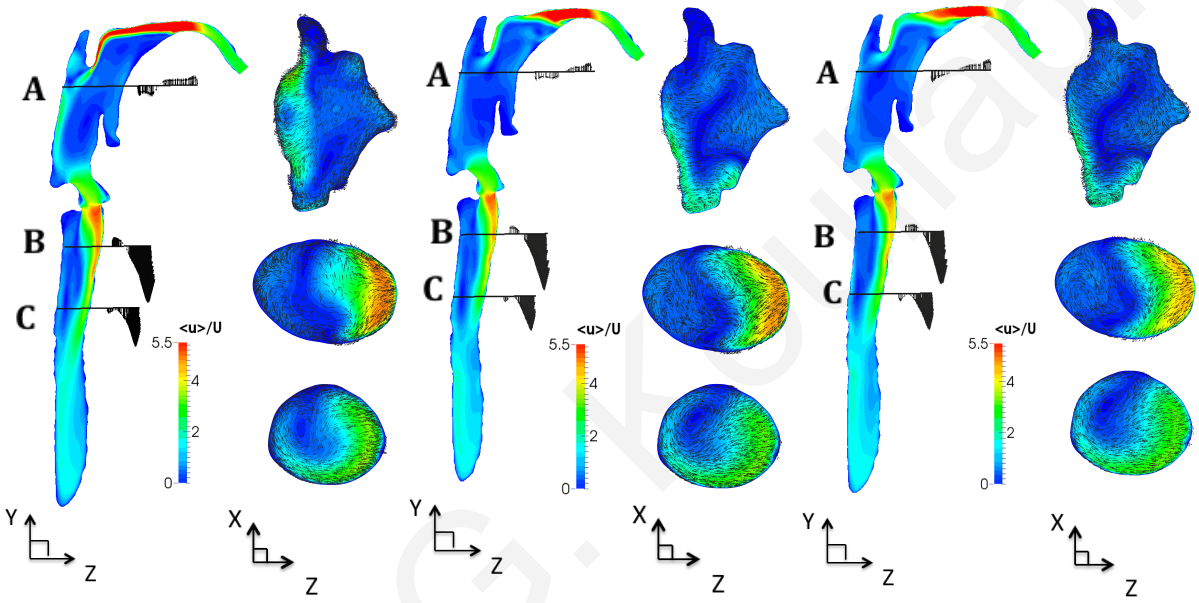

Figure 3.9: *Contours and vectors of normalised mean velocity. (a) $\dot{Q} = 15.2$ Lt/min, (b) $\dot{Q} = 30$ Lt/min, (c) $\dot{Q} = 60$ Lt/min. The figure is an adaptation of Figure 5 in Choi et al. (2009) to include the higher flowrates.*

Fig. 3.10 shows the contours of normalised TKE in a vertical and three horizontal cut-planes. The results for the lowest inhalation rate (15.2 *Lt/min*) are again in good agreement with the study Choi et al. (2009), but we also note modifications as the flowrate is increased above this value. TKE in the oral region rises rapidly after the constriction due to the soft palate. The location of maximum TKE in this region depends on the Reynolds number. At the lower flowrate of $\dot{Q} = 15.2$ Lt/min, the high TKE region is located downstream of the oral jet impingement, at the entrance of oropharynx, while in the cases of the higher flowrates, TKE maximum is found upstream in the oral cavity region. This is also supported by the study of Kwon and Seo (2005), who found that turbulence intensities on the shear layers of round jets are gradually increased as the Reynolds number increases. Further downstream in the pharynx, TKE is suppressed due to the increased flow cross section, but it is augmented again by the glottis constriction. A high TKE region is found at the mixing

layer between the cavity-like flow in the recirculation zone and the free stream velocity. A second region of high TKE in the trachea is located near the end of the jet core and is attributable to the transition of the jet to turbulence. These two regions extend in greater areas as Reynold number is increased. TKE is reduced as we move further downstream to the lower part of the trachea.

Fig. 3.11 displays the contours of turbulence intensity in a vertical plane cutting through lower trachea and major bronchial airways, at the three flowrates considered. At higher flowrates, higher values of turbulent intensities are recorded that persist further downstream in the trachea as well as in the main bronchi.

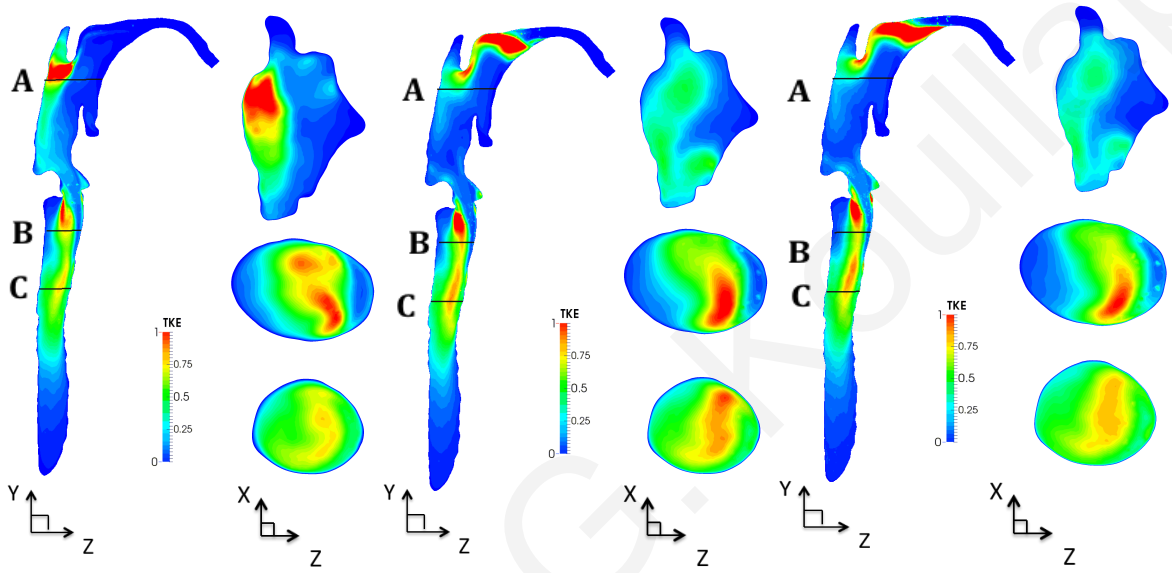

(a) **(b)** **(c)**

Figure 3.10: *Contours of normalised turbulent kinetic energy. (a) $\dot{Q} = 15.2$ Lt/min, (b) $\dot{Q} = 30$ Lt/min, (c) $\dot{Q} = 60$ Lt/min. The figure is an adaptation of Figure 5 in Choi et al. (2009) to include the higher flowrates.*

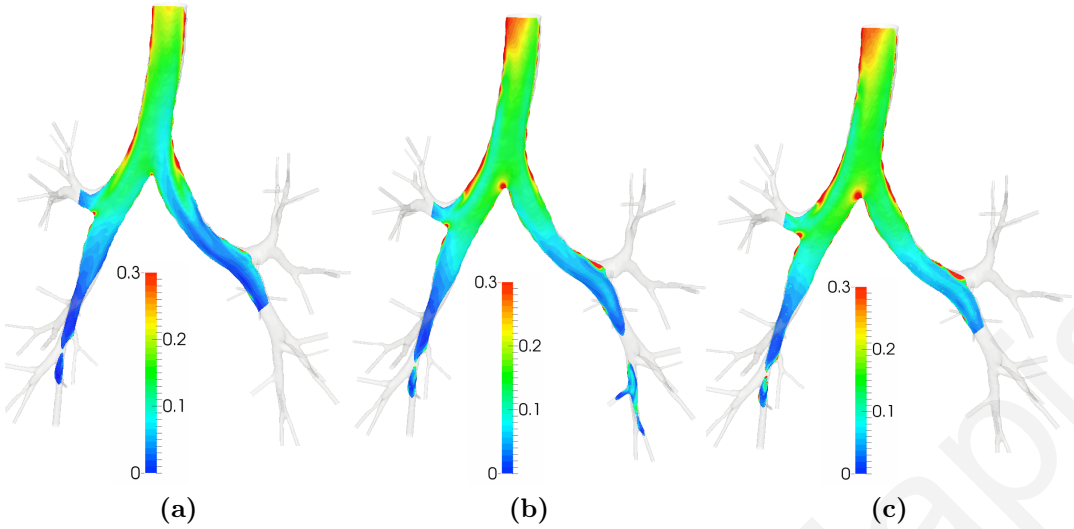

Figure 3.11: *Contours of turbulence intensity in lower trachea and major bronchial airways. (a) $\dot{Q} = 15.2$ Lt/min, (b) $\dot{Q} = 30$ Lt/min, (c) $\dot{Q} = 60$ Lt/min. The figure is an adaptation of Figure 20 in Choi et al. (2009) to include the higher flowrates.*

Particle deposition

Figs. 3.12(a), (d) and (g) present the overall and regional (sub-regions as depicted in figure 3.1(a)) DF of uncharged particles as a function of particle size and flowrate.

Independently of the flowrate, almost all of the 10μm particles are deposited in the curvatures of the mouth-throat region, as shown in fig. 3.12(b), (e) and (h). The deposition hot spots for these particles are the upper area after the first curvature and above the tongue (hard and soft palate) as well as the rear wall of the oral cavity, known as uvula (marked by arrows in fig. 3.12(b)). In the two higher flow rate cases, the first curvature filters approximately 97% of 10μm of these particles. In general, larger particles, due to their high inertia deviate from the fluid streamlines and impact at the curved airway walls in the mouth region.

The effect of flowrate is more pronounced on the deposition of 2.5 and 5μm diameter particles. Increasing the flowrate from 15.2 to 30 Lt/min augments the overall DF of 5μm particles by approximately 40%, while for 2.5μm particles, increasing the flowrate from 15.2 to 60 Lt/min causes a rise in overall DF of about 70%. For these particles, the oral jet at the uvula causes significant impaction as shown in fig. 3.12(b), (e) and (h). Considerable deposition also occurs on the sidewalls of the larynx immediately upstream of the glottis constriction and on the sidewalls of the upper trachea due to inertial impaction arising from the laryngeal jet and the associated secondary motions (fig. 3.12(c), (f) and (i)). Left and right lung DF of 5μm particles are reduced for higher flow rates as a result of the more efficient filtering on the upper airways. Increasing the flowrate causes a similar DF enhancement for the 1μm particles as well.

In order to examine the effect of Brownian diffusion on the deposition of sub-micron particles, two separate simulations, with and without Brownian force, were performed

at a flowrate of 15.2 Lt/min (residence times are longer at this low flowrate, and thus Brownian motion is expected to be more important). Results show that differences in the overall DF are less than 1%, suggesting that Brownian force can be neglected for deposition studies of particles sizes larger than 0.1μm, at least under similar flow conditions in the upper airways.

The trends described above are consistent with previous studies, such as the mouth-throat deposition experiments of Grgic et al. (2004a), who performed measurements in casts of seven oral airway configurations (S1-S5b) at flowrates of 30 and 90 Lt/min and particle diameters of 3-6.5μm. Fig. 3.13 present the DF in the mouth throat region as a function of Stokes number, based on inlet conditions. In spite the scattering due to different geometric configuration downstream of the inlet, our result have the same trend as the experimental depositions.

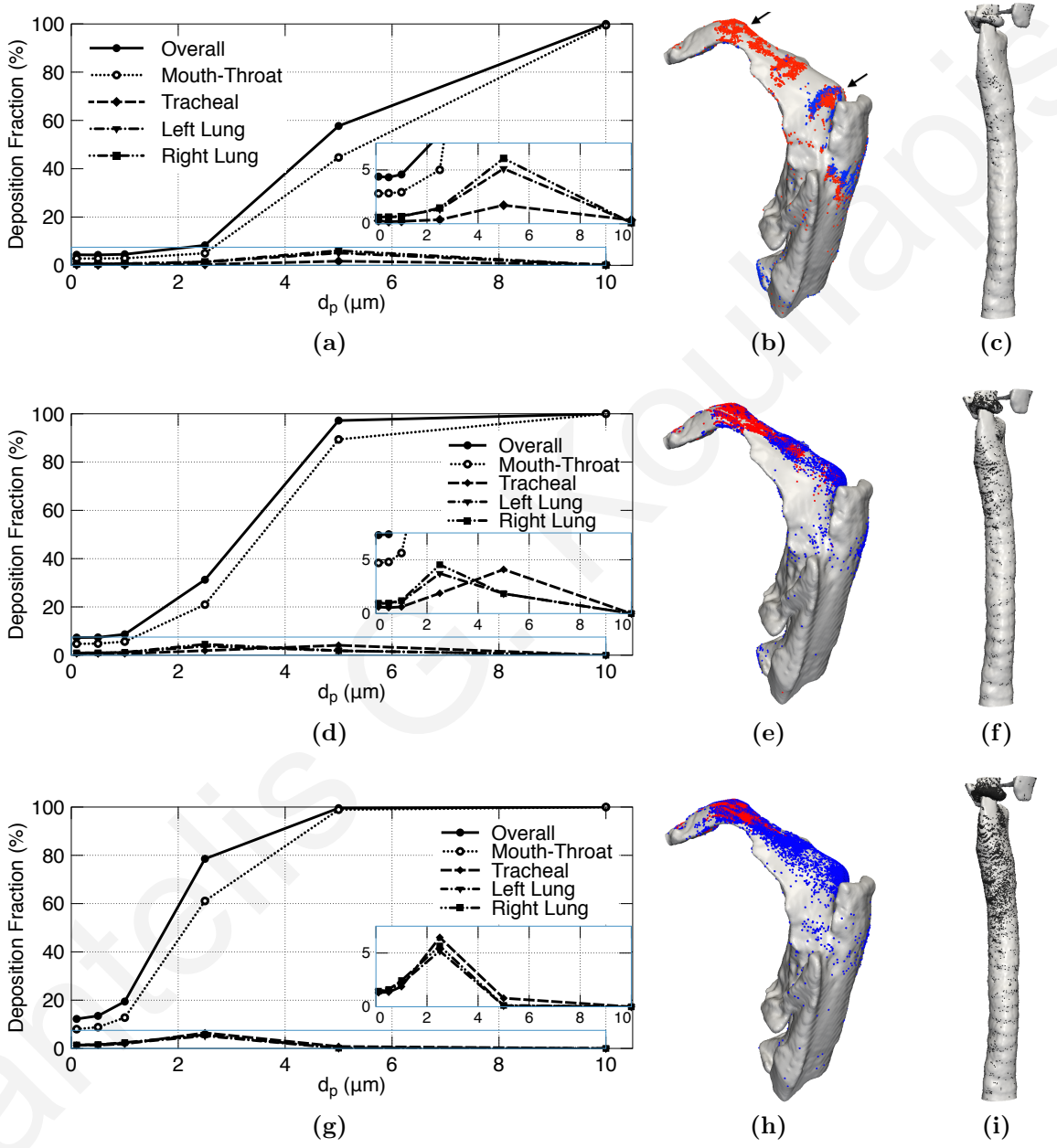

Figure 3.12: *DF and deposition locations under different flowrates (q=0). (a)-(c)* $\dot{Q} = 15.2$ *lt/min, (d)-(f)* $\dot{Q} = 30$ *lt/min, (g)-(i)* $\dot{Q} = 60$ *lt/min. In (b),(e),(h): blue for* d_p *=5μm and red for* d_p *=10μm diameter particles. In (c),(f),(i):* d_p *=2.5 μm*

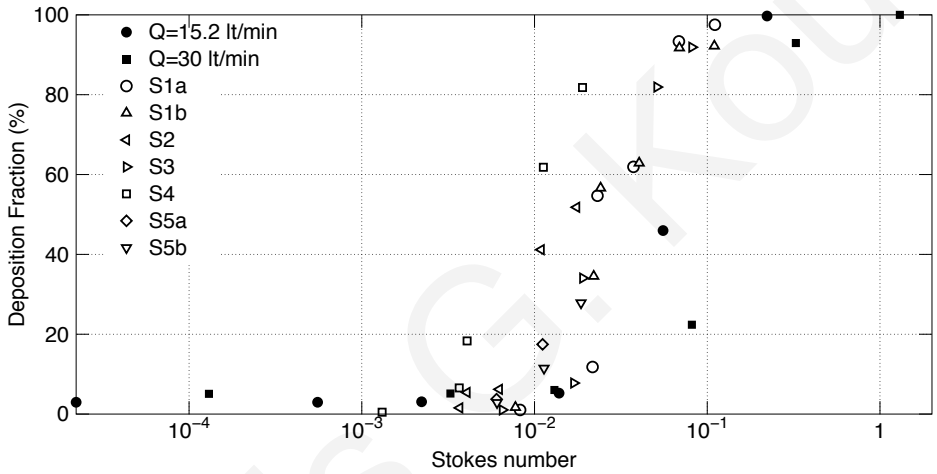

Figure 3.13: *Comparison of mouth-throat deposition with experimental results of Grgic et al. (2004a).*

3.4.3 Effect of particle charge

The level of charge on particles depends on the size and physical properties of these aerosols. In the current study five charge levels, i.e. 0, 50, 250, 500 and 1000 elementary charges (e) were considered. These charge levels are below the Rayleigh charge limit, which is the maximum amount of charge a liquid droplet can carry.

Fig. 3.14 presents the overall Deposition Fractions (DF) of particles as a function of the particle charge at the three flowrates considered. Note that 5 and 10μm particles are not shown due to insignificant variation in DF - inertial impaction remains the dominant deposition mechanism for these particles even when charged. Results show considerable increases in overall deposition due to electrostatic effects, especially for smaller particles (the slope of the curves in fig. 3.14 increases as the particle size decreases). Specifically, the overall DF of 0.1 μm particles with 1000 elementary charges at a flowrate of 15 Lt/min is approximately 7 times greater than that with no charge while the corresponding increase for 2.5 μm particles is 1.5 times. We note that in eqn. (2.39), the ratio Inc/Stk scales with $1/d^3$ and this explains the significantly greater effect of charge on deposition for the smaller particles. At the same flowrate and charge level, the value of the ratio Inc/Stk is four orders of magnitude greater for 0.1μm diameter particles compared to 2.5μm particles.

A similar deposition enhancement with increasing charge level is observed at all three flowrates, indicating a relatively small impact of inhalation flowrate on the deposition of charged particles of sizes ranging from 0.1-1 μm. However, in the case of 2.5μm particles, the increase in flowrate dominates the deposition enhancement due to electrostatic charge (DF curve becomes almost horizontal at the highest flowrate of 60 Lt/min). In other words, these particles are deposited primarily due to inertial impaction and electrostatic precipitation becomes negligible as the flowrate is increased. This agrees qualitatively with eqn. (2.39), in which the ratio Inc/Stk scales with $1/U_0^2$. The magnitude of mean fluid velocity U_0 in an airway is proportional to the flowrate. Thus, doubling the flowrate causes fourfold decrement of the ratio Inc/Stk and this results in reduced deposition arising from electrostatic attraction compared to impaction.

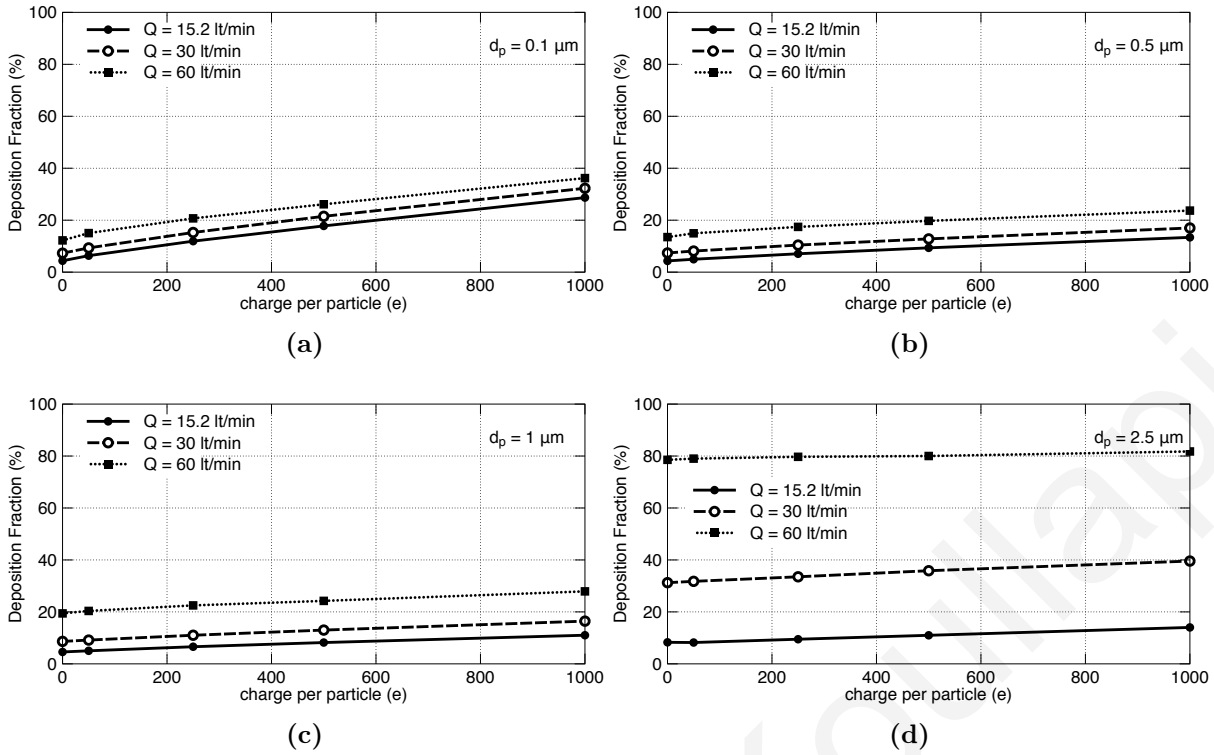

Figure 3.14: *Overall DF of particles as a function of the electrostatic charge at various flowrates.*

Bar graphs in figure 3.15 illustrate the overall and sub-regional DFs at a flowrate of $\dot{Q} = 15.2$ Lt/min (sub-regions shown in fig. 3.1a). Based on these graphs, most of the deposition enhancement due to electrostatic charge is found to occur in the mouth-throat sub-region. The airway geometry is quite complex in this region comprising of curvatures, constriction, expansions, bifurcating regions and cavities. As a result, the flowfield is also very complex and includes a high velocity jet, recirculation regions, cavity-like flows and strong secondary flows. Therefore, correlation of deposition characteristics with particle dimensionless parameters defined previously is not straightforward in the mouth-throat sub-region, since these parameters are more suitable for idealised circular airways. Of course, the effect of charge and particle size on deposition enhancement due to electrostatic effect is still evident, as discussed in the previous paragraph. Furthermore, mouth-throat sub-region constitutes approximately 40% of the total wall surface area. Consequently, the wall surface area that attracts the particles in this region is much larger compared to the other sub-regions. In conjunction with the complex flow characteristics described in the previous paragraph, which are likely to bring particles close to the walls, it results in enhanced deposition. Figure 3.16 shows the deposition enhancement in the mouth-throat for 0.1 and 2.5μm diameter particles and electrostatic charges of 0, 250 and 1000e. We observe that deposition is enhanced mostly in regions which already have high deposition due to impaction, namely the rear wall of the oral cavity (marked by the right arrow in fig. 3.12(b)) and the rear wall of oropharynx. The uncharged particles follow the fluid streamlines

and move close to the airway walls of these two locations. A group of these particles hits the wall and gets deposited while the rest of the particles avoid the collision with the wall. Nevertheless, these particles are still close to the airway walls and if they are charged, they are intercepted by electrostatic attraction. Thus, in these regions electrostatic and inertia effects seem to act synergistically. This is more evident for smaller particles since they are more sensitive to the electrostatic deposition mechanism, as discussed before. Furthermore, deposition of 0.1μm particles is more evenly dispersed compared to 2.5μm particles, since smaller particles have lower Stokes number and therefore they are more influenced from secondary flows and turbulent velocity fluctuations.

In general, high mouth-throat deposition of inhaled aerosols is not desirable for therapeutic purposes since the target sites in this case are usually the central conducting airways or the alveolar region of the deep lung. Therefore, care must be taken when assessing the inhaled drug dose of aerosol formulations carrying electrostatic charges. On the other hand, deposition enhancement due to electrostatic effects in the oral airways can act as a filtering mechanism for toxic sub-micron particles that would otherwise be able to penetrate in the deeper lung.

Conducting airways might be primary targets for inhaled drug delivery in local therapies, such as asthma and chronic bronchitis. Based on the bar graphs in figure 3.14, we observe approximately a sevenfold rise in DF in the left and right lung subregions (cumulative) for 0.1μm diameter particles carrying 1000 elementary charges. While the respective DF increases for 0.5 and 1μm particles are much lower, they still amount to over 200%. Thus, electrostatic charge increases substantially deposition in the conducting airways, especially for sub-micron particles. As indicated by the dimensionless parameter Inc (eqn. 2.38), the increase in deposition due to electrostatic attraction in the deeper conducting airways is expected to be more pronounced since airway diameter (D) and mean fluid velocity (U_0) decrease in these airways.

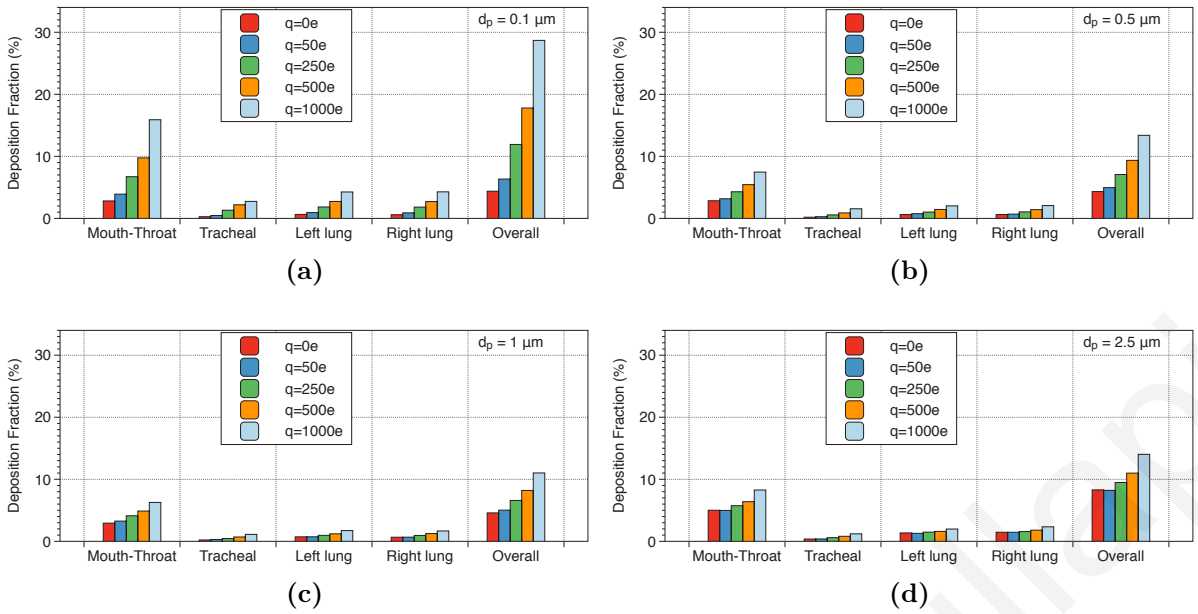

Figure 3.15: *Overall and sub-regional DF of particles with different charge levels at* $\dot{Q} = 15.2$ *Lt/min.*

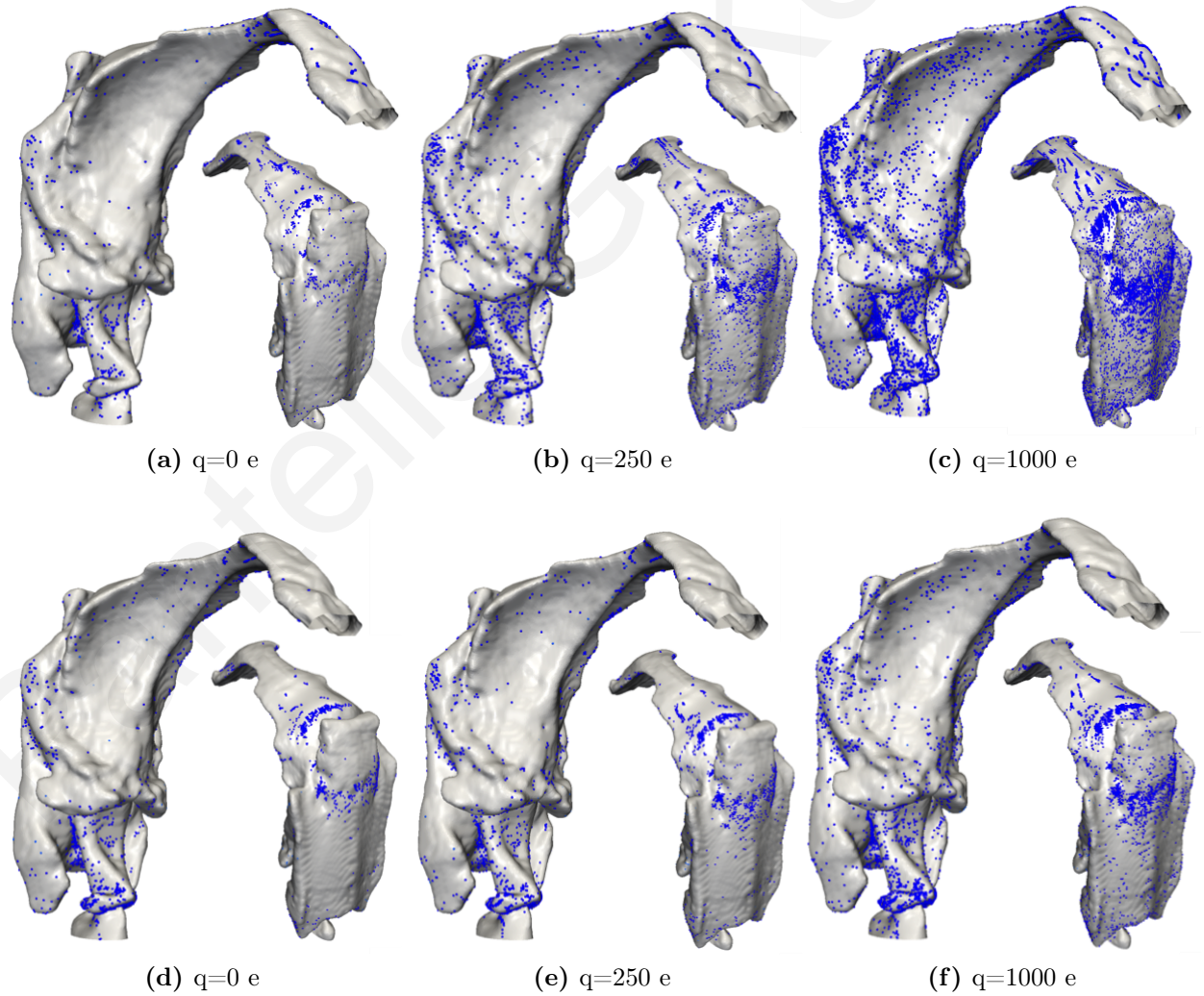

Figure 3.16: *Deposition locations in the mouth-throat region under different charges* ($\dot{Q} = 15.2$ *Lt/min). (a)-(c) 0.1 μm particles, (d)-(e) 2.5 μm particles*

3.5 Conclusions

Large Eddy Simulations were used to investigate deposition of inhaled aerosol particles in a realistic geometry of the human upper airways reconstructed from CT-scans. The effects of inlet velocity profile, inhalation flowrate and aerosol charge on particle deposition were examined.

Although the mean velocity fields are almost identical even at small distances from the mouth inlet as a result of the complex geometry, the number of deposited particles is increased in the case of measured velocity inlet conditions. Larger particles with greater inertia impact at the tongue as a result of their higher initial velocities while sub-micron particles are deposited uniformly due to diffusion in the same region. The DEs in the subsequent sub-regions are the same for particle sizes below $5\mu m$, while for $10\mu m$ some differences occur in the oral cavity and and the larynx.

The mean flow structures at the three flowrates are qualitatively similar regardless of Reynolds number. Greater values of turbulent intensities persist more downstream in the trachea and the main bronchi. The Deposition Fraction of particles is increased with flowrate due to greater inertial impaction, especially for 2.5 and 5μm diameter particles (enhanced deposition in the mouth-throat region), while 0.1, 0.5 and 1μm diameter particles have similar DF at a given flowrate.

The effect of charge is more significant for smaller particle sizes; the overall Deposition Fraction of 0.1 μm with 1000 elementary charges is approximately 7 times greater than that with no charge. The impact of inhalation flowrate on the deposition of charged particles is negligible for $d_p \leq 1\mu$m, while for $d_p \geq 2.5\mu$m inertial impaction prevails over electrostatic deposition mechanism. Deposition enhancement due to electrostatic effects is located mostly in the mouth-throat sub-region due to the large wall surface area that attracts the particles and the complex flowfield found in that region. Considerable increases in deposition of sub-micron particles are also found in the left and right lung sub-regions of our geometry, suggesting electrostatic charge manipulation as a possible mechanism for increasing deposition in the conducting airways of the respiratory tree. This could be beneficial in the treatment of diseased airways with inhaled medicines. Further future studies on the topic are therefore recommended.

Chapter 4

In silico assessment of mouth-throat effects on regional deposition in the human conducting airways

Journal Publication: *P. G. Koullapis, L. Nicolaou, S.C. Kassinos. In silico assessment of mouth-throat effects on regional deposition in the human conducting airways. Journal of Aerosol Science, 117: 164-188, 2018.*

Conference Presentation: *P. G. Koullapis, L. Nicolaou, S.C. Kassinos. In silico assessment of mouth-throat effects on regional deposition in the human conducting airways. CMBBE 2016, Tel Aviv, Israel (2016).*

Conference Presentation: *P. G. Koullapis, L. Nicolaou, S.C. Kassinos. The effect of mouth-throat geometry on regional deposition in the tracheobronchial tree. CMBE 2017, Pittsburgh, United States (2017).*

4.1 Outline

Motivated by the need to minimize the computational cost of high-fidelity numerical approaches for the prediction of localised deposition, the present study is designed to assess the role of the extrathoracic airways in determining regional deposition in the upper bronchial airways. Three mouth-throat geometries, with significantly different geometric and filtering characteristics, are merged onto the same tracheobronchial tree that extends to generation 8, and Large Eddy Simulations are carried out at steady inhalation flowrates of 30 and 60 L/min. At both flowrates, large flow field differences in the extrathoracic airways across the three geometries largely die out below the main bifurcation. Importantly, localized deposition fractions are found to remain practically identical for particles with aerodynamic diameters of up to $d_p = 4\mu m$ and $d_p = 2.5\mu m$ at 30 and 60 L/min, respectively. For larger particles, differences in the localized depo-

sition fractions are shown to be mainly due to variations in the mouth-throat filtering rather than upstream flow effects or differences in the local flow field. Deposition efficiencies in the individual airway segments exhibit strong correlations across the three geometries, for all particle sizes. The results indicate that regional deposition in the central airways can be estimated if the particle size distribution that escapes filtering in the mouth-throat of a particular patient is known. Our findings suggest that the computational cost in assessing aerosol deposition in the upper airways can be reduced, which is of great importance in population studies.

4.2 Introduction

With increasing gains in computing power, LES are nowadays widely used for research purposes in applications related to deposition in the human upper airways. However, application of LES in population studies (where a large sample would need to be simulated) and in routine clinical use on a patient-specific basis still remains challenging. Therefore, there is a need to reduce the computational times required to predict regional deposition. Moreover, whereas CT-reconstruction of the imaged TB airways is straightforward and semi-automated in specialized imaging softwares (Miyawaki et al., 2016a), reconstruction of the extrathoracic airways is more challenging due to the complexity of the structures in this region. Consequently, *in silico* assessments of regional deposition in the TB region can be accelerated further if reconstruction of a patient's MT geometry is not required. In addition to this, a large amount of chest CT-scans, which typically exclude the extrathoracic airways (Miyawaki et al., 2017), are available and could potentially be used for population studies of lung deposition.

The pronounced effect of geometric variation on deposition in the extrathoracic airways is well documented in the literature (Grgic et al., 2004a; Heenan et al., 2004; Burnell et al., 2007; Nicolaou and Zaki, 2013). Grgic et al. (2004a) performed measurements in several realistic MT geometries at flowrates of 30 and 90 L/min for particle diameters of 3-6.5μm. They found that both total and regional deposition exhibit large inter-subject differences, as well as intra-subject variability to a lesser extent. Deposition was found to occur primarily via impaction, and the mouth area was identified as the largest obstacle for inhaled aerosols. Rapid flow changes and small local cross-sectional areas were identified as the two main factors dictating local deposition. An empirical Reynolds number correction, $Re^{0.37}$, was applied to the Stokes number (Grgic et al., 2004b), which reduced scatter in the reported deposition efficiencies, and provided better collapse of their data onto a single curve.

In a later study, Nicolaou and Zaki (2013) examined the flow in a subset of four MT geometries used by Grgic et al. (2004a). Adopting an immersed boundary method to simplify the task of grid generation for the realistic airway geometries (Nicolaou et al., 2015), the authors performed DNS of the flow and related the predicted flow

to the variations in deposition observed in the *in vitro* measurements. It was found that geometric variation, even within the same subject, has a large impact on both the mean velocity profiles and the turbulence intensities. Their analysis also provided a physical explanation for the dependence of deposition on the flow Reynolds number. Their analysis revealed that the empirical correlation $StkRe^{0.37}$ arises due to the fact that deposition in the airways occurs via both impaction and turbulent diffusion. More recently, the authors proposed the use of an instantaneous Stokes number, based on the local properties of the flow field, for a more accurate representation of particle transport and deposition in the airways (Nicolaou and Zaki, 2016).

In an effort to identify key geometric parameters governing MT deposition, Burnell et al. (2007) investigated retention of drug aerosols inhaled from four delivery devices in 12 physical MT models *in vitro*. They found that deposition in the 12 models was dependent on the inhalation delivery system and that the most influential factor in MT deposition was the total volume. The airway geometries were ranked based on their retention efficiency and three models that represent high, median and low oropharyngeal filtration were identified. They suggested that these three models may reasonably cover the range of MT dimensions in the adult population and could therefore be used to indicate the expected range of MT deposition.

Besides the effect of geometric variability, previous studies have shown the importance of taking into account the laryngeal jet in order to accurately predict the airflow and aerosol deposition in the central airways. Lin et al. (2007) published the first DNS study in a subject-specific model of the upper airways with and without the MT region. They highlighted the role of the laryngeal jet in the production of turbulence downstream of the glottis constriction and concluded that subject-specific evaluations should include the extrathoracic airways. In a similar study, Xi et al. (2008) examined airflow and particle deposition in the upper TB airways in models with and without an approximate larynx using RANS. Significant differences were revealed between the two TB models in terms of flow patterns, aerosol dynamics, and wall deposition values. Notably, preserving the larynx increased particle deposition in the trachea by factors ranging from 2 to 10, while lowering deposition at the first carina and in some subsequent bifurcations.

In an LES study, Choi et al. (2009) investigated further the effect of truncation of the extrathoracic airways on the airflow in the trachea and downstream regions, in an effort to reduce imaging and computational costs. It was observed that the larger the truncation, the more inaccurate the flow fields. In fact, truncating the geometry just below the glottis resulted in laminar flow through the trachea and the bronchial regions. Even when part of the extrathoracic airways was included, the characteristics of the laryngeal jet were not entirely reproduced when pressure inlet conditions were prescribed. However, when the geometry was truncated at the midpharynx and a uniform velocity boundary condition was imposed, the predicted maximum mean ve-

locity and rms fluctuations in the trachea and the distal bronchial airways were in fair agreement with the complete geometry. In addition, both the pressure drop between the inlet and the subglottis as well as the turbulent kinetic energy levels in the distal bronchial airways were well predicted. Working towards the same goal, Miyawaki et al. (2017) proposed an idealised laryngeal model that can be attached to the imaged central airways starting from the trachea. The laryngeal model geometry was defined using only five parameters: (a) glottis location, (b) hydraulic diameter of the glottis, (c) hydraulic diameter proximal to the glottis, lengths of the larynx (d) proximal and (e) peripheral to the glottis. These parameters were empirically determined to construct an idealized laryngeal model. It was found that by imposing isotropic turbulent conditions proximal to the glottis, the laryngeal model approximation could reproduce a realistic level of turbulence compared to the full geometry containing the patient's mouth-throat. It was concluded that if the airway geometry proximal to the trachea is unknown, the turbulent flow generated with this laryngeal model would be accurate enough. In addition, if particle deposition in the central airways is of interest, inclusion of the extrathoracic region may not be necessary. On the other hand, if the focus are the flow structures and particle deposition close to the glottis, subject-specific models of the extrathoracic airways are certainly important.

While these previous studies focused primarily on the factors contributing to the well-documented inter-subject variability of aerosol deposition in the extrathoracic airways, here we attempt to answer a different question. In the current study, an *in silico* assessment of MT effects on deposition in the central airways is carried out. Three extrathoracic airway geometries, with different geometric and deposition characteristics, are merged onto the same TB tree that extends to generation 8. LES simulations are performed at steady inhalation flowrates of 30 and 60 L/min, which are relevant to drug delivery applications. The objective of this investigation is to quantify the effect of geometric (and thus flow field) variations in the extrathoracic airways on regional aerosol deposition in the first few generations of the human TB tree. The critical question we address is whether standardized MT models can be used to predict regional deposition in the bronchial airways with acceptable accuracy. A positive answer to this question would result in three important advantages:

1. Imaging and reconstructing the patient's extrathoracic airways would not be required. This would accelerate *in silico* assessments, and would be beneficial for the patient as it reduces exposure to radiation.

2. Precomputed flow fields in these standard MT models could be adopted for predictions of deposition in the bronchial tree, which would result in significant computational savings.

3. It could provide a rational approach to using the large number of chest CT-scans lacking MT data for *in silico* population studies.

4.3 Computational Details

4.3.1 Airway geometries

Three extrathoracic geometries, extending from a circular inlet at the mouth to the upper trachea, were merged onto the same model of the intrathoracic airways. The three MT models are shown in fig. 4.1.

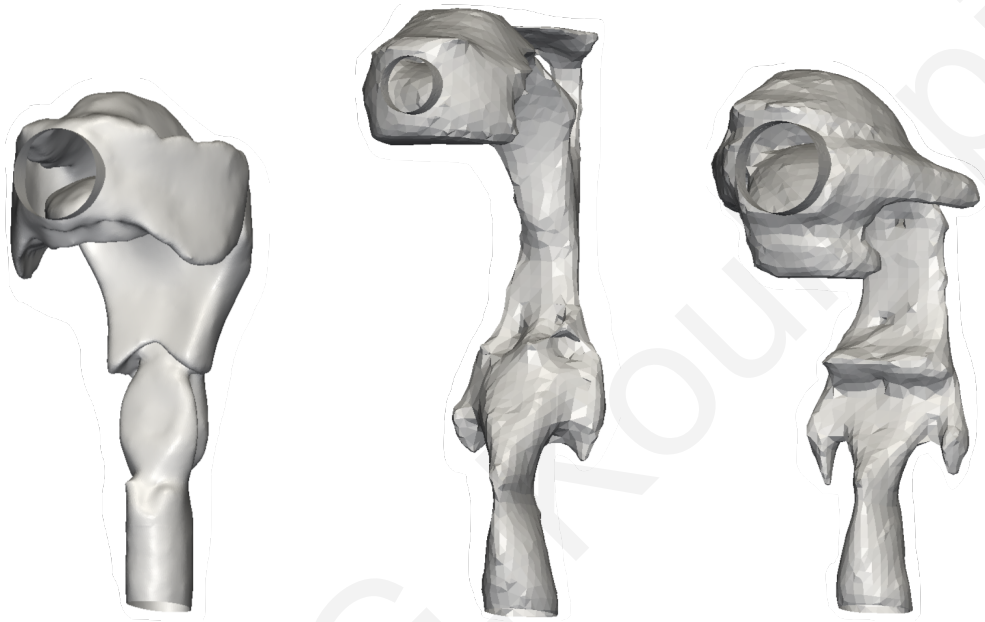

(a) **(b)** **(c)**

Figure 4.1: *Mouth-throat geometries adopted in the study: (a) R1, (b) S1a and (c) S2.*

The first geometry, R1, was developed by Lovelace Respiratory Research Institute. Details on the dimensions of the model are provided in Cheng et al. (1997). The anterior oral cavity was molded from an *in vivo* dental impression of a living Caucasian male at approximately 50% of full opening, and the remaining model was cast postmortem. The two other MT geometries, S1a and S2, were used in the *in vitro* deposition measurements of Grgic et al. (2004a) and in the DNS study of Nicolaou and Zaki (2013). These models were obtained using magnetic resonance imaging (MRI), as explained in detail by McRobbie et al. (2003). The main dimensions of the three MT models are listed in Table 4.1. The equivalent mean diameter was calculated assuming a circular cross-sectional area,

$$D_{mean} = 2\sqrt{\frac{V}{\pi L}}\,, \tag{4.1}$$

where V is the volume of the geometry and L is the sagittal length. The degree of area constriction at the glottis, which affects the characteristics of the laryngeal jet (Choi et al., 2009), is also reported in Table 4.1 ($A_{glottis}/A_{trachea}$).

Mouth-throat model	R1	S1a	S2
D_{inlet} (cm)	2	1.3	2.3
Volume (cm^3)	69.25	51.56	81.73
Length (cm)	15.86	19.1	18.6
D_{mean} (cm)	2.36	1.85	2.37
$A_{glottis}/A_{trachea}$	0.716	0.456	0.492

Table 4.1: *Dimensions of the mouth-throat geometries.*

The considerable variations in the geometric characteristics of the three MT models result in notable differences in their respective filtering efficiencies. This is reflected in fig. 4.2, where the CFD-predicted deposition fractions for the three MT models are shown as a function of particle size at an inhalation flowrate of $30\,L/min$. Model R1 has the lowest deposition and S1a the highest. In all three cases, deposition increases with particle size. For the purpose of the present study, differences in the extrathoracic airways are desirable since we are seeking to quantify their effect on the regional deposition in the upper TB region. Thus, the three models (R1, S1a and S2) were chosen so as to maximize the degree of variability in the geometric characteristics, the flow field, and the filtering properties.

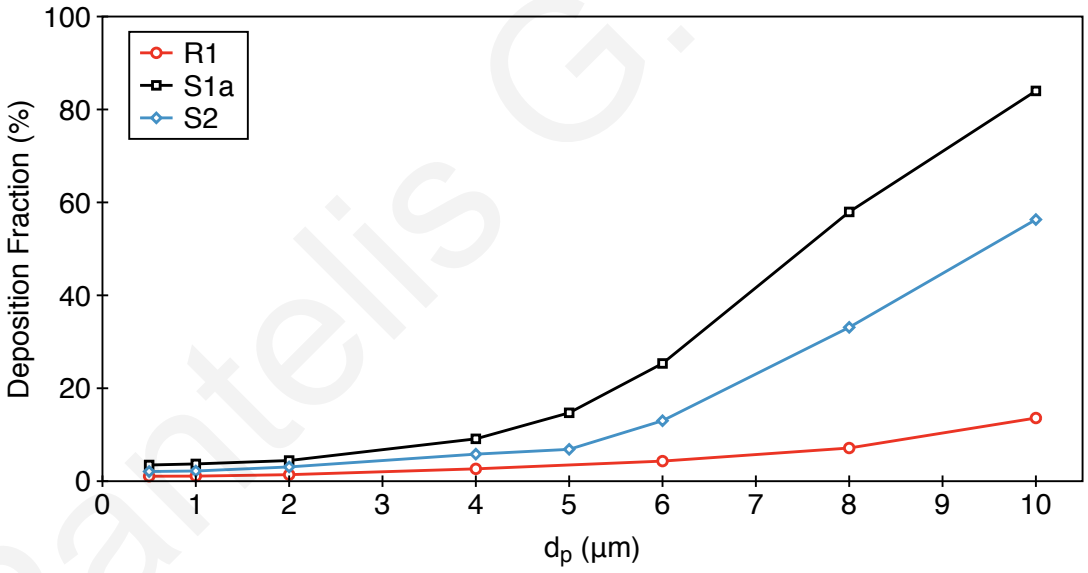

Figure 4.2: *Deposition fractions in the three MT models versus particle size at an inlet flowrate of* $30\,L/min$.

The TB geometry is shown in fig. 4.3. The model was obtained from a high-resolution CT of the lungs of an adult male free of pathological alterations, excised at autopsy and fixed in nearly end-inspiratory volume (Schmidt et al., 2004). Geometrical details can be found in Lizal et al. (2015). Segments 23-32 are outlets used for connecting the relatively small terminal branches into one larger outlet. The TB airway geometry together with the R1 MT model were used by Lizal et al. (2015) to

measure regional aerosol deposition *in vitro* via PET. In section 4.3.4, we use these *in vitro* results for validation of our *in silico* predictions.

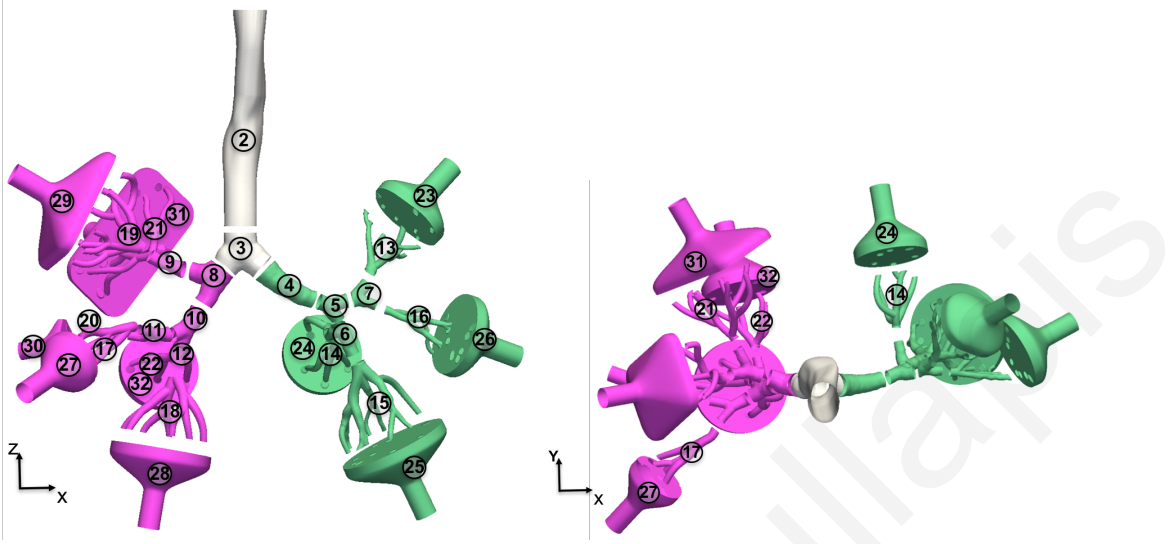

(a) **(b)**

Figure 4.3: *Front (a) and upper (b) views of the tracheobronchial geometry used in the simulations. The numbering of the various segments is also shown. Segments in the left and right lung are colored in green and purple, respectively.*

Finally, fig. 4.4 shows the three merged geometries used in our study. The MT geometries S1a and S2 were merged with the TB tree so that the location of the glottis constriction remained at the same height level as in geometry R1. In order to ensure a smooth geometric transition from the MT to the TB region, cubic spline interpolation was applied at multiple points along the circumferences of the MT outlet and the TB model inlet. The curves were then used to generate smooth surfaces that join the two domains. The merging procedure was carried out in Ansys ICEM CFD meshing software. Zoom-in locations in fig. 4.4(b) and (c) illustrate front and side views of the merging regions, in the upper and lower panels respectively.

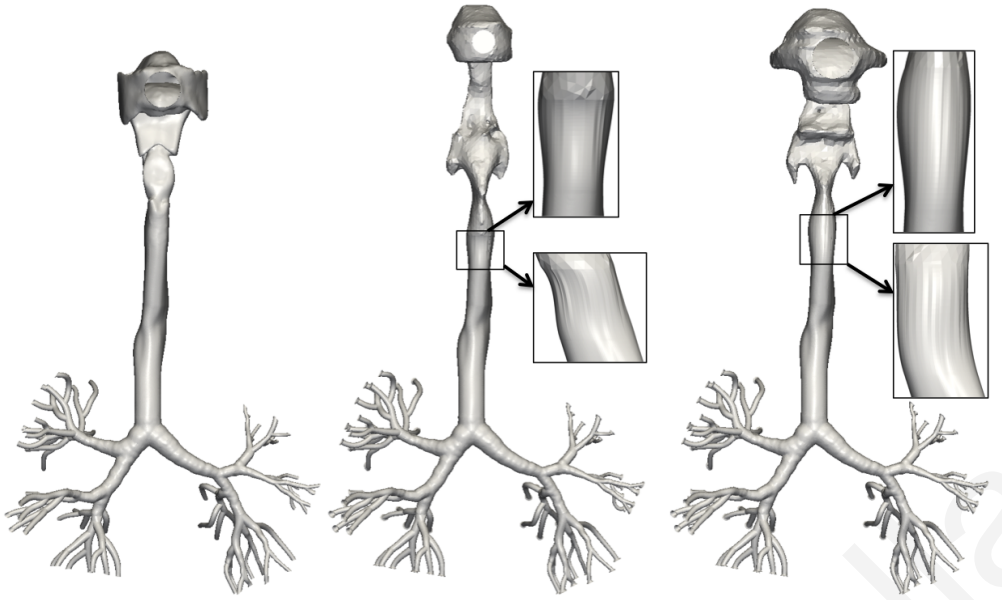

(a) **(b)** **(c)**

Figure 4.4: *Final merged geometries corresponding to (a) R1, (b) S1a and (c) S2.*

4.3.2 Continuous phase

Large Eddy Simulations (LES) are performed using the dynamic version of the Smagorinsky-Lilly subgrid scale model (Lilly, 1992) in order to examine the unsteady flow in the realistic airway geometries. The effect of the MT geometry on deposition in the central airways is examined for steady inhalation flowrates of 30 and 60 L/min. Table 4.2 summarizes the bulk velocity and Reynolds number at the mouth inlet and the trachea, which are given by,

$$U_b = \frac{Q}{A}, \qquad Re = \frac{U_b D}{\nu},$$

where the inlet and trachea diameters are used for the mouth inlet and the trachea, respectively.

Mouth-throat model	R1	S1a	S2
$Q(L/min)$	30 / 60	30 / 60	30 / 60
$\mathrm{U_{inlet}}$ (m/s)	1.59 / 3.18	3.77 / 7.54	1.2 / 2.4
$\mathrm{U_{trachea}}$ (m/s)	2.4 / 4.8	2.4 / 4.8	2.4 / 4.8
$\mathrm{Re_{inlet}}$	1871 / 3742	2883 / 5766	1628 / 3256
$\mathrm{Re_{trachea}}$	2300 / 5600	2300 / 5600	2300 / 5600

Table 4.2: *Mean velocity and Reynolds number at the inlet and the trachea for the three geometries at the two flowrates examined.*

For the lower flowrate of 30 L/min, the Reynolds number at the inlet of models R1 and S2 is in the laminar regime and thus a parabolic velocity profile is imposed. For all other cases, the Reynolds number at the inlets is in the transitional to turbulent regime. In order to generate appropriate inlet velocity conditions, a mapped inlet (or recycling)

boundary condition is used (Tabor et al., 2004). To apply this boundary condition, the pipe at the inlet is extended by a length equal to ten times its diameter. The pipe section is initially fed with an instantaneous turbulent velocity field generated in a separate pipe flow LES. During the simulation, the velocity field from the mid-plane of the pipe domain is mapped to the inlet boundary. Scaling of the velocities is applied to enforce the specified bulk flow rate. In this manner, turbulent flow is sustained in the extended pipe section, and a turbulent velocity profile enters the mouth inlet.

The volumetric flowrates at the 10 terminal outlets are prescribed based on the values measured *in vitro* (Lizal et al., 2015). These outlet conditions result in high asymmetry in the ventilation of the two lungs: the left lung receives 29% of the inhaled air whereas the right lung receives 71%. A no-slip velocity condition is imposed on the airway walls and atmospheric pressure is set at the inlet boundary.

To ensure numerical stability the time steps used are 5 and 2.5 $\times 10^{-6}$ s for the cases of 30 and 60 L/min, respectively. The mesh densities used in the three cases are determined based on a preliminary mesh sensitivity study carried out in the S1a MT model. The final generated meshes consist of approximately 50 million computational cells. Further details on the mesh convergence study are provided in Section 4.3.4.

4.3.3 Particle phase

Spherical, rigid and non rotating particles are introduced at the mouth inlet. The motion of each particle is individually computed by solving equations 2.18 and 2.19 to determine the particle velocity, $\vec{u}_p$, and position, $\vec{x}_p$. The forces taken into account are gravity, Drag and Brownian force. The gravitational acceleration vector, $\vec{g}$, points in the downward vertical direction At every time step 10 particles for each size are released from random positions at the mouth inlet. Particles are released over a time period equal to a flow-through in the trachea, and the total number of injected particles is 100,000 for each particle size. The initial velocity of the particles is set to match the air velocity at the inlet.

4.3.4 Mesh sensitivity study and validations

Airflow

In order to determine the required mesh density for our simulations, a set of preliminary LES in MT model S1a were performed on different mesh sizes, and the results were compared to DNS data (Nicolaou and Zaki, 2013). Geometry S1a was selected among the three MT models as the most challenging case due to the higher inlet Reynolds number, which results in turbulent inlet conditions even at the lower flowrate of 30 L/min. Since the flow relaminarizes in the downstream regions, the mesh convergence study

was limited to the MT region. Turbulent velocity conditions were imposed at the inlet using the mapped inlet boundary condition. At the outlet, a convective outflow condition was applied, in accordance to the DNS simulations of Nicolaou and Zaki (2013).

Four meshes with increasing densities were generated, designated as Meshes 1 to 4. The near-wall region was resolved with prismatic elements, while the core of the domain was meshed with tetrahedral elements. Cross-sectional views of the four meshes near the inlet of S1a are shown in fig. 4.5. Table 4.3 reports grid characteristics, such as the initial cell height (Δr_{min}), the number of prism layers near the walls, the average expansion ratio of the prism layers (λ), the total number of computational cells, the average cell volume ($V_{cell,avg.}$) and the average and maximum $y+$ values. In upper airway applications, turbulence is usually most active in the shear layers formed between high and low speed regions, such as the laryngeal jet (Tawhai and Lin, 2011). Thus, use of a strict $y^+ = 1$ condition for the near wall mesh is not essential. Based on this observation, the average cell volume of the generated meshes was approximately halved in every grid refinement. To further assess the mesh resolution near the walls, the number of prism layers was doubled and the spacing of the first computing node was reduced to one third in Mesh 4 compared to Mesh 3.

Mesh	1	2	3	4
$\Delta r_{min}(mm)$	0.081	0.065	0.065	0.022
Prism layers	4	4	4	8
λ	1.22	1.22	1.22	1.22
Comp. cells ($\times 10^6$)	7	12	24	42
$V_{cell,avg.}(mm^3)$	0.01	0.0063	0.0032	0.0018
Max y^+	3.27	3.73	3.76	1.48
Avg. y^+	0.88	0.73	0.71	0.24

Table 4.3: *Characteristics of Meshes 1-4 generated for the preliminary tests in the S1a mouth-throat geometry. Δr_{min} is the initial cell height, λ the average expansion ratio of the prism layers and $V_{cell,avg.}$ the average cell volume in the domain.*

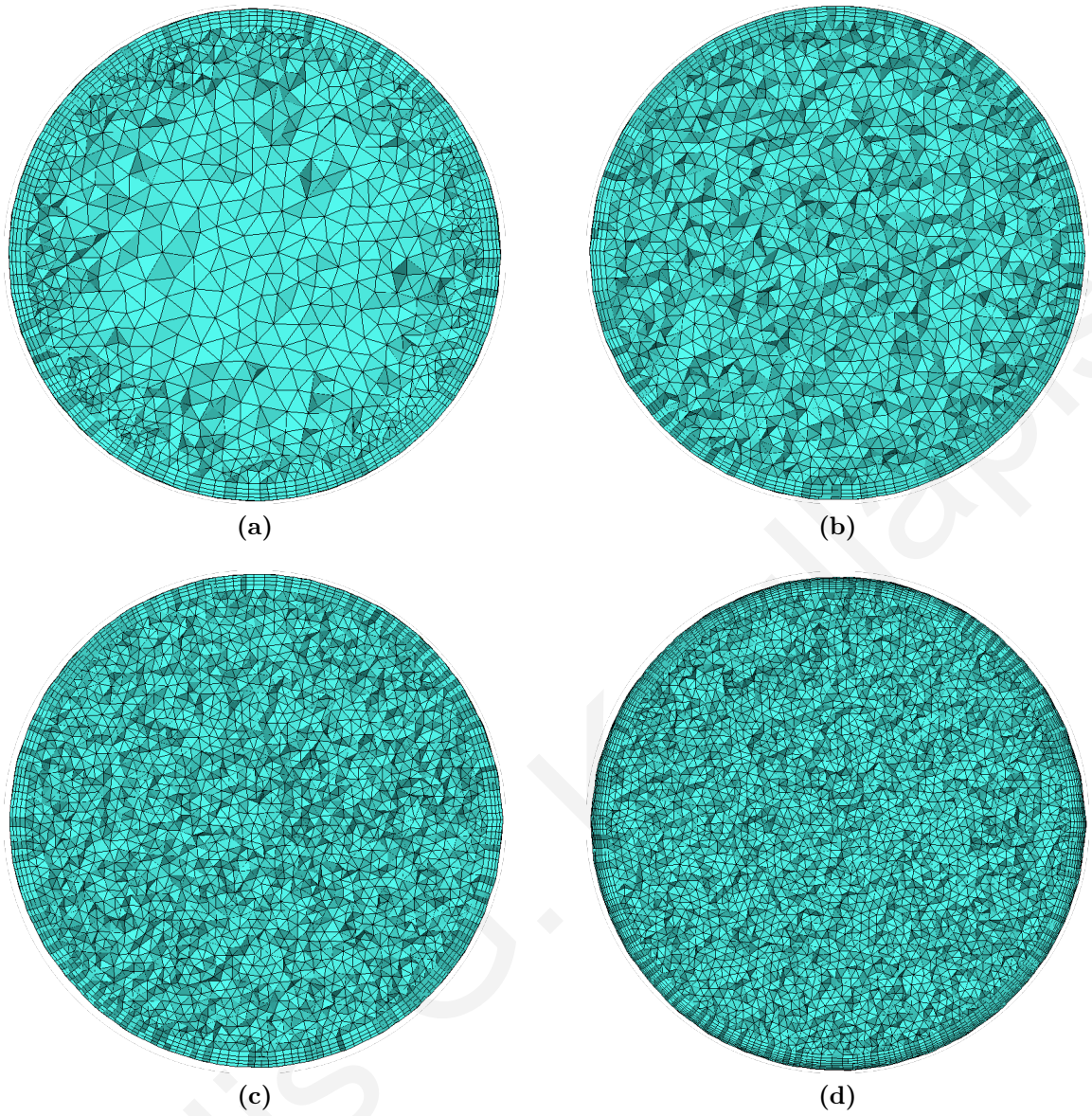

Figure 4.5: *Cross-sectional views of the four meshes near the inlet of geometry S1a: (a) Mesh 1 (7 million cells), (b) Mesh 2 (12 million cells), (c) Mesh 3 (24 million cells), (d) Mesh 4 (42 million cells).*

Fig. 4.6 displays the contours of mean velocity magnitude in the central sagittal plane and at various cross-sections of MT S1a. Results obtained with the four different meshes are shown alongside the DNS data obtained using an immersed boundary method (Nicolaou et al., 2015). Fig. 4.7 shows 2D profiles of the mean velocity magnitude at the lines of intersection between cross-sections A1-A2 to E1-E2 and the central sagittal plane. The mean velocity contours and 2D profiles indicate small differences among the four meshes. The LES and DNS results are in good agreement overall, which suggests adequate resolution for this flow configuration. Some differences are found in the low-speed regions at cross-section C1-C2, which are likely due to numerical or subgrid turbulence modelling aspects.

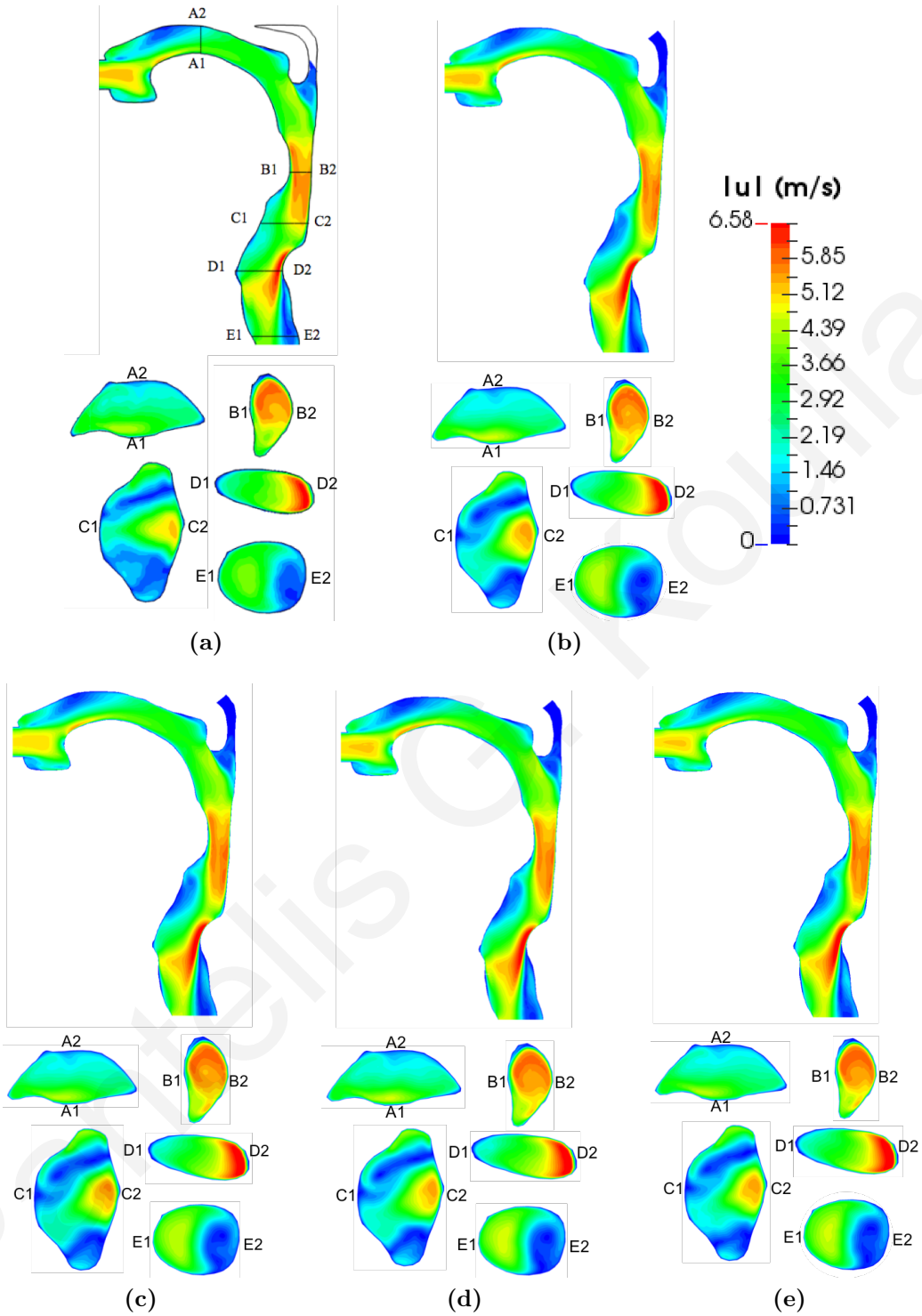

Figure 4.6: *Contours of mean velocity magnitude in the central sagittal plane and at various cross-sections of MT S1a: (a) DNS, (b) LES - Mesh 1, (c) LES - Mesh 2, (d) LES - Mesh 3, (e) LES - Mesh 4.*

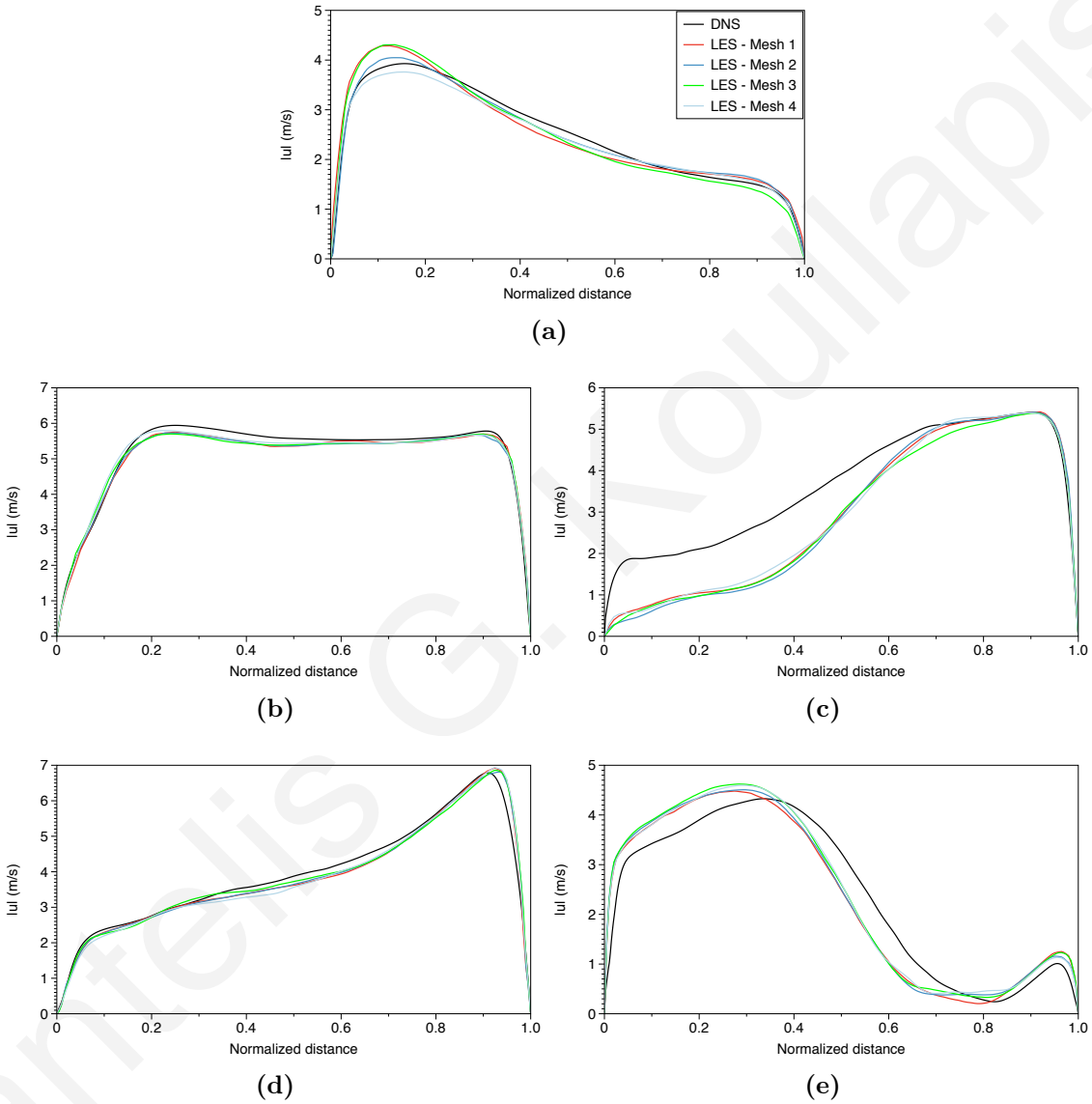

Figure 4.7: *Profiles of mean velocity magnitude at the lines of intersection between cross-sections A1-A2 to E1-E2 and the central sagittal plane. (a) A1-A2 (b) B1-B2 (c) C1-C2, (d) D1-D2, (e) E1-E2.*

Based on the findings presented above, meshes with densities similar to Mesh 2 were generated for the three MT-TB models, and LES simulations were carried out at inlet flowrates of 30 and 60 L/min.

Particle deposition

For validation purposes, deposition in geometry R1 was compared to the *in vitro* measurements by Lizal et al. (2015). Fig. 4.8 displays the deposition fractions at the individual geometry segments numbered in fig. 4.3, for particles of size 4.3μm at flowrates of 15 and 60 L/min. The error bars attached to the *in vitro* results at $Q = 60\,L/min$ correspond to the estimated experimental uncertainties as reported by the authors (Lizal et al., 2015). Numerical and experimental results are shown to be in reasonable agreement. Possible reasons for the observed discrepancies include experimental uncertainties at the inlet related to the velocity profile and the particle distribution. The *in vitro* inlet conditions might deviate from the velocity profiles and uniform particle distribution assumed in the CFD simulations due to the effect of the devices located upstream of the mouth in the experimental apparatus (Lizal et al., 2015). Similar levels of deviation between numerical and *in vitro* deposition results were reported by Koullapis et al. (2017), who applied six different LES and RANS solvers with different particle-tracking schemes to geometry R1.

In order to assess the degree of uncertainties as compared with other existing measurement data, we have plotted our CFD-predicted deposition efficiencies in the distal branches along with *in vitro* results from Lizal et al. (2015), Zhou and Cheng (2005) and Chan and Lippmann (1980). Fig. 4.9 displays deposition efficiencies versus the Stokes number (Stk), which is calculated using the diameter and bulk velocity of the parent airway in a particular bifurcation. As can be seen in the deposition plot, our results fall within the scatter of the experimental data.

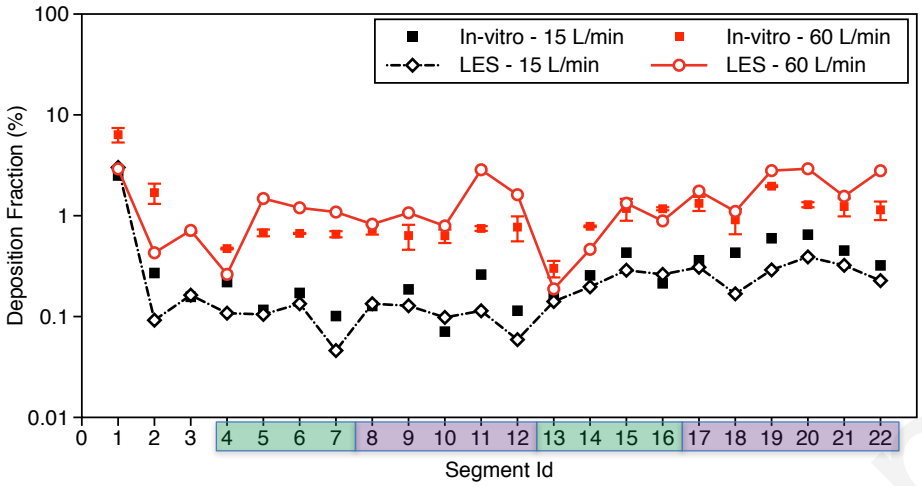

Figure 4.8: *Deposition fractions per segment in geometry R1 for particles of size* $4.3\mu m$ *at inlet flowrates of* 15 *and* $60\,L/min$*. The numbering of the segments is shown in fig. 4.3. The green and purple coloring denotes segments in the left and right lung, respectively. Segment 1 corresponds to the MT region.*

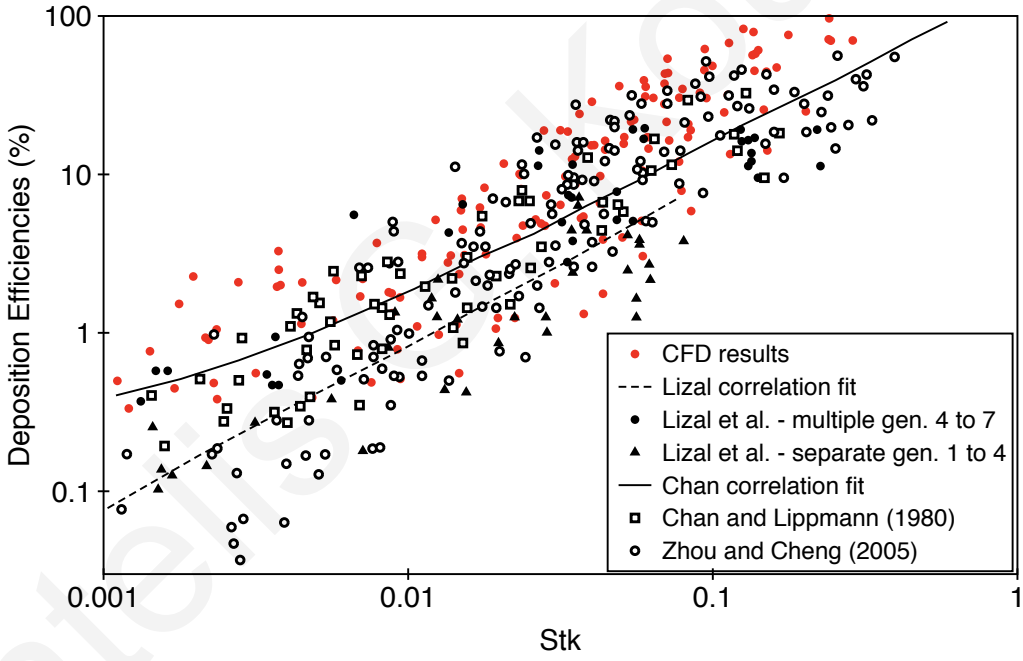

Figure 4.9: *Comparison of the CFD-predicted deposition efficiencies with previously published experimental data (symbols) and correlation fits (lines).*

4.4 Results

We begin by examining the flow and aerosol deposition across the three geometries at the lower inhalation flow rate, $Q = 30L/min$. The mean and turbulent flow characteristics in the extra- and intra-thoracic airways are presented first, followed by the results for regional deposition. The validity of the findings is then assessed at a higher inhalation flow rate, $Q = 60L/min$, in order to provide a conclusive picture of MT

effects on the flow and regional deposition in the TB airways.

4.4.1 Lower inhalation rate, $Q = 30\,L/min$

Airflow

Figures 4.10 and 4.11 show contours of the mean velocity magnitude and turbulent kinetic energy, $k = \frac{1}{2}\,\overline{u_i' u_i'}$ (u_i' are the fluctuating velocities), in the MT region and the trachea across the three geometries. Fig. 4.10(a) also displays isosurfaces of the mean velocity that outline the laryngeal jet. The mean velocity and turbulent kinetic energy are normalized by the bulk velocity in the trachea. Large qualitative differences in the flow characteristics can be observed in the oral cavities, pharyngeal and laryngeal regions of the three models. In the oral cavities of R1 and S2, lower velocities are observed, due to the larger cross-sectional areas compared to S1a. Moreover, the recirculation regions at the top and bottom walls of the oral passage are larger in these two geometries. Differences can also be identified in the turbulent kinetic energy levels. The airflow entering the mouth of model S1a is in the transitional regime. As a result, higher values of k are recorded near the inlet of S1a compared to the other two geometries, where the inflow is laminar. Low velocities and levels of turbulent kinetic energy persist in the pharynx and larynx of R1. In S1a, the flow accelerates in the narrow larynx, and high turbulent kinetic energy levels appear at the height of the epiglottis, which are attributed to the formation of the separated shear layer. In S2, the flow accelerates at the entrance of the pharynx as a result of the large reduction in cross-sectional area, and the maximum kinetic energy is observed in this region. In all three geometries, recirculation zones are found near the anterior wall at the height (R1, S2) and downstream (S1a) of the epiglottis, due to the airway curvature. These flow characteristics are consistent with the observations of Nicolaou and Zaki (2013), where a more detailed description of the airflow in geometries S1a and S2 is provided.

An important flow feature in the extrathoracic airways, which determines the mean and fluctuating behaviors of the flow downstream, is the laryngeal jet (Choi et al., 2009). The characteristics of the laryngeal jet are notably different in the three cases and are largely affected by the degree of constriction at the glottis (see Table 4.1). Geometry R1 has a mild glottal constriction ($< 30\%$ reduction in area at the glottis), resulting in a low-speed jet that is too weak to induce significant mixing with the ambient air, as indicated by the low turbulent kinetic energy levels in the trachea (fig. 4.11(b)). On the other hand, the higher degree of glottal constriction in S1a and S2 results in much stronger turbulent fluctuations that are convected down to the trachea. In S1a, the narrower glottal passage, in conjunction with the forward inclination of the trachea, shifts the jet core towards the anterior wall of the upper trachea (velocity isosurfaces and stations A-C for S1a in fig. 4.10(a) and (b)) and leads to the formation of a large

recirculation region near the rear wall. In S2, the laryngeal jet expands over a shorter length and a less pronounced recirculation zone develops due to the vertical orientation of the trachea below the glottis.

As we move to the mid-height of the trachea (station C), the flow has time to develop and differences in the mean velocity fields start to diminish notably, although variations are still evident in the turbulent kinetic energy levels. Further downstream (station D), differences in the mean flow and turbulence characteristics across geometries are further reduced and only small discrepancies remain, due to the effects of the upstream flow.

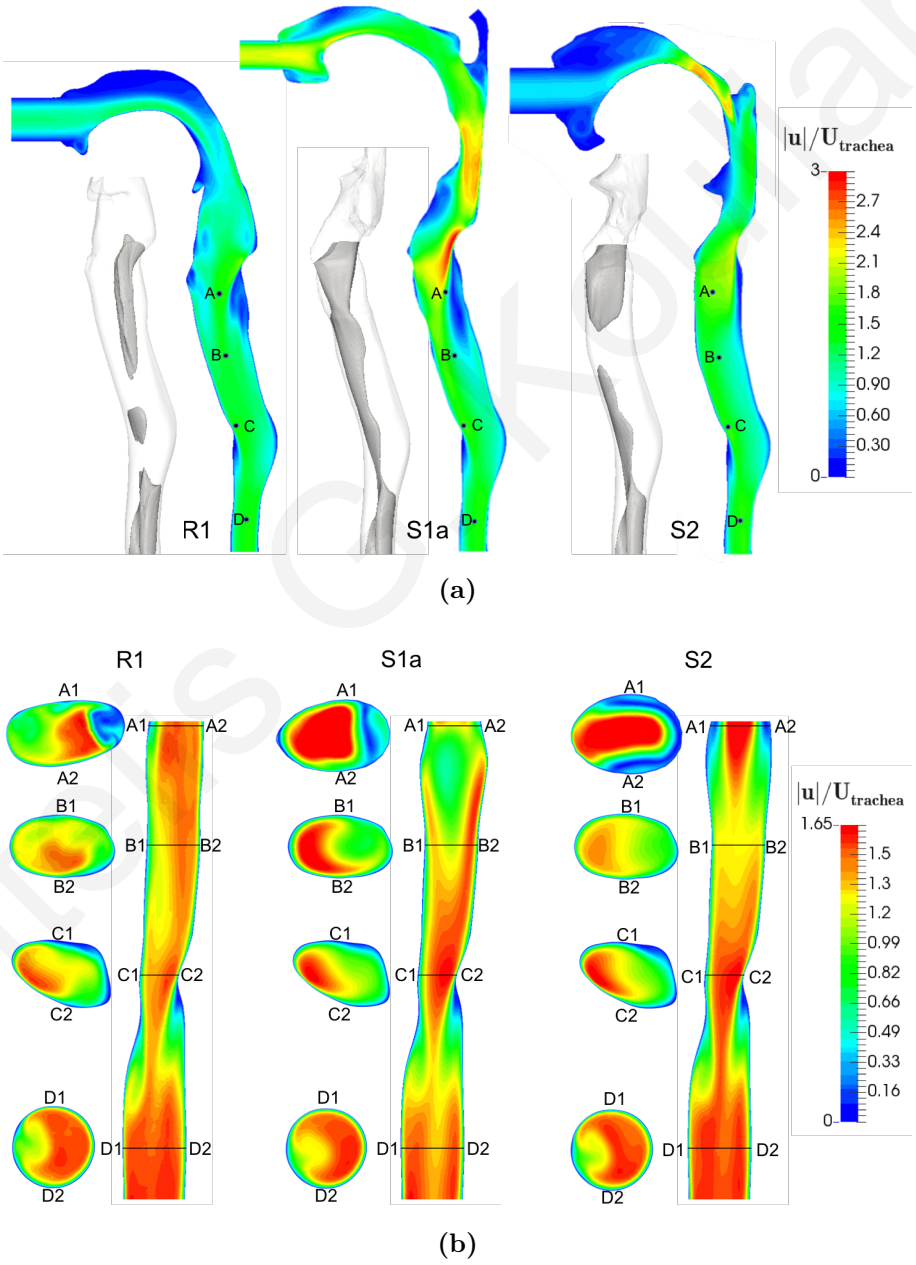

Figure 4.10: *Contours of normalized mean velocity magnitude in (a) the mouth-throat region (side view), and (b) the trachea (top and front views) at* $Q = 30\,L/min$*. In (a) isosurfaces of* $|u|/U_{trachea} = 1.45$ *are shown.*

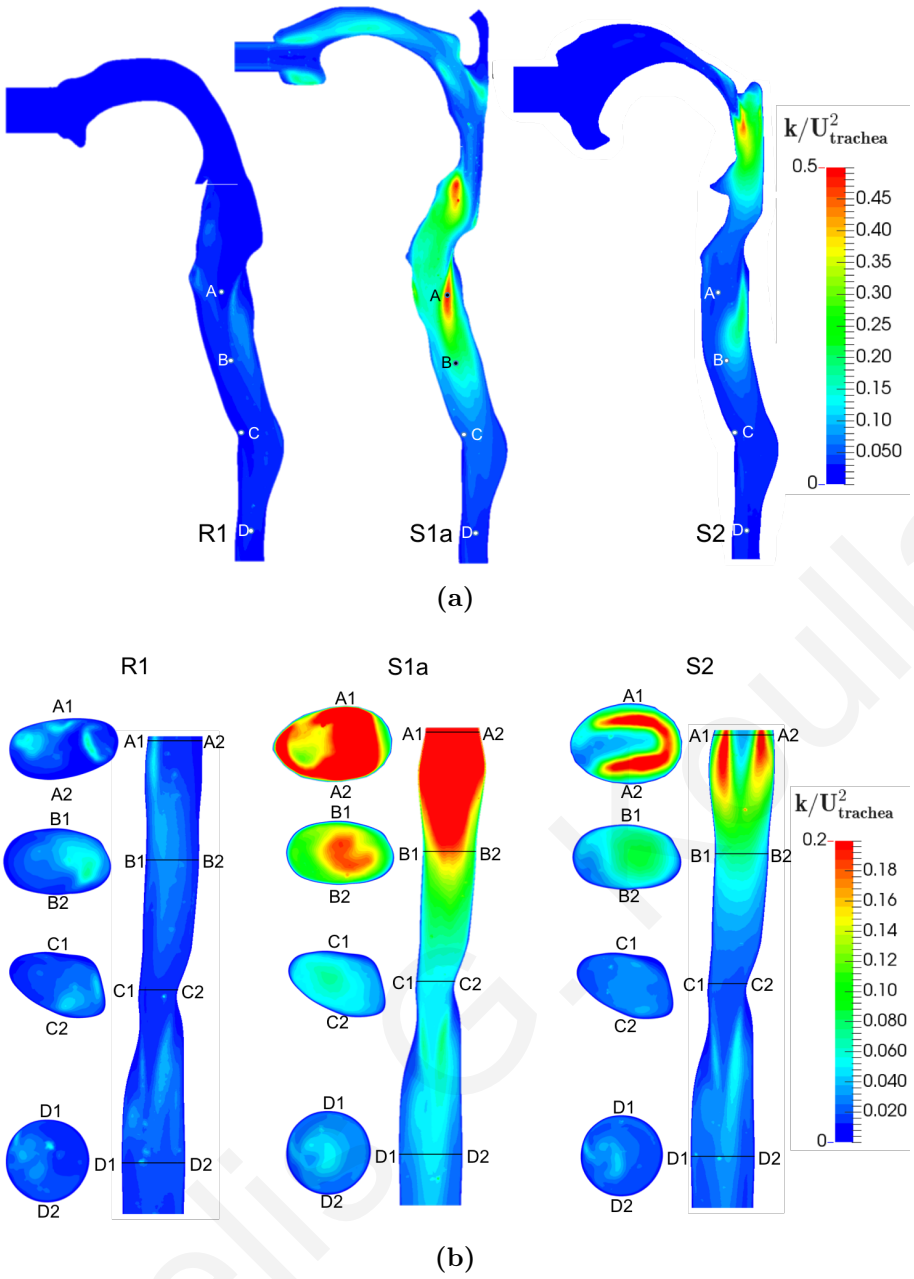

Figure 4.11: *Contours of normalized turbulent kinetic energy in (a) the mouth-throat region (side view), and (b) the trachea (top and front views) at* $Q = 30\,L/min$.

Contours of the normalized mean velocity magnitude in the main bronchi, and in the smaller airways of generations 3 and 4, are shown in fig. 4.12. A notable feature of the flowfield is the pronounced asymmetry at the main bifurcation, marked by a much larger recirculation zone near the outer wall of the left main bronchus (fig. 4.12(a)). The asymmetry in the flow reflects that of the airways; the left main bronchus branches off the carina at an angle of 60^o, significantly larger than the 48^o branching angle of the right bronchus. The recirculation regions are qualitatively similar across the three geometries, and only minor differences are observed at the main bifurcation and in the left main bronchus (fig. 4.12(a)). Slightly larger variations exist in the right main bronchus, which can be attributed to the higher ventilation of the right lung. Further down the TB tree, we continue to observe a similar trend. Variations in the flow are

more prominent in the right lung, mainly in the recirculation regions, as shown in fig. 4.12(c). Overall however, despite significant differences in the extrathoracic flow dynamics, the mean velocity in the TB tree remains qualitatively similar across the three geometries.

The corresponding results for the turbulent field in the TB tree are shown in fig. 4.13. Higher levels of turbulent kinetic energy are observed in the central bifurcation and the right main bronchus of models S1a and S2 (fig. 4.13(a)) compared to geometry R1. These differences can be attributed to the stronger turbulent intensities arising in the upstream regions of S1a and S2 that are then convected into the TB tree. Minor differences in turbulent kinetic energy levels, between S1a and S2 on one hand and R1 on the other, persist in the distal regions of the left and right lungs, as shown in figs. 4.13(b) and 4.13(c), respectively. It should be noted that turbulent kinetic energy levels in the bronchial airways are approximately an order of magnitude smaller than the values recorded in the extrathoracic regions, and thus the transport of particles is not expected to be affected significantly by these low intensity turbulent fluctuations.

In summary, the effect of geometric variation on the mean and turbulent flow characteristics in the extrathoracic region was found to be significant across the three geometries. This is to be expected, since the three models were chosen so as to provide a large degree of variability. The differences in the flow fields, however, settled down to relatively minor discrepancies in the bronchial tree. In the next section, we examine the regional particle deposition, in order to determine the impact of upstream flow effects and differences in the local flow field on TB deposition.

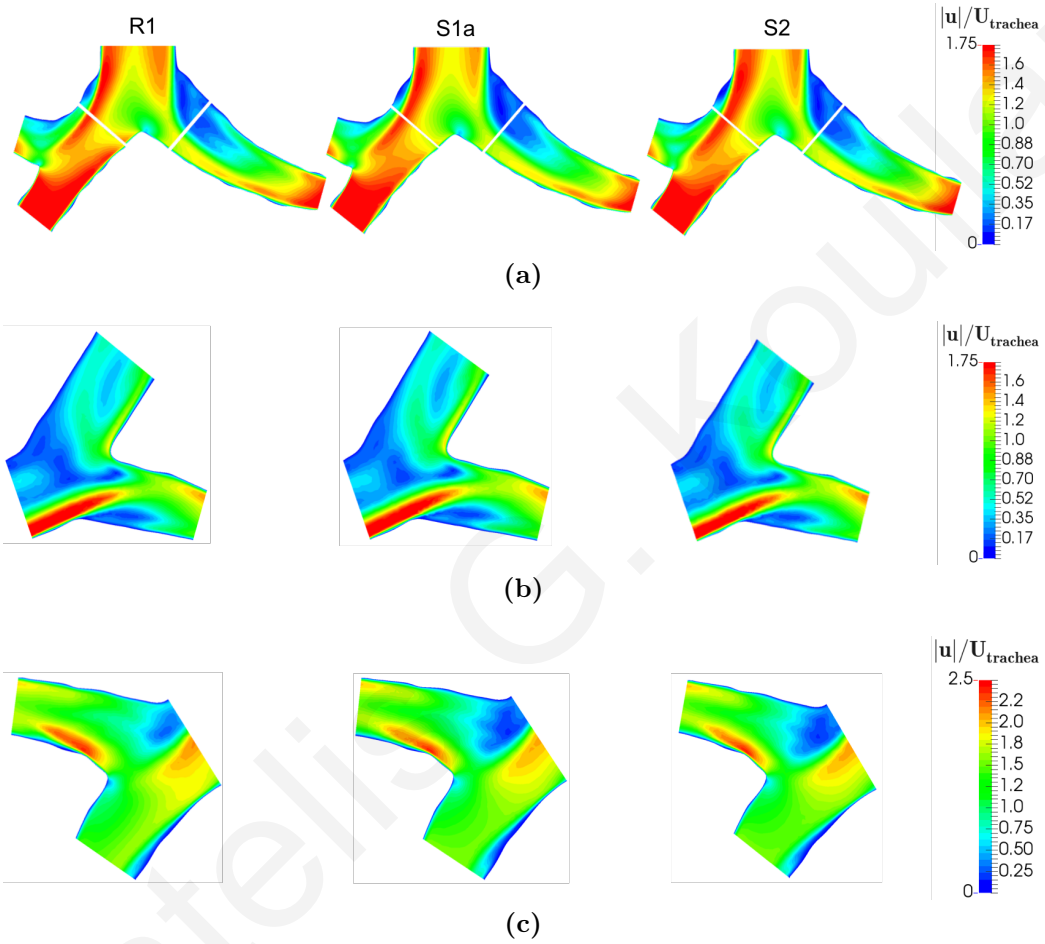

Figure 4.12: *Contours of normalized mean velocity magnitude in the tracheobronchial tree at $Q = 30\,L/min$: (a) first bifurcation and main bronchi; (b) third to fourth generation bifurcation in the left lung; and (c) third to fourth generation bifurcation in the right lung.*

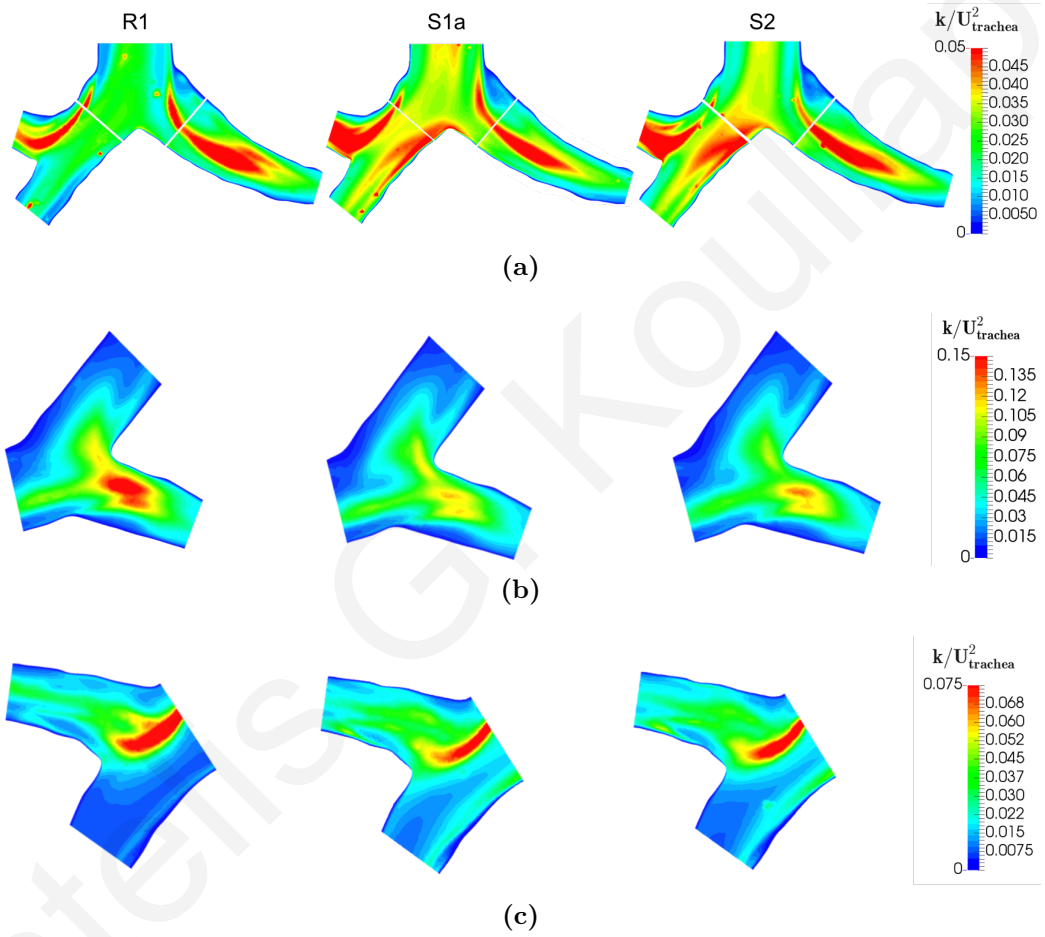

Figure 4.13: *Contours of normalized turbulent kinetic energy in the tracheobronchial tree at $Q = 30\,L/min$: (a) first bifurcation and main bronchi; (b) third to fourth generation bifurcation in the left lung; and (c) third to fourth generation bifurcation in the right lung.*

Particle deposition

Fig. 4.14 shows the deposition fractions as a function of particle size at $30\,L/min$ in (a) the overall geometry, (b) the mouth-throat region, and (c) the tracheobronchial tree. In addition, Fig. 4.14(c) displays particle sizes in terms of the Stokes number based on the mean diameter and bulk velocity in the trachea,

$$Stk_{trachea} = \frac{\rho_p d_p^2 U_{trachea}}{18\mu_f D_{trachea}}\,, \tag{4.2}$$

where $U_{trachea}$ is given in Table 4.2 and $D_{trachea} = 1.63\,cm$.

Deposition results in the overall geometry follow a similar trend to MT deposition, with model S1a having the highest values and R1 the lowest. However, differences in the overall deposition across the three geometries are significantly smaller than those noted for MT deposition. This is due to reverse filtering effects occurring in the TB and MT regions that tend to partially compensate for each other. While in the MT region the highest and lowest deposition fractions correspond to models S1a and R1, respectively, in the TB region these trends are reversed, as shown in fig. 4.14(c). It is also worth noting that in the TB region, deposition appears to be appreciable at seemingly very small Stokes numbers ($Stk < 5 \times 10^{-2}$). This is attributed to the fact that the reported Stokes numbers are calculated based on the mean diameter and bulk velocity in the trachea and thus do not reflect the local properties of the geometry and the flowfield (Nicolaou and Zaki, 2016). In geometry S1a, deposition of the $10\mu m$ particles in the TB region is lower than for the smaller particles of 6 and $8\mu m$, due to the significant filtering that occurs upstream in the extrathoracic airways. It is important to note that for particles smaller than $4\mu m$ ($Stk_{trachea} < 5.94 \times 10^{-3}$), TB deposition is unaffected by the MT model. Even for $6\mu m$ particles ($Stk_{trachea} = 1.34 \times 10^{-2}$), the maximum variation in TB deposition is less than 4% and, reduces below 3% if differences in deposition in the trachea (segment 2) are excluded. Therefore, these results suggest that for particle sizes typically used in drug delivery applications, i.e. 1-5 microns, localized deposition in the central airways is largely unaffected by the MT geometry.

Deposition within the TB tree can be examined in further detail by determining the deposition fractions in individual airway segments, as shown in fig. 4.15 for various particle sizes at $30\,L/min$. Beyond the trachea, and for particles smaller than $6\mu m$, similar deposition fractions are observed across the three geometries, even at the localized level. Essentially, for particles smaller than $4\mu m$, differences are negligible in the vast majority of segments within the TB region. For larger particles with diameters above $8\mu m$, variability in TB regional deposition across the three geometries becomes more significant. This variation arises due to the large differences in the MT

filtering, which are as high as 70% for $10\mu m$ particles between geometries S1a and R1 (fig. 4.14(b)).

The conclusions made herein are based on results at $30\,L/min$. However, many inhaler devices, such as DPIs, typically operate at higher inhalation flowrates (Wong et al., 2012). Therefore, in the following section, we assess the validity of these findings at a higher flowrate of $60\,L/min$.

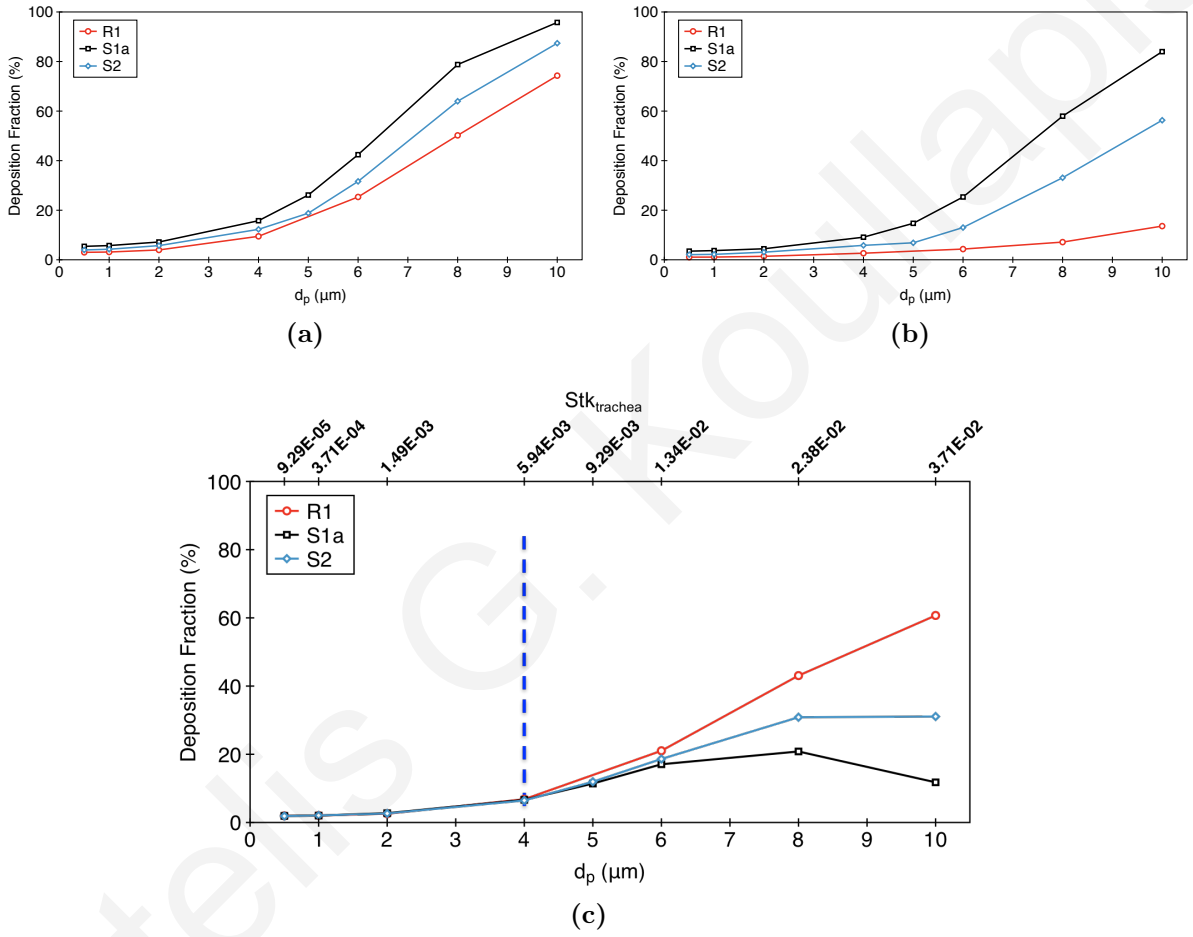

Figure 4.14: *Deposition fractions versus particle size at $Q = 30\,L/min$: (a) overall; (b) mouth and throat; and (c) tracheobronchial. In (c), the Stokes numbers based on tracheal parameters are also displayed.*

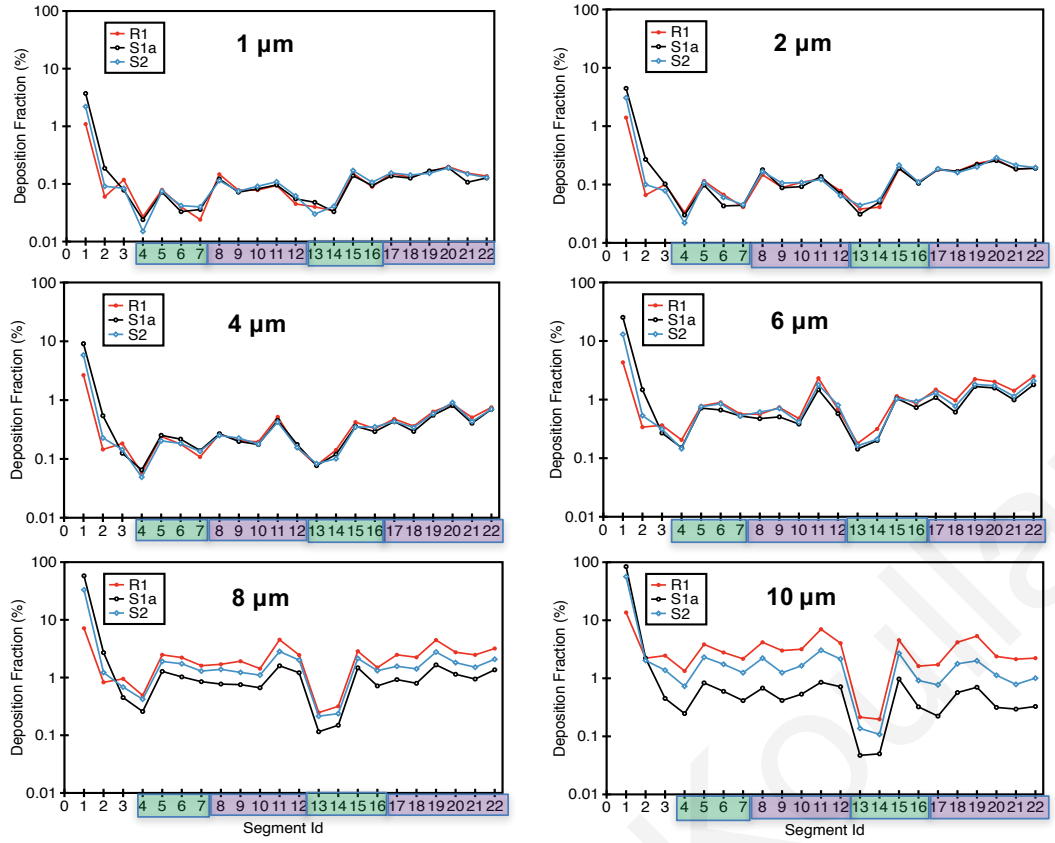

Figure 4.15: *Deposition fractions per segment at $Q = 30\,L/min$ for various particle sizes. The numbering of the segments is shown in fig. 4.3. The green and purple coloring denotes segments in the left and right lung, respectively. Segment 1 corresponds to the mouth-throat region.*

4.4.2 Higher inhalation rate, $Q = 60\,L/min$

Airflow

Figures 4.16 and 4.17 show contours of the normalized mean velocity magnitude and turbulent kinetic energy in the MT region and the trachea across the three geometries at a flowrate of $60\,L/min$. Fig. 4.16(a) also displays isosurfaces of normalized mean velocity that outline the laryngeal jet. The mean flow features remain similar to those noted for the lower flowrate. Nevertheless, small reductions in the magnitudes of the normalized mean velocities are evident at this higher flowrate. These lower velocities result from the increased turbulent mixing that occurs as the flowrate, and hence the Reynolds number, doubles. Turbulent kinetic energy levels in the MT and the trachea also exhibit strong resemblance to those observed at the lower flowrate, with the local maxima appearing at the same locations. As in the lower flowrate case, the effect of geometric variation is clearly evident in the MT region. However, at the exit to the trachea (D1-D2), the flow is qualitatively similar across all three geometries despite the higher flowrate and increased turbulence levels.

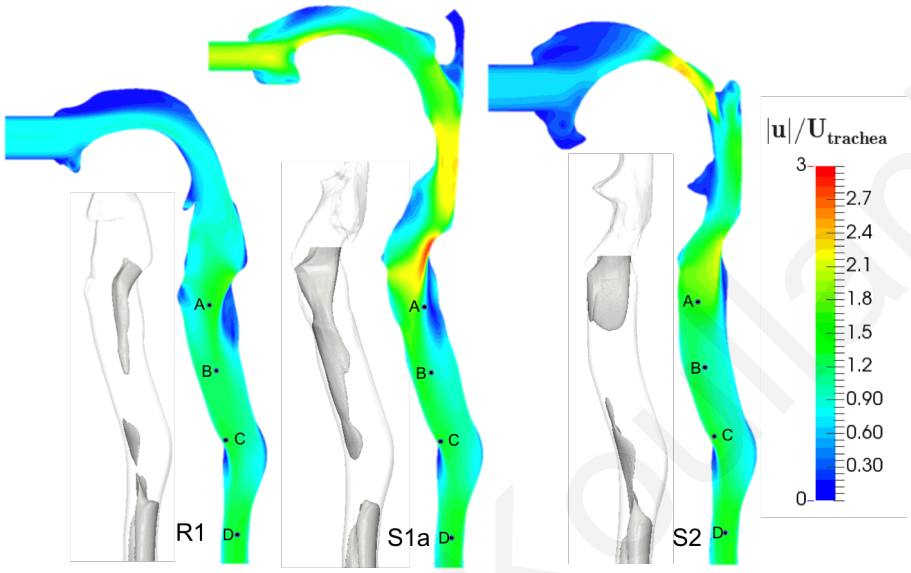

(a)

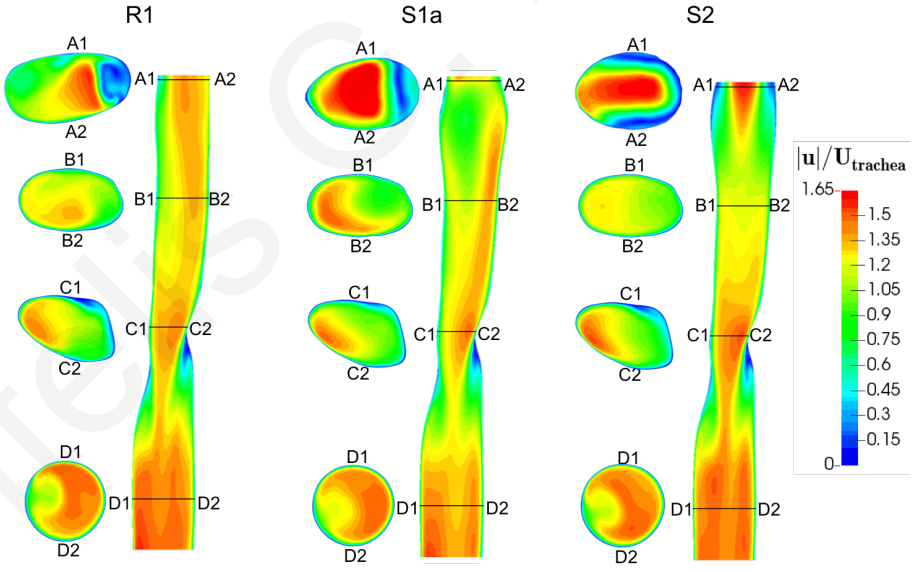

(b)

Figure 4.16: *Contours of normalized mean velocity magnitude in (a) the mouth-throat region (side view), and (b) the trachea (top and front views) at* $Q = 60\,L/min$*. In (a) isosurfaces of* $|u|/U_{trachea} = 1.35$ *are shown.*

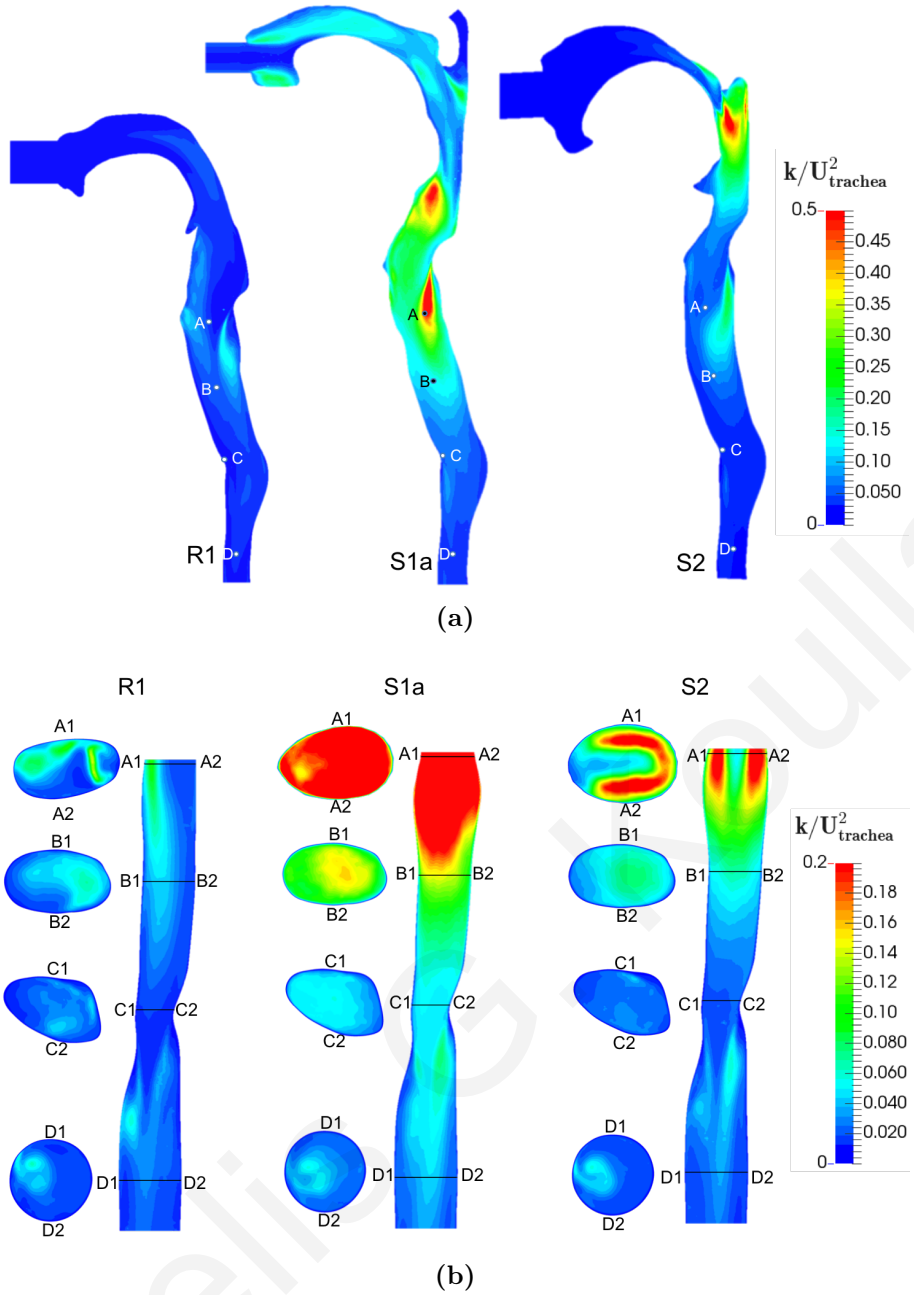

Figure 4.17: *Contours of normalized turbulent kinetic energy in (a) the mouth-throat region (side view), and (b) the trachea (top and front views) at* $Q = 60\,L/min$.

As we move deeper into the TB tree, first into the main bronchi and then into bronchial generations 3 and 4, the mean velocity fields are again found to remain similar across the three cases, as shown in fig. 4.18. The same holds for the turbulent kinetic energy levels in the TB region, shown in fig. 4.19. In conclusion, despite significant differences in the extrathoracic flow features, the mean and turbulent fields in the TB tree remain qualitatively similar across the three geometries even at a flowrate of $60\,L/min$.

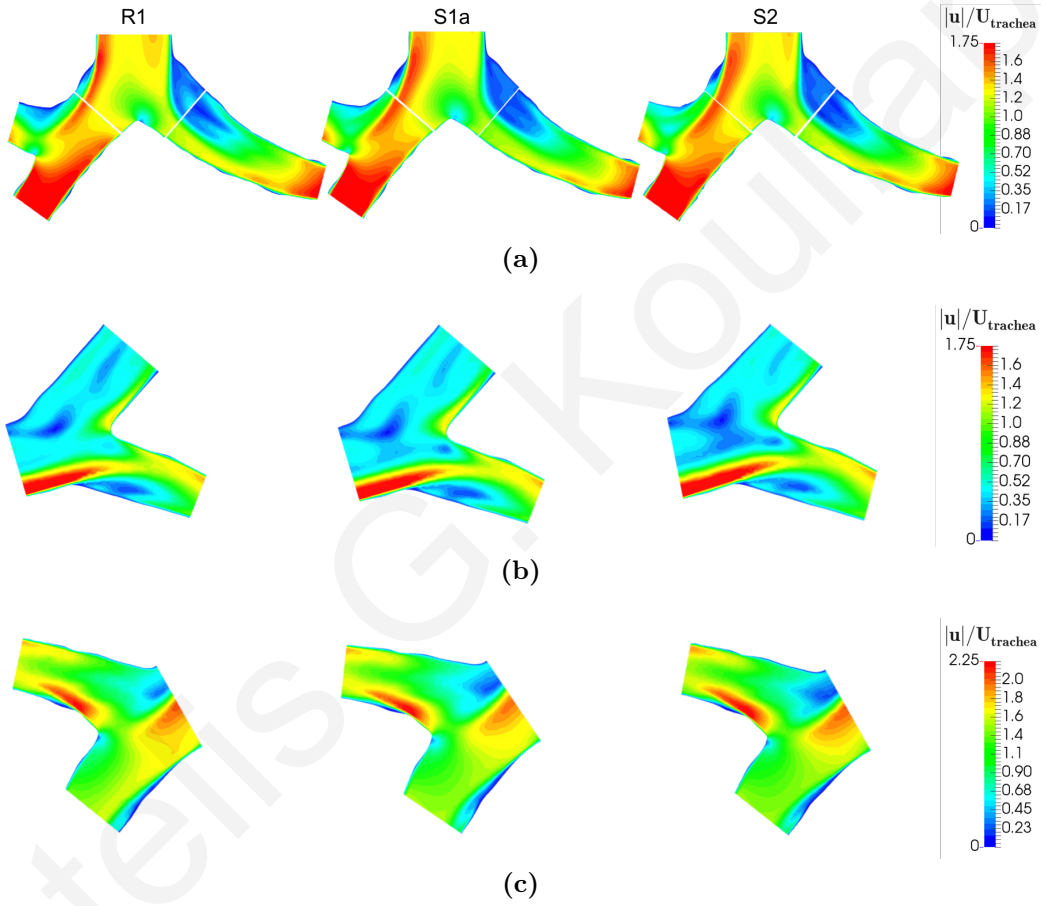

Figure 4.18: *Contours of normalized mean velocity magnitude in the tracheobronchial tree at $Q = 60\,L/min$: (a) first bifurcation and main bronchi; (b) third to fourth generation bifurcation in the left lung; and (c) third to fourth generation bifurcation in the right lung.*

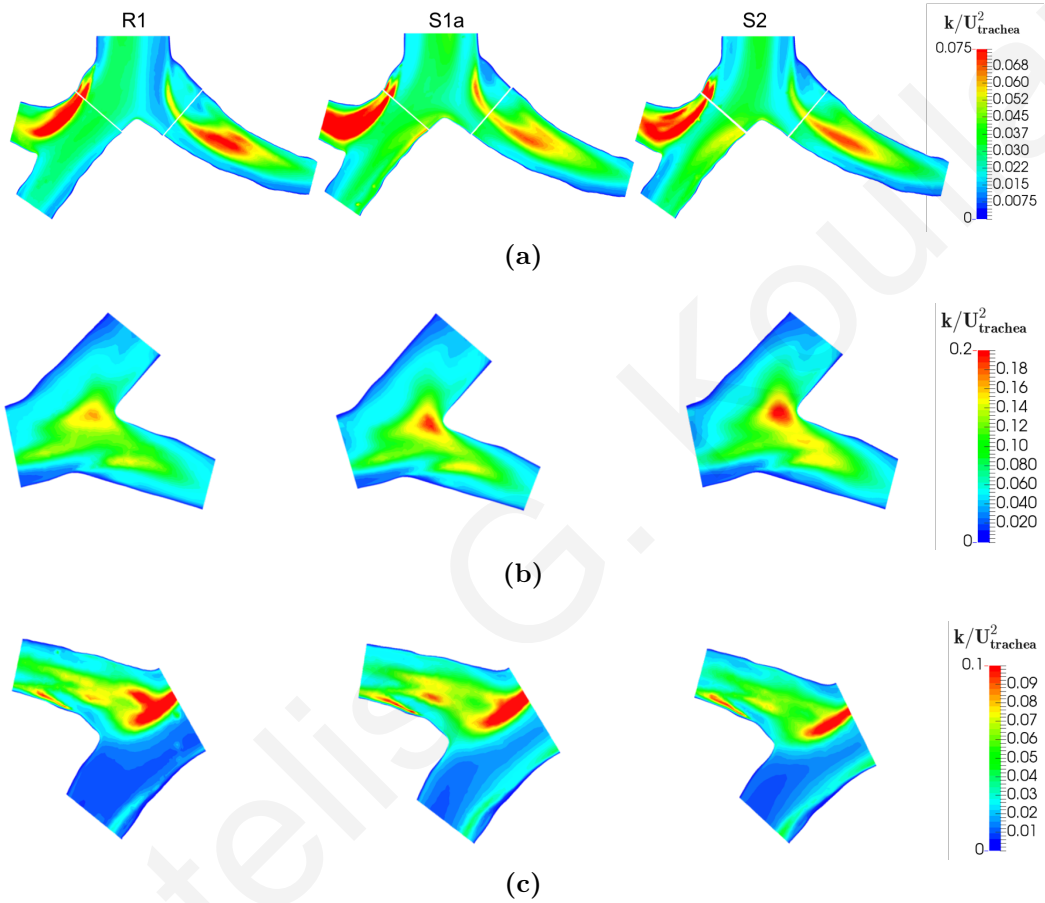

Figure 4.19: *Contours of normalized turbulent kinetic energy in the tracheobronchial tree at $Q = 60\,L/min$: (a) first bifurcation and main bronchi; (b) third to fourth generation bifurcation in the left lung; and (c) third to fourth generation bifurcation in the right lung.*

Particle deposition

Fig. 4.20 shows the deposition fractions versus particle size at $60\,L/min$ in (a) the overall geometry, (b) the mouth-throat region, and (c) the tracheobronchial tree. In fig. 4.20(c), the Stokes number based on tracheal parameters is also displayed. At this flowrate, greater differences are observed in the overall deposition of the smaller particles among the three models (fig. 4.20(a)). MT deposition is again significantly different across the three geometries, and notably at this flowrate, a larger variation is observed for the intermediate particle sizes. In S1a, the largest particles are almost entirely filtered out in the MT (fig. 4.20(b)). For particles larger than $2.5\mu m$, deposition in the TB region is inversely related to the MT filtering: model R1 has the highest TB deposition, and S1a the lowest. For particles smaller than $2.5\mu m$ ($Stk_{trachea} < 4.64 \times 10^{-3}$), TB deposition is unaffected by the MT, whereas for $4\mu m$ particles ($Stk_{trachea} = 1.19 \times 10^{-2}$) the maximum variation in TB deposition is 7.5%.

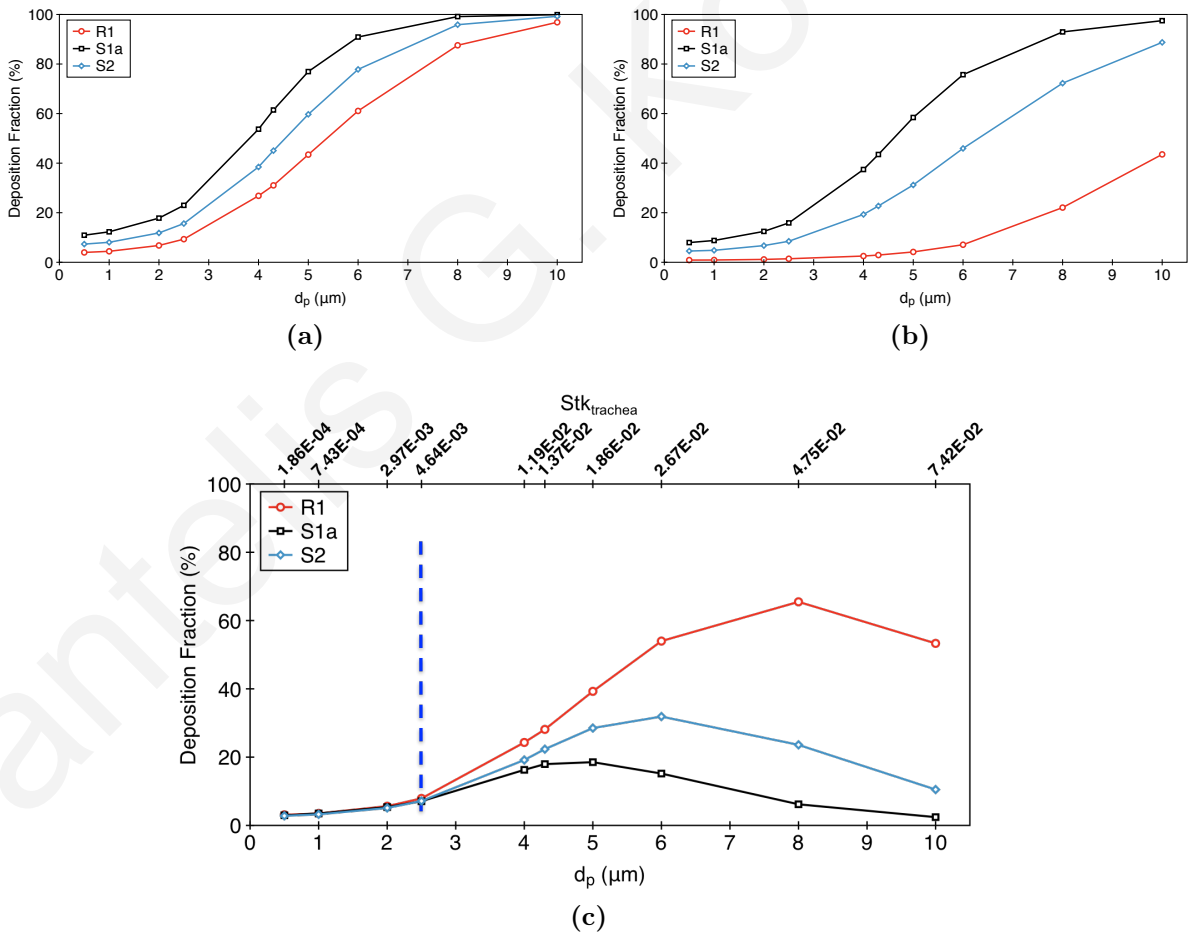

Figure 4.20: *Deposition fractions versus particle size at $Q = 60\,L/min$: (a) overall; (b) mouth and throat; and (c) tracheobronchial. In (c), the Stokes numbers based on tracheal parameters are also displayed.*

Fig. 4.21 shows the deposition fractions in the individual airway segments for various particle sizes. For particles smaller than $2.5\mu m$ and downstream of the first bifurcation

(segment 3), segmental deposition fractions are in good agreement across the three geometries. At $d_p = 4\mu m$, slight differences in localized deposition are observed. For larger particle sizes, the differences become non-negligible in most of the segments.

In order to assess whether the observed differences in localized deposition in the TB tree are partly due to local flowfield variations or entirely due to the differential filtering that occurs in the MT region, we examine the segmental deposition efficiencies, defined as the ratio of the number of particles depositing in a particular segment to the number of particles entering that segment. Fig. 4.22 shows the segmental deposition efficiencies for various particle sizes in the three models. The results show that localized filtering in the TB tree is practically unchanged among the three models for all particle sizes. Pairwise deposition efficiency scatter plots for the various particle sizes are shown in fig. 4.23. In order to quantify the degree of similarity across the three geometries, pairwise correlation coefficients, r, are also reported in fig. 4.23. A good collapse of the deposition efficiency values on the $y = x$ line is evident, and the correlation coefficients, which in all but one case ($1\mu m$, R1 vs S2, $r = 0.9816$) are above 0.99, confirm a strong linear correlation. These results indicate that the minor differences observed in the local TB flow field are largely inconsequential as far as deposition is concerned, and that the variation in regional deposition fractions results from the differences in MT filtering.

Interpretation of results

The findings in this section provide useful insight on the suitability of standardized MT models for accurate predictions of regional deposition in the upper TB region. For particles with $Stk_{trachea} < 5.94 \times 10^{-2}$ ($d_p < 4\mu m$) at $Q = 30\,L/min$ and $Stk_{trachea} < 4.64 \times 10^{-2}$ ($d_p < 2.5\mu m$) at $Q = 60\,L/min$, localized deposition fractions in the TB tree remain practically unchanged independent of the MT geometry employed. By adopting the precomputed flow field from a standard MT model, simulations could therefore be restricted to the tracheobronchial tree resulting in significant computational savings. For larger particles however, TB deposition, as expressed in terms of deposition fractions, depends on the MT filtering. Therefore, in order to obtain accurate localized deposition estimates, a standardized MT model with similar filtering as the patient's MT should be selected. The question then becomes how to identify the standard model with similar filtering properties; the answer depends on the underlying objective. For example, one scenario is that of population studies aimed at identifying functional/structural parameters of the intrathoracic airways that determine regional TB deposition for various classes of patients. In this context, one could envisage using a small number of standardized MT geometries, selected so as to be representative of the expected variability in target patient populations. The aerosol size distribution that escapes MT filtering (ex-cast dose) and the precomputed flow field in these par-

ticular MT models could then be adopted, which would significantly minimize the time and cost required to compute regional deposition in the central airways. This would be of significant advantage in the context of population studies where large numbers of simulations have to be carried out in order to have an adequate statistical sample. A different scenario is that of patient-specific simulations. Here, the primary motivation is to spare the patient the need to image the extrathoracic airways and to minimize diagnosis time. In this context, further work is needed to identify key parameters that could be used to match the patient to a specific MT model. For example, Burnell et al. (2007) conducted an *in vitro* study across a number of MT geometries, in order to determine the key geometric characteristics governing mouth-throat deposition. Of 51 dimensional variables investigated, the single most influential factor was found to be the total volume of the extrathoracic airways. While not conclusive, such studies point to the possibility that a combination of structural and/or functional parameters (such as the patient's inhalation profile) could eventually be shown to provide a reliable means of classifying the patient's extrathoracic airways. Clearly, further work is needed in this direction in the form of combined *in vitro* and *in silico* studies, a goal that we are currently pursuing.

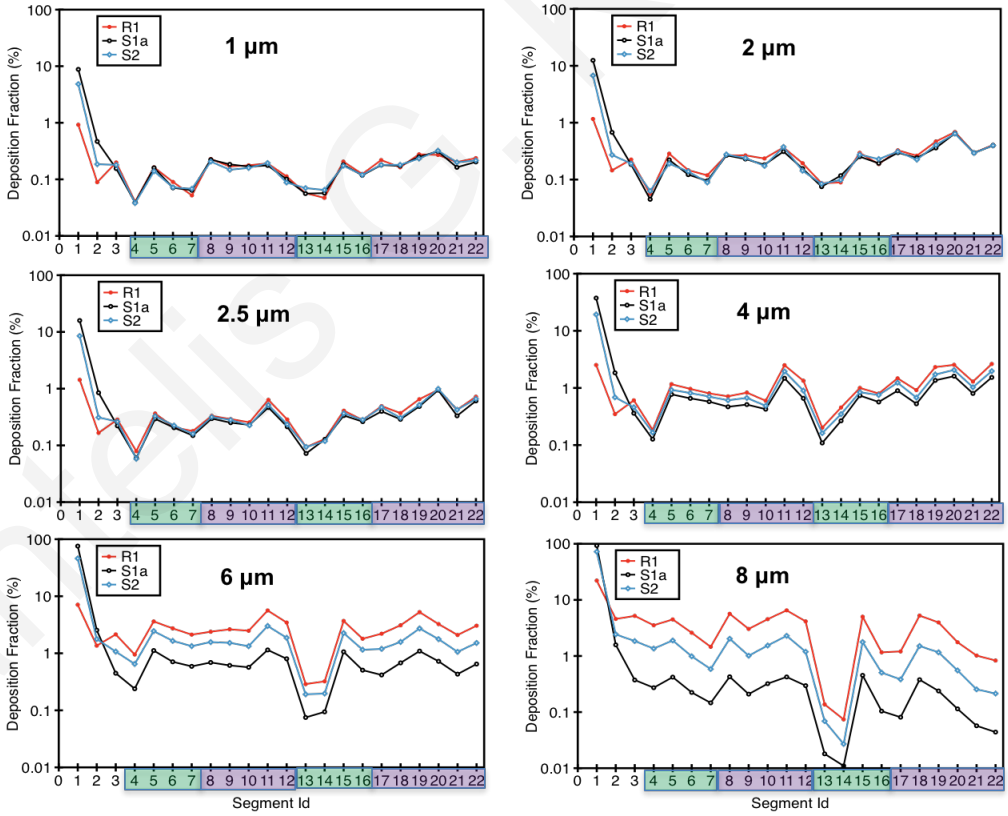

Figure 4.21: *Deposition fractions per segment at $Q = 60\,L/min$ for various particle sizes. The numbering of the segments is shown in fig. 4.3. The green and purple coloring denotes segments in the left and right lung, respectively. Segment 1 corresponds to the mouth-throat region.*

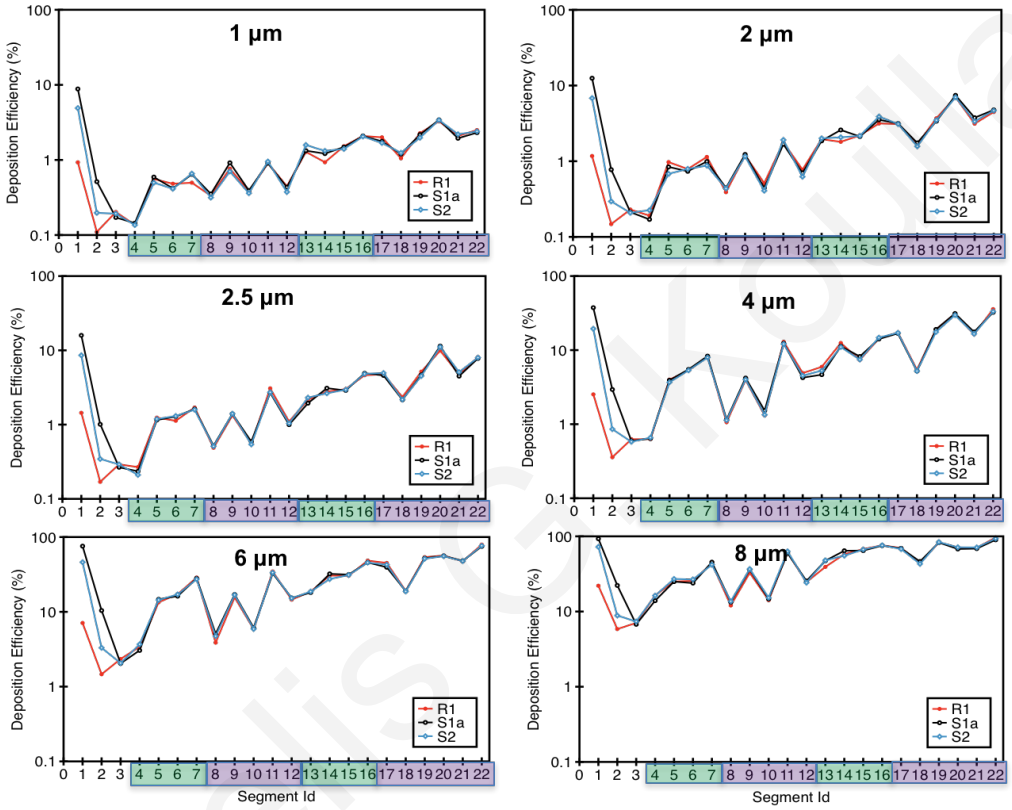

Figure 4.22: *Deposition efficiencies per segment at $Q = 60\,L/min$ for various particle sizes. The numbering of the segments is shown in fig. 4.3. The green and purple coloring denotes segments in the left and right lung, respectively. Segment 1 corresponds to the mouth-throat region.*

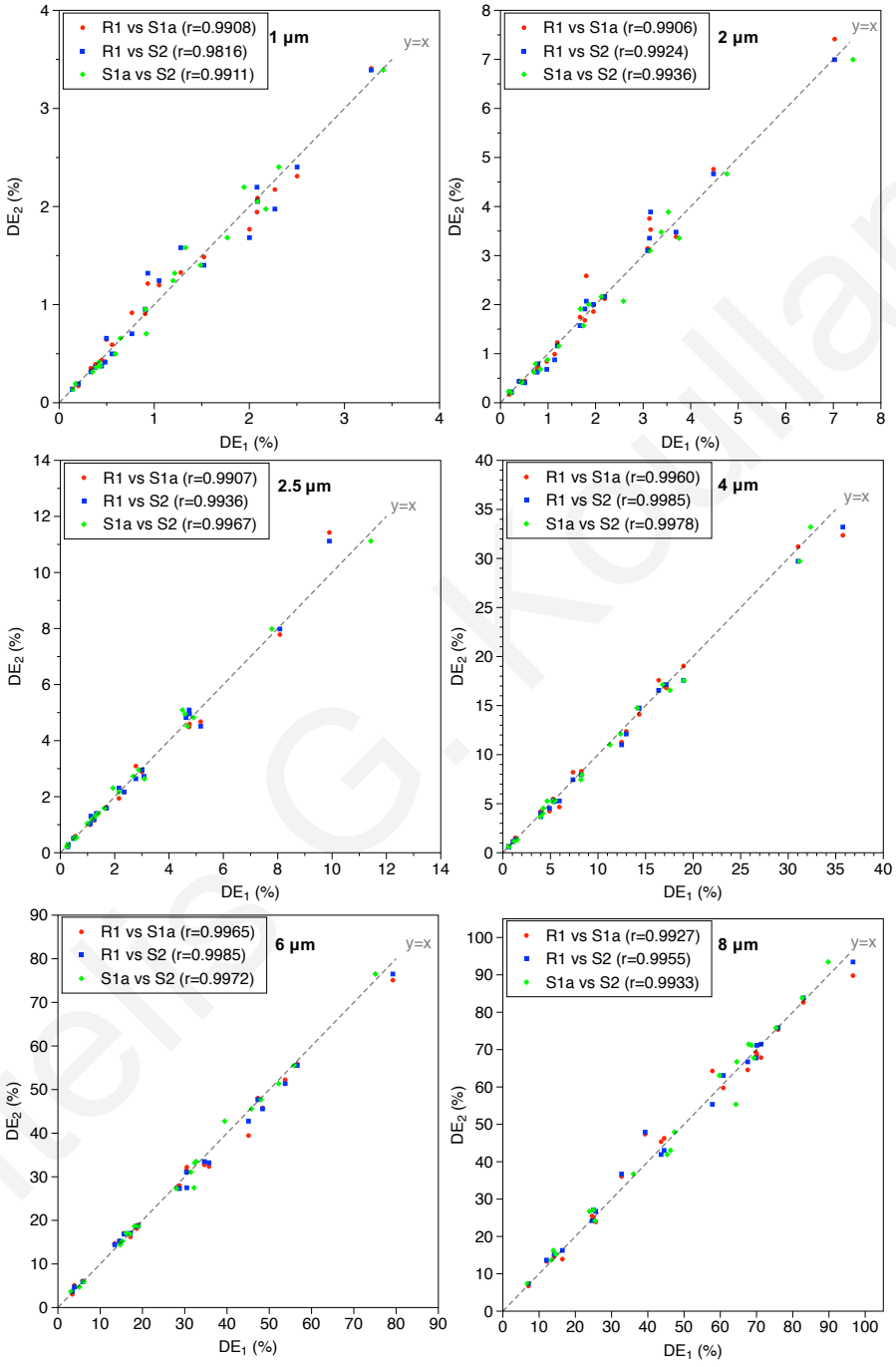

Figure 4.23: *Pairwise scatter plots of segmental deposition efficiencies for various particle sizes at* $Q = 60\,L/min$*. Pairwise correlation coefficients,* r*, are also displayed.*

4.5 Conclusions

The objective of the current study was to quantify the effect of geometric variation in the mouth and throat on regional deposition in the first generations of a realistic TB tree. Three extrathoracic airways with different geometric and deposition characteristics were merged onto the same TB geometry, and the airflow and particle transport were simulated using LES under steady inhalation conditions at 30 and $60\,L/min$. The large flowfield differences observed in the extrathoracic airways and the trachea were found to largely vanish by the first bifurcation, and the mean flow features and turbulent kinetic energy levels in the TB region remained similar, regardless of the inhalation flowrate and the degree of glottal constriction. Localized deposition in the TB tree was practically unaffected by the MT filtering for particles smaller than $4\mu m$ ($Stk_{trachea} = 5.94 \times 10^{-3}$) at $30\,L/min$, and $2.5\mu m$ ($Stk_{trachea} = 4.64 \times 10^{-3}$) at $60\,L/min$. The variability in the deposition fractions at larger particle sizes was shown to be due to variation in the MT filtering across geometries, rather than differences in the local flow field. These findings suggest that accurate predictions of regional deposition in the TB airways can therefore be obtained using standardized MT models with similar filtering characteristics as the patient's extrathoracic airways. This approach would circumvent the need to image and reconstruct the extrathoracic airways, reducing patient exposure to radiation and accelerating *in silico* studies. Furthermore, by adopting the ex-cast dose and precomputed flow field from standardized MT models, significant computational savings can be achieved as simulations can be restricted to the TB region, without the need to include the extrathoracic airways.

In the work presented herein, we have merged three MT geometries with significantly different airflow characteristics as well as filtering efficiencies to a single TB tree. One would need to repeat this study with more geometries before attempting to generalize observations, nevertheless the prospect is promising. If the current results are found to be repeatable with different combinations of airway geometries, large-scale *in silico* studies of regional deposition in a large sample of TB tree geometries could be performed using a small set of representative ex-cast particle distributions that cover the desired cross-sections of patient populations. The large number of chest CT-scans that are available on medical databases, which typically exclude the extrathoracic airways, could therefore be utilized in population studies aimed at identifying the key factors that influence regional deposition patterns.

We note that in the present study we have adopted steady inspiratory flow rates, whereas patient-specific or inhaler-dependent inhalation waveforms are transient. Transient flow simulations would be required in order to assess whether the present findings are also valid under these inhalation conditions. Tian et al. (2011) numerically investigated the effect of transient vs. steady-state conditions and found that transient inhalation influences the deposition of particles in the MT and upper TB airways

through the third generation, where the Womersley number is greater than 1. On the other hand, transient conditions were shown to have little influence on deposition in the TB regions located distally to the fourth generation, and a steady-state approximation accurately captured deposition. Deposition in the upper airways during the exhalation phase is considered to be minor compared to deposition upon inhalation (Finlay, 2001). For this reason, the majority of *in vitro* and *in silico* deposition studies in the upper airways consider only the inhalation phase (Grgic et al., 2004a; Lizal et al., 2015; Lambert et al., 2011). In addition to the flowrate profile, the velocity profiles at the mouth inlet were assumed to be parabolic or turbulent in the present study. In actual drug delivery applications through an inhaler, however, the inlet velocity profile could deviate from these conditions due to airflow structures convected from the device. The effect of inlet velocity profile on aerosol deposition in the upper airways was examined by Koullapis et al. (2016). Although the authors found that imposed conditions at the mouth inlet did indeed affect aerosol filtering in the oral cavity, differences in the flow field dissipated by the time the flow reached the mid-trachea. Therefore, while one might anticipate a weak effect of inlet conditions on localized deposition fractions in the TB tree, we expect the deposition efficiencies to remain fairly insensitive, and the conclusions of the present study to hold for different inlet conditions as well.

In our study the walls of the airway models were assumed rigid. In reality, however, lungs deform and thus, airway diameter and length vary during breathing. In a recent study, Miyawaki et al. (2016b) examined the effect of rigid vs deforming airways on particle transport and deposition in a subject-specific airway model of the central airways. A difference of 22% on average, depending on the generation number, was observed between the rigid and deforming models. Furthermore, the cumulative average deposition fraction in the rigid model was consistently smaller and the relative difference between the two models reached 13% in generation 4. In our study, since the same TB geometry is used in the three cases considered, the degree of uncertainty in deposition results due to airway deformation is expected to be similar in all cases.

Finally, we also note that for certain DPIs, flow rates as high as $90\,L/min$ are relevant (Islam and Cleary, 2012). Extrapolating from the conclusions of the present work, at this high inhalation rate, one would expect smaller particle sizes to be affected by the differences in the MT filtering. Nevertheless, the expectation is that the deposition efficiencies would remain largely unaffected. Therefore, one of the main outcomes of this work would remain valid: ex-cast particle distributions (adjusted for flowrate and patient class) could be used to compute regional deposition in the proximal TB tree for *in silico* population studies or routine clinical use on a patient-specific basis.

Chapter 5

An efficient *in silico* method for deposition studies in the deep lung

Journal Publication: *P. G Koullapis, P. Hofemeier, J. Sznitman, S.C. Kassinos. An efficient computational fluid-particle dynamics method to predict deposition in a simplified approximation of the deep lung. European Journal of Pharmaceutical Sciences, 113:132-144, 2018.*

Conference Presentation: *P. G. Koullapis, Hofemeier, J. Sznitman, S.C. Kassinos. An efficient in silico method for deposition studies in the deep lung. EAC 2017, Zurich, Switzerland (2017).*

5.1 Outline

Towards large-scale simulations of the entire human lung, in this chapter we introduce a numerical methodology to predict aerosol deposition in the deep lung under various breathing scenarios. The geometrical model employed consists of an idealised bronchial tree that represents generations 10 to 19 of the conducting zone and a heterogeneous acinar model, created using a space-filling algorithm. The computational cost of the coupled simulation is reduced by taking advantage of the flow similarity across the central conducting regions in order to decompose the bronchial tree into representative subunits. Topological information is used to account for the correct gravitational force on the particles in the representative bifurcations, emulating their transport characteristics in the actual bronchial tree. Eventually, airflow and particle transport at a certain generation level of the bronchial tree are simulated in single bifurcations, whereas a single acinar model is used for the alveolar region. An Eulerian-Lagrangian approach has been used for solving the flow and particle equations. Two cases with different breathing conditions have been examined: (1) quiet breathing, approximated as an ideal sinusoidal function and (2) deep inhalation followed by 10s of breath hold.

The latter case is a breathing maneuver typically employed for inhalation therapy with DPIs (Tian et al., 2011).

The resulting deposition estimates agree rather well with the known deposition trends reported in the literature, while offering additional insights. For 1-5μm particles, deposition during the exhalation phase of quiet breathing is comparable to deposition upon inhalation, suggesting that it is important to account for complete breathing cycles for accurate deposition predictions in the deep lung. Airway orientation relative to gravity was found to have a significant impact on deposition rates, especially for particles above 2μm and to be higher in the more distal generations, due to the wider range of angles relative to the direction of gravity. Deposition increases significantly when deep inhalation is employed and approximates 100% for particles larger than 1μm when a breath hold of 10s follows. The vast majority of deposition during the deep inhalation maneuver occurs in the acini, since stronger convective flows during deep inhalation bolster particles to reach deeper into the alveolar regions. Finally, a simplified semi-analytical approach is introduced that can lead to even further reduction in computational costs, while incurring only a small loss in accuracy.

5.2 Introduction

High resolution simulations of airflow and particle deposition in the total lung are beyond the reach of current computers. Even with the projected increases in computing power, tackling the entire lung in routine simulations is likely to remain challenging for the foreseeable future. As a result, existing computational studies of airflow and particle transport in the human respiratory tract mainly focus on truncated geometries, either in the upper bronchial region (Choi et al., 2009; Nicolaou and Zaki, 2013) or in the terminal alveolar regions (Hofemeier and Sznitman, 2015). Few studies to date have tackled the intermediate central conducting airways that are thought to play a significant role on the characteristics of the particle phase entering the acinus (Islam et al., 2017; Kleinstreuer and Zhang, 2009; Tian et al., 2011). One question lies for example in determining the size as well as spatial distribution of inhaled aerosols crossing through the central airways and entering into the alveolar regions. These are expected to be influenced primarily by particle size and airway orientation and thus to deviate from a simple uniform spatial distribution, commonly used in the majority of existing studies (Hofemeier and Sznitman, 2015; Khajeh-Hosseini-Dalasm and Longest, 2015). Deposition in the deeper alveolar regions can also be expected to be affected by the characteristics of transport and deposition of particles transiting through the proximal airways. Moreover, current studies of deposition in the central bronchial airways, consider particle deposition only during the inhalation phase since particles that escape distally from the truncated geometry (i.e. the tree outlets) cannot be tracked

back during the exhalation phase (Soni and Aliabadi, 2013; Walters and Luke, 2010). In order to take into account the impact of exhalation on particle deposition in the human lungs, coupled simulations of bronchial and alveoli regions are required to close the system.

The objective of the current work is to develop a CFD-based methodology for the prediction of aerosol deposition in the deep lung under various breathing scenarios. A procedure to reduce the computational cost of the coupled simulation by decomposing the tree is presented, based on the flow similarity across the central conducting regions. A notable feature of the present work, and one that differentiates it from previous efforts, is the inclusion of a physiologically realistic model of the acinar region, which enables the simulation of deposition over a complete breathing cycle. Furthermore, the effects of gravity, which are expected to be quite significant in deep lung regions, are properly accounted for. Simulation results confirm the importance of gravity effects on deposition.

5.3 Review of previous studies

Looking back at past studies, Kleinstreuer and co-workers (Kleinstreuer and Zhang, 2009; Zhang et al., 2008, 2009a) documented an *in silico* methodology for prediction of particle deposition in a simplified 16-generation airway tree model, following a symmetric branching morphology (Weibel, 1963). The tracheobronchial tree was geometrically decomposed into planar triple-bifurcation airway units. In parallel, kinematically adjusted multilevel outlet/inlet conditions were used for both airflow and particle simulations. Rotation of subsequent triple-bifurcation units was allowed in order to take into account non-planarity. Air-particle outflow conditions from an oral airway model were imported as inlet conditions for the first-level triple-bifurcation. Overall, deposition statistics for the entire tree agreed rather well with those calculated using analytical modelling results (NCRP, 1997). Locally, however, deposition fractions based on analytical formulas differed greatly (from a few percent to 70% differences) from the simulation results. Differences were attributed to the local geometrical features as well as ensuing flow characteristics and particle distributions. Furthermore, geometry and upstream effects were found to be more pronounced in the deposition of micron-sized particle rather than nanoparticles. It was also observed that for micron-sized particles in lower bronchial airways, sedimentation may alter the local impaction-based deposition patterns seen in larger airways. In a follow-up study, Kolanjiyil and Kleinstreuer (2013) merged a realistic representation of the upper airways to the 16-generation simplified model and developed a model of the entire respiratory tract. Here, the alveolar regions were modelled by adding spherical alveoli to the most distal triple-bifurcation airway units. Nanoparticle deposition at steady inhalation was modelled using the

Euler-Euler approach. Shortcomings of the aforementioned studies include among others the use of planar triple-bifurcation airway models and limiting simulations to steady inhalation conditions only.

In parallel to such efforts, Longest and co-workers (Longest et al., 2012a,b; Tian et al., 2011) have developed a stochastic individual pathway (SIP) model in which individual continuous pathways beyond the third bifurcation (B3) are generated extending into each lobe of the lung through the terminal bronchioles (B15). Along each pathway, one daughter branch of each bifurcation is continued whereas the other is not. The idea is to simulate a sufficient number of stochastically generated pathways until deposition results converged to an ensemble average. It was found that a single SIP model can be used to adequately characterize deposition within a lobe of the lung. Specifically, using a single SIP, regional and local deposition values were predicted to within approximately 5% and resulted in reductions in computational time by a factor of 3×10^5, compared to the simulation of all branches in a lung lobe. A drawback of the SIP model, however, is the assumption of symmetric outflow conditions at each bifurcation level (B4-B15) of the SIP model, which is valid only when the flow in the parent branch is fully developed and axisymmetric (i.e. parabolic for laminar flow) such that the flow splits evenly in the subsequent daughter branches. More recently, Tian et al. (2015) integrated the SIP model with CFD-based estimates of deposition in the alveolar regions in an effort to validate *in silico* predictions with *in vivo* deposition data. Namely, total lung deposition agreed within a relative error of 6% for the case of monodisperse aerosol with sizes of 1-7μm. In the case of polydisperse aerosols released from a Dry Powder Inhaler and a Soft Mist Inhaler, CFD predictions produced an average relative error$<$ 10% for each inhaler. Their study represents the first comparison of whole-lung CFD predictions with regional *in vivo* deposition data of pharmaceutical inhalers.

Soni and Aliabadi (2013) simulated airflow and particle deposition in an idealized lung geometry consisting of a 10-generation, nonplanar, bronchial tube model using a finite element/finite volume hybrid solver. The tree geometry was based on Weibel's morphology for generations 4-13 with nonplanar angles chosen randomly between 0^o and 180^o and comprised 512 exits and 1023 distinct branches. The final generated mesh contained approximately 36 million elements. Steady-state inspiratory and unsteady laminar flows were simulated ($Re_{inlet} = 319$) and a Lagrangian-based particle tracking model was used for the simulation of particle transport. A constant zero pressure condition was applied at each of the 512 outlets, although it should be noted that this is physiologically unrealistic as not all bronchial pathways are equally ventilated (Asgharian and Price, 2006; Yin et al., 2010). In the unsteady simulations, the maximum inlet velocity was varied with time as a sine-wave to generate an oscillatory breathing flow. Computational times for steady-state inhalation and for one cycle of unsteady simulation were 56 hours on 152 processors and 190 hours on 64 processors, respec-

tively. The most important finding of this study was the higher deposition of particles that were released later in the inhalation phase compared to deposition of particles released earlier during inhalation. The differences in deposition due to release time of particles were attributed to slight differences in secondary flows in terms of vortex strength. This emphasizes the importance of unsteady nature of breathing on particle deposition. A shortcoming of this study was that deposition only during the inhalation phase of the breathing cycle was considered. Therefore, deposition of particles that remained suspended in the airways at the end of inhalation was not considered.

5.4 Model geometry

The geometry used in the current study represents a simplified model of the deep lung, extending from generation 10 in the central conducting airways to the alveolar region. The model consists of an idealised bronchial tree that spans generations 10-19 and represents part of the conducting zone of the human lung, coupled to multiple acini models that represent the respiratory zone. The resulting model is "closed", in the sense that the fate of the particles that remained suspended in the domain at the end of inhalation, either in the bronchial or the acinar region, can be determined during the exhalation phase. This allows the comparison of regional deposition fractions during inhalation and exhalation. Fig. 5.1(a) exemplifies the entire deep lung model whereas fig. 5.1(b) shows the coupled bronchial-acinar regions spanning a single path. The complete model consists of 511 bifurcations and 512 acini models. In the following paragraphs, the characteristics of bronchial and acinar geometries are discussed in more detail.

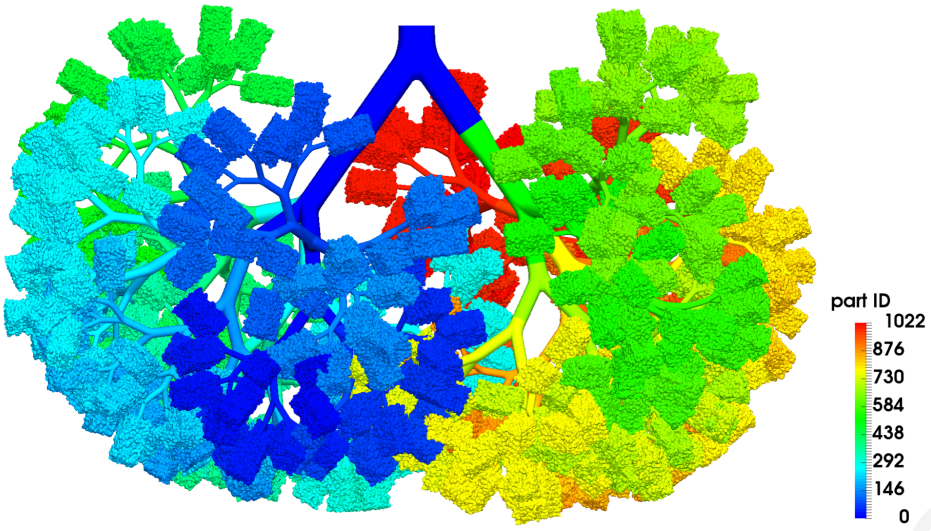

(a)

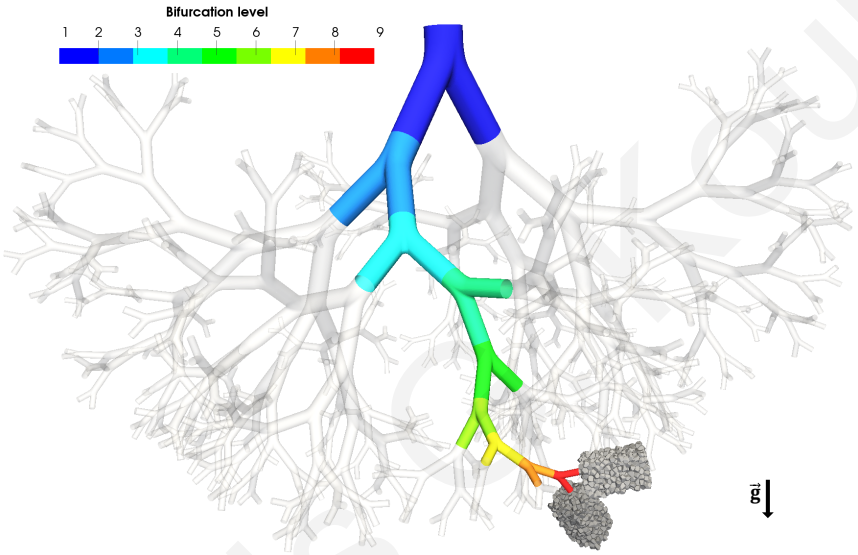

(b)

Figure 5.1: *(a)The developed simplified deep lung model. (b) The coupled bronchial-acinar regions are shown in one path of the entire model (the rest of the bronchial tree is shown transparent).*

5.4.1 Bronchial tree

The idealised model of the bronchial tree, shown in Fig. 5.2(a), consists of a 10-generation bifurcating tree that represents generations 10 to 19 of the bronchial airways. The model holds 9 bifurcation levels as shown in fig. 5.1(b), denoted herein as B1-B9 (B1 for generations 10-11 and so on). The bronchial tree is generated starting from an idealised bifurcation unit, shown in Fig. 5.2(b), with a branching angle of 70^o, constant parent-to-daughter diameter ratio ($D_p/D_d = 1.2445$) and length-to-diameter ratio ($L/D_d = 3$). The bifurcation geometry is based on the physiologically-realistic bifurcation model of Heistracher and Hofmann (1995), with some modifications in the region near the carinal ridge as previously introduced by Stylianou et al. (2016)

to smooth the sharp carinal region of the original geometry. The bifurcation unit is repeatedly scaled, translated and rotated to build the final 10-generation tree. The non-planarity of the tree is taken into account by randomly selected out-of plane angles between 0^o and 180^o. Although the dimensions of the idealised bronchial tree do not exactly match any established morphometry model, the overall dimensions of the tree are in fair agreement with morphometry measurements of Yeh and Schum (1980). Table 5.1 summarizes the dimensions (diameter and lengths) of the present model and that of Yeh and Schum (1980). The resulting tree consists of 511 bifurcations, 1023 branches and 512 outlets.

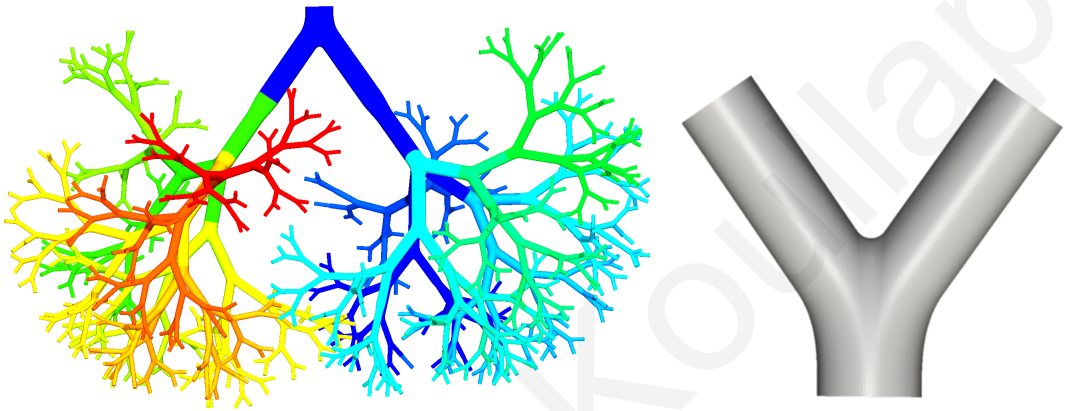

(a) **(b)**

Figure 5.2: *Geometries used for the simplified model of the bronchial tree: (a) 10-generation bifurcating tree; (b) Idealised bifurcation used as the fundamental unit of the bronchial tree.*

Generation	Current model diameter (cm)	Yeh and Schum (1980) model diameter (cm)	Current model length (cm)	Yeh and Schum (1980) model length (cm)
10	0.250	0.257 (0.199-0.347)	0.75	0.667 (0.527-0.880)
11	0.200	0.198 (0.147-0.317)	0.6	0.556 (0.394-0.900)
12	0.161	0.156 (0.106-0.249)	0.483	0.446 (0.266-0.591)
13	0.129	0.118 (0.083-0.181)	0.387	0.359 (0.225-0.449)
14	0.104	0.092 (0.064-0.134)	0.312	0.275 (0.172-0.337)
15	0.084	0.073 (0.051-0.101)	0.252	0.212 (0.118-0.257)
16	0.067	0.060 (0.048-0.077)	0.201	0.168 (0.105-0.222)
17	0.054	0.054 (0.046-0.066)	0.162	0.134 (0.091-0.158)
18	0.043	0.050 (0.044-0.058)	0.129	0.120 (0.080-0.131)
19	0.035	0.047 (0.044-0.054)	0.105	0.092 (0.072-0.110)

Table 5.1: *Dimensions (diameters and lengths) for generations 10-19 of the developed bronchial tree and the anatomical model of Yeh and Schum (1980). For the data from Yeh and Schum (1980), the average values in the whole lung as well as the minimum and maximum values in the five lobes (in parenthesis) are reported.*

5.4.2 Acinus Geometry

The 512 most distal branches of the bronchial tree are coupled to 512 acinar models that constitute the complete respiratory zone located distally to the bronchial tree. Here, the same sub-acinar model geometry is used to represent the 512 acini, as it

was found to sufficiently capture the respiratory region (Hofemeier et al., 2017). The orientation of gravity varies among acinar units, always being adjusted so as to take into account the orientation of the corresponding distal airway relative to gravity. The acinar model is illustrated in Fig. 5.3 and was created using the mathematical model of Koshiyama and Wada (2015). This model generates heterogeneous acinar structures composed of irregular sized alveolar cavities that are assembled into an intricately branched, space-filling ductal tree. Thusly, the model captures important anatomical features of the respiratory region, namely, the local heterogeneity and the space-filling tree (see Hofemeier et al. (2017). The model of Koshiyama and Wada (2015), which was validated using rodents, was adapted to the characteristic length scales of human acini. Meaning, the average equivalent alveolar diameter was determined to be $313\mu m$ at functional residual capacity (FRC) according to the anatomical survey by McDonough et al. (2015). Alveolar sizes or the acinar heterogeneity varied with a relative standard deviation of 12% (Ochs et al., 2004). In average, 4.85 acinar generations were created featuring the characteristic volume of a sub-acinus (Haefeli-Bleuer and Weibel, 1988). Consequently, the acinar tree is populated with around 500 alveoli and exhibits an average path distance of 2.4 mm. As such, the acinar model presented here is the most morphometrically faithful representation of the respiratory region in the absence of image-reconstructed human pulmonary acinar data.

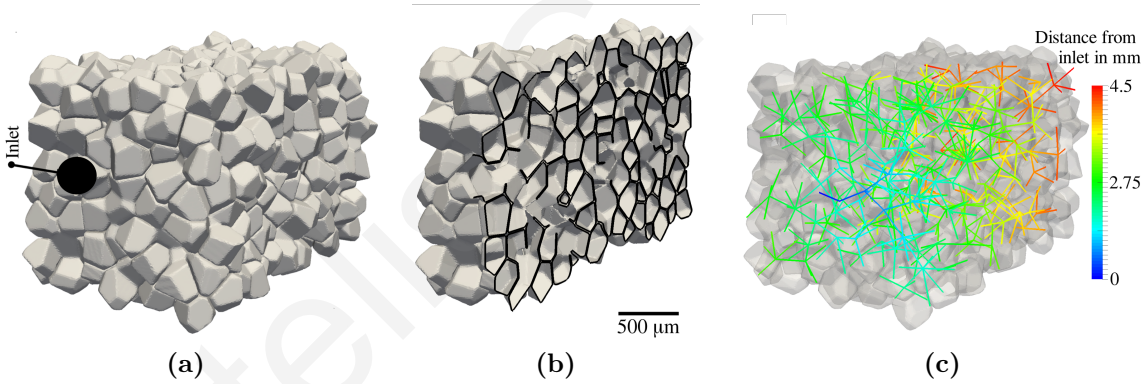

Figure 5.3: *Heterogeneous acinar model created using the mathematical model of Koshiyama and Wada (2015). (a) Whole view; (b) Cross-sectional cut through the acinar structure; (c) Colour-coded skeleton of the acinar tree structure (colourbar indicates distance in mm from inlet).*

5.4.3 Decomposition of the tree

The mesh requirements for simulation of the 10-generation bronchial tree coupled to 512 sub-acinus units (a sub-acinus at each of the 512 outlets of the bronchial tree) would be on the order of $\mathcal{O}(10^9)$ elements, making such a simulation computationally infeasible. An efficient methodology is thus developed in order to overcome constraints related to computational resources, based on the low Reynolds number in the bronchial

tree and the simplified geometry with constant branching angles, airway diameters and airway lengths at any given generation. For example, the Reynolds number at the level of generation 10 in the model bronchial tree (entrance of B1) is approximately 15 for an inhalation flowrate of 15 L/min through the trachea. At such low Reynolds number, the airflow recovers and becomes fully developed at the outlets of the daughter tubes, as shown for B1 in Fig. 5.4. Therefore, the airflow entering the two bifurcations of the subsequent generation (B2) is axisymmetric and parabolic, even though these bifurcations have different orientations in space. The same analogy holds true for the bifurcations in all successive generations since the Reynolds number reduces further as we proceed deeper in the lung. Thus the flow is anticipated to remain identical across the various bifurcations of a certain generation. The reduction in flow complexity allows us hence to decompose the tree and simulate the airflow in one representative bifurcation at each generation level. Thus, while the complete 10-generation lung model consists of 511 bifurcations, the above methodology allows us to simulate the airflow in only 9 bifurcations (B1-B9). The same procedure is then applied in the alveoli region, resulting in the simulation of one sub-acinus unit instead of 512.

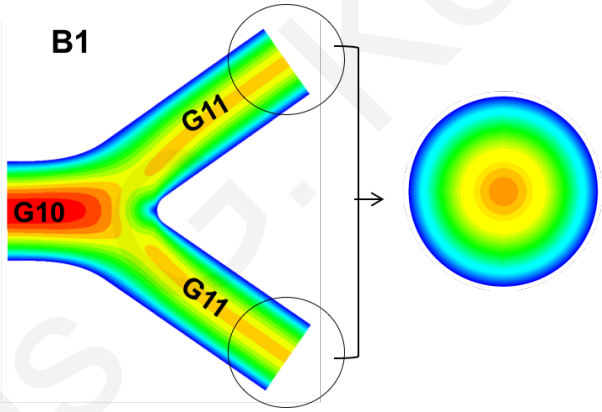

Figure 5.4: *Airflow in B1(generations10-11) for a flowrate of 15L/min in the trachea. It can be observed that the airflow rapidly recovers in the entrance region of the daughter airways and thus becomes fully developed at the outlets of the daughter tubes.*

Regarding the particle phase, gravitational sedimentation is the dominant deposition mechanism in the distal airways for particles greater than $1\mu m$ (Sznitman, 2013). It is therefore important to properly account for gravitational effects. In the deep lung model developed herein, the bifurcations of a certain generation are oriented differently with regards to gravity. Thus, gravity is allowed to break the symmetry of the model. As a result, deposition can differ greatly from bifurcation to bifurcation, even within the same generation. The same holds true in the differently oriented acini. Therefore, to accurately predict deposition in the decomposed domain, the direction of the gravity forces acting on the particles should take into account the exact positions of these particles in the airway tree. Fig. 5.5 illustrates a schematic representation of the decomposition of a 3-generation/2-bifurcation tree. Particles exiting B1 and entering

B2.1 and B2.2 experience variations in the direction of the gravity, i.e. g2.1 and g2.2, respectively, in the decomposed domain. In this manner, particles are transported by the same flow in the representative B2 bifurcation but experience changes in gravitational orientation as they cross through the bronchial tree. Eventually, airflow and particle transport are simulated in one representative bifurcation for a certain generation, resulting in great savings in computational cost. The same applies in the alveoli region, resulting in the simulation of one sub-acinar unit.

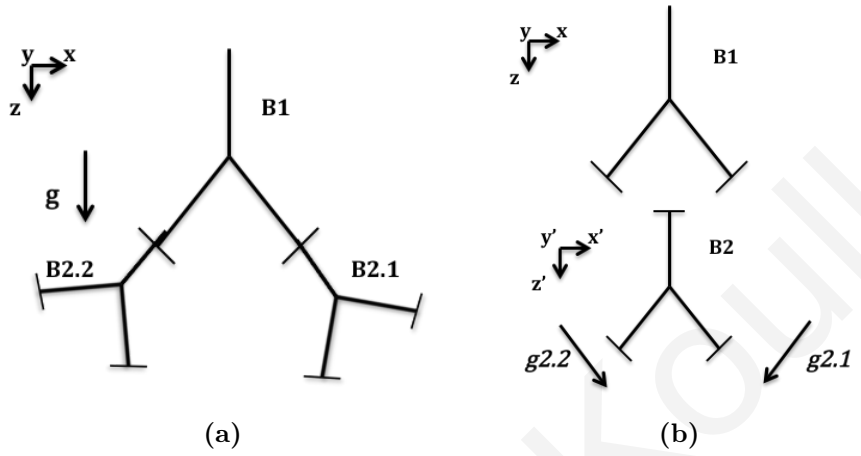

Figure 5.5: *Decomposition of a 2-generation tree: (a) Complete tree with global coordinate system and gravity vector; (b) Decomposed tree with the local coordinate system and local gravity vectors shown for B2.*

Flow is driven by the volumetric expansion of the acinar regions, as explained in the following section. Physical time runs concurrently for all model segments. Simulation of the particle phase is performed sequentially moving down (inhalation) or up (exhalation) the tree, but taking into account physical arrival times. The methodology can be described in the following steps:

1. Simulation of the air and particle phases in B1 for the inhalation phase. Positions, velocities, arrival times, diameters, gravitational vectors and labels of the particles reaching the outlets are stored. Deposited as well as suspended particles in B1 are also stored.

2. Particles that have reached the outlets of B1 are injected, at their arrival times, in the representative B2, where the flowfield and the particle motion are simulated for the inhalation phase. The positions, velocities and gravitational vectors of these particles are transformed in the local coordinate system (x',y',z'), using topological information of the initially generated complete tree (branching and non-planar angles, etc.), such that the particles entering the representative B2 experience the correct gravitational forces (Fig. 5.5). As in B1, positions, velocities, arrival times, diameters, gravitational vectors and label of the outlet of

particles reaching the outlets of B2 are stored along with deposited and suspended particles.

3. The same procedure is applied for the next generations of the airway tree (B3-B9), until particles reach the alveolar region. For the alveolar region, the full breathing cycle is simulated (flow and particles that have reached this region). Again, particles experiencing different gravitational forces are simulated taking into account the orientation of the multiple acini in the lung model. Positions, velocities, arrival times, diameters, label of the acinus and gravitational vectors of particles that are exhaled back from the acinus model (they have reached the acinar inlet/outlet), are stored.

4. The exhalation phase is simulated for the terminal bifurcation of the airway tree (B9, proximal to the acinar region). Particles that were exhaled back from the acinar region are injected, at their arrival times, in the terminal bifurcation. The positions, velocities and gravitational vectors of these particles are transformed in the local coordinate system, such that the particles entering the representative terminal bifurcation experience the correct gravitational forces.

5. The same procedure is applied sequentially for the proximal bifurcations (B8-B1) and the simulation ends when the exhalation phase in B1 is completed.

5.5 Computational details

5.5.1 Continuous phase

The airflow in the deep conducting airways and in the respiratory zone can be characterized as Newtonian, time dependent (due to unsteady breathing), incompressible and laminar, with Reynolds numbers on the order of $\mathcal{O}(10)$ in generation 10 and on the order of $\mathcal{O}(10^{-3})$ in most distal acinar regions. In the current study, the bronchial tree is considered non-moving, whereas wall breathing expansions and contractions are assumed for the acinar domain.

In the non-moving conducting airways, the governing equations for the airflow include the conservation of mass and momentum, eqs 2.1 and 2.2. In the moving acinar domain, mass and momentum equations are solved in an arbitrary Lagrangian-Eulerian framework, and thus Eq.(2.2) is expressed as:

$$\frac{\partial u_i}{\partial t} + (u_{mesh,\,i} - u_i)\frac{\partial u_j}{\partial x_j} = -\frac{1}{\rho}\frac{\partial p}{\partial x_i} + \frac{\partial}{\partial x_j}\Big[\nu\frac{\partial u_i}{\partial x_j}\Big]. \tag{5.1}$$

where $u_{mesh,\,i}$ is the velocity of the moving mesh.

An unstructured computational grid was generated in the representative bifurcations domain, consisting of 300,000 elements (the vast majority being hexahedras). The generated mesh is expected to be sufficient for the laminar flows examined in the current study (Longest and Vinchurkar, 2007; Stylianou et al., 2016). A mesh consisting of 16.5 million tetrahedral elements was constructed for the acinus model. This mesh resolution is expected to be adequate for the current acinar model (Hofemeier et al., 2017). The meshes for both the bifurcation and acinar domains were generated using ANSYS ICEM software.

5.5.2 Particle phase

Spherical, rigid and non rotating particles are introduced at the inlet of B1 (generation 10). The motion of each particle is individually computed (Lagrangian approach) by solving equations 2.18 and 2.19 to determine the particle velocity, $\vec{u}_p$, and position, $\vec{x}_p$. The forces taken into account are gravity, Drag and Brownian force.

Particles are released uniformly from the inlet of the bronchial tree (in B1) during the inhalation phase. A total of 10 million particles are injected in the domain, employing a log-uniform size distribution for particles in the range of 0.1-10μm. The total number of particles is chosen in order to have a sufficient sample in the distal alveolar region since the model branches to 512 ending segments. In analysing deposition statistics, the particles are grouped in six distinct size bins, based on the similarity of their deposition characteristics: 0.1-0.2, 0.2-0.5, 0.5-1, 1-2, 2-5 and 5-10μm.

5.6 Case study 1: Quiet breathing

5.6.1 Simulation details

In this scenario, quiet (normal) breathing is simulated in the deep lung model. Wall breathing expansions and contractions of the acinus are modelled with an idealised sinusoidal motion (Hofemeier and Sznitman, 2015):

$$x_i(t) = x_{0,i}\Big[1 + \frac{\beta}{2} + \frac{\beta}{2} sin\Big(\omega t + \frac{\pi}{2}\Big)\Big] \tag{5.2}$$

where x_i is the local position (in 3D) of the wall boundary, $x_{0,i}$ is the position at t=0, $\omega = 2\pi T$ is the breathing frequency where T is the breathing period and β is the length-scale expansion factor, defined as:

$$\beta = \left(1 + \frac{V_T}{V_{FRC}}\right)^{1/3} - 1 \tag{5.3}$$

In equation 5.3, V_T is the tidal volume and V_{FRC} is the lung volume at functional residual capacity.

Physiological breathing conditions mimicking tidal breathing of an average human adult at rest are considered with $V_T = 0.5L$, $V_{FRC} = 3L$ and T=3 s, resulting in a length scale expansion factor $\beta = 0.053$. The resulting variation of volume and volumetric flowrate in time of the acinus model are shown in fig. 5.6.

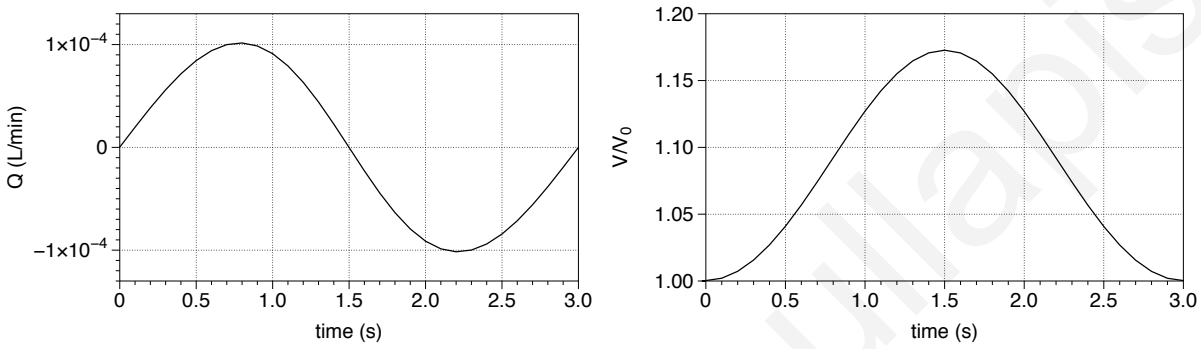

(a) **(b)**

Figure 5.6: *Variation of volumetric flowrate (a) and volume (b) in time of the acinus model for quiet breathing.*

In the decomposed domain, a time-varying sinusoidal parabolic velocity profile is applied at the inlet of bifurcations B1-B9 in accordance with the breathing motion of the acinus:

$$u_{in,Bi}(t) = 2\left(\frac{2^{10-i}\,Q_{acinus}(t)}{A_{in,Bi}}\right)\left[1 - \left(\frac{r}{R_{in,Bi}}\right)^2\right], \qquad i = 1 - 9. \tag{5.4}$$

where $Q_{acinus}(t)$ is the volumetric flowrate in the acinus, determined by the volume expansion characteristics of the model, and $A_{in,Bi}$ and $R_{in,Bi}$ are the cross sectional area and the radius at the inlet of Bi. The resulting flowrate at generation 10 (inlet of B1) is $0.05L/min$ during peak inhalation / exhalation. The equivalent peak flow rate in the trachea is approximately $25.6L/min$ which corresponds to a flow rate of $17.1L/min$ for “equivalent" steady state inhalation conditions. The Reynolds number during peak inhalation/exhalation at the inlet (generation 10 / B1) of the bronchial tree is 25, whereas the Womersley number is 0.88 at the same location. Since this is the maximum value in the tree and is below 1, unsteady effects are not important under these conditions. In the decomposed domain, a no slip velocity and constant pressures are applied at the walls and the two outlets of the bifurcations, respectively. For the acinar region, both fluid and particle motions arise solely as a result of the distensions of the acinar model. Thus, zero pressure at the inlet/outlet and a no slip condition at the moving wall are prescribed as boundary conditions in this region. Particles are released during the inhalation phase for a time period of t/T=0.4.

5.6.2 Airflow

As discussed before, airflow in the idealised bronchial tree is fully developed parabolic in most of the branches due to the low Reynolds number, especially as we move in the most distal generations (Kleinstreuer and Zhang, 2009). Weak secondary effects can be found near the carinas in B1 and B2, where the Reynolds number reaches 25 and 16, respectively, at peak conditions. The magnitude of the secondary velocity component at these locations is more than an order of magnitude smaller than the streamwise component and drops quickly in the circular branches, even at the peak flowrates for both inhalation and exhalation phases. Therefore, flow inertial effect are rather insignificant in the bronchial tree under the examined flow conditions and our study for this region focuses on particle deposition.

In the acinus we find that flow patterns are consistent with previous studies (Sznitman et al., 2007; Hofemeier and Sznitman, 2015), where the alveolar flow changes from recirculating to radial flow with increasing acinar depths. These characteristic acinar flow pattern remain quasi-steady throughout the breathing cycle, as predicted under self-similar expansion (Hofemeier and Sznitman, 2016).

5.6.3 Particle transport and deposition

In order to firstly assess the validity of our CFD-based deposition estimates, we have compared our predictions to the deposition results of the 1D model of Yeh and Schum (1980), as implemented in the Mimetikos Preludium v1.1.3 software (Emmace Consulting AB, 2017). The parameters of the models, such as the tidal volumes, volume at Functional Residual Capacity, volumetric flowrate profile, aerosol injection etc. were chosen to be as close as possible. The comparison is shown in fig. 5.7. Very good agreement is observed, suggesting that the CFD-model can provide deposition estimates in the deep lung that are aligned with the literature.

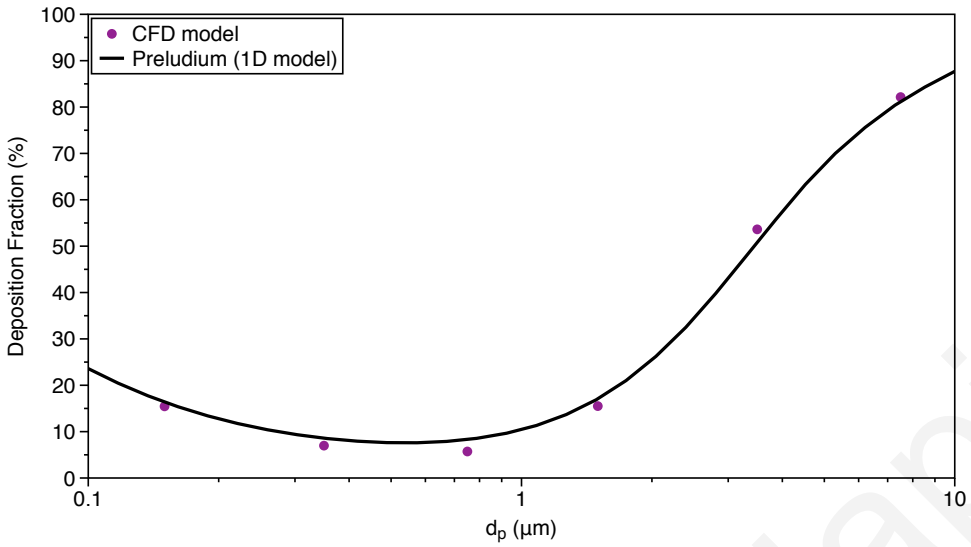

Figure 5.7: *Comparison of deposition fractions in the deep lung obtained by the CFD-model and the 1D model of Yeh and Schum (1980) for quiet (normal) breathing.*

Fig. 5.8 displays the fate of particles in the entire model, as a fraction of the total injected particles. As discussed earlier, particles are grouped in six size groups according to their governing transport mechanism and deposition characteristics. Particles above $5\mu m$ exhibit the highest deposition fractions due to gravitational settling. Deposition due to inertial impaction is rather insignificant in the deep lung model since the maximum Stokes number, which is used to quantify the importance of inertial effects, is well below unity even for the largest particles. It is worth to note that particles larger than $5\mu m$ have low probability to reach the distal lung generations since they are usually filtered out in the upper bronchial regions. Deposition is reduced as the particle size decreases and reaches a minimum for particles in the $0.5 - 1\mu m$ range. With further decreasing particle size deposition fractions increase again as Brownian diffusion becomes more important. A small fraction of particles, mostly $d_p < 2\mu m$, remains suspended in the domain at the end of the breathing cycle (maximum fraction of suspended particles is 6.86% for $1 < d_p < 2\mu m$). The fate of these particles can be determined by simulating additional breathing cycles. The location of deposition minimum suggests that particles in the $0.2 - 1\mu m$ range are the least susceptible to the combined effects of gravitational sedimentation and Brownian diffusion, which are the two main deposition mechanisms in this part of the lung (Kleinstreuer and Zhang, 2009). In fact, it is striking that almost 90% of these particles are exhaled despite the tidal way carrying these particles deep into the respiratory tree (Hofemeier and Sznitman, 2016). On either side of this bin, one of the two deposition mechanisms becomes progressively more efficient. Yet, even in the next size bin of $1 < dp < 2\mu m$, which is more relevant to drug delivery applications (Finlay, 2001), the exhaled fraction remains striking large at almost 78%. The large fraction of suspended particles in this size range suggests that perhaps inhalation maneuvering could help improve somewhat deposition efficiency.

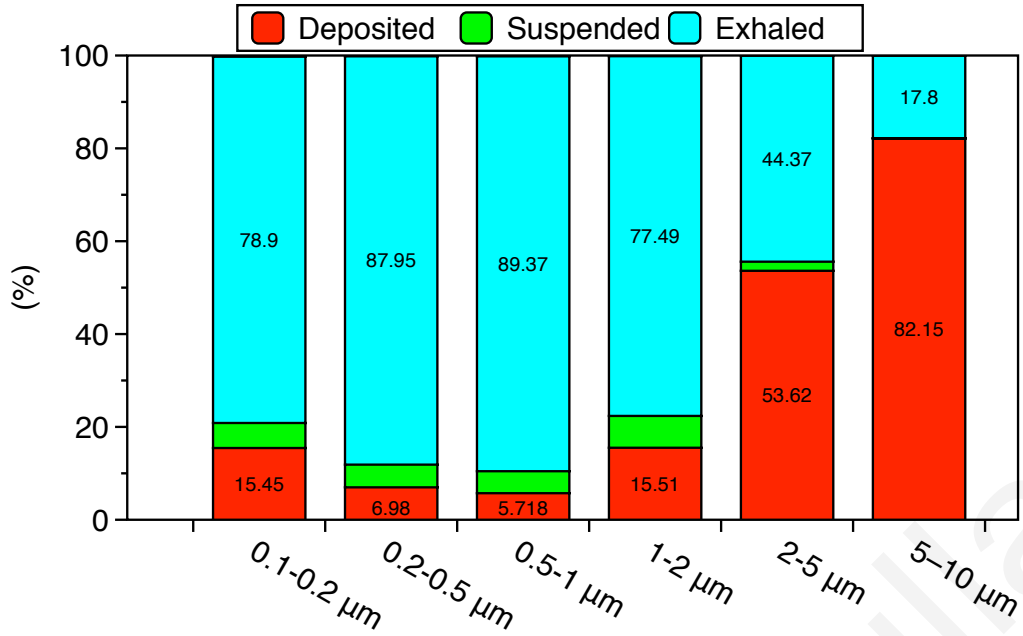

Figure 5.8: *Fate of particles in the overall deep lung model, shown as fraction of the total injected particles.*

Fig. 5.9 illustrates Deposition fractions as a function of particle size. Deposition is distinguished based on the phase of breathing (inhalation or exhalation) and the location where it occurs, i.e. cumulative for conducting generations G10-19 or acinar region. The majority of larger particles ($5 < d_p < 10\mu m$) deposit during the inhalation phase in the bronchial tree. Non negligible deposition also occurs in the acinar region during inhalation and in the bronchial tree during exhalation. Deposition of these largest particles in the acinus during the exhalation phase is considerably smaller. This indicates that the majority of the largest particles that enter the acinus during inhalation proceed to deposit during the inhalation phase. Based on this observation, one can further infer that the fraction of the largest particles that deposit in the bronchial tree during exhalation must arise from particles that remained suspended in the bronchial tree at the end of inhalation. For smaller particles ($d_p < 5\mu m$) deposition is more or less uniformly divided between the phases of breathing (inhalation/exhalation) and the region of deposition (bronchial/acinar). In fact, deposition during exhalation surpasses inhalational deposition for particle sizes $1 - 2\mu m$. For this particular size bin, the largest contribution to deposition comes from the acinar region during exhalation. This suggests that a large fraction of these particles remain suspended at the end of inhalation, even in the acinar region. Overall, deposition upon exhalation for particles in the range $1 < dp < 5\mu m$ is quite important, pointing to the need to account for complete breathing cycles in drug delivery studies. Following these findings, one could design breathing maneuvers that target the apparently large fraction of particles in this size range that remain suspended in the brief interlude between inhalation and exhalation. For example, since in this size range the amount of aerosol depositing is approximately proportional to the time available for sedimentation (Finlay, 2001),

higher deposition can be achieved through a pause after inhalation (breath hold). This concept was tested by Imai et al. (2012) in a subject-specific airway model of the upper airways, that included generations 3 to 6. It was found that breath holding effectively increases deposition of $5\mu m$ particles in the third to sixth airway generation. Specifically, after $10s$ of breath holding, particle deposition fraction increased more than 5 times for these particles. It is expected that increase in deposition due to sedimentation when a breath-hold maneuver is employed will be even higher in the more distal lung regions since the distance a particle must settle before depositing decreases as the tube diameters decrease. This hypothesis is supported from the study of Khajeh-Hosseini-Dalasm and Longest (2015), who found that the optimal breath hold times to allow 95% deposition of inhaled 1, 2, and $3\mu m$ particles once inside the alveolar region were approximately 10, 2.7, and 1.2 s, respectively. Similar findings for the respiratory region were observed in Hofemeier et al. (2017). One such scenario, i.e. deposition in the deep lung model for a pause after deep inhalation, is examined in the next section.

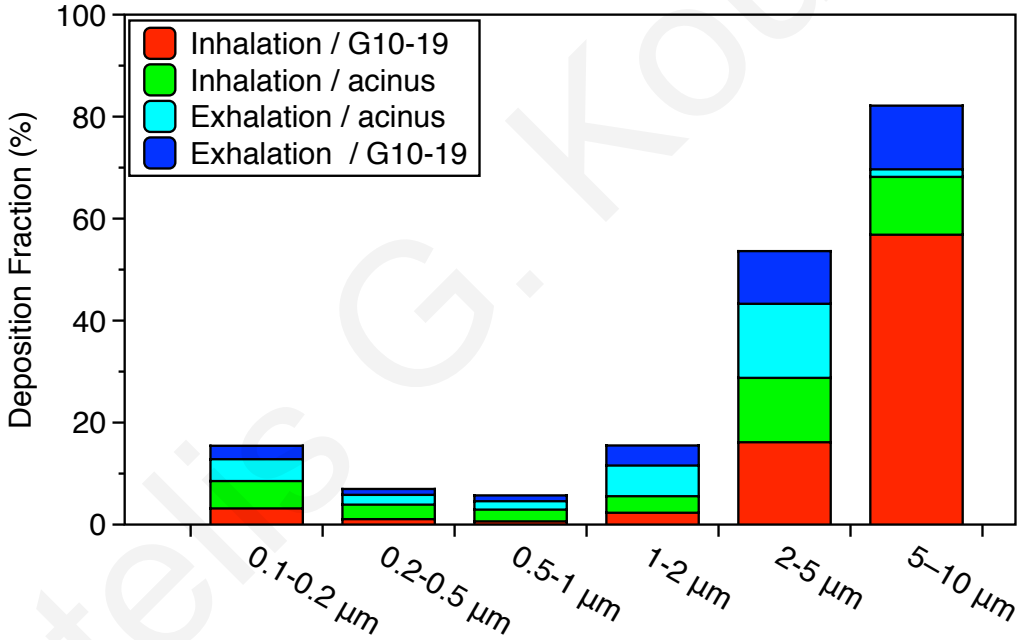

Figure 5.9: *Deposition Fractions as a function of particle size. Deposition is distinguished between the phase of breathing (inhalation or exhalation) and the region (conducting or acinar) that takes place.*

Fig. 5.10 shows the relative deposition according to bronchial (B1-B9) and acinar generations. Relative deposition is expressed in the form of Normalised Deposition Fractions, which are formed by dividing the local Deposition Fraction for each segment by the total Deposition Fraction for that particular particle size. Thus, the sum of Normalised Deposition Fractions for each size bin equals 1. In other words, fig. 5.10 serves to discriminate the regional distribution of aerosol deposition according to particle penetration depth. It can be observed that relative deposition in the acinar region prevails significantly over deposition in any of the bronchial generations, especially for $d_p < 5\mu m$, for which it accounts for more than 50% of total deposition. It

is worth mentioning that although the acinus model consists of multiple generations (average of 4.85 generations), overall deposition in the acinus is considered here. For $5 < d_p < 10\mu m$, deposition in most of the bronchial generations is comparable to deposition in the acinus, although acinar deposition remains higher than deposition in any particular bronchial generation taken individually. However, if we consider overall deposition for these larger particles in the bronchial tree (sum of deposition in all 10 bronchial generations), it accounts for approximately 80% of total deposition and therefore cumulative bronchial deposition dominates over acinar for the larger particles. For $d_p < 5\mu m$, relative deposition increases monotonically as we move towards the distal bronchial generations. Such a regular increase is not evident for the largest particles ($5 < dp < 10\mu m$) and deposition is more uniform in size, but with small irregular variations across bronchial generations.

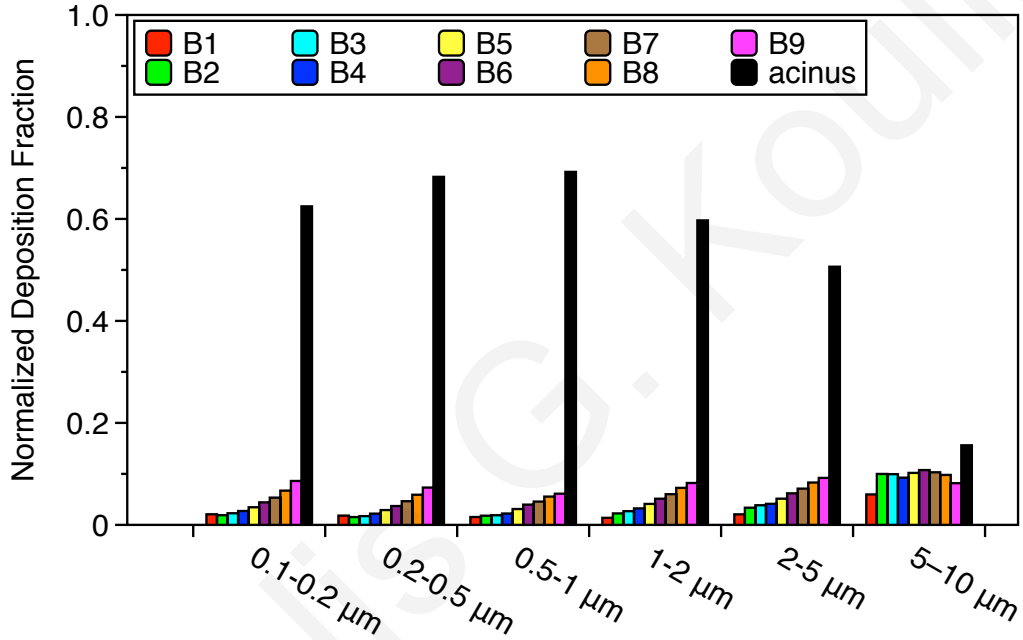

Figure 5.10: *Relative deposition discriminated according to bronchial (B1-B9) and acinar generations. Deposition fractions are normalized by the total Deposition fraction for a certain particle size.*

In order to assess the effect of orientation in the filtering efficiency of the bronchial and acinar generations, average and standard deviation of deposition efficiencies are calculated for B3-B9 and the acinus. Average and standard deviation of deposition efficiencies are calculated as:

$$DE_{Bi} = \frac{1}{2^{i-1}} \sum_{j=1}^{2^{i-1}} \frac{\text{deposited particles in Bi,j}}{\text{particles entering Bi,j}}, \quad \sigma_{DE_{Bi}} = \sqrt{\frac{1}{2^{i-1}} \sum_{j=1}^{2^{i-1}} \left(DE_{Bi,j} - DE_{Bi}\right)^2}.$$

where i denotes the bifurcation level (i=3-9) or the acinus (i=10). As i increases, the sample for the statistics is increased, i.e. the sample for B3 is 4 whereas for acinus is 512. On the other hand, due to the finite number of particles injected in the domain that decreases as we move in the most distal generations due to multiple divisions and

filtering, the particle sample decreases in these regions. Fig. 5.11 displays average and standard deviation of deposition efficiencies. In the bronchial region, the orientation-induced variability in Deposition Efficiency (indicated by the error bars) is largest for the larger particles ($2 - 10\mu m$). This is expected since heavier particles are more susceptible to gravity and their deposition is highly influenced by the path they follow in the model domain. Moreover, variance in deposition efficiencies also increases as we move in the more distal generations, and reaches 17% in B9 for $5 < d_p < 10\mu m$. This is attributed to the fact that the distal branches span a wider range of angles relative to the direction of gravity. Variance in deposition for particles smaller than $1\mu m$ is rather small in the bronchial region. For particles in the range $2 - 5\mu m$, average deposition increases as we move in the distal lung regions which can be mainly attributed to the reduction of diameters and the larger residence time that favor gravitational sedimentation. Moreover, variation in deposition efficiencies also increases as the generation number increases but in this case the variance is less than 4% in B9.

In the acinus, particles larger than $5\mu m$ are entirely filtered and the variance in deposition efficiency is less than 1%. Particles in the $2 - 5\mu m$ range have quite high average deposition efficiency that reaches approximately 75% and also show considerable variation (12.4%). Filtering of smaller particles also appears increased in the acinus compared to the bronchial generations. Variance is larger for particles in the $1 - 2\mu m$ range, for which gravity still plays a role in their transport and deposition. Overall, particle deposition is well aligned with predictions of whole lung deposition by Hinds (1999). Thus, we are confident that the model presented herein, including the conducting and respiratory region, enables realistic particle entry into the acinus, a crucial boundary condition for acinar simulations (Oakes et al., 2016). Combining the acinus with the conducting airway tree opens not only the possibility to accurately predict particle inflow into the acinus under healthy conditions, but also under diseased, or rather, heterogeneous conditions.

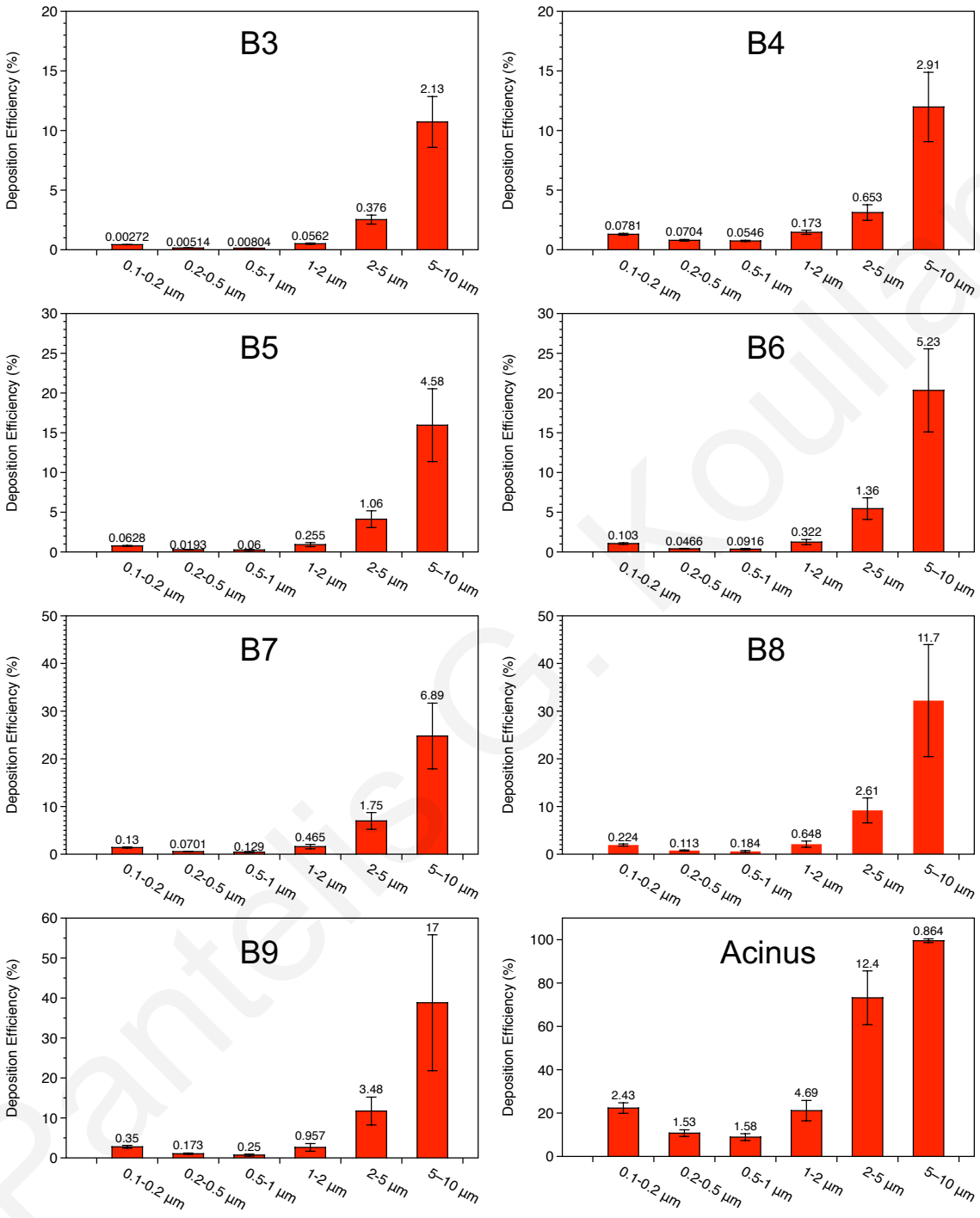

Figure 5.11: *Average and standard deviation (error bars) of deposition efficiencies in B3-B9 and the acinus. Standard deviation values are also displayed.*

A tool to reconstruct the bronchial-acinar tree and to visualize the deposition patterns across the entire model is developed. The positions of deposited particles in the decomposed domain are reconstructed back in the complete geometry using topological information of the initially generated tree (branching and non-planar angles etc.). Figures 5.12 and 5.13 illustrate the deposited particles in the bronchial and acinar regions, respectively, coloured by their deposition time (one every five deposited particles is shown). Gravitational sedimentation dominates deposition of particles above $1\mu m$ and thus the locations of deposited particles are clearly shifted towards the direction of gravity (vertical). Particles in size range $0.2 - 1\mu m$ have the minimum deposition and they are more or less affected equally by sedimentation and difussion. Smaller particles below $0.2\mu m$ are more uniformly distributed across the airway walls, indicating the prevalence of Brownian diffusion at these particle sizes.

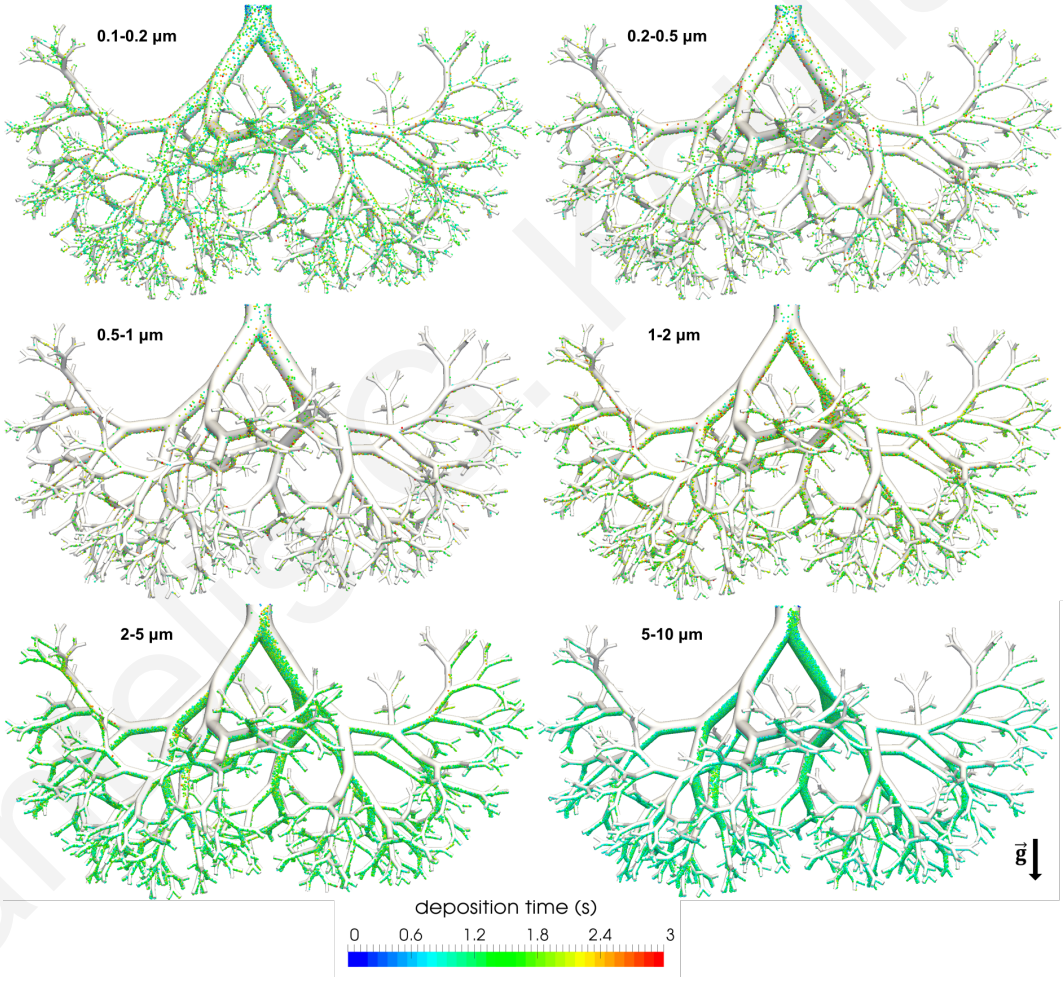

Figure 5.12: *Deposition patterns in the bronchial tree. Particles are coloured by their deposition time.*

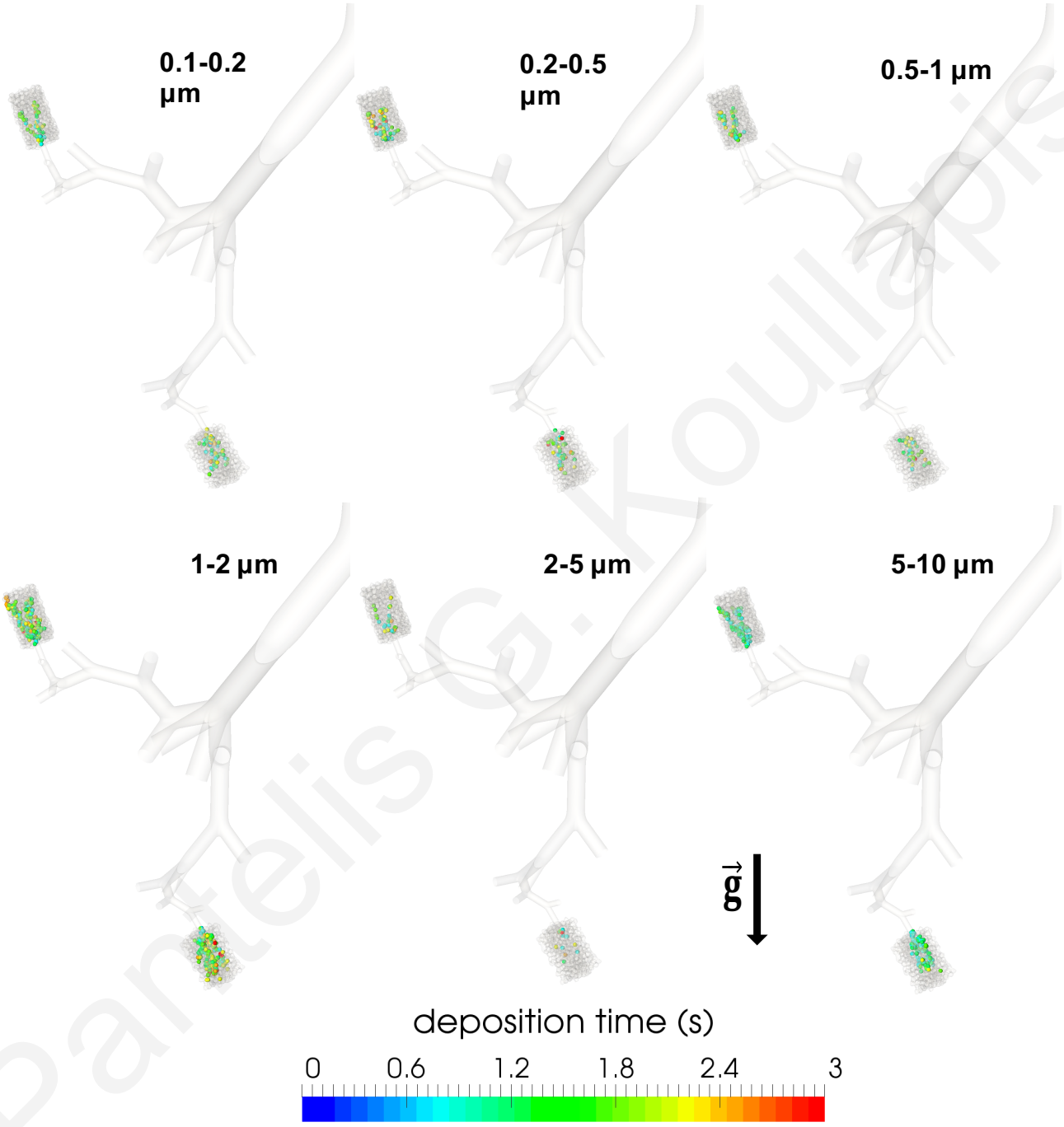

Figure 5.13: *Deposition patterns in the acinus, along two paths of the entire model. Particles are coloured by their deposition time.*

5.7 Case study 2: Deep inhalation maneuver

5.7.1 Simulation details

In this second scenario, a realistic inhalation waveform consistent with high resistance DPIs is considered (Tian et al., 2011). The inspiratory phase is followed by 10s of breath hold. This breathing maneuver is usually employed to allow sedimentation of the drug aerosols and thus increase the deposited dose.

Similar to the case of sinusoidal breathing, the flow is driven by the wall expansion of the acinus. To produce the desired inhalation waveform $Q_{acinus}(t)$, and in accordance to the case of sinusoidal breathing (eq. 5.2), a function $f(t)$ that describe the wall motion of the acinus must be found:

$$x_i(t) = x_{0,i} f(t) \tag{5.5}$$

The procedure to find the unknown function $f(t)$ is described below. Firstly, the desired function for the inhalation waveform $Q_{acinus}(t)$ is defined. In this study, a sine-cosine function is adopted to mimic rapid inhalation (Khajeh-Hosseini-Dalasm and Longest, 2015), as shown in fig. 5.14(a). The volume variation in the acinus can be derived by integrating the function $Q_{acinus}(t)$:

$$V(t) = V_0 + \int_0^t Q_{acinus}(t)dt \tag{5.6}$$

From the resulting volume variation (shown in fig. 5.14(b)), we can calculate the length expansion of the acinus over time and the function $f(t)$:

$$f(t) = \frac{L(t)}{L_0} = \left(\frac{V(t)}{V_0}\right)^{1/3} \tag{5.7}$$

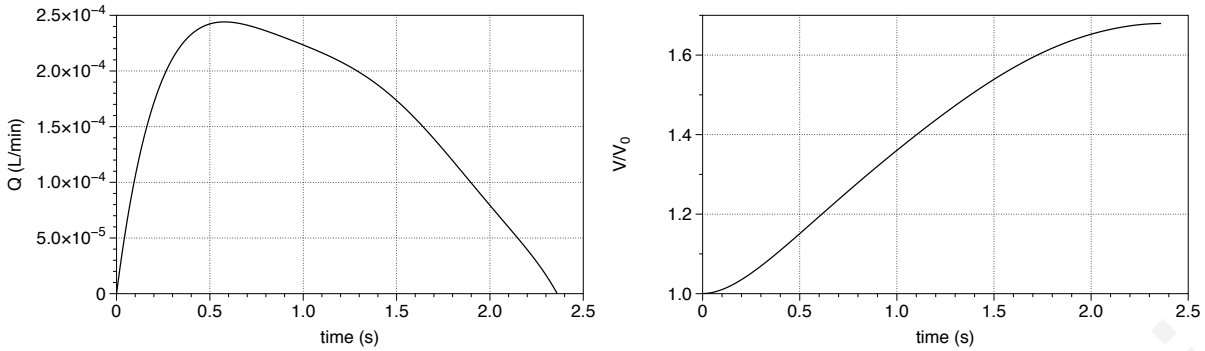

(a) **(b)**

Figure 5.14: *Variation of volumetric flowrate (a) and volume (b) in time of the acinus model for the deep inhalation maneuver.*

The resulting tidal volume in this case is $V_T = 1.67L$ for an inhalation period of 2.36s. Eq. 5.4 is used to specify time-varying parabolic velocity profiles at the inlet of bifurcations B1-B9. At peak inhalation, the flowrate at generation 10 (inlet of B1) is $0.12L/min$. The equivalent peak flow rate in the trachea is $65.5L/min$, which is a reasonable value for inhalation through a DPI (Islam and Cleary, 2012). The Reynolds number during peak inhalation/exhalation at the inlet (generation 10 / B1) of the bronchial tree is 64, which is low enough to allow us to use the decomposition methodology described in paragraph 5.5. All other boundary conditions for the airflow are the same as in the case of quiet breathing described before. In this case, particles are released from the inlet of the bronchial tree (in B1) for 1s starting from 0.1s, which is the transit time to cross over proximal generations, as estimated by the 1D model implemented in the Mimetikos Preludium v1.1.3 software. When breath hold is considered, the air velocities are set to zero and only the equations for the motion of the particles are solved.

Although the Reynolds number in the bronchial tree reaches higher values in this case study than in the case of quiet breathing, flow inertial effect remain unimportant and the flow is again fully developed parabolic in most of the circular branches of the bronchial tree. Therefore, in the following we report results only for particle transport and deposition.

5.7.2 Particle transport and deposition

To further test the validity of the predictions made from the developed CFD model, the deposition results for the case of deep inhalation are again compared to the deposition estimates of the 1D model. The comparison of predicted depositions during only the inhalation phase is shown in fig. 5.15 (deposition during breath hold is excluded). For the deep inhalation scenario, there is reasonable agreement in the deposition estimates

from the two models for particles above $0.3\mu m$, whereas for the smaller particles, about 10% differences are found.

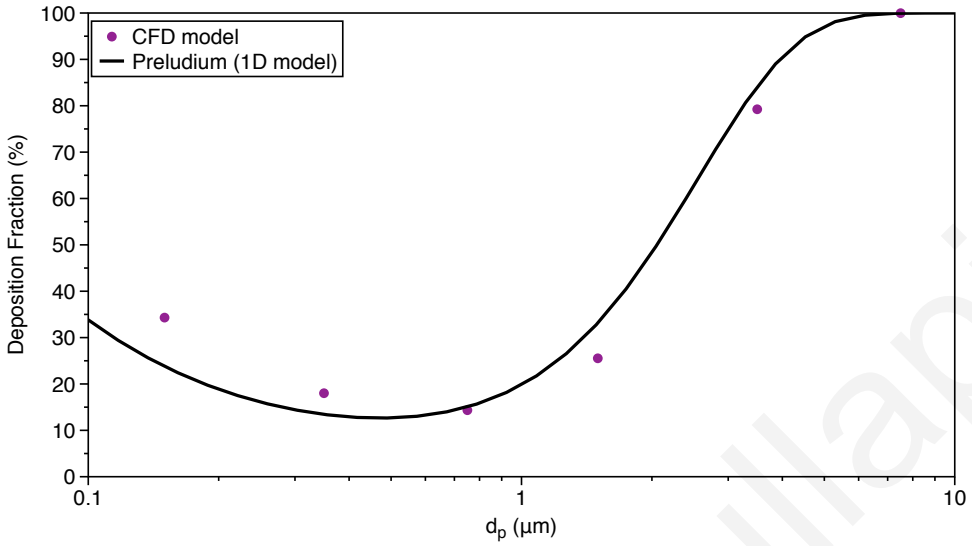

Figure 5.15: *Comparison of deposition fractions in the deep lung obtained by the CFD-model and the 1D model of Yeh and Schum (1980) for deep inhalation (inspiratory phase only).*

In fig. 5.16, deposition fractions during (1) the inhalation phase of quiet breathing (examined before), (2) deep inhalation and (3) deep inhalation followed by 10s of breath hold, are compared. Deposition increases significantly when deep inhalation is employed and approximates 100% for particles larger than $1\mu m$ when a breath hold of 10s follows. For particles in the size range $5 - 10\mu m$, deposition reaches 100% at the end of deep inhalation. A breath hold of 10s results in a rise of approximately 70% in the deposition of $1 - 2\mu m$ particles. When deep inhalation combined with a pause of 10s is employed, the minimum deposition across the aerosol sizes examined is 46.28% for particles in the range $0.2 - 0.5\mu m$. Still, this is considerably higher compared to deposition levels during quiet breathing for an aerosol size traditionally associated with the lowest deposition levels.

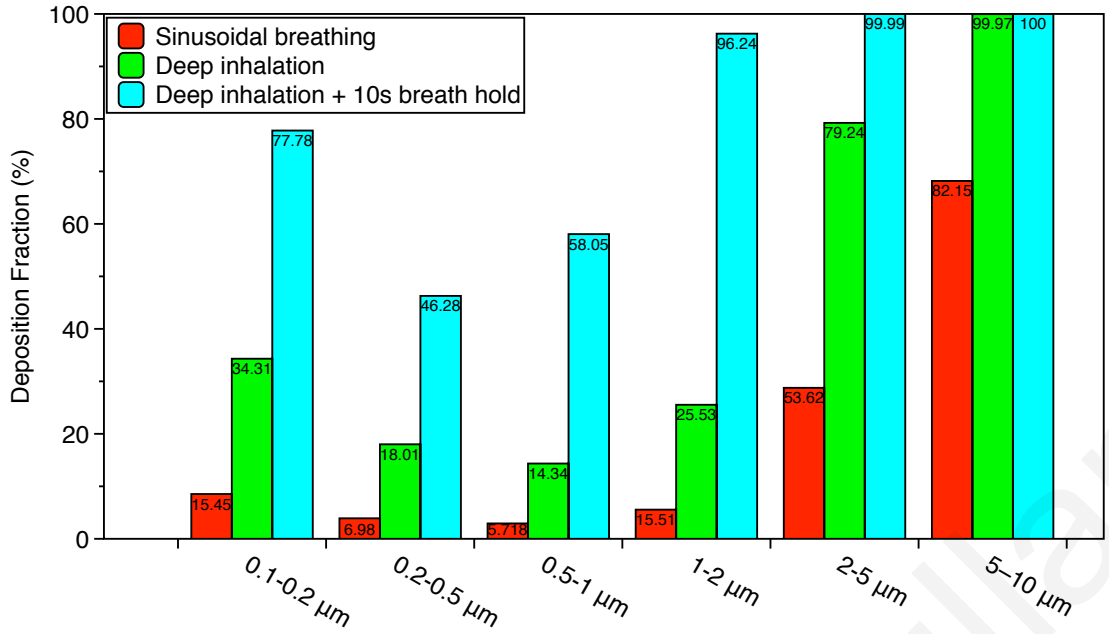

Figure 5.16: *Comparison of deposition fractions in the deep lung during (1) the inhalation phase of quiet breathing (examined before), (2) deep inhalation and (3) deep inhalation followed by 10s of breath hold.*

Fig. 5.17 compares deposition during the inhalation phase of quiet breathing (left column) and the case of deep inhalation maneuver (right column). Deposition in the bar graph is distinguished based on the location where it occurs (cumulative for conducting generations G10-19 or acinar region) and, for the case of the deep inhalation maneuver, based on the phase of breathing (inhalation or breath hold). Deposition levels in the conducting region during the inspiratory phase (red part) are similar for quiet breathing and deep inhalation for $d_p < 2\mu m$ and consist of a very small fraction of the overall deposition. For the case of deep inhalation, deposition in the conducting region decreases for particles larger than $2\mu m$ compared to the case of quiet breathing. This results from the smaller residence times of particles that travel with higher velocities in the bronchial generations in deep inhalation. The vast majority of deposition during the deep inhalation maneuver occurs in the acinus (green and blue parts). On the other hand, there is almost zero deposition in the conducting region during breath hold. As a result of higher velocities during deep inhalation, particles that avoided deposition in the bronchial generations manage to penetrate in the acinar region, where they are deposited, either during inspiratory or breath hold periods. In other words, there are very few particles that have remained suspended in the conducting region to be deposited during breath hold. A factor that also contribute to the considerably higher deposition in the acinar region during deep inhalation maneuver is the larger surface area of the acinus. This results from the larger volume expansion of the acinus in deep inhalation compared to quiet breathing (see fig. 5.6(b) and fig. 5.14(b)). As a consequence, the particles that penetrate in the acinar region have a higher probability to be intercepted on the wall surfaces. Furthermore, stronger convective flows during

deep inhalation bolster aerosols to reach deeper into the acinar volume resulting in higher deposition. This is evident in fig. 5.18, that shows snapshots of the particles that have penetrate in one of the 512 acini models at the end of inspiratory phase during quiet breathing and deep inhalation. In deep inhalation, particles have spread in the acinus occupying it's whole volume. On the other hand, in quiet breathing, only a part of the acinar volume receives the aerosol bolus. This is in agreement with the observations made from Hofemeier et al. (2017), that have examined aerosol deposition in a similar heterogeneous acinar domain under quiet breathing and deep inhalation.

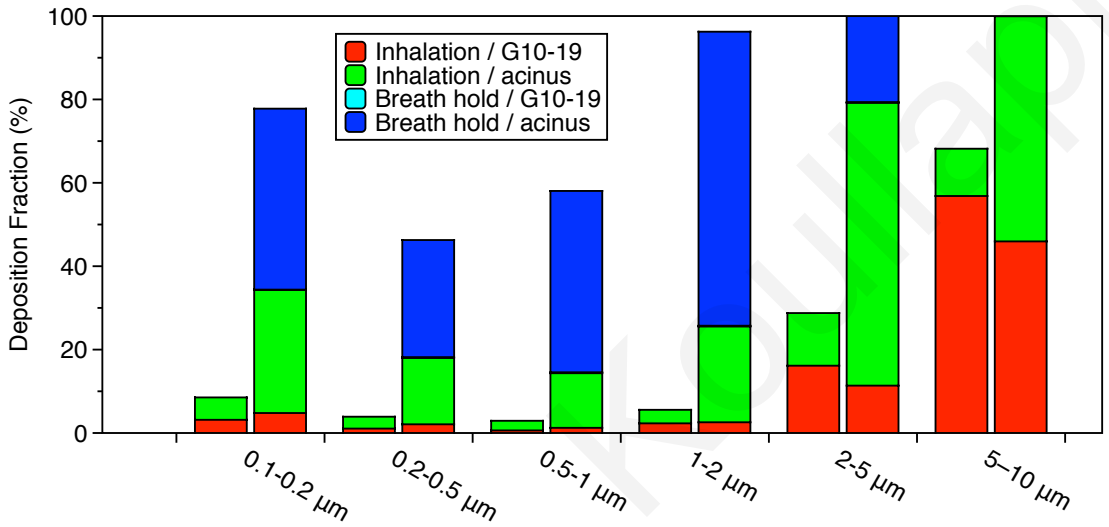

Figure 5.17: *Comparison of deposition during the inhalation phase of quiet breathing (left columns) and the case of deep inhalation maneuver (right columns). Deposition in the bar graph is distinguished based on the location where it occurs (cumulative for conducting generations G10-19 or acinar region) and, for the case of the deep inhalation maneuver, based on the phase of breathing (inhalation or breath hold).*

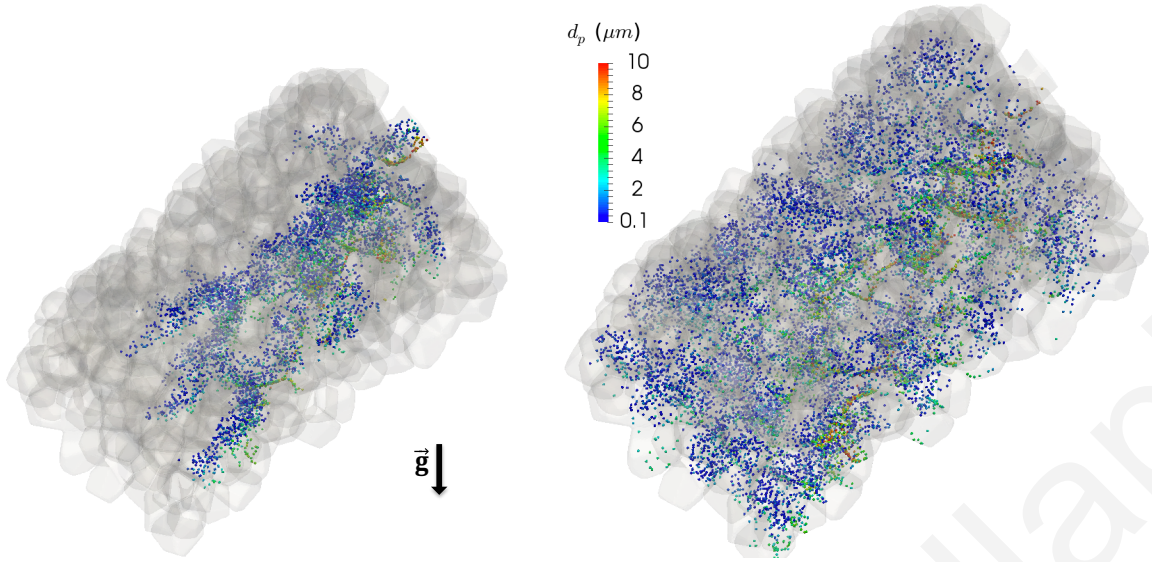

(a) **(b)**

Figure 5.18: *Snapshots of the particles that have penetrate in one of the 512 acini of the deep lung model at the end of inspiratory phase under quiet breathing (a) and deep inhalation (b).*

A valuable piece of information that can be extracted from this study is the optimal breath hold time for sufficient deposition of the inhaled drug aerosol in the acinar region. It is desirable to have a breath hold period as short as possible since patients with lung diseases often struggle to keep their breath. Fig. 5.19 displays the Deposition Efficiencies in the acinar region as a function of time, for the particle sizes under consideration. As discussed previously, larger particles in the range $5\mu m < d_p < 10\mu m$ are deposited entirely during the inspiratory phase. For particles in the $2\mu m < d_p < 5\mu m$, less than 3s of breath hold is sufficient to reach 100% deposition. For lighter particles of $1\mu m < d_p < 2\mu m$ deposition approaches 100% at the end of breath hold (t=12.36s). Thus, for full retention of these particles in the alveolar region, a large breath hold period is needed. Although breath hold improves deposition levels of smaller (sub-micron) particles, it seems unachievable to reach total retention of these particles in the deep pulmonary acinar airways.

In conclusion, if the target of inhalation therapies are the respiratory airways, a deep inhalation combined with a breath hold period is a good strategy to significantly augment deposition.

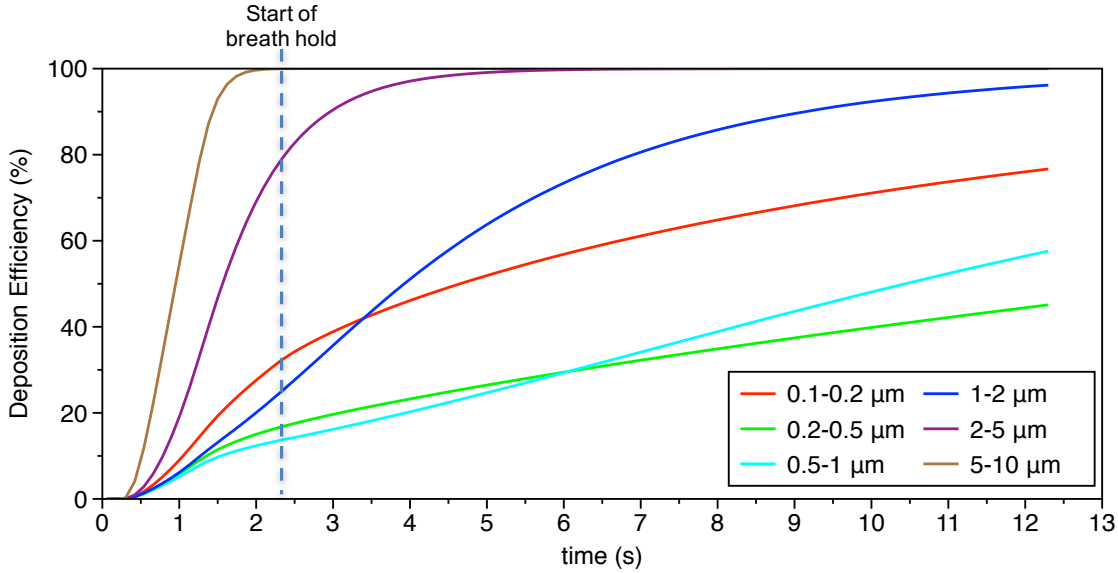

Figure 5.19: *Deposition Efficiencies in the acinar region as a function of time, for the six particle groups considered.*

5.8 Potential for further reductions in computational cost

At this point, we need to remind ourselves that we have embarked on this effort in view of the prohibitively high cost of computing the airflow and aerosol deposition in the entire lung over a complete cycle. Thus, we have sought a simplified approximation of the deep lung that would render the simulation of deposition over a complete cycle computationally feasible. The use of one representative bifurcation for each generation level and one acinus model, while still accounting for the effects of gravity, resulted in a drastic reduction of computational cost compared to the simulation of the complete model. One could argue that the resulting computational cost is acceptable. For quiet breathing, the average computing time for half of the breathing cycle in a bifurcation was approximately 20 hours on 128 processors. The computing times varied depending on the number of particles in the domain, e.g. longer times were observed in B1 during the simulation of the inhalation phase, when more particles needed to be tracked, as compared to exhalation. The simulation of the full cycle for quiet breathing in the acinus model took about 250 hours on 192 processors. Clearly, the proposed approach renders the simulation of a large-scale airway model using CFD techniques feasible, at least for research purposes. Yet, for routine use in the clinical setting, or in the context of large-scale in silico population studies, the resulting computational demands remain quite high. Thus, reducing computing time further through additional simplifications would be highly desirable.

In this respect, a method that applies a semi-analytical velocity solution in the representative bifurcations has been tested and the results are shown below. Such an

approach is made possible due to the simplicity of the airflow in the decomposed bifurcations. Specifically, the velocity field characteristics are quite similar in all bifurcation levels. Although small differences do exist, such as the intensity of the developed secondary motions near the carina due to the different flowrates through the bronchial generations, we hypothesised that these would have a minor effect on deposition characteristics in the deep lung Fig. 5.20 depicts velocity contours at peak inhalation during quiet breathing in B1 (G10-11), B5 (G14-G15) and B9 (G18-19). It can be observed that, although there are significant differences in the velocity magnitude, the flow-field features show notable resemblance. Some differences are evident near the region of the carina, especially in B1, that are associated to the higher flow inertia in the intermediate generations.

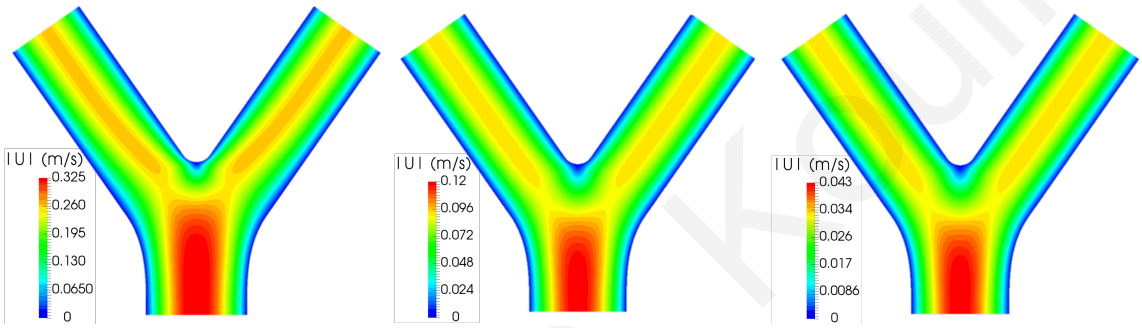

Figure 5.20: *Contours of the velocity field at peak inhalation during quiet breathing in: (a) B1 (G10-11); (b) B5 (G14-G15) and (c) B9 (G18-19).*

Based on these observations, the following relation is use to impose an approximation of the numerical solution of the time-varying velocity field in Bi during quiet breathing , where $i = 1$ to 9 indicates the bifurcation rank:

$$\mathbf{u}_{Bi}(\mathbf{x}', t) = \frac{2^{5-i}}{(D_p/D_d)^{2(5-i)}} \mathbf{u}_{B_5}(\mathbf{x}, t = T/4) sin(\omega t), \qquad i = 1 - 9. \tag{5.8}$$

Here, $\mathbf{u}_{Bi}(\mathbf{x}', t)$ is the velocity field in Bi at any given point and time and $\mathbf{u}_{B_5}(\mathbf{x}, t = T/4)$ is the velocity field in B5 during peak inhalation obtained from the numerical solution of the Navier-Stokes equations. Therefore, the computed velocity field in B5 during peak inhalation is mapped at any given representative bifurcation (Bi) using the appropriate scaling to account for both the geometry and flowrate alterations. Then, a sine-wave function is used to scale the instantaneous velocity field and thus emulate the unsteady velocity field during sinusoidal breathing. In this approximation, B5 has been chosen as the velocity field source because it lies in the mid-level of the bronchial tree model, which offers a number of advantages. For example, mapping over longer distances in the bronchial tree and the effects of inlet and outlet conditions can be avoided.

We tested the accuracy of the above mentioned approximation by comparing the resulting deposition in the bronchial tree during the inspiratory phase of quiet breathing to the corresponding results obtained by numerically solving the Navier-Stokes equations to obtain the velocity field in each bifurcation. Fig. 5.21 illustrates generational Deposition fractions in the bronchial tree at the end of inhalation, as predicted when the velocity field is computed (left column at a certain particle size) or approximated (right column at a certain particle size). Overall deposition, given by the sum of generational Deposition fractions, show remarkable agreement, with the largest differences being less than 1% for particles in the size range $0.1 - 0.2\mu m$. Quite reasonable agreement also exists in terms of generational Deposition indicating that local deposition characteristics are well captured when an approximation of the velocity field is employed.

The average computing time for half of the breathing cycle in a bifurcation when the approximate velocity field is used, reduces to approximately an hour on 128 processors. In conclusion, using an approximate solution of the velocity field, computing times can be reduced by a factor of 20 with a loss of accuracy less than 1% in the calculation of overall deposition.

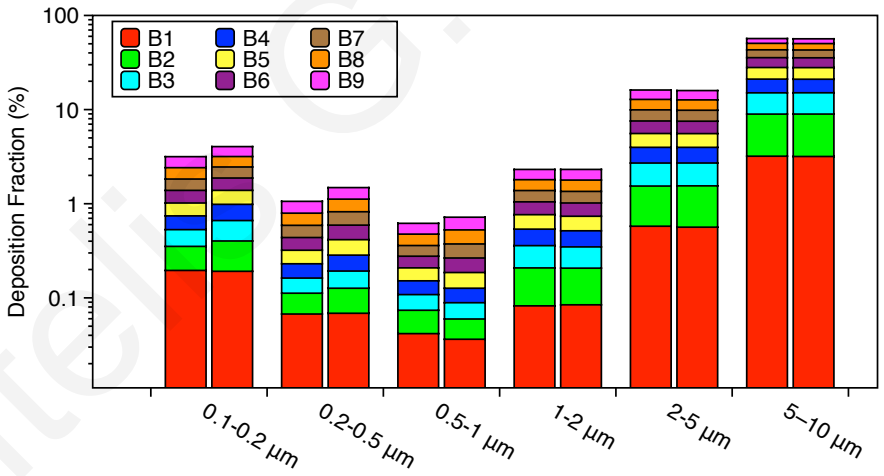

Figure 5.21: *Deposition fractions per generation in the bronchial tree at the end of inhalation, as predicted when the velocity field is computed (left column at a certain particle size) or approximated (right column at a certain particle size).*

Although the method that applies an approximate velocity solution in the representative bifurcations has been tested only for quiet breathing (approximated as an ideal sinusoidal function), it can be used for any inhalation profile. For this purpose, an adequate analytical function that describes the breathing profile must be used to replace the sine-wave function in equation 5.8.

5.9 Model limitations

Several assumptions and simplifications were made in developing the methodology we have presented herein. The first approximation relates to the bronchial tree geometry. A single bifurcation model was used to generate the tree, with constant branching angles and ratios of parent-to-daughter diameter and length-to-diameter. In reality, there are variations in the dimensions among generations as well as variability of the branching angle, even in the same generation (Yeh and Schum, 1980). Furthermore, a rigid bronchial tree was assumed herein which is not valid, especially as we move in the most distal parts of the lung (West, 1996). Regarding the geometry of the acinus, the same heterogeneous acinar structure represents the whole respiratory zone (Hofemeier et al., 2017), as particle deposition is largely dominated by particle size rather than the details of the acinar morphology. However, it should be noted that the acinar model domain employed herein represents approximately a 1/8th of a total acinus. As such, acinar deposition is potentially underestimated here compared to a full-sized acinus, as indicated by the study of Hofemeier et al. (2017).

The proposed methodology for the domain decomposition assumes uniform ventilation across the bronchial generations, which might not be realistic, especially in the case of respiratory diseases in the deep lung that alter air ventilation, such as emphysema. Moreover, it was assumed that the airflow recovers fully within the branches downstream of the carina. While in general this is a reasonable assumption deep in the lung, where it can be applied depends on the flowrate. In the case of simulation of higher flowrates, this assumption might not hold true in upper part of the bronchial tree and the beginning of the tree might have to be shifted deeper in the lung, where flow inertia effects become unimportant. On the other hand, the model can be extended in more proximal generations as long as the airflow recovers fully within the branches downstream of the carina. This can be examined by simulating the airflow at peak conditions in the most proximal bifurcation level of the model.

Finally, the aerosol bolus was injected during a time window in the inhalation phase, assuming a homogeneous spatial distribution. In reality, temporal and spatial distribution of particles reaching the deep lung generations are anticipated to display an inhomogeneous behaviour that is influenced by their path while crossing through the proximal generations. For example, a small fraction of particles above $5\mu m$ inhaled through the mouth is expected to reach the deep lung generations, whereas a log-uniform size distribution of the aerosol bolus was assumed herein.

5.10 Conclusions

In the current chapter, we have present a CFD-based methodology that can be used to predict aerosol deposition in the deep lung under various breathing scenarios. An idealised bronchial tree model that represents generations 10 to 19 of the conducting zone of the human lung is generated, starting from an idealised bifurcation unit. The acinar model was created using a space-filling algorithm that creates heterogeneous alveolar cavities that populate the bifurcating acinar airways. A methodology to reduce the computational cost of the coupled simulation by decomposing the tree is presented, based on the flow similarity across the central conducting regions. Topological information is used to account for the correct gravitational force on the particles in the representative bifurcations, emulating their transport characteristics in the bronchial tree. Eventually, airflow and particle transport are simulated in one representative bifurcation for a certain generation and one representative sub-acinus unit, resulting in great savings in computational cost. An Eulerian-Lagrangian approach was adopted to solve the flow and particle equations in the decomposed domain during two distinct breathing scenarios, namely quiet breathing and deep inhalation followed by 10s of breath hold.

The overall deposition predictions of the newly developed method agree rather well with the known deposition trends reported in the literature and the output of the 1D deposition model of Yeh and Schum (1980), as implemented in a commercial software. During quiet breathing, overall deposition for particles above $5\mu m$ reaches 82%, with the higher deposition occurring in the bronchial generations during inhalation. In this size range, particles that manage to enter the acinar region are entirely filtered out, whereas deposition of suspended particles in the bronchial tree during exhalation is non-negligible ($> 10\%$). Particles below $1\mu m$ are exhaled out in a large percentage that peaks at almost 90% for particles in the size range $0.5 - 1\mu m$. Deposition of $1 - 5\mu m$ particles during exhalation surpasses deposition upon inhalation, suggesting that a large fraction of these particles remain suspended and sediment at the early stages of exhalation. The effect of orientation in the filtering efficiency was assessed by calculating the variance of deposition efficiencies in the bronchial and acinar generations during quite breathing. In the bronchial region, the orientation-induced variability in deposition efficiency was found largest for the particles above $2\mu m$, which are more susceptible to gravity. Furthermore, variance in deposition efficiencies increases as we move in the more distal generations as result of the wider range of angles relative to the direction of gravity. Variance in deposition for particles smaller than $1\mu m$ is rather small in the bronchial region. Particles in the $2 - 5\mu m$ range have quite high average deposition efficiency in the acinus that reaches approximately 75%. In addition, their acinar deposition shows considerable variation (12.4%).

Deposition outcomes are dramatically affected under deep inhalation followed by a

breath hold. In particular, deposition increases significantly under deep inhalation and reaches 100% for particles larger than $1\mu m$ when a breath hold of 10s follows. The vast majority of deposition occurs in the acini, since aerosols reach deeper into the alveolar generations and the larger volume expansion of the acinus under deep inhalation results in a larger surface area for particle retention. The methodology presented in this chapter, can be used to establish optimal breath hold times for full retention of the inhaled aerosol and thus maximise the therapeutic outcome in inhalation therapy.

In an effort to reduce the required computational times, a method that applies a semi-analytical velocity solution in the representative bifurcations was presented. Such an approach is made possible due to the simplicity of the airflow in the decomposed bifurcations, that despite significant differences in the velocity magnitudes across different generations, flowfield features show notable resemblance. Deposition fractions in the bronchial tree at the end of the inspiratory phase of quiet breathing, as predicted when the velocity field is computed or approximated, were compared. Overall deposition showed remarkable agreement, with the largest differences being less than 1%. Quite reasonable agreement also exists in terms of generational deposition indicating that local deposition characteristics are well captured when an approximation of the velocity field is employed. In conclusion, using an approximate solution of the velocity field, computing times can be reduced by a factor of 20 with a loss of accuracy less than 1% in the calculation of overall deposition. The method that applies an approximate velocity solution in the representative bifurcations can be utilized for any inhalation profile.

The developed methodology can be adopted in future studies that deal with deposition in the diseased peripheral lung. This can be achieved by replacing the current healthy bifurcation or acinus model geometries with diseased ones, such as a bifurcation with constrictions (Longest et al., 2006; Sul et al., 2014) or an emphysematous acinus model (Oakes et al., 2016). The proposed methodology can potentially be utilized to investigate deposition characteristics in the developing peripheral lung of children and young infants. Adequate age-dependent geometries are required to conduct such a study (Tenenbaum et al., 2016). Another possible use is the simulation of transport and deposition of non spherical particles in the distal airways, such as fibers. Furthermore, the outcomes of the CFD methodology for a range of factors known to influence aerosol transport in the deep lung can be used to derive accurate correlations of deposition which can then be incorporated in current analytical 1-D models.

Chapter 6

Conclusions

6.1 Outcomes

Regional deposition characteristics of inhaled aerosols in the airways play a critical role in applications where targeted drug delivery is needed in order to maximize efficacy and minimize side-effects. They are also important in health effect evaluations of human exposure to aerosol contaminants. *In silico* techiques offer a powerful tool to predict localized deposition in the extrathoracic and intrathoracic airways. In the current work, we have provided new insights concerning airflow physics and deposition mechanisms in both the upper airways and the peripheral lung using computational methods.

Large Eddy Simulations were used to investigate deposition of inhaled aerosol particles in a realistic geometry of the human upper airways reconstructed from CT-scans. A realistic inlet velocity profile, measured at the breathing zone of a thermal breathing manikin was used to assess the effect of inlet conditions on deposition in the extrathoracic airways. Mean velocity fields were almost identical even at small distances from the mouth inlet as a result of the complex geometry that quickly smoothes out any differences in the flowfield due to inlet conditions. However, the number of deposited particles is increased in the case of measured velocity inlet conditions since particles with greater inertia impact at the tongue as a result of their higher initial velocities. Deposition in the subsequent sub-regions is rather unaffected for particle sizes below $5\mu m$, while for $10\mu m$ some differences occur in the oral cavity and and the larynx. Qualitatively similar mean flow structures were observed at the three flowrates examined, that correspond to sedentary, light and heavy exercise conditions. As the flowrate increases, greater values of turbulent intensities were found to persist more distally in the trachea and the main bronchi. Deposition Fraction of particles is increased with flowrate due to greater inertial impaction. This effect was more clearly evident for 2.5 and 5μm diameter particles and resulted in enhanced deposition in the mouth-throat region. Electrostatic charge increased the overall deposition of smaller particles by as much as sevenfold, with most of the increase located in the mouth-throat. For particles larger than $2.5\mu m$ impaction prevailed over electrostatic deposition for larger particles

as the flowrate was increased. Deposition enhancement due to electrostatic effects was located mostly in the mouth-throat due to the large wall surface area that attracts the particles and the complex flowfield found in that region. Significant enhancement in deposition was also found in the left and right lung sub-regions of the reconstructed geometry.

In the second part, we have examined the effect of the extrathoracic airways on localized deposition in the tracheobronchial tree, in order to assess whether standard mouth-throat models can be used to predict deposition in the central airways. By adopting precomputed flowfields in these standard models, simulations can be restricted to the tracheobronchial tree resulting in significant savings in computational cost, that is still prohibitively high for population studies or routine clinical use. Three mouth-throat geometries, with significantly different geometric and filtering characteristics, were merged onto the same tracheobronchial tree that extends to generation 8. Large Eddy Simulations were performed at steady inhalation flowrates of 30 and 60 L/min. At both flowrates, our results reveal that upstream flow field differences become immaterial beyond the main bifurcation. As a result, filtering of inhaled particles in the central airways, expressed by Deposition efficiencies, is practically decoupled from the mouth-throat geometry for the cases examined. In addition, the amount of deposited particle doses locally, expressed by segmental deposition fractions, were found to remain practically identical for particles with aerodynamic diameters up to $d_p = 4\mu m$ and $d_p = 2.5\mu m$ at 30 and 60 L/min, respectively. For larger particles however, differences in the localized deposition fractions were evident that are attributed to variations in the mouth-throat filtering. Our results indicate that deposition in the tracheobronchial airways can be estimated without the need to take into account airflow features in the extrathoracic airways. For particles with $Stk_{trachea} < 4.5 \times 10^{-3}$, localised deposition fractions are unaffected by mouth-throat filtering, whereas for larger $Stk_{trachea}$ numbers, the amount of deposited dose can be obtained if the particle size distribution that escapes filtering in the mouth-throat (ex-cast dose) of a particular patient is known or can be estimated. Our results point out the potential for significant reductions in the computational cost for predicting deposition in the tracheobronchial airways. This is highly beneficial in the context of *in silico* population studies, since the large numbers of tracheobronchial trees available in chest-CT databases could be exploited to derive population-specific deposition estimates. Moreover, estimation of deposition in patient-specific basis could be accelerated, rendering the use of *in silico* methods in achieving better efficiency of inhaled therapies.

We have developed a CFD-based methodology for the prediction of aerosol deposition in the peripheral lung under various breathing scenarios. The peripheral lung model consists of a simplified geometry that spans the distal bronchial airways to the respiratory alveolar region. The computational cost of the coupled simulation is reduced by taking advantage of the flow similarity across the branching tree in order to

decompose the bronchial and acinar generations into representative subunits. Topological information is used to account for the correct gravitational forces acting on the particles, emulating their motion in the actual peripheral lung model. This is important since our results show that airway orientation relative to gravity has a significant impact on deposition rates, especially for particles above $2\mu m$ in the more distal generations. The resulting deposition estimates agree rather well with the known deposition trends reported in the literature. The potential of the method to provide detailed deposition insights as well as guidance for targeting a specific site in an inhaled therapy was highlighted in two case studies, namely quiet breathing and deep inhalation followed by a pause of 10s. The developed methodology offers a valuable tool for deposition studies in the peripheral lung, especially in cases where simple models cannot be used. Such scenarios include aerosol deposition in the distal airways of patients with asthma or COPD and the transport of non spherical particles.

6.2 Future directions

Our investigation in chapter 4 point to the potential for significant reductions in the computational cost for predicting deposition in the tracheobronchial airways. As a next step, we could utilise the large number of available chest-CT databases in order to assess deposition in a particular population. For example, deposition characteristics in asthmatic subjects at different disease stages could be examined. Another application could be to examine the variation of deposition in populations from different countries or sex-based differences. The outcomes of such investigations could be used to develop population-specific guidelines and devices for more effective inhaled therapies. Besides population studies, our findings in chapter 4 have implications in patient-specific deposition assessments. For example, the chest CT-scan of a patient can be used along with pre-computed ex-cast aerosol size distribution data to estimate the amount of deposited dose in the upper tracheobronchial airways. Therefore, the amount of inhaled drug dose for efficient treatment of the airways can be defined *a priori*. As pointed out before, estimating deposition in the central airways could be accelerated when the geometry of the extrathoracic airways is not reconstructed. Moreover, avoiding simulation of the airflow in the mouth-throat can result in considerable speed up of the computation.

The developed peripheral lung model could be extended to examine deposition in diseased conditions. For example, the two main forms of COPD are chronic bronchitis and emphysema. The former is characterised by airflow obstruction due to narrowing of the distal bronchial airways, whereas in emphysema there is enlargement of the alveolar airspace caused by deterioration of the pulmonary tissue leading to a loss of inter-alveolar septa. The peripheral lung model can be employed to assess how deposition is modified due to chronic bronchitis or emphysema. Moreover, there are

very few studies dealing with deposition in the distal lung regions of child and infants. This is another research area where our developed methodology could be utilised to provide insights concerning transport and deposition of inhaled aerosols.

It is generally known that inhaled fibers can penetrate deep into the lungs and reach the distal pulmonary acinar airways due to their aerodynamic properties. Fiber-like particles tend to align with the flow and thus stay longer airborne relative to spherical particles with equivalent aerodynamic diameters, due to higher drag forces that resist sedimentation. Combined with their high surface-to-volume ratio, fibers are attractive airborne carriers for drug delivery. Since our understanding of the dynamics of inhaled aerosols in the distal regions of the lungs has been mostly limited to spherical particles, our developed methodology could be used to unravel the fate of non-spherical aerosols in the peripheral lung.

Towards simulation of the entire lung, a sample subset of the outlets in an upper airway model could be merged to peripheral lung models. The sample subset of outlets could be selected such that each peripheral lung model represents a characteristic region of the lung, e.g. a lung lobe. The objective in one such assessment would be to test whether a finite number of peripheral lung models could be used to provide reasonable deposition estimates in the entire lung. The challenging task in such a scenario would be the different ventilation conditions in the distal lung models that will require separate simulations for each model. In addition the particle distributions, spatially and temporally, that reach the outlets of the upper airways (and the inlets of the distal lung models) would be different as a result of different ventilation and filtering in the upstream regions.

Bibliography

V. Agnihotri, G. Ghorbaniasl, S. Verbanck, and C. Lacor. An eddy interaction model for particle deposition. *Aerosol Science*, 47:39–47, 2012.

M. Ali, R.N. Reddy, and M. K. Mazumder. Electrostatic charge effect on respirable aerosol particle deposition in a cadaver based throat cast replica. *Journal of Electrostatics*, 66:401–406, 2008.

V. Armenio, U. Piomelli, and V. Fiorotto. Effect of the subgrid scales on particle motion. *Physics of Fluids*, 11(10):3030–3042, 1999.

B. Asgharian and O. T. Price. Airflow distribution in the human lung and its influence on particle deposition. *Inhalation Toxicology*, 18(10):795–801, 2006. URL `http://dx.doi.org/10.1080/08958370600748687`.

T. J. Baker. Interpolation from a cloud of points. In: 12th International Meshing Roundtable, pages 55–63., Santa Fe, New Mexico, 2003.

Imre Balashazy, Werner Hofmann, and Thomas Heistracher. Local particle deposition patterns may play a key role in the development of lung cancer. *Journal of Applied Physiology*, 94(5):1719–1725, 2003.

C. G. Ball, M. Uddin, and A. Pollard. Mean flow structures inside the human upper airway. *Flow, Turbulence and Combustion*, 81(1):155–188, Jul 2008.

M. P. Bivolarova. *Control of Indoor Airflows for Reduction of Human Exposure to Aerosol Contaminants*. PhD thesis, Department of Civil Engineering, Technical University of Denmark, 2017.

M. Breuer, H.T. Baytekin, and E.A. Matida. Prediction of aerosol deposition in 90 bends using LES and an efficient lagrangian tracking method. *Aerosol Science*, 37: 1407–1428, 2006.

P. K. P. Burnell, L. Asking, L. Borgstrom, S. C. Nichols, B. Olsson, D. Prime, and I. Shrubb. Studies of the human oropharyngeal airspaces using magnetic resonance

imaging IV - the oropharyngeal retention effect for four inhalation delivery systems. *Journal of Aerosol Medicine*, 20(3):269–281, 2007.

P.R. Byron, J. Peart, and J.N. Staniforth. Aerosol electrostatics. i: Properties of fine powders before and after aerosolization by dry powder inhalers. *Pharmaceutical Research*, 14(6):698–705, 1997.

Tai Chan and Morton Lippmann. Experimental measurements and empirical modelling of the regional deposition of inhaled particles in humans. *American Industrial Hygiene Association Journal*, 41(6):399–409, 1980. doi: 10.1080/15298668091424942.

Y.S. Chen and C.P. Yu. Particle deposition from duct flows by combined mechanisms. *Aerosol Science and Technology*, 19(3):389–395, 1993.

K. H. Cheng, Y. S. Cheng, and H. C. Yeh. Measurements of airway dimensions and calculation of mass transfer characteristics of the human oral passage. *Biomechanical Engineering*, 119:476–482, 1997.

J. Choi, M.H. Tawhai, E.A. Hoffman, and C.-L. Lin. On intra- and intersubject variabilities of airflow in the human lungs. *Phys. Fluids*, 21(101901), 2009.

Valérie Codrons, Francis Vanderbist, Bernard Ucakar, Véronique Préat, and Rita Vanbever. Impact of formulation and methods of pulmonary delivery on absorption of parathyroid hormone (1–34) from rat lungs. *Journal of Pharmaceutical Sciences*, 93 (5):1241 – 1252, 2004.

A. Comerford, C. Forster, and W. A. Wall. Structured tree impedance outflow boundary conditions for 3d lung simulations. *Journal of Biomechanical Engineering*, 132: 081002–1–10, August 2010.

J. Conway. Lung imaging - two dimensional gamma scintigraphy, SPECT, CT and PET. *Advanced Drug Delivery Reviews*, 64(4):357–368, 2012.

Chantal Darquenne, John S Fleming, Ira Katz, Andrew R Martin, Jeffry Schroeter, Omar S Usmani, Jose Venegas, and Otmar Schmid. Bridging the gap between science and clinical efficacy: Physiology, imaging, and modeling of aerosols in the lung. *Journal of Aerosol Medicine and Pulmonary Drug Delivery*, 29(2):107–126, 2016.

J. W. De Backer, W. G. Vos, C. D. Gorlé, P. Germonpré, B. Partoens, F. L. Wuyts, P. M. Parizel, and W. De Backer. Flow analyses in the lower airways: Patient-specific model and boundary conditions. *Medical Engineering and Physics*, 30(7):872–879, 2008.

Wilbur de Kruijf and Carsten Ehrhardt. Inhalation delivery of complex drugs—the next steps. *Current Opinion in Pharmacology*, 36:52 – 57, 2017.

Eugene de Villiers. *The Potential of Large Eddy Simulation for the Modeling of Wall Bounded Flows*. PhD thesis, Thermofluids Section, Department of Mechanical Engineering, Imperial College of Science, Technology and Medicine, London, UK, 2006.

Wesley H. DeHaan and Warren H. Finlay. In vitro monodisperse aerosol deposition in a mouth and throat with six different inhalation devices. *Journal of Aerosol Medicine*, 14(3):361–367, 2001.

A. Einstein. *Investigations on the Theory of the Brownian Movement*. New York: Dover, 1926.

S. Elghobashi. On predicting particle-laden turbulent flows. *Applied Scientific Research*, 52(4):309–329, 1994.

Emmace Consulting AB. *Mimetikos Preludium*. Lund, Sweden, version 1.1.3 edition, 2017. URL `http://www.emmace.se/mimetikos-preludium/`.

Y. Feng and C. Kleinstreuer. Analysis of non-spherical particle transport in complex internal shear flows. *Phys. Fluids*, 25:091904–1–26, 2013.

W. H. Finlay. *The Mechanics of Inhaled Pharmaceutical Aerosols*. Academic Press, New York, 2001.

B. Forsyth and F. J Liu, B.Y. H.and Romay. Particle charge distribution measurement for commonly generated laboratory aerosols. *Aerosol Science and Technology*, 28: 489–501, 1998.

D. O. Frank-Ito, M. Wofford, J. D. Schroeter, and J. S. Kimbell. Influence of mesh density on airflow and particle deposition in sinonasal airway modeling. *Journal of Aerosol Medicine and Pulmonary Drug Delivery*, 28(0):1–11, 2015.

Massimo Germano, Ugo Piomelli, Parviz Moin, and William H. Cabot. A dynamic subgrid-scale eddy viscosity model. *Physics of Fluids A: Fluid Dynamics*, 3(7):1760–1765, 2018/02/08 1991.

B. Grgic, W. H. Finlay, P. K. P. Burnell, and A. F. Heenan. In vitro intersubject and intrasubject deposition measurements in realistic mouth–throat geometries. *Journal of Aerosol Science*, 35(8):1025–1040, 2004a.

B. Grgic, W. H. Finlay, and A. F. Heenan. Regional aerosol deposition and ow measurements in an idealized mouth and throat. *Journal of Aerosol Science*, 35:21–32, 2004b.

Beatrice Haefeli-Bleuer and Ewald R. Weibel. Morphometry of the human pulmonary acinus. *The Anatomical Record*, 220(4):401–414, 1988. ISSN 1097-0185. doi: 10.1002/ar.1092200410. URL `http://dx.doi.org/10.1002/ar.1092200410`.

A. H. Hashish. *The influence of electrostatic charge on the deposition of therapeutic aerosols and airbourne pollutant particles within the human respiratory system*. Ph.d. thesis, University of Southampton, 1988.

A.F. Heenan, W.H. Finlay, B. Grgic, A. Pollard, and P.K.P. Burnell. An investigation of the relationship between the flow field and regional deposition in realistic extrathoracic airways. *Journal of Aerosol Science*, 35:1013–1023, 2004.

T. Heistracher and W. Hofmann. Physiologically realistic models of bronchial airway bifurcations. *Journal of Aerosol Science*, 26(3):497 – 509, 1995. ISSN 0021-8502. doi: http://dx.doi.org/10.1016/0021-8502(94)00113-D.

W. C Hinds. *Aerosol Technology: Properties, Behavior, and Measurement of Airborne Particles*. Wiley-Interscience, New-York, 1999.

P. Hofemeier and J. Sznitman. Revisiting pulmonary acinar particle transport: convection, sedimentation, diffusion and their interplay. *Journal of Applied Physiology*, 118(11):1375–1385, 2015.

P. Hofemeier and J. Sznitman. The role of anisotropic expansion for pulmonary acinar aerosol deposition. *Journal of Biomechanics*, 49(14):3543–3548, 2016.

Philipp Hofemeier, Kenishiro Koshiyama, Wada Shigeo, and Josué Sznitman. One (sub-)acinus for all: Fate of inhaled aerosols in heterogeneous pulmonary acinar structures. *European Journal of Pharmaceutical Sciences*, ,to be published, 2017.

W. Hofmann. Modelling inhaled particle deposition in the human lung - a review. *Journal of Aerosol Science*, 42:693–724, 2011.

K. Horsfield, G. Dart, D.E. Olson, G.F. Filley, and G. Cumming. Models of the human bronchial tree. *Journal of applied physiology*, 31(2):207–217, 1971.

C. Housiadas and M. Lazarides. *Inhalation dosimetry modelling*, volume 17 of *Human Exposure to Pollutants via Dermal Absorption and Inhalation*, pages 185–236. Springer, Netherlands, 2010.

Yohsuke Imai, Takahito Miki, Takuji Ishikawa, Takayuki Aoki, and Takami Yamaguchi. Deposition of micrometer particles in pulmonary airways during inhalation and breath holding. *Journal of Biomechanics*, 45:1809–1815, 2012.

D. B. Ingham. Diffusion of aerosols from a stream flowing through a cylindrical tube. *Journal of Aerosol Science*, 6:125–132, 1975.

Mohammad S. Islam, Suvash C. Saha, Emilie Sauret, Tevfik Gemci, and Y.T. Gu. Pulmonary aerosol transport and deposition analysis in upper 17 generations of the human respiratory tract. *Journal of Aerosol Science*, 108:29 – 43, 2017. ISSN

0021-8502. doi: https://doi.org/10.1016/j.jaerosci.2017.03.004. URL http://www.sciencedirect.com/science/article/pii/S0021850216303445.

N. Islam and M. J. Cleary. Developing an efficient and reliable dry powder inhaler for pulmonary drug delivery - a review for multidisciplinary researchers. *Medical Engineering and Physics*, 34:409–427, 2012.

H. Jasak. *Error Analysis and Estimation for the Finite Volume Method with Applications to Fluid Flows*. PhD thesis, Department of Mechanical Engineering, Imperial College of Science, Technology and Medicine, London, UK, 1996.

S.T. Jayaraju, M. Brouns, C. Lacor, B. Belkassem, and S. Verbanck. Large eddy and detached eddy simulations of fluid flow and particle deposition in a human mouth–throat. *Journal of Aerosol Science*, 39(10):862 – 875, 2008. ISSN 0021-8502. doi: http://dx.doi.org/10.1016/j.jaerosci.2008.06.002. URL http://www.sciencedirect.com/science/article/pii/S002185020800102X.

A. Johnstone, M. Uddin, A. Pollard, A. Heenan, and W. H Finlay. The flow inside an idealised form of the human extra-thoracic airway. *Experiments in Fluids*, 37: 673–689, 2004.

Stefan Karner and Nora Anne Urbanetz. The impact of electrostatic charge in pharmaceutical powders with specific focus on inhalation-powders. *Journal of Aerosol Science*, 42(6):428 – 445, 2011.

Navvab Khajeh-Hosseini-Dalasm and P. Worth Longest. Deposition of particles in the alveolar airways: Inhalation and breath-hold with pharmaceutical aerosols. *Journal of Aerosol Science*, 79:15 – 30, 2015. ISSN 0021-8502. doi: http://dx.doi.org/10.1016/j.jaerosci.2014.09.003. URL http://www.sciencedirect.com/science/article/pii/S0021850214001487.

Wojciech Kierat, Mariya Bivolarova, Eva Zavrl, Zbigniew Popiolek, and Arsen Melikov. Accurate assessment of exposure using tracer gas measurements. *Building and Environment*, 131:163 – 173, 2018.

C. Kleinstreuer and Z. Zhang. Laminar-to-turbulent fluid-particle flows in a human airway model. *International Journal of Multiphase Flow*, 29(2):271 – 289, 2003.

C. Kleinstreuer and Z. Zhang. An adjustable triple-bifurcation unit model for air-particle flow simulations in human tracheobronchial airways. *Journal of Biomechanical Engineering*, 131:021007–1–10, 2009.

C. Kleinstreuer and Z. Zhang. Airflow and particle transport in the human respiratory system. *Annual Review of Fluid Mechanics*, 42:301–334, 2010.

Clement Kleinstreuer and Yu Feng. Computational analysis of non-spherical particle transport and deposition in shear flow with application to lung aerosol dynamics—a review. *Journal of Biomechanical Engineering*, 135(2):021008–021008–19, 02 2013.

Arun V. Kolanjiyil and Clement Kleinstreuer. Nanoparticle mass transfer from lung airways to systemic regions—part i: Whole-lung aerosol dynamics. *Journal of Biomechanical Engineering*, 135(12):121003–121003–11, 10 2013.

K. Koshiyama and S. Wada. Mathematical model of a heterogeneous pulmonary acinus structure. *Computers in Biology and Medicine*, 62:25–32, 2015.

P. Koullapis, S. C. Kassinos, J. Muela, C. Perez-Segarra, J. Rigola, O. Lehmkuhl, Y. Cui, M. Sommerfeld, J. Elcner, M. Jicha, I. Saveljic, N. Filipovic, F. Lizal, and L. Nicolaou. Regional aerosol deposition in the human airways: The siminhale benchmark case and a critical assessment of in silico methods. *European Journal of Pharmaceutical Sciences*, 2017. doi: https://doi.org/10.1016/j.ejps.2017.09.003. URL `http://www.sciencedirect.com/science/article/pii/S0928098717304992`.

P. G. Koullapis, S.C. Kassinos, M. P. Bivolarova, and A. K. Melikov. Particle deposition in a realistic geometry of the human conducting airways: Effects of inlet velocity profile, inhalation flowrate and electrostatic charge. *Journal of Biomechanics*, 49: 2201–2212, 2016.

P. C. L. Kwok, W. Glover, and H. K. Chan. Electrostatic charge characteristics of aerosols produced from metered dose inhalers. *Journal of Pharmaceutical Sciences*, 94(12):2789–2799, 2005.

S. J. Kwon and I. W. Seo. Reynolds number effects on the behavior of a non-buoyant round jet. *Experiments in fluids*, 38:801–812, 2005.

A.R. Lambert, P.T. O'Shaughnessy, M.H. Tawhai, E.A. Hoffman, and C.-L. Lin. Regional deposition of particles in an imaged-based airway model: Large eddy simulation and left-right lung ventilation asymetry. *Aerosol Science and Technology*, 45: 11–25, 2011.

H.E. Lewis, A.R. Foster, B.J. Mullan, R.N. Cox, and R.P. Clark. Aerodynamics of the human microenvironment. *Lancet*, 322:1273–1277, 1969.

A. Li and G. Ahmadi. Dispersion and deposition of spherical particles from point sources in a turbulent channel flow. *Aerosol Science and Technology*, 16:209–226, 1992.

D. Licina, A. Melikov, J. Pantelic, C. Sekhar, and K.W. Tham. Experimental investigation of the human convective boundary layer in a quiescent indoor environment. *Building and Environment*, 75:79–91, 2014.

D. Licina, A. Melikov, J. Pantelic, C. Sekhar, and K.W. Tham. Human convection flow in spaces with and without ventilation: personal exposure to floor-released particles and cough-released droplets. *Indoor Air*, DOI:10.1111/ina.12206, 2015a.

D. Licina, A. Melikov, C. Sekhar, and K.W. Tham. Transport of gaseous pollutants by convective boundary layer around a human body. *Science and Technology for the Built Environment*, 00:1–12, 2015b.

D. K. Lilly. A proposed modification of the Germano subgrid-scale closure method. *Physics of Fluids A*, 4(3):633–635, 1992.

C.-L. Lin, M.H. Tawhai, G. Mclennan, and E.A. Hoffman. Characteristics of the turbulent laryngeal jet and its effect on airflow in the human intra-thoracic airways. *Respiratory Physiology and Neurobiology*, 157:295–309, 2007.

F. Lizal, M. Belka, J. Adam, J. Jedelsky, and M. Jicha. A method for in vitro regional aerosol deposition measurement in a model of the human tracheobronchial tree by the positron emission tomography. *Proceedings IMechanical E Part H, Engineering in Medicine*, 229(10):750–757, 2015.

P. W. Longest and L. T. Halbrook. In silico models of aerosol delivery to the respiratory tract - development and applications. *Advanced Drug Delivery Reviews*, 64:296–311, 2012.

P. W. Longest, J. T. McLeskey Jr., and M. Hindle. Characterization of nanoaerosol size change during enhanced condensational growth. *Aerosol Science and Technology*, 44 (6):473–483, 2010.

P. W. Longest, G. Tian, R. Delvadia, and M. Hindle. Development of a stochastic individual path (SIP) model for predicting the deposition of pharmaceutical aerosols: effects of turbulence, polydisperse aerosol size, and evaluation of multiple lung lobes. *Aerosol Science and Technology*, 46:1271–85, 2012a.

P. W. Longest, G. Tian, R. L. Walenga, and M. Hindle. Comparing MDI and DPI aerosol deposition using in vitro experiments and a new stochastic individual path (SIP) model of the conducting airways. *Pharm Res.*, 29:1670–88, 2012b.

P. Worth Longest and Jinxiang Xi. Effectiveness of direct lagrangian tracking models for simulating nanoparticle deposition in the upper airways. *Aerosol Science and Technology*, 41(4):380–397, 2007.

P. Worth Longest, Samir Vinchurkar, and Ted Martonen. Transport and deposition of respiratory aerosols in models of childhood asthma. *Journal of Aerosol Science*, 37 (10):1234 – 1257, 2006. doi: https://doi.org/10.1016/j.jaerosci.2006.01.011.

P.W. Longest and S. Vinchurkar. Effects of mesh style and grid convergence on particle deposition in bifurcating airway models with comparisons to experimental data. *Medical Engineering and Physics*, 29(3):350–366, 2007.

P.W. Longest, M. Hindle, S. D. Choudhuri, and J. Xi. Comparison of ambient and spray aerosol deposition in a standard induction port and more realistic mouth-throat geometry. *Aerosol Science*, 39:572–591, 2008.

G. B. Macpherson, N. Nordin, and G. Weller. Particle tracking in unstructured, arbitrary polyhedral meshes for use in CFD and molecular dynamics. *Communications in Numerical Methods in Engineering*, 25(3):263–273, 2009.

E.A. Matida, W.H. Finlay, C.F. Lange, and B. Grgic. Improved numerical simulation of aerosol deposition in an idealized mouth–throat. *Journal of Aerosol Science*, 35 (1):1 – 19, 2004.

Martin R. Maxey and James J. Riley. Equation of motion for a small rigid sphere in a nonuniform flow. *Physics of Fluids A*, 26(4):883–889, 1983.

John E. McDonough, Lars Knudsen, Alexander C. Wright, W. Mark Elliott, Matthias Ochs, and James C. Hogg. Regional differences in alveolar density in the human lung are related to lung height. *Journal of Applied Physiology*, 118(11):1429–1434, 2015. ISSN 8750-7587. doi: 10.1152/japplphysiol.01017.2014. URL `http://jap.physiology.org/content/118/11/1429`.

D.W. McRobbie, S. Pritchard, and R.A. Quest. Studies of the human oropharyngeal airspaces using magnetic resonance imaging. I. Validation of a three-dimensional MRI method for producing ex vivo virtual and physical casts of the oropharyngeal airways during inspiration. *Journal of Aerosol Medicineournal of Aerosol Medicine*, 16:401–415, 2003.

R. Mei. An approximate expression for the shear lift force on a spherical particle at finite reynolds number. *International Journal of Multiphase Flow*, 18(1):145–147, 1992.

C. Melandri, G. Tarroni, V. Prodi, T. De Zalacomo, and M. Formignani. Deposition of charged particles in the human airways. *Aerosol Science*, 14:657–669, 1983.

Michele Miragoli, Paola Ceriotti, Michele Iafisco, Marco Vacchiano, Nicolò Salvarani, Alessio Alogna, Pierluigi Carullo, Gloria Belén Ramirez-Rodríguez, Tatiana Patrício, Lorenzo Degli Esposti, Francesca Rossi, Francesca Ravanetti, Silvana Pinelli, Rossella Alinovi, Marco Erreni, Stefano Rossi, Gianluigi Condorelli, Heiner Post, Anna Tampieri, and Daniele Catalucci. Inhalation of peptide-loaded nanoparticles improves heart failure. *Science Translational Medicine*, 10(424), 2018.

S. Miyawaki, M. H. Tawhai, E. A. Hoffman, S. E. Wenzel, and C.-L. Lin. Automatic construction of subject-specific human airway geometry including trifurcations based on a CT-segmented airway skeleton and surface. *Biomechanics and Modeling in Mechanobiology*, pages 1–14, 2016a.

Shinjiro Miyawaki, Eric A Hoffman, and Ching-Long Lin. Effect of static vs. dynamic imaging on particle transport in CT-based numerical models of human central airways. *Journal of Aerosol Science*, 100:129–139, 10 2016b. doi: 10.1016/j.jaerosci.2016.07.006. URL `http://www.ncbi.nlm.nih.gov/pmc/articles/PMC5224794/`.

Shinjiro Miyawaki, Eric A. Hoffman, and Ching-Long Lin. Numerical simulations of aerosol delivery to the human lung with an idealized laryngeal model, image-based airway model, and automatic meshing algorithm. *Computers & Fluids*, 148:1–9, 2017. doi: https://doi.org/10.1016/j.compfluid.2017.02.008. URL `http://www.sciencedirect.com/science/article/pii/S0045793017300531`.

NCRP. Deposition, retention, and dosimetry of inhaled radioactive substances. Report 125, National Council on Radiation Protection and Measurements, Bethesda, MD, 1997.

L. Nicolaou and T. A. Zaki. Direct numerical simulations of flow in realistic mouth-throat geometries. *Journal of Aerosol Science*, 57:71–87, 2013.

L. Nicolaou and T. A. Zaki. Characterization of aerosol Stokes number in 90^o bends and idealized extrathoracic airways. *Journal of Aerosol Science*, 102:105–127, 2016.

L. Nicolaou, S. Y. Jung, and T. A. Zaki. A robust direct-forcing immersed boundary method with enhanced stability for moving body problems in curvilinear coordinates. *Computers and Fluids*, 119:101–114, 2015.

J. M. Oakes, P. Hofemeier, J. Sznitman, and I. E. Vignon-Clementel. Aerosols in healthy and emphysematous in silico pulmonary acinar rat models. *Journal of Biomechanics*, 49(11):2213–2220, 2016.

Matthias Ochs, Jens R. Nyengaard, Anja Jung, Lars Knudsen, Marion Voigt, Thorsten Wahlers, Richter Joachim, and Hans Jorgen G. Gundersen. The number of alveoli in the human lung. *Am J Respir Crit Care Med*, 169(1):120–4, 2004.

D. E. Olson, L. Borgstrom, Lundback. H., and M. Svensson. Validation of a general in vitro approach for prediction of total lung deposition in healthy adults for pharmaceutical inhalation products. *Journal of Aerosol Medicine and Pulmonary Drug Delivery*, 26(0):1–115, 2013.

B. Olsson and P. Backman. Mouth-throat models for realistic in vitro testing - a proposal for debate. *Respiratory Drug Delivery*, 1:287–294, 2014.

OpenFOAM Foundation. *OpenFOAM Programmer's Guide*. London, UK, version 2.2.1 edition, 2013a.

OpenFOAM Foundation. *OpenFOAM User Guide*. London, UK, version 2.2.1 edition, 2013b.

J. S. Patton and P. R. Byron. Inhaling medicines: delivering drugs to the body through the lungs. *Nature Reviews: Drug discovery*, 6:67–74, 2007.

John S. Patton. Mechanisms of macromolecule absorption by the lungs. *Advanced Drug Delivery Reviews*, 19(1):3–36, 1996.

John S Patton, C Simone Fishburn, and Jeffry G Weers. The lungs as a portal of entry for systemic drug delivery. *Proc Am Thorac Soc*, 1(4):338–344, 2004.

U. Piomelli. Large-eddy simulation: achievements and challenges. *Progress in Aerospace Sciences*, 35(4):335–362, 1999.

V. Prodi and A. Mularoni. Electrostatic lung deposition experiments with humans and animals. *Annals of Occupational Hygiene*, 29(229-240), 1985.

H. Radhakrishnan and S. Kassinos. CFD modeling of turbulent flow and particle deposition in human lungs. *31st Annual International Conference of the IEEE EMBS, Mineapolis, Minnesota, USA*, pages 2867–2870, September 2-6 2009.

P. G. Saffman. The lift on a small sphere in a slow shear flow. *Journal of Fluid Mechanics*, 22(2):385–400, 1965.

P. G. Saffman. The lift on a small sphere in a slow shear flow - corrigendum. *Journal of Fluid Mechanics*, 31(3):624–624, 1968.

L. Schiller and Z. Naumann. *Ver. Deutsch Ing*, 1935.

R. B. Schlesinger and M. Lippmann. Selective particle deposition and bronchogenic carcinoma. *Environmental Research*, 15(424-431), 1978.

A. Schmidt, S. Zidowitz, and A. Kriete. A digital reference model of the human bronchial tree. *Comput Med Imaging Graph*, 28:203–211, 2004.

Camby Mei King Se, Kiao Inthavong, and Jiyuan Tu. Inhalability of micron particles through the nose and mouth. *Inhalation Toxicology*, 22(4):287–300, 2010.

H. D. C. Smyth and A. J. Hickey. *Controlled Pulmonary Drug Delivery, Advances in Delivery Science and Technology Series*. Springer, New York, 2011.

B. Soni and S. Aliabadi. Large-scale CFD simulations of airflow and particle deposition in lung airway. *Computers and Fluids*, 88:804–812, 2013.

K.W Stapleton, E Guentsch, M.K Hoskinson, and W.H Finlay. On the suitability of k-turbulence modeling for aerosol deposition in the mouth and throat: a comparison with experiment. *Journal of Aerosol Science*, 31(6):739 – 749, 2000.

Fotos S. Stylianou, Josué Sznitman, and Stavros C. Kassinos. Direct numerical simulation of particle laden flow in a human airway bifurcation model. *International Journal of Heat and Fluid Flow*, 61, Part B:677 – 710, 2016. ISSN 0142-727X. doi: https://doi.org/10.1016/j.ijheatfluidflow.2016.07.013. URL `http://www.sciencedirect.com/science/article/pii/S0142727X16304052`.

Bora Sul, Anders Wallqvist, Michael J. Morris, Jaques Reifman, and Vineet Rakesh. A computational study of the respiratory airflow characteristics in normal and obstructed human airways. *Computers in Biology and Medicine*, 52:130 – 143, 2014. doi: https://doi.org/10.1016/j.compbiomed.2014.06.008.

Josué Sznitman. Respiratory microflows in the pulmonary acinus. *Journal of Biomechanics*, 46(2):284 – 298, 2013. ISSN 0021-9290. doi: http://dx.doi.org/10.1016/j.jbiomech.2012.10.028. URL `http://www.sciencedirect.com/science/article/pii/S0021929012006355`.

Josué Sznitman, Fabian Heimsch, Thomas Heimsch, Daniel Rusch, and Thomas Raisgen. Three-dimensional convective alveolar flow induced by rhythmic breathing motion of the pulmonary acinus. *Journal of Biomechanical Engineering*, 129(5):658–665, 2007.

G. R. Tabor, M. H. Baba-Ahmadi, E. de Villiers, and H. G. Weller. Construction of inlet conditions for LES of turbulent channel flow. European Congress on Computational Methods in Applied Sciences and Engineering (ECCOMAS), 2004.

M.H. Tawhai and C.-L. Lin. Airway gas flow. *Comprehensive Physiology*, 1:1135–1157, 2011.

Katan Janna Tenenbaum, Hofemeier Philipp, and Sznitman Josué. Computational models of inhalation therapy in early childhood: Therapeutic aerosols in the developing acinus. *Journal of Aerosol Medicine and Pulmonary Drug Delivery*, 29(3):288–298, 2016. doi: 10.1089/jamp.2015.1271.

G. Tian, P. W. Longest, G. Su, R. L. Walenga, and M. Hindle. Development of a stochastic individual path (SIP) model for predicting the tracheobronchial deposition of pharmaceutical aerosols: effects of transient inhalation and sampling the airways. *Journal of Aerosol Science*, 42:781–99, 2011.

G. Tian, M. Hindle, S. Lee, and P. W. Longest. Validating cfd predictions of pharmaceutical aerosol deposition with in vivo data. *Pharm Res.*, 32:3170–3187, 2015.

C. J. Tsai and D. Y. H. Pui. Numerical study of particle deposition in bends of a circular cross-section-laminar flow regime. *Aerosol Science and Technology*, 12:813–831, 1990.

D. K. Walters and W. H. Luke. A method for three-dimensional navier-stokes simulations of large-scale regions of the human lung airway. *J Fluids Engineering*, 132(5): 051101–051101–8, 2010.

O. D. Wangensteen, L. A. Schneider, S. C. Fahrenkrug, G. M. Brottman, and R. C. Maynard. Tracheal epithelial permeability to nonelectrolytes: species differences. *Journal of Applied Physiology*, 75(2):1009–1018, 1993.

E. R. Weibel. *Morphometry of the human lung*. Springer-Verlag, Berlin, 1963.

John B. West. *Respiratory physiology: The essentials*. Lippincott Williams and Wilkins, ninth edition, 1996.

William Wong, David F. Fletcher, Daniela Traini, Hak-Kim Chan, and Paul M. Young. The use of computational approaches in inhaler development. *Advanced Drug Delivery Reviews*, 64(4):312 – 322, 2012. URL `http://www.sciencedirect.com/science/article/pii/S0169409X11002730`.

J. Xi and P. W. Longest. Transport and deposition of micro-aerosols in realistic and simplified models of the oral airway. *Annals of Biomedical Engineering*, 35:560–581, April 2007.

J. Xi, P. W. Longest, and T. B. Martonen. Effects of the laryngeal jet on nano- and microparticle transport and deposition in an approximate model of the upper tracheobronchial airways. *Journal of Applied Physiology*, 104:1761–1777, 2008.

H.-C. Yeh and G. M. Schum. Models of human lung airways and their application to inhaled particle deposition. *Bulletin of Mathematical Biology*, 42:461–480, 1980.

Y. Yin, J. Choi, E.A. Hoffman, M.H. Tawhai, and C.-L. Lin. A multiscale mdct image-based breathing lung model with time-varying regional ventilation. *Journal of Computational Physics*, 244:168–192, 2013.

Youbing Yin, Jiwoong Choi, Eric A. Hoffman, Merryn H. Tawhai, and Ching-Long Lin. Simulation of pulmonary air flow with a subject-specific boundary condition. *Journal of Biomechanics*, 43(11):2159 – 2163, 2010. doi: http://dx.doi.org/10.1016/j.jbiomech.2010.03.048.

C.P. Yu. Theories of electrostatic lung deposition of inhaled aerosols. *Annals of Occupational Hygiene*, 29:219–227, 1985.

Yan Zang, Robert L. Street, and Jeffrey R. Koseff. A dynamic mixed subgrid-scale model and its application to turbulent recirculating flows. *Physics of Fluids A: Fluid Dynamics*, 5(12):3186–3196, 2018/02/09 1993.

Z. Zhang and C. Kleinstreuer. Airflow structures and nano-particle deposition in a human upper airway model. *Journal of Computational Physics*, 198:178–210, 2004.

Z Zhang, C Kleinstreuer, and C.S Kim. Micro-particle transport and deposition in a human oral airway model. *Journal of Aerosol Science*, 33(12):1635 – 1652, 2002.

Z. Zhang, C. Kleinstreuer, and C. S. Kim. Airflow and nanoparticle deposition in a 16-generation tracheobronchial airway model. *Annals of Biomedical Engineering*, 36 (12):2095–2110, 2008.

Z. Zhang, C. Kleinstreuer, and C. S. Kim. Comparison of analytical and cfd models with regard to micron particle deposition in a human 16-generation tracheobronchial airway model. *Aerosol Science*, 40:16–28, 2009a.

Zhao Zhang, Xi Chen, Sagnik Mazumdar, Tengfei Zhang, and Qingyan Chen. Experimental and numerical investigation of airflow and contaminant transport in an airliner cabin mockup. *Building and Environment*, 44(1):85 – 94, 2009b.

Yue Zhou and Yung-Sung Cheng. Particle deposition in a cast of human tracheobronchial airways. *Aerosol Science and Technology*, 39(6):492–500, 2005. doi: 10.1080/027868291001385.

Appendix A

Finite volume discretization in OpenFOAM

A.1 Outline

This appendix describes the discretization within the finite volume framework of continuous PDE?s. The first step is to descritize the solution domain, described in section A.1. The second step is to descritize the continous transport equation, this is discussed in section A.2. More details on the discretization method within OpenFOAM can be found in the PhD thesis of Jasak (1996) and de Villiers (2006).

A.2 Discretization of the solution domain

The spatial discretisation features unstructured boundary fitted meshes with a collocated cell-centred variable ar-rangement. The solution domain is subdivided into control volumes, that fill the domain and do not overlap. A typical control volume is shown in fig.A.1. Each of these control volumes (CV) encapsulates a computational point P at its centroid. The control volume is bounded by a set of flat faces and each face is shared with only one neighbouring CV. For the shaded face in fig. A.1, the owner and neighbour cell centres are marked with P and N. The topology of the control volume is not important - it is a general polyhedron.

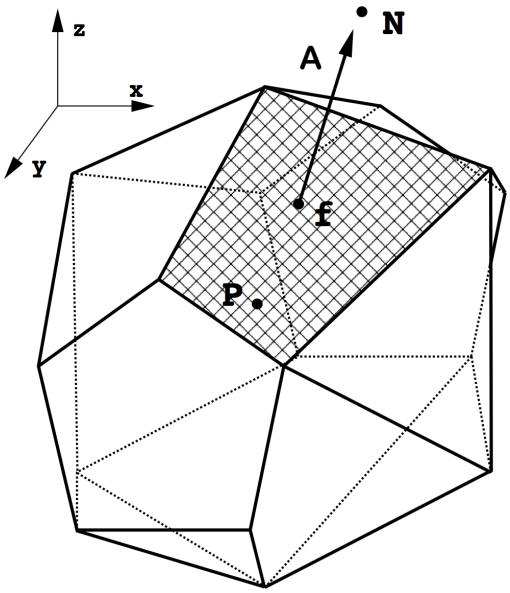

Figure A.1: *Control volume for finite volume discretisation (Jasak, 1996).*

The face area vector **A** is constructed for each face in such a way that it points outwards from the owner cell, is normal to the face and has the magnitude equal to the area of the face. For simplicity, all faces of the control volume will be marked with f, which also represents the point in the middle of the face . While all main dependent variables, such as pressures and velocity, are defined at the cell centroid P, resulting in a collocated arrangement, some derived properties may be defined at the cell face, f.

A.3 Discretization of the transport equation

The standard form of the transport equation for a scalar property ϕ is:

$$\underbrace{\frac{\partial \phi}{\partial t}}_{\text{Temporal term}} + \underbrace{\frac{\partial (u_j \phi)}{\partial x_j}}_{\text{Convection}} - \underbrace{\frac{\partial}{\partial x_j}\left(\Gamma_\phi \frac{\partial \phi}{\partial x_j}\right)}_{\text{Diffusion}} = \underbrace{S_\phi(\phi)}_{\text{Sources}} \tag{A.1}$$

Here ϕ is the transported quantity, i.e. velocity, and Γ_ϕ is the diffusivity coefficient. In the finite volume framework this yields the following integral for the transport equation over a control volume around P:

$$\begin{aligned} \int_t^{t+\delta t} \left[\frac{\partial}{\partial t} \int_{V_P} \phi dV + \int_{V_P} \frac{\partial (u_j \phi)}{\partial x_j} dV - \int_{V_P} \frac{\partial}{\partial x_j}\left(\Gamma_\phi \frac{\partial \phi}{\partial x_j}\right) dV \right] dt \\ = \int_t^{t+\delta t} \left[\int_{V_P} S_\phi(\phi) dV \right] dt \end{aligned} \tag{A.2}$$

It is assumed that the value of ϕ varies linear in space and time, so that:

$$\phi(x_i) = \phi_P + (x_i - x_{P,i}) \frac{\partial \phi}{\partial x_i} \tag{A.3}$$

$$\phi(t+\Delta t) = \phi^t + \Delta t \frac{\partial \phi}{\partial t}_t \tag{A.4}$$

Each of the terms in eq.A.2 will now be treated separately, starting with the spatial functions. Gauss' theorem will be used throughout to reduce many of the volume integrals to their surface equivalents e.g.

$$\int_V \frac{\partial \phi}{\partial x_i} dV = \int_{\partial V} \phi dA_i \tag{A.5}$$

where ∂V is the surface bounding the volume V and dA_i is an infinitesimal surface element with outward pointing normal on the surface ∂V. Using eq. A.3 and the fact that P is located at the centroid of the volume, it follows that:

$$\int_{V_P} \phi dV = \phi_P V_P \tag{A.6}$$

where V_P is the cell volume. Using the fact that the control volume has a finite number of convex faces, integration of the divergence operator over the cell surface produces:

$$\int_{V_P} \frac{\partial \phi}{\partial x_j} dV = \int_{\partial V} \phi dA_i = \sum_f \left(\int_f \phi dA_i \right) = \sum_f A_i \phi_f \tag{A.7}$$

where the subscript f denotes face centred indexing and A_i is the outward pointing surface area vector. The face values, ϕ_f of the variables have to be calculated by some form of interpolation, to be described later.

A.3.1 Convection term

The convection term is a volume integral that contains a term under the divergence operator, therefore it can be discretized using eq. A.7:

$$\int_{V_P} \frac{\partial (u_j \phi)}{\partial x_j} dV = \sum_f A_j (u_j \phi)_f = \sum_f (A_j u_{j,f}) \phi_f = \sum_f F \phi_f \tag{A.8}$$

where F is the volume flux through the face,

$$F = A_j u_{j,f} \tag{A.9}$$

The values of ϕ_f are interpolated from the cell centers to the cells faces using the convection differencing scheme. Various schemes exist. The most obvious choice is to interpolate the values from the cell centers to the cell faces using linear interpolation:

$$\phi_f = f_x \phi_P + (1 - f_x) \phi_N \tag{A.10}$$

where the interpolation factor, f_x, is defined as the ratio of the distances fN and PN (see fig. A.2).

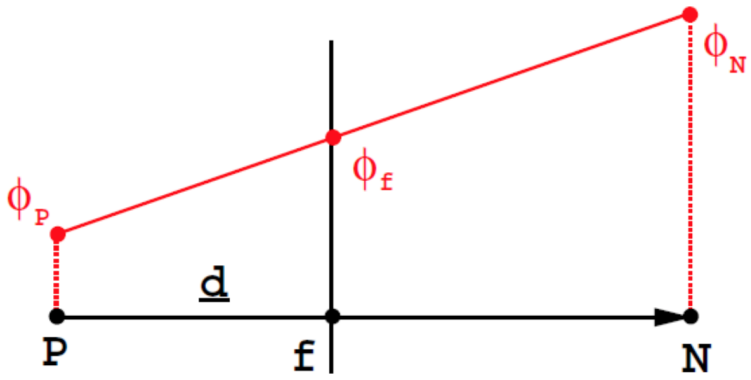

Figure A.2: *Interpolation for the calculation of face values from the values at the cell centers (P and N).*

The linear scheme, also known as Central Differencing scheme, has been shown to be second order accurate even on unstructured meshes. However, this scheme leads to numerical instabilities when the convection term strongly dominates the rest of the system.

An alternative discretisation that improves stability and boundedness is Upwind Differencing. The face value of ϕ is determined according to the direction of the flux.

$$\phi_f = \begin{cases} \phi_P & \text{if } F \geq 0 \\ \phi_N & \text{if } F < 0\,. \end{cases} \tag{A.11}$$

Unfortunately, even second order variations of UD like linear upwind tend to introduce numerical diffusion into the system. This is particularly problematic with LES since the contribution of the modeled turbulent diffusivity is typically very small, so that even modest false diffusion can produce large inaccuracies.

Another option is the mid-point scheme, given as:

$$\phi_f = 0.5\phi_P + 0.5\phi_N \tag{A.12}$$

The midPoint scheme is kinetic energy conservative and 2nd order accurate when there is no cell-stretching. However, it's accuracy reduces to 1st order in non-uniform meshes.

In the current work, a central-differencing interpolation scheme using clipped-weights to improve stability on meshes with very rapid variations in cell size. The selected scheme provides a good compromise between the accuracy of the linear scheme and the stability of the mid-point scheme. It reads as,

$$\phi_f = f_{x,clipped}\phi_P + (1 - f_{x,clipped})\phi_N \tag{A.13}$$

where $f_{x,clipped}$ is given as,

$$f_{x,clipped} = max\Big(min\big(f_x, 1 - \frac{\gamma}{1+\gamma}\big), \frac{\gamma}{1+\gamma}\Big) \tag{A.14}$$

and γ is the clipping factor. In this scheme the value of f_x is set to a maximum (or minumum), determined by the clipping factor. This effectively reduces the instabilities originating from the stretched part of the mesh. After some analysis of stability, a clipping factor 0.8 was determined since using less clipping gave instabilities.

A.3.2 Diffusion term

The diffusion term is discretized in a similar manner as the convective term:

$$\int_{V_P} \frac{\partial}{\partial x_j}\Big(\Gamma_\phi \frac{\partial \phi}{\partial x_j}\Big) dV = \sum_f A_j \Big(\Gamma_\phi \frac{\partial \phi}{\partial x_j}\Big)_f = \sum_f \Gamma_\phi A_j \Big(\frac{\partial \phi}{\partial x_j}\Big)_f \tag{A.15}$$

If the mesh is orthogonal then a straightforward discretization for the face gradient of ϕ would be:

$$A_j \Big(\frac{\partial \phi}{\partial x_j}\Big)_f = |A_i| \frac{\phi_N - \phi_P}{|d_i|} \tag{A.16}$$

where A_i and d_i are parallel and thus the face is orthogonal An example of a non-orthogonal face is shown in fig. A.3.

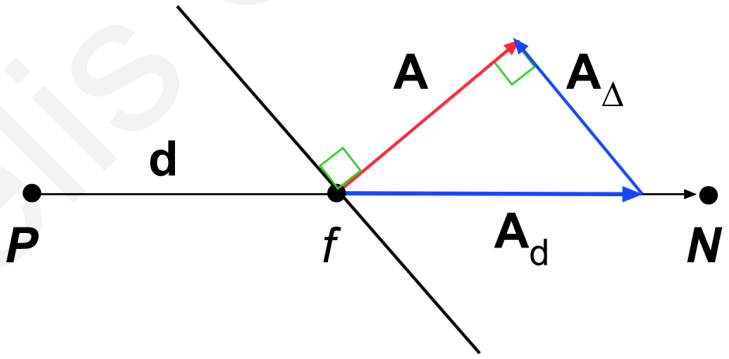

Figure A.3: *Decomposition of the face area vector due to non-orthogonality using the 'over-relaxed' approach.*

For the treatment of the non-orthogonal faces the, eq. A.16 is no longer second order accurate and needs to be supplemented as follows:

$$A_j \Big(\frac{\partial \phi}{\partial x_j}\Big)_f = \underbrace{|A_{d,i}| \frac{\phi_N - \phi_P}{|d_i|}}_{\text{orthogonal}} + \underbrace{A_{\Delta,j} \Big(\widetilde{\frac{\partial \phi}{\partial x_j}}\Big)_f}_{\text{non-orthogonal}} \tag{A.17}$$

where the vector $A_{d,i}$ represents the component parallel to d and $A_{\Delta,i}$ the non-

orthogonal part. It holds that

$$A_i = A_{d,i} + A_{\Delta,i} \tag{A.18}$$

In eq. A.19, the non-orthogonal contribution is given as:

$$\Big(\widetilde{\frac{\partial\phi}{\partial x_i}}\Big)_f = f_x\Big(\frac{\partial\phi}{\partial x_i}\Big)_P + (1-f_x)\Big(\frac{\partial\phi}{\partial x_i}\Big)_N \tag{A.19}$$

where

$$\Big(\frac{\partial\phi}{\partial x_i}\Big)_P = \frac{1}{V}\sum_f \phi_f \tag{A.20}$$

and the tilde signifies the interpolated gradient quantity. Since the non-orthogonal term has a larger computational molecule, it is treated explicitly using values either from the previous iteration or old timestep to keep the number of entries in the system matrix low.

Many possible decompositions exist for the component vectors $A_{d,i}$ and $A_{\Delta,i}$ within the constraints of eq. A.18. Several such configurations are explored by Jasak (1996) with the conclusion that the approach known as 'over-relaxed' is the most robust, convergent and computationally efficient. In the over-relaxed approach the orthogonal vector component is calculated from,

$$A_{d,i} = \frac{d_i}{d_j A_j} A_j A_j \tag{A.21}$$

This approach increases the importance of the term in ϕ_P and ϕ_N with increased non-orthogonality, as shown by the face area decomposition in fig. A.3.

While the diffusion term is bounded on orthogonal meshes, addition of the non-orthogonal correction can produce negative coefficients leading to unboundedness and instability, particularly if the mesh non-orthogonality is high. Under such conditions, the non-orthogonal contribution has to be limited, which reduces the formal accuracy of the diffusion term. In LES, where the results are particularly sensitive to the order accuracy of the equations system, care must thus be taken to keep mesh non-orthogonality within reasonable bounds.

A.3.3 Source terms

All terms of a transport equation that cannot be written as convection, diffusion or temporal contributions are here loosely classified as source terms. Source terms typically consist of a general function of ϕ and other variables, that need to be linearized to be incorporated in the solution matrix:

$$S_\phi(\phi) = S_c + S_p\phi \tag{A.22}$$

where S_c and S_p can also depend on ϕ. Using eq. A.6, this gives the following discretization :

$$\int_{V_P} S_\phi(\phi) dV = S_c V_P + S_p V_P \phi_P \tag{A.23}$$

A.3.4 Time Integration

In the previous Section, the discretisation of spatial terms has been presented. Next we consider the temporal derivative and integration of the generalised transport equation in time. Using eqs. A.8, A.15, A.23 and assuming that the control volumes do not change in time, eq. A.2 can be rewritten as:

$$\begin{aligned} \int_t^{t+\delta t} \left[\left(\frac{\partial \phi}{\partial t} \right)_P V_P + \sum_f F \phi_f - \sum_f \Gamma_\phi A_j \Big(\frac{\partial \phi}{\partial x_j} \Big)_f \right] dt \\ = \int_t^{t+\delta t} \Big[S_c V_P + S_p V_P \phi_P \Big] dt \end{aligned} \tag{A.24}$$

The above expression is usually called the "semi-discretised" form of the transport equation. Having in mind the prescribed variation of ϕ in time, eqn. A.4, the temporal integrals and the time derivative can be calculated directly as:

$$\left(\frac{\partial \phi}{\partial t} \right)_P = \frac{\phi_P^n - \phi_P^{n-1}}{\Delta t}, \tag{A.25}$$

$$\int_t^{t+\delta t} \phi(t) dt = \frac{1}{2} (\phi^{n-1} + \phi^n) \Delta t, \tag{A.26}$$

where $\phi^n = \phi(t + \Delta t)$ and $\phi^{n-1} = \phi(t)$ represent the value of the dependent variable at the new and previous times respectively. Combining eqs. A.24, A.25 and A.26 produces,

$$\begin{aligned} \frac{\phi_P^n - \phi_P^{n-1}}{\Delta t} V_P + \frac{1}{2} \Big[\sum_f F \phi_f - \sum_f \Gamma_\phi A_j \Big(\frac{\partial \phi}{\partial x_j} \Big)_f \Big]^n \\ + \frac{1}{2} \Big[\sum_f F \phi_f - \sum_f \Gamma_\phi A_j \Big(\frac{\partial \phi}{\partial x_j} \Big)_f \Big]^{n-1} \\ = \frac{1}{2} \big[S_c V_P + S_p V_P \phi_P \big]^n + \frac{1}{2} \big[S_c V_P + S_p V_P \phi_P \big]^{n-1} \end{aligned} \tag{A.27}$$

This form of temporal discretisation is called the Crank-Nicholson method. It is second-order accurate in time. It requires the face values of ϕ and $\frac{\partial \phi}{\partial x_j}$ as well as the cell values for both old and new time-level. The face values are calculated from the cell values on each side of the face, using the appropriate differencing scheme for the convection term, and eqn. A.17 for diffusion. Our task is to determine the new value of ϕ_P. Since ϕ_f and $(\frac{\partial \phi}{\partial x_j})_f$ also depend on values of ϕ in the surrounding cells, eqn. A.27 produces

an algebraic equation:

$$\alpha_P \phi_P^n + \sum_N \alpha_N \phi_N^n = R_P \tag{A.28}$$

For every control volume, one equation of this form is assembled. The value of ϕ_P^n depends on the values in the neighbouring cells, thus creating a system of algebraic equations:

$$[A][\phi] = [R] \tag{A.29}$$

where [A] is a sparse matrix, with coefficients α_P on the diagonal and α_N off the diagonal, ϕ is the vector of $\phi's$ for all control volumes and [R] is the source term vector. The sparseness pattern of the matrix depends on the order in which the control volumes are labelled, with every off-diagonal coefficient above and below the diagonal corresponding to one of the faces in the mesh. When this system is solved, it gives a new set of ϕ values. The coefficient α_P in eqn. A.28 includes the contribution from all terms corresponding to ϕ_P^n (the temporal derivative, convection and diffusion terms as well as the linear part of the source term). The coefficients α_N include the corresponding terms for each of the neighbouring points. The summation is done over all CV-s that share a face with the current control volume. The source term includes all terms that can be evaluated without knowing the new $\phi's$, namely, the constant part of the source term, and the parts of the temporal derivative, convection and diffusion terms corresponding to the old time-level.

Besides Crank-Nicholson method, there are several other methods of temporal discretisation. In explicit discretisation, the face values of ϕ and $\frac{\partial \phi}{\partial x_j}$ are determined from the old time-field whereas the Euler Implicit method expresses these values in terms of the new time-level cell values. In explicit discretisation, the new values of ϕ_P can be calculated directly without the need to solve the system of linear equations but the explicit system becomes unstable if the Courant number is greater than unity,

$$Co = \frac{u_j d_j}{\Delta t}. \tag{A.30}$$

Euler Implicit method creates a system of equations and the system is stable even if the Courant number limit is violated. However, it is only first order accurate.

Another temporal discretisation scheme is the second order Backward Differencing, which is second-order accurate in time and uses an extra old time level to calculate the temporal derivative,

$$\phi^{n-2} = \phi(t - \Delta t). \tag{A.31}$$

Now time level n-2 expressed as a Taylor expansion around n is written as:

$$\phi^{n-2} = \phi^n - 2\left(\frac{\partial \phi}{\partial t}\right)^n \Delta t + 2\left(\frac{\partial^2 \phi}{\partial t^2}\right)^n \Delta t^2 + O(\Delta t^3) \tag{A.32}$$

The Taylor expansion for time level n-1 around n with a third order truncation error is given by,

$$\phi^{n-1} = \phi^n - \left(\frac{\partial\phi}{\partial t}\right)^n \Delta t + \frac{1}{2}\left(\frac{\partial^2\phi}{\partial t^2}\right)^n \Delta t^2 + O(\Delta t^3) \tag{A.33}$$

Combining eqs. A.32 and A.33 produces a second order approximation of the temporal derivative at the new time, n:

$$\left(\frac{\partial\phi}{\partial t}\right)^n = \frac{\frac{3}{2}\phi^n - 2\phi^{n-1} + \frac{1}{2}\phi^{n-2}}{\Delta t} \tag{A.34}$$

By neglecting the temporal variation in the face fluxes and derivatives, the final form of the discretised equation with Backward Differencing in time is:

$$\begin{aligned}\frac{\frac{3}{2}\phi^n - 2\phi^{n-1} + \frac{1}{2}\phi^{n-2}}{\Delta t} V_P + \sum_f F\phi_f^n - \sum_f \Gamma_\phi A_j \Big(\frac{\partial\phi}{\partial x_j}\Big)_f^n \\ = S_c V_P + S_p V_P \phi_P^n\end{aligned} \tag{A.35}$$

This produces a system of algebraic equations that must be solved for ϕ_P^n . Backward differencing scheme is cheaper and considerably easier to implement than the Crank-Nicholson method. However, the leading term of the truncation error is four times larger than for the Crank-Nicholson method leading to added numerical diffusion similar to that produced by upwind differencing of the convection term. In practice, the timestep tends to be very small due to the stability constraint of having a Courant number below 1, which keeps the size of temporal diffusion error to a minimum.

A.4 Navier-Stokes Discretisation

Two issues require special attention in the Naver-Stokes equations (eq. 2.2 and 2.4): non-linearity of the momentum equation and the derivation of the pressure equation. .

The non-linear term in the momentum equation is $\frac{\partial}{\partial x_j}(u_i u_j)$, i.e. velocity is 'being transported by itself'. The discretised form of this expression would be quadratic in velocity and the resulting system of algebraic equations would therefore be non-linear. Linearization is achieved by substituting the value of the velocity from the previous iteration for one of the terms as follows:

$$\int_{V_P} \frac{\partial(u_i u_j)}{\partial x_j} dV = \sum_f A_j (u_j u_i)_f \approx \sum_f (A_j u_{j,f}^{n-1}) u_{i,f}^n = \sum_f F^{n-1} u_{i,f}^n \tag{A.36}$$

The flux used to solve the velocity at the new time is thus lagged via the previously known velocity field. The face based quantities in eq. A.36 are approximated by cell values using an appropriate scheme and the cell based momentum convection term is

derived:

$$\sum_f F^{n-1} u_{i,f}^n = \alpha_{cP} u_{i,P}^n + \sum_N \alpha_{cN} u_{i,N}^n \tag{A.37}$$

where the coefficients α_{cP} and α_{cN} are explicit functions of u_i^{n-1}. In transient flows, if the time step is small, the change between consecutive solutions will also be small and it is therefore possible to lag the non-linearity without any significant effect.

Regarding the pressure equation, a semi-discretised form of the momentum equation is used. If eq. A.28 is written for the momentum equation and ϕ is replaced by u_i, we obtain:

$$\alpha_P u_{i,P} = H_i - \frac{\partial p}{\partial x_i} \tag{A.38}$$

The pressure gradient term is not discretised at this stage. Now α_P consists of the sum of the coefficients of $u_{i,P}$,

$$\alpha_P = \alpha_{cP} + \alpha_{dP} + \alpha_{tP} \tag{A.39}$$

where α_{dP} and α_{tP} are the coefficient of $u_{i,P}$ from diffusion and temporal schemes, respectively. The H_i vector consists of the matrix coefficients for all neighbours multiplied with their velocities and the 'source part', that includes the source part of the transient term and all other source terms apart from the pressure gradient,

$$H_i = \sum_N \alpha_N u_{i,N} + \alpha_{tC} + \alpha_{dC} \tag{A.40}$$

where α_{tC} is the portion of the temporal derivative not dependent on u_i^n (which depends on the time discretisation scheme) and α_{dC} is the non-orthogonal contribution from the discretised diffusion term. Dividing both sides of eq. A.38 by α_P produces an expression for $u_{i,P}$,

$$u_{i,P} = \frac{H_i}{\alpha_P} - \frac{1}{\alpha_P}\frac{\partial p}{\partial x_i} \tag{A.41}$$

Interpolating eq. A.41 to express the face velocity gives,

$$u_{i,f} = \left(\frac{H_i}{\alpha_P}\right)_f - \left(\frac{1}{\alpha_P}\right)_f \left(\frac{\partial p}{\partial x_i}\right)_f \tag{A.42}$$

The discretised form of the continuity equation can be written as:

$$\frac{\partial u_j}{\partial x_j} = \sum_f A_j u_{j,f} = 0 \tag{A.43}$$

Substituting eq. A.42 in eq. A.43, produces the pressure equation:

$$\frac{\partial}{\partial x_j}\left(\frac{1}{\alpha_P}\frac{\partial p}{\partial x_j}\right) = \frac{\partial}{\partial x_j}\left(\frac{H_j}{\alpha_P}\right) = \sum_f A_j \left(\frac{H_j}{\alpha_P}\right)_f \tag{A.44}$$

The Laplacian on the l.h.s. of eq. A.44 can be discretised similarly to the diffusion

term.

The final form of the discretised incompressible Navier-Stokes system is:

$$\alpha_P u_{i,P} = H_i - \frac{\partial p}{\partial x_i} \tag{A.45}$$

$$\sum_f A_j \left(\frac{1}{\alpha_P}\right)_f \left(\frac{\partial p}{\partial x_j}\right)_f = \sum_f A_j \left(\frac{H_j}{\alpha_P}\right)_f \tag{A.46}$$

Appendix B

Dispersed phase validations

B.1 Outline

In this section several validation tests are presented for the dispersed phase. Firstly, the Lagrangian particle tracking algorithm of OpenFOAM along with the selected integration and interpolation schemes are validated in a 90^o bent pipe configuration under laminar flow conditions. Next, the developed module for the Electrostatic image charge force is tested against analytical solutions available in the literature. Finally, the implementation of the Brownian force model in OpenFOAM is compared to analytical expressions. In addition, the effect of time step for accurate computation of the Brownian force is investigated.

B.2 Particle tracking algorithm, integration and interpolation schemes

In order to test and validate the particle tracking algorithm and the selected integration and interpolation schemes available in OpenFOAM, we have used a simple laminar case, which consists of a 90^o bent pipe along with straight inlet and outlet sections. The bent pipe geometry serves an excellent validation case since it resembles the human mouth-throat geometry and the flow features are similar to the ones observed in an airway bifurcation under steady laminar conditions. In addition, the same case has been studied previously by Stylianou et al. (2016) and Breuer et al. (2006).

B.2.1 Geometry and mesh

The geometry of the bent pipe is shown in fig. B.1. The pipe radius R is used to normalize all length scales. The 90^o bent pipe has a curvature radius of $R_b = 5.6R$,

whereas the inlet and outlet sections have lengths of $2R$ and $4R$, respectively.

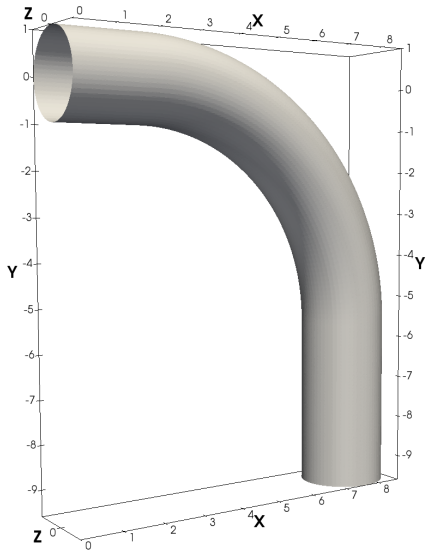

Figure B.1: *Bent pipe geometry.*

Two computational meshes are generated in order to examine the performance of the the tracking scheme on both structured and unstructured meshes. Although structured hexahedral meshes have several advantages over unstructured meshes that employ tetrahedral elements (Longest and Vinchurkar, 2007), the latter are used more often in complex geometries such as the human airways examined in this thesis. This is because the generation of good quality hexahedral meshes requires significant time and effort compared to tetrahedral meshes. Cross-sectional views of these meshes at the inlet of the geometry are shown in fig. B.2. The first mesh (fig. B.2(a)) consists of prismatic cells in the core region ($0 \leq r \leq \frac{R}{2}$) and hexahedral cells in the outer-core region ($\frac{R}{2} \leq r \leq R$). The first grid point from the wall is located at $\Delta r_{min} = 0.003R$ and the expansion ratio of the hexahedral layers is set to $\lambda = 1.030594$. These parameters result in 60 grid radial spaces in the outer-core region. At the wall, the circumferential direction includes 150 equally-spaced grid points. In the core region, constant radial spacing is used ($\Delta r = 0.02R$) and the the number of circumferential spaces is reduced by a factor of 6 for each increment Δr towards the center of the circular section. The streamwise direction includes 200 grid spaces (27/54 for the inlet/outlet sections and 119 for the bent section) resulting in an average grid spacing of 0.074R. The total number of computational cells is 2550000.

The second mesh consists of tetrahedral cells in the core region ($0 \leq r \leq 0.832R$) and prismatic cells in the outer-core region ($0.832R \leq r \leq R$). For the tetra/prism mesh, 11 prism layers are used, with the first grid point from the wall located at $\Delta r_{min} = 0.0075R$ and an expansion ratio of the prismatic zone equal to $\lambda = 1.135$. The circumferential direction at the wall includes 150 equally-spaced grid points. The average grid spacing in the streamwise direction is equal to 0.017R. The total number of

computational cells is 3626376. Therefore the tetra/prism mesh has a coarser resolution in a cross-section, but includes more grid points in the streamwise direction.

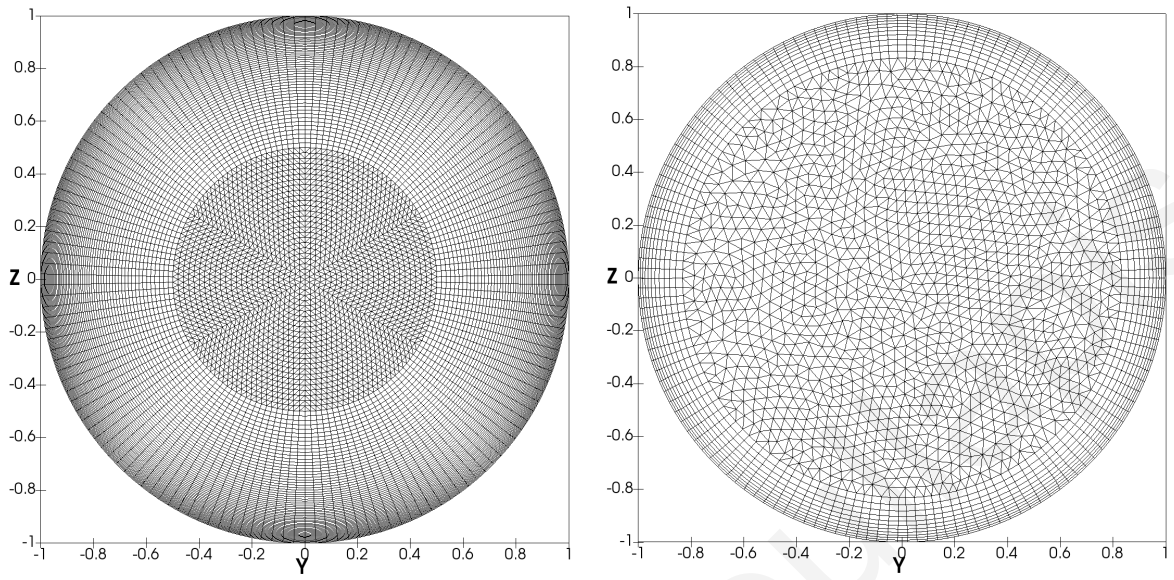

Figure B.2: *Cross-sectional views of the meshes at the inlet of the bent pipe geometry: (a) Hexahedral/prism mesh and (b) Tetrahedral/prism mesh.*

B.2.2 Flowfield

Laminar flow for a bulk Reynolds number of 1000 is simulated ($Re_b = 2Ru_b/\nu_f$). A parabolic velocity profile is specified at the inlet of the geometry. The radius of the pipe (R) and the bulk velocity (u_b) are set to unity. The Navier-Stokes equation for steady laminar flow are solved in OpenFOAM until steady state is achieved.

Fig. B.3 illustrates the velocity magnitude and pressure contours at the mid-plane of the geometry, for the two meshes employed. At the bend, the maximum axial velocity is deflected away from the center and towards the outer side. This results in a thinner/thicker boundary layer at the outer/inner side of the bend. High pressure is found at the outer side of the bend as a result of the "blockage" of the incoming velocity by the pipe walls and the formation of a stagnation region. The velocity fields in the two meshes are in very good agreement, whereas some differences are evident in the pressure fields in the outlet section.

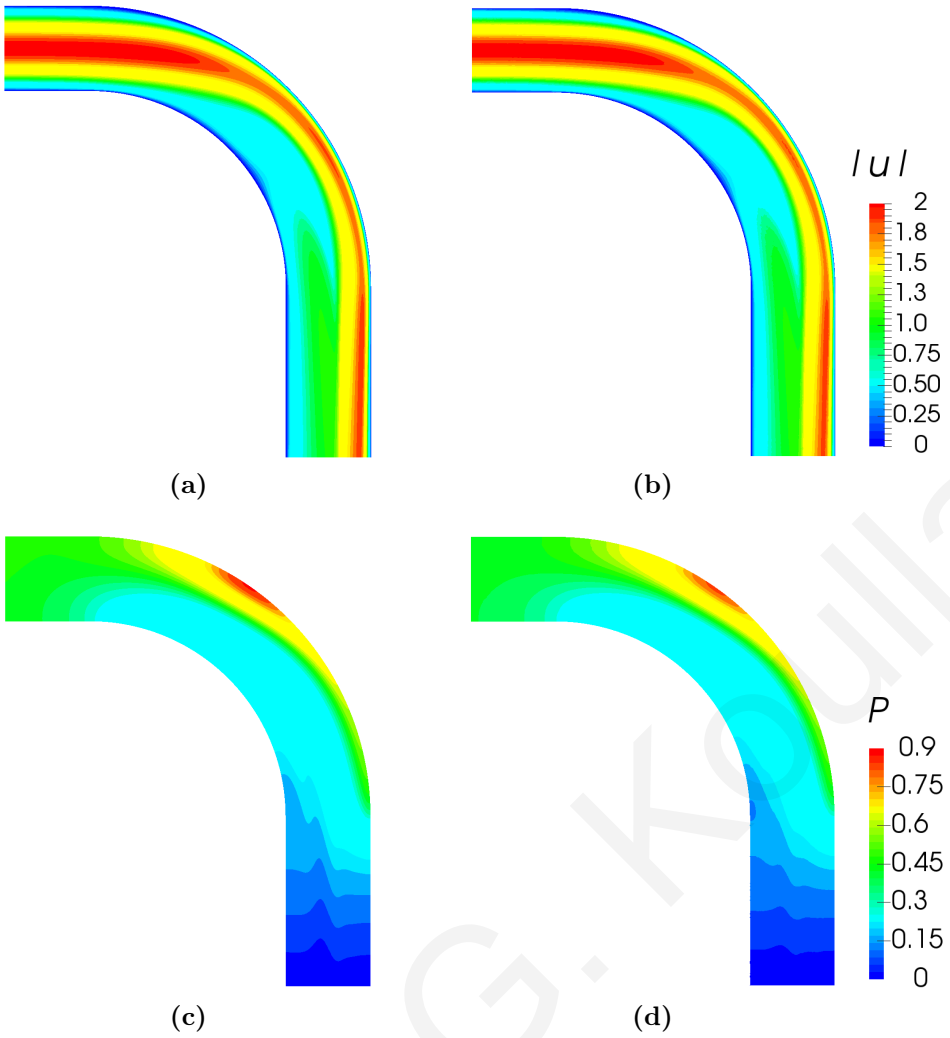

Figure B.3: *Velocity magnitude, (a) and (b), and pressure contours, (c) and (d) at the mid-plane of the geometry, for the two meshes employed.*
(a) and (c): hexa/prism mesh; (b) and (d): tetra/prism mesh.

Our predicted secondary velocities at the outlet section downstream the bend are further compared to the calculations from Breuer et al. (2006). Fig. B.4 displays streamlines of the secondary velocity components from our results (lower part) and the results of Breuer et al. (2006) (upper part). For our results, contours of the local streamwise velocity are also shown.

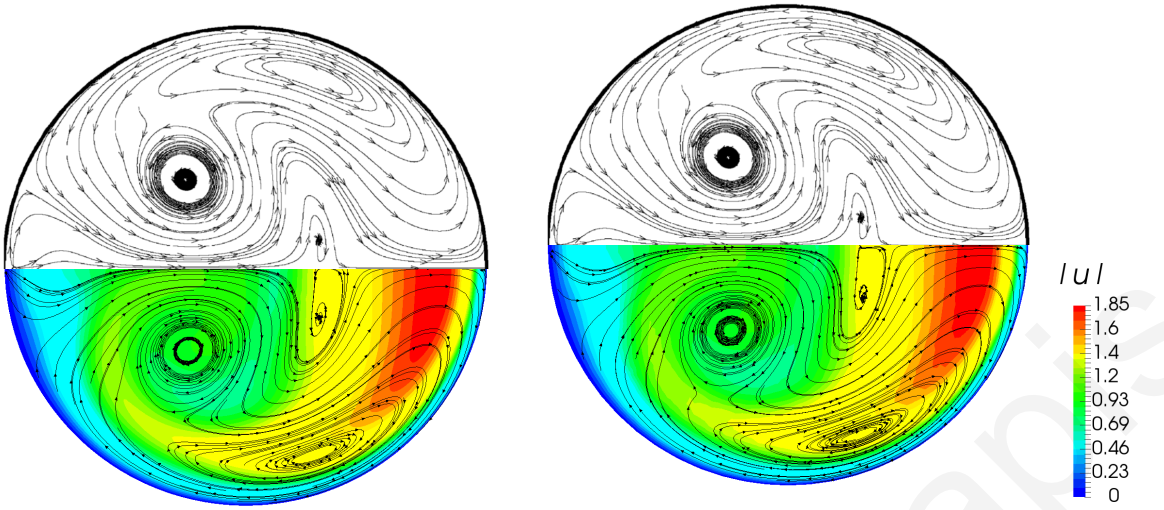

(a) **(b)**

Figure B.4: *Comparison of our results (lower part) with the results of Breuer et al. (2006) (upper part) at the outlet section downstream the bend. Streamlines are constructed using the local in-plane velocities. Contours of the local streamwise velocity are also shown for our predictions.*
(a): hexa/prism mesh; (b): tetra/prism mesh.

Three pair of secondary vortices are evident at this location: (a) the primary Dean vortices, which is a pair of symmetric, counter-rotating vortices formed when a geometry bends, (b) a second pair of smaller vortices near the core of the bent pipe, and (c) a third pair located near the outer sides of the bent pipe. Very good agreement is observed between all sets of data, with all pair of vortices present.

B.2.3 Lagrangian Phase: Particles

Particles are tracked under laminar steady state conditions and assuming one-way coupling between the phases. We have considered particles with density ratio of $\frac{\rho_p}{\rho_f} = 755$, and Stokes numbers ranging from 0.1 to 1. Stokes number is defined as:

$$Stk = \frac{1}{9}\frac{\rho_p}{\rho_f}\frac{d_p^2}{4R^2}Re_b \tag{B.1}$$

For each Stk number, we have released 50000 particles uniformly and randomly from the inlet. The initial velocity of each particle was chosen to be the same with the fluid velocity field at its location of release. All particles were evolved and tracked in the carrier fluid until they either deposit or escape the domain. In order to be able to compare our deposition results to the results of Breuer et al. (2006), we have calculated the deposition efficiencies using the control volume approach defined by Tsai and Pui

(1990):

$$DE(\%) = \frac{\sum_i^{deposited} u_i N_i A_i}{\sum_i^{all} u_i N_i A_i} \text{x}100 \tag{B.2}$$

where u_i, N_i and A_i are the axial flow velocity, the particle concentration, and the area of the i_{th} control volume at the inlet surface, respectively. The numerator represents the sum of the number of depositing particles that were released from the i_{th} control volume. The comparisons between our simulations and the results of Breuer et al. (2006) are shown in fig. B.5.

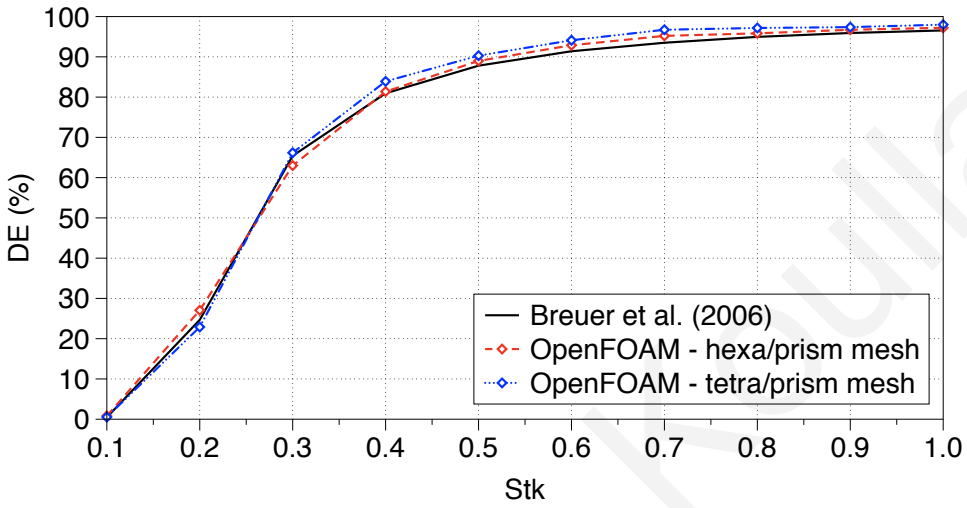

Figure B.5: *Comparison of Deposition efficiencies for laminar flow in bent pipe.*

Overall, good agreement is observed between our results on the two meshes and the results of Breuer et al. (2006). Slight deviations between our results and the results of Breuer et al. (2006) can be attributed to the different interception mechanisms used. Breuer et al. (2006) used a simplified interception mechanism that allows particles to deposit only when they are hosted in a grid volume that is attached to the wall and the particle's centroid is closer to the wall than the center of the control volume. However, for Stk=1, the particle diameter is $d_p = 0.0069m$, which is larger than the distance of the first grid point used in Breuer et al. (2006) ($\Delta r_{min} = 0.0013m$). Therefore, small differences in the numerical solutions are reasonable.

Regarding the effect of mesh style on the deposition predictions, slight deviations are evident between the results on the hexa/prism and the tetra/prism meshes. These differences are about 4% for Stk=0.2. To further assess these differences, we have recorded the initial positions of deposited and escaped particles with Stk=0.2, as shown in fig. B.6. Again, our results on the two different meshes are compared to results reported from Breuer et al. (2006). In these tests, an excellent performance is characterized by distinct patterns of deposited and escaped particles. As observed in fig. B.6(a), this is the case for the hexa/prism mesh. On the other hand, when the tetra/prism mesh is used, overlapping in deposition patterns is observed. The differences between our predicted particle patterns and the results from Breuer et al. (2006)

are more likely attributed to the different interception conditions.

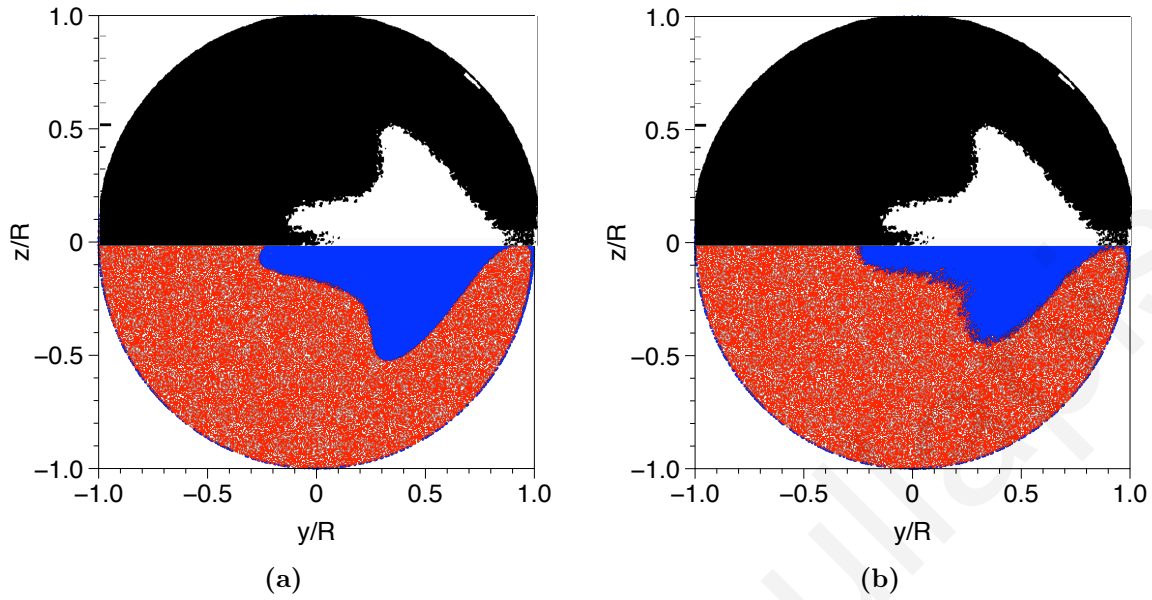

Figure B.6: *Initial positions of deposited (blue or white) and escaped (red or black) particles with St=0.2. Our predictions on the two different meshes (lower row) are compared to results reported from Breuer et al. (2006) (upper row).*
(a) hexa/prism mesh; (b) tetra/prism mesh.

From the above, it is concluded that the tracking scheme performs excellent when a hexahedral/prism mesh is used. When a tetrahedral/prism mesh is employed, which is usually the case when deposition in the airways is assessed, slight deviations are observed compared to the results on hexa/prism mesh. Nevertheless, the accuracy of deposition results is satisfactory even in the tetra/prism mesh.

B.3 Electrostatic image charge force

We created a module in OpenFOAM that accounts for the interaction between the particles and the airway walls due to the electrostatic image charge force. The accuracy of the module is validated by computing the deposition efficiency of spherical particles in laminar pipe flow and comparing to the analytical expression of Chen and Yu (1993). For this purpose, we considered the fully developed and parabolic flow at a Reynolds number of 556 ($U_{bulk} = 1.85333 m/s$) in a 5.6 cm long circular pipe with a diameter of 0.45 cm. Care was taken to ensure that the inlet particle distribution are consistent with the local mass flow rate and the initial particle velocities are matched to the local fluid velocity (Longest and Vinchurkar, 2007). Particles ranging from 1 to 10 ?m are considered with 500 elementary charge units each. Fig. B.7 shows good agreement between our computations and the results of Chen and Yu (1993). Therefore, it is concluded that the CFD model employed in this study is adequate for predicting aerosol

deposition due to the image charge force.

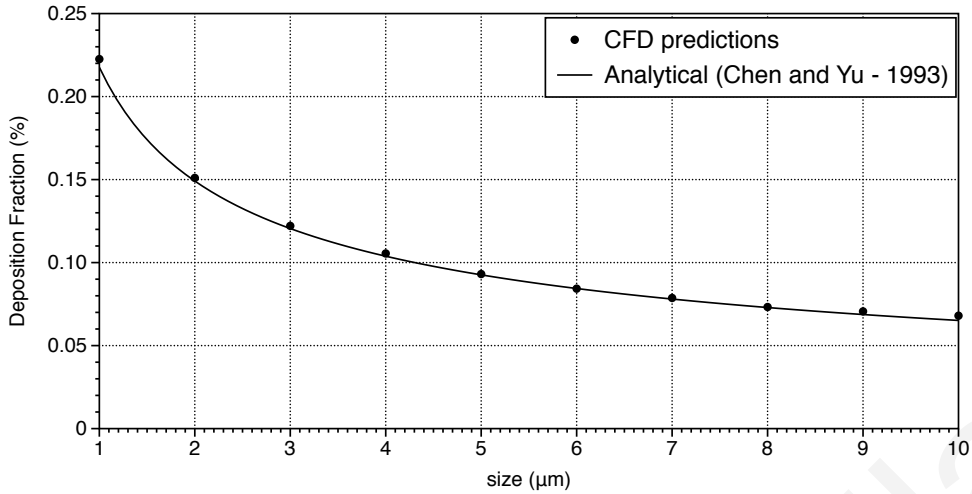

Figure B.7: *Comparison of CFD predicted aerosol deposition due to the electrostatic image charge force with the analytic expression of Chen and Yu (1993) - q=500e per particle.*

B.4 Brownian motion force

To validate the implementation of the Brownian force model in OpenFOAM, two tests are carried out. In the first test, the predicted radial root-mean-square (rms) displacements of particles originating from a single position are assessed and compared with analytical expression for particle ensembles. In the second test, our deposition predictions in a fully developed tubular flow are compared to the analytic expression of Ingham for deposition due to Brownian diffusion. We need to note that the calculation of Brownian force using equation 2.32 contains the time step for particle integration (Δt), and thus, Brownian force might be influenced by the selected time step. In our case, a constant time step is used and it's value is selected based on the tests presented below.

For the first test, groups of 500 particles are released in a box with uniform flow in one direction. Since the flow is unidirectional, dispersion of particles in the transverse direction can occur only as a result of Brownian motion. Therefore, the rms of their displacement in the transverse direction is computed and compared to the expected standard deviation value over time, given by (Einstein, 1926):

$$r_{rms} = \sqrt{4\tilde{D}t} \tag{B.3}$$

where $\tilde{D}$ is the diffusion coefficient. Fig. B.8 displays the predicted rms displacements over time for groups of 100nm and 500nm particles, along with the theoretical standard deviation values given by eq. B.3. In addition, numerical results obtained with $\Delta t = 1e-04s$ and $\Delta t = 1e-05s$ are shown.

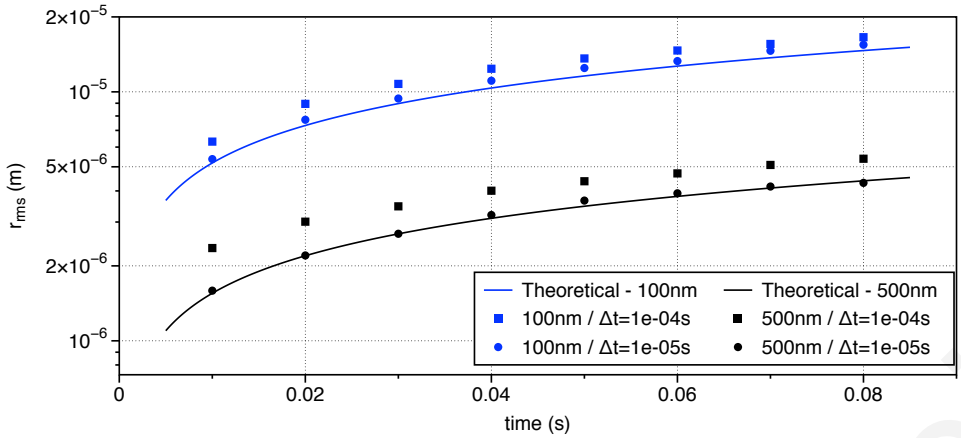

Figure B.8: *Comparisons of predicted root-mean-square displacements (r_{rms}) in the transverse direction over time to analytical standard deviation values. Results for two particle sizes, 100nm and 500nm, and two selected time steps are presented.*

For $\Delta t = 1e-05s$, good agreement is observed between the computed and analytical results, whereas for the larger time step, deviations are evident compared to the theoretical values. Based on the findings presented above, time steps smaller than $1e-05s$ are used when the Brownian force is included in our simulations.

Considering deposition due to Brownian motion in a fully developed tubular flow, Ingham (1975) suggested the following expression for deposition efficiency (DE) based on a steady Eulerian model:

$$DE(\%) = 100 \cdot \left(1 - 0.819e^{-14.63\cdot\Delta} - 0.0976e^{-89.22\cdot\Delta} - 0.0325e^{-228\cdot\Delta} - 0.0509e^{-125.9\cdot\Delta^{2/3}}\right) \tag{B.4}$$

where Δ is a dimensionless diffusion parameter, defined as:

$$\Delta = \frac{\tilde{D}L}{4UR^2} \tag{B.5}$$

with L and R being the length and radius of the tube and U the bulk velocity. Fully developed and parabolic flows at Reynolds numbers of 278, 556 and 1113 are considered through a 5.6cm long circular pipe with a diameter of 0.45cm. Similar flow conditions are found in the airways of fourth generation of an adult male during inhalation flow rates of 15, 30, and 60 L/min through the trachea, which correspond to sedentary, light and heavy activity conditions (Longest and Xi, 2007). Inlet particle distribution are consistent with the local mass flow rate and the initial particle velocities are matched to the local fluid velocity. Fig. B.9 shows the Deposition efficiencies as predicted in OpenFOAM and in comparison to the analytic results given by eq. B.4.

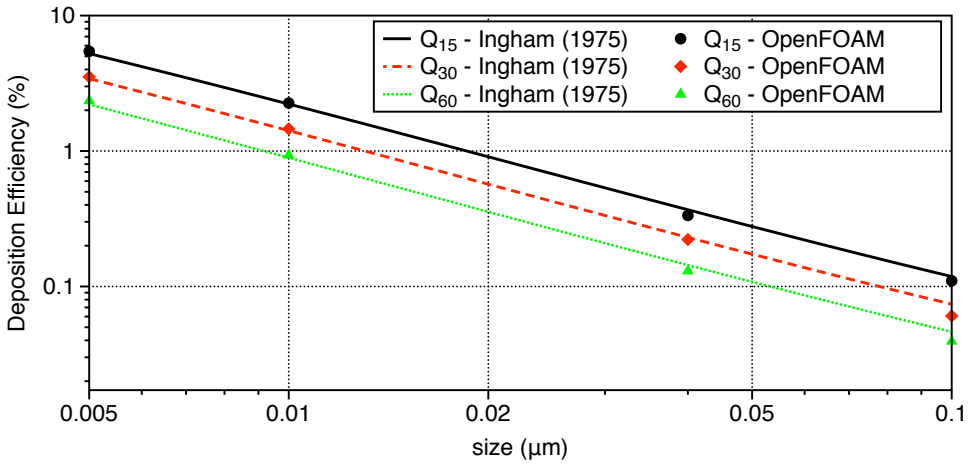

Figure B.9: *Deposition efficiencies for fully developed and parabolic flows through a circular pipe in comparison to the analytic results of Ingham (1975).*

The agreement is quite good for all particle sizes and flowrates considered.

The deposition characteristics in this simple configuration are also examined. Fig. B.10 illustrates the deposition patterns in the tube for 5, 10 and 100nm particles for a tracheal flowrate of 30L/min. The release positions (at the inlet) of the deposited particles are also shown.

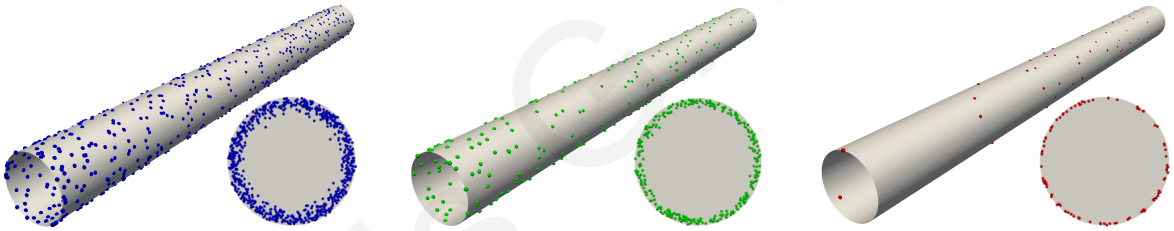

(a) **(b)** **(c)**

Figure B.10: *Deposition patterns for a tracheal flowrate of 30L/min. The release positions of deposited particles are also shown. (a) 5nm; (b) 10nm; (c) 100nm particles.*

It can be observed that deposition is increased as the particle size decreases and the deposited particles are uniformly distributed on the airway walls. Smaller particles exhibit larger fluctuations in their movement and thus they have a higher probability to deposit when they are released close to the walls of the tube. This is clearly evident in the simulation results.